INVESTIGATION OF THE MECHANISMS OF OXYGEN DELIVERY AND CELL DEATH IN OXYGEN-ENHANCED SONODYNAMIC THERAPY

Alexandra Vasilyeva

Department of Engineering Science

Institute of Biomedical Engineering

University of Oxford

Supervised by Prof. Eleanor Stride

2022

Nullius in verba

- Motto of the Royal Society of London
for Improving Natural Knowledge

Table of contents

Abstract

Sonodynamic therapy, which is usually defined as ultrasound-mediated activation of certain drugs, is of substantial interest in the field of oncology. However, currently there is no consensus on the mechanisms of its action, and elucidating them would assist in the transition of sonodynamic therapy into clinical practice. There is a discrepancy between the observed low quantities of reactive oxygen species produced by drugs combined with ultrasound and the substantial *in vivo* effects seen in a number of studies; in addition, for oxygen-enhanced sonodynamic therapy, there is also a mismatch between the low dose of oxygen transported by the carrier agents and the observed improvements in therapy outcomes. The overall goal of this thesis was to investigate these discrepancies. Hypotheses were proposed to explain both mismatches, and new setups and experiments were designed to test them, resulting in a better understanding of oxygen-enhanced sonodynamic therapy mechanisms.

Acknowledgements

I would like to thank my supervisor Prof Eleanor Stride for her amazing support and her continuing faith in my project. I would also like to extend my gratitude to Dr Luca Bau for many helpful discussions, Kritika Singh and Veerle Brans for their help with cell experiments, Dr Michael Gray for his thoughtful design and patient support of ultrasound setups, Romain Guyon for teaching me the technique of working with polymers, Dr Shamit Shrivastava for his help with optical setups, as well as many other BUBBL members and collaborators for their help and input. My deepest gratitude goes to James Fisk for providing excellent support in the workshop and Daphne Cunningham for her help in numerous management queries. Last but not least, a big thank you to my family (my Mom and Dad and Mr Darcy) and my partner Lev.

Papers:

- Investigation of the ultrasound-mediated toxicity mechanisms of sonosensitive drugs in different cell line models

  A. Vasilyeva, K. Singh, V. Brans, M. Gray, E. Stride

  In preparation

- Investigation of mechanisms of oxygen delivery by non-haemoglobin-based oxygen carriers

  A. Vasilyeva, A. Bush, E. Stride

  In preparation

- Comparison of reactive oxygen species types produced during ultrasound and light activation of sonosensitive drugs

  K. Singh, A. Vasilyeva, V. Choi, M. Gray, E. Stride

  In preparation

- Orally administered oxygen nanobubbles enhance tumor response to sonodynamic therapy

  J. Owen, K. Logan, H. Nesbitt, S. Able, A. Vasilyeva, E. Bluemke, V. Kersemans, S. Smart, K. Vallis, A. McHale, J. Callan, E. Stride
  Nano Select (2021)

- Studying Cavitation Enhanced Therapy

  M. Gray, A. Vasilyeva, V. Brans, E. Stride
  JoVE (2021)

Conference presentation:

- Investigation of the effect of orally administered oxygen bubbles upon tumour response to sonodynamic therapy

  J. Owen, K. Logan, H. Nesbitt, A. Vasilyeva, E. Bluemke, S. Able, K. Vallis, A. McHale, J. Callan, E. Stride
  The 25th European symposium on Ultrasound Contrast Imaging (16-17 January 2020, Rotterdam, The Netherlands) – *poster and oral presentation*

List of abbreviations

2,3-DPG	2,3-diphosphoglycerate
ABDA	9,10-anthracenediyl-bis(methylene)dimalonic acid
CAM	calcein acetoxymethyl (AM)
CMB	Cell Mask Blue
CMDR	Cell Mask Deep Red
DBPC	1,2-dibehenoyl-sn-glycero-3-phosphocholine
DC	duty cycle
DOX	doxorubicin
DPBF	1,3-diphenylisobenzofuran
DPBS	Dulbecco's phosphate-buffered saline
DPPA	1,2-dipalmitoyl-sn-glycero-3-phosphate
DPPE	1,2-dipalmitoyl-sn-glycero-3-phosphorylethanolamine
DPPG	1,2-dipalmitoylphosphatidylglycerol
DSPC	1,2-distearoyl-sn-glycero-3-phosphocholine
DSPE	1,2-distearoyl-sn-glycero-3-phosphoethanolamine
FFA	furfuryl alcohol
Hb	haemoglobin
HBO	hyperbaric oxygen
HBOC	haemoglobin-based oxygen carrier
HIF-1α	hypoxia-inducible factor 1-α
HPLC	high-performance liquid chromatography
ID	inner diameter
IR	infrared
HSA	human serum albumin
MB	microbubble
MPEG	methoxyl poly(ethylene glycol)

MPEG5000 DPPE	N-(carbamoyl-methoxypolyethylene glycol 5000)-1,2-dipalmitoyl-cephalin sodium
NB	nanobubble
ND	nanodroplet
OD	outer diameter
PBOC	perfluorocarbon-based oxygen carrier
PBS	phosphate-buffered saline
PDMS	polydimethylsiloxane
PDT	photodynamic therapy
PEG	polyethylene glycol
PEG40S	polyethylene glycol (40) stearate
PFB	perfluorobutane (decafluorobutane)
PFC	perfluorocarbon
PFD	perfluorodecalin
PFDB	perfluorodecyl bromide
PFH	perfluorohexane
PFOB	perfluorooctyl bromide (perflubron)
PFP	perfluoropropane (octafluoropropane)
PFTBA	perfluorotributylamine
PFTPA	perfluorotripropylamine
PI	propidium iodide
pk-pk	peak to peak
PLGA	polylactic-co-glycolic acid
PMCP	perfluoro N-(4-methylcyclohexyl)piperidine
PRF	pulse repetition frequency
PTFE	polytetrafluoroethylene
PVA	poly (vinyl alcohol)
RB	rose bengal
RBC	red blood cell

ROS	reactive oxygen species
RT	radiotherapy
SDT	sonodynamic therapy
SF_6	sulfur hexafluoride
SOSG	Singlet Oxygen Sensor Green
TSC	trans-sodium crocetinate
US	ultrasound
VEGF	vascular endothelial growth factor

Chapter 1. Literature review

1.1 Introduction

It is a truth universally acknowledged that, despite remarkable progress in both prevention and treatment, cancer remains an immense healthcare burden. Numerous directions in cancer therapy are currently in active development, with the main goal of enhancing the efficiency of the intervention while at the same time reducing its side-effects, which is a well-known challenge for many oncological treatments.

One of the therapies that is especially promising for this balance is sonodynamic therapy (SDT), which is usually defined as localised ultrasound-mediated activation of drugs. While localisation is in itself a beneficial strategy utilised in many types of targeted drug delivery, ultrasound as an activating stimulus has additional advantages of a well-known good safety profile, larger penetration depth compared to light, as used in the analogous photodynamic therapy (PDT), and its ability to promote drug extravasation deeper into the tumour and better uptake due to transient cell membrane perforation.

Nevertheless, SDT has yet to be widely adopted clinically, with few clinical trials having reached later stages. One of the reasons behind this is that SDT is a relatively new therapy and, unlike PDT, currently lacks a detailed understanding of its mechanisms. It is widely accepted that SDT may, similarly to PDT, induce cell death via generating reactive oxygen species (ROS), and therefore would be hindered by tumour hypoxia and enhanced by localised oxygen delivery. However, the currently existing studies on the exact ROS species generated during SDT have not come to a unified conclusion, and for oxygen-enhanced SDT there seems to be a discrepancy between the amount of oxygen that could be carried in gas-transporting agents and the magnitude of effects seen in *in vivo* studies. Therefore, the work in the present thesis has focused on further

researching the mechanisms of, firstly, oxygen delivery by artificial carriers and, secondly, of ROS generation and cell toxicity mechanisms of SDT drugs.

The literature review in this Chapter is hence focused on these two topics. The sub-chapter 1.2 addresses the questions of tumour hypoxia, targeted delivery of oxygen to tumours by artificial carriers and the current understanding of the mechanisms of this process. The sub-chapter 1.3 discusses the current knowledge of the SDT action and the generated ROS types, as well as possible additional considerations of the drug toxicity mechanisms introduced by ultrasound.

1.2 Oxygen delivery to tumours: context and mechanisms

1.2.1 Role of oxygen and reactive oxygen species in cancer progression

Hypoxia, i.e., an imbalance between oxygen supply and consumption, is a common feature of locally advanced solid tumours. Its primary cause is the disorganized microarchitecture of vascular network in cancerous tissues which results in impaired blood flow and inadequate oxygen delivery to cells[1]. Hypoxia can be further exacerbated by disease- or treatment-associated anemia[2]. Tumour hypoxia is associated with impaired therapeutic response, malignant progression and worse clinical outcomes[3] and in particular it has been shown to lower the efficiency of treatments dependent on reactive oxygen species (ROS) generation, such as chemo- and radiotherapy[4,5].

Although the negative role of hypoxia in cancer is well-established, the relationship between oxygen levels, ROS concentrations and tumour progression is complicated and involves several different processes, some of which are not yet fully understood. The most apparent factor is that lower oxygen concentration directly results in less efficient ROS generation, which hinders ROS-dependent therapies such as chemo-, radio- and photodynamic therapy. Hypoxia is also believed

to play a role in the development of aggressive cell phenotypes which have suppressed apoptosis pathways and are more resistant to therapeutic interventions[6]. In addition, there are various relationships between oxygen content and therapeutic outcomes which are correlative rather than causative, but which can still contribute to the apparent connection between hypoxia and diminished treatment efficiency. For instance, impaired vascularization, which is the major cause of low oxygen content in tumours, also prevents therapeutic agents, such as drugs or sensitizers, from efficiently diffusing into cancerous cells that are too remote from blood vessels[7].

Despite the difficulty in clarifying some of the mechanisms, the links between hypoxia and negative treatment outcomes, as well as hypoxia alleviation and more positive results, are well-established. Developing safe and effective strategies of tumour oxygenation are therefore of substantial interest for cancer treatment. The following section outlines various approaches to changing the oxygenation state of tumours, as well as their advantages and drawbacks.

1.2.2 Methods of alleviating tumour hypoxia

There are various approaches one can take to change the oxygenation status of tissues. Many different methods have been tested for alleviating tumour hypoxia, which can be roughly classified as follows: manipulating breathing gas composition; making changes to the circulatory system components; decreasing oxygen consumption of cells; enabling *in situ* oxygen production and introducing exogenous oxygen carriers.

Arguably the most straightforward solution for alleviating hypoxia is increasing oxygen concentration in the breathing gas of the patient. Hyperbaric oxygen (HBO) therapy is a well-known method involving breathing 100% oxygen under increased pressure; it has been widely used for treatment of such conditions as decompression sickness and carbon monoxide poisoning.

It has also shown promise in alleviating tumour hypoxia when used in combination with radio-, chemo- and photodynamic therapy[8]; however a certain number of studies that found no benefit[9], possibility of systemic oxygen toxicity, as well as technical difficulties and safety concerns associated with combining hyperbaric oxygen chambers with other therapies, have prevented its widespread use.

Another breathing gas examined for tumour oxygenation is carbogen – a mixture of CO_2 and O_2; CO_2 content in carbogen is usually 5% but can be as low as 1.5% and as high as 50% in different compositions. Its action is based on increasing blood levels of carbon dioxide, which trigger mechanisms associated with suffocation, such as deeper breathing and increase in heart rate, and lead to better blood oxygenation. However, similar to HBO, despite allegedly alleviating tumour hypoxia[10], it has not yet shown sufficient therapeutic efficiency compared to the risks and difficulties of introducing it in clinical practice.

A different approach to increasing local oxygen levels is manipulating the circulatory system or its components. Different methods of enhancing oxygen transport include stimulation of red blood cell production by erythropoietin treatment[11] and introducing haemoglobin O_2 release co-factors, for example 2,3-diphosphoglycerate[12]. Although manipulating the circulatory system and enhancing the existing mechanisms in the body to fight hypoxia is an elegant concept, a major problem of such methods is insufficient selectivity that can lead to serious systemic side effects.

It is possible to look at the problem from a different angle. Hypoxia is, by definition, an imbalance between oxygen consumption and supply; therefore it is possible to relieve it not only by delivering more oxygen to target cells, but also by decreasing their intake of O_2. In particular, it has been attempted to mediate tumour oxygenation status via introducing drugs that inhibit O_2 consumption[13], glucose (making use of the Warburg effect)[14], or by such simple mechanisms as

regulating tumour area temperature[15]. Unfortunately, these methods, just as the ones described above, still suffer from insufficient efficiency and/or unwanted side effects.

To achieve high efficiency of oxygenation, some strategies have been put forward for *in situ* oxygen production. Usually such a system is based on nanoparticles[16,17], but other complex solutions, such as O_2-generating implants[18], have also been suggested. The major limitation of artificial oxygen generation in the body is the need for extremely careful regulation and localization to avoid systemic toxicity, which has not yet been met.

Since the methods described above have not yet achieved the necessary levels of efficiency and safety, the remaining solution is to introduce biocompatible exogenous oxygen carriers. This is an especially promising approach since tumour hypoxia is partly caused by disease- or treatment-related anaemia, which limits oxygen-carrying capabilities of blood and therefore calls for introducing additional O_2 carriers.

A well-established way to introduce exogenous oxygen carriers is by blood transfusion. This procedure is widely used to treat traumatic and surgical blood loss; however, it is capable of promoting an immune response and has not been shown to give a sufficient advantage in cancer therapy[19]. Consequently, the main efforts in this area have been directed at developing and testing artificial oxygen-carrying agents.

Various types of artificial oxygen carriers, as well as the possible mechanisms of their action, are described in the following section.

1.2.3 Types of oxygen carriers

Artificial oxygen carriers have applications in many areas. Most notably, a large number of agents has been developed for transfusions in circumstances when safe donor blood is not readily available (in this context such carriers are commonly referred to as “artificial blood”, or “blood substitutes”, although they are not intended to replace all the other functions of blood). Various types of agents, including ones enabling stimuli-responsive oxygen release, have been developed for other applications, such as management of myocardial infarction or stroke. Consequently, artificial oxygen carriers can be sub-divided based on the primary intended application into the agents for continuous delivery via blood circulation (such as blood substitutes) and carriers for localized oxygen release.

The two main types of artificial oxygen carriers are haemoglobin-based and perfluorocarbon-based particles; however, a number of other types of carriers were also developed for specific applications. Agents made from various materials have been utilized for both systemic and local oxygenation, but perfluorocarbon carriers in particular are widely used for both continuous and localized oxygen delivery due to their high inertness, good oxygen-loading capability and responsiveness for ultrasound.

A wide variety of agents has been implemented to alleviate tumour hypoxia, and their proposed mechanisms of oxygen transport differ depending on the material and mode of payload release. The sub-sections below give an overview of different types of agents, starting from their initial applications as artificial blood, followed by an overview of current progress in oncology, and then discuss the proposed mechanisms of systemic and localized oxygen delivery.

1.2.3.1 Haemoglobin-based blood substitutes

A wide class of artificial oxygen carriers is based on the main O_2-transporting component of blood – haemoglobin (Hb). Haemoglobin-based oxygen carriers (HBOCs) were among the first scientific attempts at creating artificial blood, attempted after the oxygen-carrying function of haemoglobin was understood. However, the first HBOCs were based on cell-free haemoglobin and, unfortunately, caused severe side effects: free haemoglobin readily dissociates into dimers that cause kidney damage, triggers systemic vasoconstriction by excessive binding of nitric oxide and has high affinity to oxygen due to the lack of oxygen-release co-factors such as 2,3-DPG[20]. In addition, red blood cells (RBCs) store a variety of enzymes that prevent oxidative damage caused by spontaneous oxidation of the ferrous heme iron, as well as catalyse the reduction of the ferric iron back to its oxygen-binding ferrous state; these mechanisms are disrupted in cell-free haemoglobin[21].

After these initial failures, substantial progress was made in developing cross-linked haemoglobin-based agents. Several methods for creating such agents were proposed, and some of them showed promising safety and efficiency profiles and reached the clinical trials stage. To date, however, the clinical trials attempted with HBOCs have failed, primarily because their complication rates were higher than those of traditional blood transfusions. This stalled further development of haemoglobin-based artificial blood; although research in this area continues[22], to date it remains problematic[23]. To this day there are no HBOCs approved for clinical use as a blood substitute in EU, UK or the USA; their approval remains limited to a small number of locations and/or compassionate use protocols[24,25]. (The bovine haemoglobin-based agent HBOC-201 (Hemopure) holds clinical approval in South Africa; compassionate use, i.e., use in eligible patients when there are no alternatives, for HBOC-201 is allowed in several hospitals in the USA.)

1.2.3.2 Perfluorocarbon-based blood substitutes

HBOCs were expected to be an effective blood substitute due to the biologically fine-tuned affinity of haemoglobin to oxygen; however it became clear that the complex biological properties of Hb also cause various side-effects that were difficult to mitigate. For this reason, an alternative approach to creating a fully artificial blood substitute started to develop: even with oxygen-transporting behaviour inferior to that of natural Hb, such an agent could still be of great use if its side effects were sufficiently low.

Perfluorocarbons (PFCs) – hydrocarbons in which all hydrogen atoms have been replaced by fluorine atoms – have attracted attention as a promising candidate due to their chemical and biological inertness and high oxygen solubility[26]. Unlike haemoglobin, they have a linear oxygen release response as a function of surrounding O_2 concentration.

Several PBOC formulations have successfully reached the clinical trials stage and even received approval in several countries. First-generation PFC-based blood substitutes that have been approved for human use include Fluosol (Japan) and Perftoran (Russia). Fluosol (Green Cross, Japan) was rejected by the US FDA for treatment of anemia in 1983, but six years later was approved in a more limited capacity as an adjunct to coronary angioplasty, becoming the first oxygen-carrying agent approved by the FDA[27]. However it was withdrawn from the market in 1994 due to various issues including difficult handling procedures and some incidence of side effects, many of which have been attributed to the surfactant Pluronic F-68, which was replaced by phospholipids in later formulations[27]. Perftoran was developed by the Academy of Sciences of the USSR and later the Russian Academy of Sciences and approved for clinical use in 1997. As of 2020 Perftoran still holds clinical approval in Russia, although its current production status is unclear, and has been approved for certain periods of time in Ukraine, Kazakhstan, Kyrgyzstan, Uzbekistan

and Mexico. Perftoran has been rebranded as Vidaphor for marketing in North America, where FluorO_2 Therapeutics intended (as of 2019) to pursue regulatory approval for its use in the USA[28].

Second-generation PBOCs addressed some of the issues encountered by earlier products, in particular by utilizing phospholipid-based surfactants and developing simpler handling protocols. PFC-based agents that followed into clinical trials included Oxygent, Oxyfluor and Oxycyte; however these studies were terminated due to adverse effects[24]. The reasons behind these failures have been discussed and disputed – for example, it was argued that the incorrectly designed clinical protocol was to blame for the Oxygent side effects, rendering the trial results inconclusive[29]. Regardless of the reasons, the unsuccessful clinical trials of PBOCs have slowed the attempts to develop these blood substitutes for general clinical use, although work on improving formulations is ongoing[30].

1.2.3.3 Haemoglobin- and perfluorocarbon-based oxygen carriers for cancer hypoxia alleviation

Since neither HBOCs nor PBOCs have yet demonstrated sufficient safety for replacing blood transfusions in general clinical use, much of the focus has shifted from finding a replacement for allogeneic blood to developing agents which are acceptable in situations when donor blood is not available at all, and in that area the quest for an optimal blood substitute is still ongoing[24].

Another direction that emerged for artificial oxygen carrier research was applying blood substitutes or developing new agents for other applications which have different side effect requirements. A notable example of such an application is alleviating tumour hypoxia in order to improve diagnostic prognosis. As described above, blood transfusions have been tested for improving tumour oxygen status but showed insufficient efficiency for the therapy outcome; therefore, artificial oxygen carriers with characteristics different from those of natural RBCs could be promising in this area, especially considering that the acceptable level of side-effects in some

oncological therapies is high compared to the unwanted effects seen in latest blood substitute trials.

Consequently, some existing blood substitute solutions, as well as other haemoglobin-based agents, have been tested for reducing tumour hypoxia[31–33]. Even though some of the safety concerns of blood substitutes are still associated with these agents, this remains one of the more promising approaches to oxygen delivery in the oncological context. However, the large doses needed to achieve clinically significant tumour oxygenation and the associated side effects remain an issue that has to be addressed.

1.2.3.4 Stimuli-responsive oxygen transporters

To overcome the dose-limiting toxicity barriers encountered by artificial oxygen-carrying formulations in the field of tumour hypoxia alleviation, a number of approaches have been proposed to perform localized oxygen delivery. One approach to achieving this goal is constructing carriers that release their oxygen payload when exposed to external stimuli.

Stimuli-responsive agents can respond to various endogenous and exogenous inputs and utilize a number of different materials[34–36]; one of the commonly used combinations is ultrasound-responsive PFC-based carriers. Low boiling point PFCs are well-established in the field of diagnostic ultrasound as high molecular mass, low-diffusivity gases used in ultrasound contrast agents, to create echogenic microbubbles (MBs) [37]. Since PFCs have also been widely used in the search for blood substitutes due to their chemical and biological inertness and high oxygen solubility, PFC-based agents for local oxygen delivery were a logical candidate. As an activating stimulus for cancer oxygenation, ultrasound has a number of advantages as well, such as good penetration depth, well-established safety profile and its property to enhance extravasation, which is

especially important in the context of abnormal tumour vasculature[38]. Consequently, a number of PFC-based MB formulations have been tested for tumour oxygenation[39–46].

One of the drawbacks of using MBs for this application is their size (usually around 1-2 um), which prevents them reaching some areas of the abnormal tumour vascular network or extravasating. One solution to this problem is taking advantage of the useful property of some PFCs that have their gas/liquid transition temperature close to 37°C and constructing phase-change agents that initially exist at a smaller size (hundreds of nanometres) in the liquid state and then undergo the transition into larger gas cavitation nuclei[47].

A different approach is creating carriers that are initially smaller, i.e. instead of microbubbles using "nanobubbles" (NBs – this term is used widely for sub-micrometre-sized bubbles, although their diameters are typically between 100 and 800 nm and therefore by most conventional definitions they are not strictly nanoparticles). Some of the concerns regarding the development of ultrasound-responsive NBs include their reduced responsiveness to ultrasound – an issue that still needs to be addressed by current research in this field[48,49]. However, since successful extravasation and large penetration depth of agents are crucial for tumour oxygenation, oxygen-transporting nanobubbles have attracted considerable interest and have been successfully tested for ultrasound-mediated therapies, despite the need to elucidate the mechanisms involved[50–53].

1.2.4 Mechanisms of oxygen delivery

Whilst the range of materials and concepts used for oxygen carriers is wide, all these agents have one issue in common: in order to produce a significant effect, they have to transport enough oxygen in a single dose to make a difference compared to the quantities already being delivered by the blood. Haemoglobin (Hb) is the main oxygen-carrying constituent of blood, being able to

bind approximately 1.37 mL of oxygen per gram[54]. In human blood with normal haematocrit this results in approximately 98% of oxygen being transported by Hb and only around 2% by plasma. This means that an artificial oxygen carrier has to either have a significantly larger oxygen capacity than blood plasma or to have an enhanced transporting mechanism in order to have an effect. Different types of carriers attempt to achieve this in different ways; the main methods of oxygen transport, together with remaining questions about their mechanisms and efficacy, are described below.

1.2.4.1 Hb-based and solubility-based carriers

Based on their mechanism of carrying oxygen, most transporting agents can be divided into Hb-based (which bind oxygen molecules to haemoglobin, similar to blood) and solubility-based (which carry oxygen in a non-bound state, simply dissolved in the agent's medium and prevented from diffusing away by some sort of barrier or phase separation).

For Hb-based agents, the dependence of agent oxygen saturation on external oxygen pressure is highly non-linear. It is close to the same dependence seen for Hb in blood (although some differences are possible as an intended or unintended consequence of the carrier's design), meaning that oxygen loading and unloading is efficiently optimised for physiological conditions[55]. Although Hb-based carriers still have a number of side effects, their oxygen-carrying efficiency is high and comparable to that of blood.

Most other agents, including PFC-based carriers, are solubility-based, meaning that the oxygen solubility curve for them is linear. It is reasonably straightforward to estimate the gas content for a gas-phase agent, in equilibrium and in the absence of oxygen interactions with the carrier boundary, using Henry's law, which can be expressed as:

$$H^{cc} = \frac{c_a}{c_g}$$

where H^{cc} is a dimensionless constant and c_a and c_g are aqueous and gas phase concentrations of the payload gas respectively. In this notation, the reverse Henry's constant 1/ H^{cc} provides an estimation of the gain in oxygen-transporting ability by a gas-phase agent (stabilized by a low-diffusivity gas) compared to the liquid phase (for oxygen in water at body temperature this would mean around 30-fold increase in oxygen concentration in gas phase compared to liquid phase[56]). In the equilibrium state in blood, this increase should be calculated relative to normal plasma oxygen levels, which for arterial blood are close to air saturation values at atmospheric pressure (around 210 uMol, or 5.4 mL/L, of oxygen in liquid phase at body temperature) and for venous blood are notably lower. Using the air-equilibrated values for a simplified estimation, this corresponds to around 600 umol, or 16 mL, of oxygen payload per 100 mL of carrier agent. (Note that in these estimates the carrier agent volume is understood as the total volume of bubbles; when recalculated to oxygen content per mL of stock agent solution, this value would be correspondingly lower and would depend on the agent concentration in the solution.)

For liquid droplets the oxygen payload estimations are based on oxygen solubility. PFCs are known for their high inertness and high oxygen solubility. Depending on the type of PFC used, the typical oxygen solubility ranges from 35-55 mL O_2 per 100 mL PFC volume for 1 atm O_2 partial pressure, or correspondingly 7-11 mL O_2 per 100 mL PFC in equilibrium with air at atmospheric pressure[57,58]. This value is approximately two times lower than that for a gas-based agent, which underlines the utility of PFC emulsions for oxygen transporting. However, for any agent, the delivered oxygen dose will depend on the carrier dosage, stability and other properties. Values for common dosages for both MBs and droplets, as well as examples from specific studies, are calculated in the following section.

It is important to reiterate that the estimates given above are for air-equilibrated agents. In some literature, especially on the topic of carriers designed for localized stimuli-responsive burst release, it is oftentimes assumed or implied that the agent contains 100% oxygen, which naturally results in numbers that are around 5 times higher than those for air. This is a correct assumption if the patient or laboratory animal is breathing pure oxygen; however, in most studies this is not the case. For air-breathing subjects, the dynamics of oxygen diffusing out of the carrier agent becomes important. The agent may start with up to 100% oxygen content (depending on the method of production), but as soon as it is introduced into the bloodstream it will start equilibrating with plasma oxygen concentration, which is around or below air-equilibrated values depending on the part of the blood circulation cycle. The speed of this process is fast for an agent of around 100-200 nm (liquid droplets) or 1-2 μm (gas-based bubbles), which is the reason why, for example, microbubble-based contrast agents for ultrasound are not stable enough with an air core and need a low-diffusivity gas core to be usable in the clinical setting[37]. Theoretical studies show that, even after accounting for the phospholipid barrier, the time over which this process happens is no more than a few seconds, which is in most cases clearly insufficient to bring the excessive oxygen payload to the target tissue for localized release[44]. Consequently, the simplified view that for an agent loaded with 100% oxygen the payload stays in the agent until its release is triggered by an external stimulus is, for air-breathing subjects, not entirely correct. While some transient benefit of using oxygenated agents compared to air-saturated agents can exist (depending on the time scale of the experiment, the dosage and the speed of the introduction of the agent solution), most of the oxygen-carrying capacity of a solubility-based agent depends not on holding pure oxygen until released, but on its ability to provide a stable gas phase due to its low-diffusivity core, raising the oxygen content of the solution compared to liquid phase by the factor of the Henry's constant for a given medium, or by increased solubility in liquid carriers; making theoretical estimations of

agents' oxygen-carrying capacity for air-breathing subjects based on pure oxygen loading would therefore likely result in a large overestimation.

Taking all of this into consideration, total oxygen payload can be estimated for various agents under different circumstances of their usage. This can be compared to the amount of oxygen already transported by the blood and is often found to be small, in contrast to the multiple reported effects of various agents *in vivo*. The following sections presents several examples of this discrepancy, comparing estimated oxygen payload doses in a number of studies with their reported physiological effects.

1.2.4.2 Quantitative discrepancies

Taking into account the considerations detailed above, and corresponding them with typical microbubble or nanodroplet dosages from the literature, typical oxygen payloads of solubility-based agents can be estimated. The natural frame of reference for these numbers is the amounts of oxygen transported by blood. Oxygen quantities transported by a typical dose of MBs or droplets for humans and mice, compared to oxygen delivered by blood, are estimated in Table 1.2.4.2.1.

Agent	Gas payload in stock solution	Typical dose		Total O_2 quantity in one dose (air-equilibrated estimate)		Ref
		Human	Mouse	Human	Mouse	
Blood	~1.37 mL/g Hb	~150 g Hb/L blood ~65-70 mL blood/kg weight ~4-5 L blood volume	~150 g Hb/L blood ~80 mL blood/kg weight ~1.6-2.4 mL blood volume	~1 L/min O_2 transported ~250 mL/min basal O_2 consumption	~1.6 mL/min O_2 transported ~0.7 mL/min basal O_2 consumption	54,59–62
MBs	~10^{-11} mL/MB	5*10^{10} MBs	7*10^{7} MBs	~0.1 mL O_2 transported	~0.14 uL O_2 transported	41
Droplets	~30 uL/200 uL	300 mL emulsion	100 uL emulsion	~8 mL O_2 transported	~3 uL O_2 transported	63

Table 1.2.4.2.1. Calculations for the amount of oxygen that can be transported with solubility-based carriers compared to blood. Estimates for MBs and droplets were made assuming the carrier is equilibrated with air; for carriers pre-loaded with oxygen the oxygen payload may be transiently higher, but it will decrease quickly when introduced into the bloodstream (see detailed discussion in section 1.2.4.1). The dose represented here for MBs is typical for diagnostic uses and therapeutic studies of MBs, while the dose of PFC droplets used here is rather large and comparable with the use of blood substitutes for systemic blood loss.

The estimates above are made from a range of values found in the literature, and although specific values differ between studies, these numbers represent a good order of magnitude estimate. It is worth noting that, due to the arguments presented in section 1.2.4.1, the estimates were made under the assumption of the carrier agents being in equilibrium with air as opposed to 100% oxygen loading; however, even during the transient pure oxygen stage (or in the case of subjects breathing pure oxygen) the oxygen payload estimate would only be approximately five-fold higher.

Regardless of specific assumptions, it is clear that the amount of oxygen transported by a dose of solubility-based agents is many orders of magnitude lower than what is already transported by blood. This has to be compared to the *in vivo* effects of solubility-based oxygen carriers reported in a number of studies. The mechanisms suggested in the literature, as well as relevant length- and timescales, are different for different types of carriers and their activation; consequently, the

sub-sections below look in more detail into various types of agents, as well as the proposed mechanisms of their action and whether or not these mechanisms can explain how the small oxygen payloads produce the significant *in vivo* effects.

A. Ultrasound-activated microbubbles

For therapeutic gas delivery, microbubbles are often used in combination with ultrasound for localised payload release, and this localisation is used to justify the *in vivo* effects.

A number of *in vivo* studies using ultrasound-activated MBs for oxygen delivery are summarised in the Table 1.2.4.2.2. Some of these studies look at oxygen delivery for the purpose of radiotherapy (RT) enhancement, in which case a transient increase in local oxygen levels is believed to be enough if it is correctly timed to the radiotherapy administration. However, the estimated oxygen dose of 0.02 uL for the mouse RT studies, even if it is totally and instantaneously distributed into the tumour, would correspond to only about 0.1 kPa rise in oxygen partial pressure, which is considerably below both the reported pO_2 rise measured in the tumours (20 kPa) and the pO_2 levels needed to alleviate hypoxia in tumour tissue (~5-8 kPa)[64]. The discrepancy between the pO_2 estimations and measurements can be easily explained by the tumour pO_2 heterogeneity which is not captured by the measurement; however, the oxygen payload of the agent is still insufficient to make a meaningful difference in pO_2 levels across the tumour, even for a transient period required for RT sensitization.

A different approach is to use MB-mediated oxygen delivery to enhance chemotherapy or sonodynamic therapy, i.e., to improve the action of ROS-dependent drugs. Similarly to the RT studies, the estimated oxygen dosages in these studies are not enough to alleviate the hypoxic state across the tumour, even under the assumptions of instantaneous, fully efficient, homogenous delivery. However, in the case when the drug is either conjugated with or loaded

into the microbubble the co-localisation of oxygen and the drug can have a positive impact, which warrants further study and quantification.

Finally, a study looked at delivering oxygen for the purpose of changing the abnormal vascular network of the tumour. Again, delivered oxygen dose estimated from the agent volumes accounts for only about 0.3 mmHg instantaneous rise in pO_2 across the tumour, compared to 4 mmHg pO_2 rise over a prolonged time measured in the study. Even accounting for the imperfect tumour pO_2 measurements that could explain this discrepancy, the delivered oxygen dose still does not provide sufficient oxygenation for tumour hypoxia alleviation. It is worth noting that the long-term effects seen in this study are hypothesized to result from the oxygen-loaded MBs influencing the HIF1α/VEGF pathway, and further research is needed to understand the specific pO_2 levels and durations needed to influence it; however, the small oxygen dose in the study is still not likely to be sufficient.

Material	Organism	O_2 volume estimate	Therapy	Reported effects *in vivo*	Reference
Span 60, vitamin E, PFP	Mouse	0.02 uL	US + RT	Tumour pO_2 rise by 20 kPa for 1.5 min for O_2 MBs + US vs no change for O_2 MBs (no US) and saline + US; however no Hb oxygenation change detected Slower tumour growth and longer survival for US + O_2 MBs + RT vs US + MBs, O_2 MBs + RT, US + RT, US + N_2 MBs + RT	[46,64]
Span 60, vitamin E, PFP	Mouse	0.02 uL	US + RT	Slower tumour growth and longer survival for US + O_2 MBs + RT vs RT, US + N_2 MBs + RT, O_2 MBs + RT	[46,65]
DSPC, DPPE-MPEG5000, PFP+O_2	Rabbit	0.2 uL	US + RT	Rise in tumour pO_2 at 1 min by 300 mm Hg for US + O_2 MBs vs no US, no US + MBs, no US + O_2 MBs	[40]
DSPC, DSPE-PEG2000, conjugated RB, SF_6	Mouse	0.006 uL	US + drug	Tumour growth slower for O_2 MBs w RB + US vs SF_6 MBs w RB + US vs O_2 MBs w RB, SF_6 MBs w RB	[42]

DBPC, DSPE-PEG2000, conjugated RB/5-fluorouracil, PFB	Mouse	0.06 uL	US + drug	Slower tumour growth for O_2 MBs RB/5-FU + US vs O_2 MBs RB + US, O_2 MBs RB/5FU, gemcitabine, US, no treatment	[41]
DPPC, DSPE, paclitaxel, PFP/O_2	Mouse	0.1 uL	US + drug	Slower tumour growth for O_2 MBs + US vs MBs + US, O_2 MBs, MBs, drug, no-drug MBs + US, saline Apoptosis higher; VEGF staining, HIF-1α and P-gp expression lower for O_2 MBs + US vs other samples	[39,66,67]
DSPC, DSPE-PEG2000, PFP+O_2	Mouse	0.002 uL	US	Tumour pO_2 rise by 30% for O_2 MBs + US (16 to 22 mmHg) during treatment and maintained up to 60 min vs no change for PFP MBs + US, control Higher perfusion intensity at days 2,4,6 after treatment for O_2 MBs + US vs O_2 MBs, PFP MBs + US, PFP MBs, US, control No significant difference for perfusion density and tumour growth More DOX accumulation in tumour when injected at day 4 post treatment for O_2 MBs + US vs PFP MBs + US, control	[68]

Table 1.2.4.2.2. Summary of ultrasound-mediated oxygen release studies for microbubbles *in vivo*. These studies combined ultrasound with radiotherapy (RT), chemotherapy or used ultrasound on its own. Subject animals breathed air in all experiments, so in line with oxygen release dynamics considerations the oxygen payload is estimated as approximately one-fifth of total gas payload. In some cases, exact agent dosage or concentration was not specified in a study, in which case it was estimated from other doses mentioned in the paper, or from other papers with the same agent by the same research group, in which case these papers were added to the "Reference" column. All abbreviations are detailed in the List of Abbreviations.

To summarise the microbubble-mediated oxygen delivery studies, the doses of oxygen transported by MBs do not appear to be sufficient for meaningful changes in tumour pO_2 levels. None of the studies discussed above provided a delivered oxygen dose estimate, and some of

them did not even clearly state the administered MB doses, which in this case had to be deduced from other information provided; this further underlines the fact that there is no clear understanding of what oxygen dose is needed to provide an effect or what the exact mechanism of their action is.

B. Ultrasound-activated droplets

Nanodroplets are an alternative approach to ultrasound-mediated oxygen delivery. Their diameter is usually around 100-200 nm, enabling better permeation into small vessels than MBs, and the typical dosages are correspondingly larger; however, their small size also means that they lose the oxygen payload via equilibrating with the media even faster than MBs.

It is important to distinguish between ultrasound-activated phase-change droplets and the more stable emulsions that may use ultrasound as part of the treatment but do not undergo a phase transition from liquid to gas. The former agents have been utilised for a number of applications in therapeutic ultrasound[69], while the latter are close to the concept and composition of solubility-based blood substitutes.

Interestingly, while nanoscale phase-change droplets at first glance may seem superior to MBs for their potential applications in ultrasound-triggered oxygen delivery, the phase-change transition has to be taken into account. This transition increases the volume of the agents approximately five-fold and turns it from a liquid into a gas, increasing oxygen solubility around two-fold for commonly used PFCs; consequently, the phase-change transition would only increase the total oxygen capacity of this carrier, as opposed to releasing the payload. Indeed, phase-change droplets are not normally used for gas delivery and instead have found an opposite application in ultrasound-mediated oxygen scavenging[70–72].

Consequently, when it comes to oxygen delivery with droplets, more stable, non-phase-change emulsions need to be used. Several studies looked into combining ultrasound with oxygen-transporting PFC droplets (Table 1.2.4.2.3); similarly to the estimations for MBs detailed above, in most cases the oxygen dose estimate is low, and the direct stimuli-responsive oxygen release does not seem to be enough to explain the biological effects.

Notably, one study[73] acknowledged this limitation and addressed the oxygen dose problem by, firstly, conducting the study with hyperoxic breathing, which proportionally increases the oxygen loading in solubility-based agents, and, secondly, increasing the ultrasound treatment time, justified by the hypothesis that the PFC agents are loaded with oxygen in the lungs, release the oxygen payload in the target site with the help of ultrasound in addition to concentration-driven diffusion and repeat this cycle multiple times via recirculation. This is a fundamentally different framework to the hypothesis that oxygen is simply loaded into a carrier during production and then released by ultrasound, and it addresses a number of problems such as rapid oxygen dose loss after introduction into the bloodstream and small dose released with a one-time sonication. Interestingly, the agent recirculation reasoning brings this study close to the discussions of the action mechanisms of PFC-based blood substitutes as opposed to the ultrasound-mediated oxygen release literature, which are discussed in the following section.

Material	Organism	O_2 volume estimate	Therapy	Reported effects *in vivo*	Reference
PLGA, PFTBA, DOX, IR780	Mouse	0.08 uL	US + drug	Slower tumour growth for NDs + US vs NDs w/o DOX + US, DOX, US, saline Decreased HIF1α production for NDs w/o DOX and PFTBA vs NDs w/o DOX, saline (separate experiment) Increased cell viability in hypoxic vs normoxic environment (separate experiment)	[74]
C9F17-PAsp(DET), PEG-protoporphyrin IX, PFH	Mouse	0.08 uL	US + drug	Slower tumour growth for O_2 NDs + US and NDs + US vs O_2 NDs, NDs, NDs w/o PFH + US, NDs w/o PFH, control Less hypoxia staining for O_2 NDs and NDs vs NDs w/o PFH, control (separate experiment)	[63]
HSA, perfluoro-15-crown-5-ether	Mouse, hyperoxic	~10 uL/cycle	US + PDT, US + RT	Less hypoxia tumour staining, less HIF-1α for O_2 NDs + US vs O_2, O_2 + US, O_2 NDs Slower tumour growth for O_2 NDs + PDT + US vs O_2 NDs + PDT, O_2 + PDT + US, O_2 + PDT, untreated Slower tumour growth for O_2 NDs + RT + US vs O_2 NDs + RT, O_2 + RT, O_2 + RT + US, RT, untreated	[73]

Table 1.2.4.2.3. Summary of ultrasound-mediated oxygen release studies for nanodroplets *in vivo*. These studies used NDs and ultrasound in combination with chemotherapy, photodynamic therapy or radiotherapy. In two cases subject animals breathed air, so in line with oxygen release dynamics considerations the oxygen payload is estimated for air oxygen partial pressure; one study used hyperoxic breathing, for which the oxygen dose was estimated for 100% oxygen partial pressure. All abbreviations are detailed in the List of Abbreviations.

1.2.4.3 Possible explanations

As the studies discussed above show, direct ultrasound-mediated release of oxygen payload does not seem to be a sufficient explanation for the effects seen *in vivo*, since the carrier agent doses are limited by the issues of biocompatibility and safety and do not hold enough oxygen to alleviate hypoxia across the tumour, even for a short amount of time. A small oxygen dose may be sufficient if it is co-localised with an ROS-dependent drug; however, even in this case further quantifications are needed, and overall it is clear that other mechanisms need to be considered to explain the *in vivo* results.

Interestingly, a relevant discussion on oxygen transport mechanisms has taken place in the literature for PFC-based blood substitutes, signalling that even for the large agent doses used for systemic blood substitute transfusions there is still some discrepancy between the oxygen-carrying capacity of the agents and their biological effects[75,76]. Considering the similarities between ultrasound-responsive agents and PFC-based blood substitutes, the issues and mechanisms of their action may be at least partially similar and therefore worth discussing and exploring together.

Several hypotheses of the oxygen delivery mechanisms by solubility-based agents have been proposed, both in the stimuli-responsive carrier literature and the blood substitute literature. They are outlined in the sections below.

A. The recirculation hypothesis

It was proposed that some carriers can persist in blood for a prolonged time, taking up oxygen in the lungs and releasing it in the hypoxic tissue, alike to RBCs and blood substitutes[73,77]. In this case, the oxygen dose delivered by the agents is still limited by the volume estimations discussed above

per one circulation cycle, but the number of cycles is increased, allowing for the total oxygen dose to be correspondingly larger.

In the case of ultrasound-mediated gas delivery, this hypothesis is only applicable to stable agents that are not destroyed by ultrasound in one blood cycle and therefore does not apply for micrometre-sized gas-core agents. Interestingly, however, it has been seen that microbubble formulations contain significant concentrations of lipid particles below 1 μm (see Chapter 2), which are more stable and may persist for several blood cycles with ultrasound. Therefore, the recirculation hypothesis may be in some form applicable to a wide variety of agents.

The exact benefit that several blood cycles can bring to the delivered oxygen dose depends on the specifics of the experiment and the tumour perfusion, as well as the agent persistence in the bloodstream, decreased overtime by biological clearance and external stimuli such as the ultrasound intervention. Due to the similarities that many gas-carrying agents have with PFC-based artificial blood substitutes, it appears evident that recirculation may indeed play some role in the gas delivery process, unless the agents are quickly destroyed or eliminated from circulation. However, it is important to consider that recirculation would only increase the total deposited oxygen dose, and the amount of oxygen deposited per one blood cycle is still limited by the gas-carrying capacity of the agent; therefore, if the volume of artificially transported oxygen is negligible compared to the volume of oxygen already carried by blood in the same timeframe, recirculation would only bring limited benefits and would not fully explain the *in vivo* results.

B. The enhanced perfusion hypothesis

Some capillaries are too small for RBCs and are perfused only by plasma; oxygen delivery into them is therefore limited, which may be an especially important factor for the abnormal tumour vasculature. Therefore, sub-micrometre sized carriers that are able to perfuse these capillaries

may offer a meaningful increase in oxygen delivery to some tumour areas. While this is worth considering, especially for nanodroplets, the percentage of such capillaries is reported to be low, so this mechanism is unlikely to play a major role[75].

In the case of ultrasound-mediated delivery, another consideration is the enhanced extravasation and agent perfusion into the tumour triggered by ultrasound stimulation[78]. It is a well-recognised benefit of therapeutic ultrasound and should be acknowledged as a possible enhancing factor. However, similar to the hypotheses described above, it still does not explain the effects shown by agents with low oxygen doses, since even under the assumption that the oxygen dose is evenly and instantaneously distributed in the tumour, the resulting pO_2 levels are not sufficient to alleviate the hypoxic state.

C. The enhanced diffusion hypothesis

This hypothesis was first proposed for PFC-based blood substitutes, since even for large volumes of administered oxygen-carrying emulsions there is some discrepancy between the added oxygen-carrying capacity and the observed effects[26,75]. It was suggested that the primary role of PFC droplets was not to transport the oxygen between the lungs and tissue, but rather to facilitate the oxygen exchange between RBCs and tissue[76,79]. Diffusion of oxygen through plasma is one of the main speed-limiting factors of oxygen exchange; introducing PFC carriers between RBCs and tissue may increase the total diffusivity of oxygen in this process and result in higher oxygen transport into cells. Due to the near wall excess phenomenon, small round particles such as PFC carriers are expected to travel close to the vessel walls while RBCs are primarily in the middle, which would explain relatively small concentrations of agents contributing substantially to the increase in diffusivity[80]. PFC particles have also been shown to enter endothelium, which may enhance oxygen diffusion beyond blood plasma[81].

There are a number of secondary observations that point towards diffusion enhancement as a viable mechanism of action for PFC agents[75,76]; however, direct experimental evidence remains limited to a small number of carriers[79,80], and this hypothesis is not usually discussed in the context of ultrasound-responsive carriers, even though their similarities to PFC-based blood substitutes point towards the possibility of similar oxygen delivery mechanisms. Further experimental evidence is therefore needed to further explore the applicability of this hypothesis to various agents.

Interestingly, there are other, non-oxygen-transporting agents that are claimed to enhance oxygen diffusion in solutions. An example of such a substance is trans-sodium crocetinate (TSC), which is believed to increase diffusion coefficients by rearranging water molecules via hydrophobic interactions[82,83]. It has been tested for sensitizing glioblastoma multiforme to radiation in rats[84] and is currently in Phase II clinical trials for this condition in humans (combined with chemo- and radiotherapy).

1.2.5 Challenges and research objectives: oxygen delivery

As discussed above, a number of recent studies have demonstrated the potential of ultrasound-responsive oxygen carriers for reducing tissue hypoxia and promoting a therapeutic response. However, the doses of oxygen carried by these agents are small and do not appear sufficient to explain the *in vivo* effects solely via localised oxygen release with ultrasound. A number of hypotheses have been put forward to explain the oxygen delivery mechanisms, the most promising of which suggests that PFC-based carriers decrease the oxygen diffusion time from red blood cells to the tissue, therefore enhancing oxygen transfer substantially despite their own small oxygen-carrying volume. While this hypothesis holds promise and appears to have been accepted

in PFC-based blood substitute literature, the direct experimental evidence to support it is scarce, and it has not yet been applied in the context of ultrasound-responsive agents.

Consequently, the goal of this part of the presented thesis was to characterise various agents used for ultrasound-mediated oxygen delivery, such as microbubbles, nanobubbles and droplets, in terms of their size distributions, stability and oxygen-carrying properties, as well as to develop an experimental setup to directly test the diffusion enhancement hypothesis *in vitro*.

1.3 Sonoporation and sonodynamic therapy

Sonodynamic therapy (SDT), usually defined as ultrasound-mediated activation of drugs, is a rapidly growing area that has attracted attention as a possible improvement over photodynamic therapy (PDT), having a similar concept of using externally applied stimuli with a good safety profile, but without the penetration depth limitations of light. However, despite demonstrating efficacy *in vitro* and in animal studies, SDT applications in clinical use have mostly been limited to small studies in combination with other therapies, such as PDT and immunotherapy[85], and clinical trials focusing specifically on SDT are few in numbers and are still in early stages[86]. One of the reasons behind the slow clinical roll-out of SDT may be the lack of understanding of its mechanism(s): while the molecular mechanisms of PDT are relatively well-established, this is not the case for SDT. The following sections will elaborate on the current understanding of SDT and the candidate mechanisms for its effect on tissue.

1.3.1 Sonodynamic therapy overview

Targeted cancer therapy is a large and well-established field, that has arisen due to the considerable toxicity of many oncological drugs and therapies and the corresponding need to limit systemic side effects. A wide variety of localisation strategies has been proposed, such as stimuli-responsive drug release from carrier particles and antigen-based targeting. One of these methods is PDT; its principle of action is light-mediated local drug activation[87]. This therapy has been widely accepted in clinical practice; however, its significant limitation is the poor penetration of light through tissue that severely limits the treatment of deep seated tumours.

Interestingly, around three decades ago it was discovered that some of the PDT drugs also exhibit cell-killing activity after exposure to ultrasound, which resulted in the establishment of the field of

SDT[88,89]. A number of studies have shown that a combination of certain drugs and ultrasound leads to significant *in vivo* effects compared to drugs or ultrasound alone[42,90–92]; however, the number of *in vivo* studies is relatively small, with many studies limited to *in vitro* cell experiments, which can in part be explained by the continuing lack of the full understanding of SDT mechanisms[93].

The issues regarding SDT mechanistic studies are described in the following section; it is clear that overcoming these problems and achieving better understanding of SDT action would help its transition into clinical use.

1.3.2 Reactive oxygen species and sonoporation in sonodynamic therapy

SDT is usually defined as ultrasound-mediated activation of drugs, although there is as of yet no consensus or definitive proof of the exact mechanism of this activation[94]. Many studies suggest that there is some reactive oxygen species (ROS) generation after a system containing certain drugs is subjected to ultrasound, in particular in the presence of cavitation nuclei such as microbubbles; however, the questions that require further elucidation are, firstly, what the mechanisms of this ROS generation are and which ROS types are produced; and secondly, whether the quantities of ROS generated are enough to result in cell death, especially considering the short lifetimes of most ROS species.

1.3.2.1 Mechanism of ROS generation in SDT

There are a number of hypotheses about the mechanism of ROS generation in SDT. One of them is that the drug activation happens the same way as it does in PDT, i.e., via light that is generated during cavitation, which is termed sonoluminescence. While sonoluminescence is an established

phenomenon, there remains a question of whether the quantities of light produced are enough to account for the observed activation[95]. Alternative hypotheses are centred around cavitation-related phenomena as well and include pyrolysis and secondary ROS generation. There is, as of yet, no consensus on which process is the principal one; and it is important to note that ultrasound-induced cavitation causes a wide array of effects, and it is possible that more than one process plays a meaningful role in SDT activation.

1.3.2.2 ROS types produced in SDT

Next, there is the issue of which ROS types are produced. Here, again, there is no established consensus. Many comparisons are made with the better researched mechanisms of PDT. Briefly, PDT is usually divided into Type I and Type II, where Type I includes the transfer of energy via electron transport and can include such ROS species as superoxide, hydrogen peroxide and hydroxyl radical, while in Type II energy is passed through the generation of singlet oxygen ($^3O_2$)[96]. PDT drugs are typically classified as Type I or Type II depending on their main mechanism pathway. Interestingly, for SDT, different studies have produced different conclusions in regard to the type of generated ROS species by specific drugs[97,98].

There are several explanations as to why a consensus on ROS species in SDT is still to be reached. One of them is the difficulty of selecting ROS sensors that have sufficient selectivity for the target species and, in addition, are compatible with the ultrasound agents and processes in a way that does not change their specificity. For example, SOSG (Singlet Oxygen Sensor Green), which is commonly used for singlet oxygen detection, has been shown to undergo self-activation under certain conditions[99], including when exposed to ionizing radiation[100] and, importantly, ultrasound[101]. In both cases, hydroxyl radicals were believed to be involved in the SOSG activation process.

Another issue is the wide variety of ultrasound parameters and setups used in different studies. The number of ultrasound parameters that can impact the action of SDT is high: in addition to the peak field pressures and total deposited energy, the duty cycle and pulse length are also important parameters for the resulting cavitation behaviour[102]; therefore, full optimisations are time-consuming, and there is no commonly used set of parameters, with studies using any cycle lengths from single pulse to continuous, and therefore direct comparison of different experiments may be challenging. Moreover, ultrasound transducers require regular pressure field calibrations, and many of the commonly used sample holders, such as 96-well plates, distort the ultrasound field and therefore require careful quantification of the resulting acoustic field. As a result, better acoustic field characterisation and reporting in the literature is an important goal for the field of medical ultrasound; some of these issues will be touched upon below in the section on the design and characterisation of the ultrasound setup[103].

These issues, when taken together, mean that it is not surprising that SDT studies with different drugs, ultrasound parameters and setups and ROS sensing methods may produce different conclusions as to the types of ROS species involved. This question therefore still needs further study, with robust ultrasound characterisation and carefully validated ROS sensing methods.

1.3.2.3 Quantities of ROS produced during SDT

Finally, irrespective of the type of ROS, the question remains as to whether sufficient quantities are generated during sonication to explain the biological effects seen in SDT. This consideration is important, since most studies on ROS generation with ultrasound only compare values within the ultrasound experiments, e.g., ROS levels with or without ultrasound, and do not provide a positive control, which for PDT-compatible drugs would be the ROS production after being exposed to light. Importantly, comparison between light and ultrasound activation for typical therapeutic

parameters shows the fact that, at least for some drugs, there is indeed a certain amount of ROS produced during sonication, but it is orders of magnitude lower than ROS produced under light; this discrepancy has been seen both in this project and other recent work (personal communication Victor Choi). Since PDT-generated levels of ROS can be used as a benchmark for ROS levels that are needed, in the absence of other effects, to produce a clinical effect, the question that consequently arises is how the lower levels of ROS produced with ultrasound can explain its *in vivo* action.

Here it is important to underline the wide variety of effects that ultrasound is capable of inducing in tissues. Depending on exposure parameters, both light and sound can induce heating; this is used in some applications, but excessive heating is typically avoided in PDT and SDT in order to reduce tissue damage and unwanted side effects. What differentiates ultrasound, however, is that it can also cause cell membrane permeabilization (usually referred to as sonoporation) and enhanced extravasation of drugs into tumours[104,105].

1.3.2.4 Sonoporation

Sonoporation has been used for a number of intracellular delivery applications such as gene transfection[106], and it is present to some degree under most therapeutic ultrasound exposure regimes. It is usually defined as ultrasound-induced cell permeabilization. It can be reversible, resulting in cell recovery, or non-reversible, resulting in cell death.

Although the existence of sonoporation as an ultrasound-induced phenomenon is well-established, its exact mechanism is still being researched. The commonly accepted understanding is that sonoporation is the process of generating openings in cell membranes due to cavitation-induced effects such as microstreaming, or possibly direct bubble-cell interactions[107,108]. However, it was

also shown that endocytosis, as opposed to membrane rupture, may be an important or even a dominant mechanism[109–111].

Vastly different sonoporation parameters, such as the enhanced permeability time window, sonoporation efficiency and cell viability, are reported in the literature. One of the reasons is the substantial differences between the ultrasound parameters and setups used in the literature, as discussed above. Another important consideration is the differences between cell lines[112]; as specific mechanisms of sonoporation are not yet known, it is not feasible to suggest a feasible explanation for this, but it is not surprising considering the differences in membrane properties and composition between different cell types.

One more factor is the validity of cell death quantification methods. Importantly, many of the commonly used cell death markers, such as propidium iodide, which are considered to be non-toxic to healthy cells under normal conditions[113], may not be non-toxic after entering transiently permeabilised cells; therefore, it is important to validate cell viability measurement protocols in order to avoid artificially changing cell death numbers.

1.3.2.5 Role of sonoporation in sonodynamic therapy

Interestingly, although sonoporation is a well-established process for the purposes of intracellular drug delivery, and, despite the fact that it is known to occur at least to some degree under the commonly used therapeutic ultrasound parameters, in the literature sonoporation is usually completely separated from the discussions of SDT mechanisms. Nonetheless, as the ROS production in SDT is much lower than that of SDT, some mechanism has to be proposed that could explain how a low concentration of ROS, which in addition have short lifespans in physiological media, is able to induce the observed *in vivo* effects.

A hypothesis proposed for this project was that the SDT effects are possible due to the synergy of sonoporation and drug action. As sonoporation may be able to induce drug uptake by the cells, this in itself might be able to make the drug toxic to the cell despite the extracellular concentrations being harmless.

SDT studies do not typically include controls that would account for the effect of sonoporation; therefore, although sonoporation is an established process, its role in SDT remains unexplored, and the focus of most SDT studies remains on ultrasound-induced ROS production. In this project, therefore, experiments were designed specifically with the goal of distinguishing between the roles of sonoporation-enhanced cell uptake and possible ultrasound-induced activation of a widely used SDT drug Rose Bengal.

1.3.3 Challenges and research objectives: sonodynamic therapy

As outlined above, there are a number of issues in the field of SDT studies.

Firstly, there is a need for better characterisation of ultrasound exposures reported in the literature, in order for it to be possible to compare results across different experiments. This entails making ultrasound field characterisation and output monitoring, such as passive cavitation detection (PCD), more widely accepted as the standard practice in the field of therapeutic ultrasound.

Secondly, in order to assist with faster SDT translation into clinical practice, the understanding of its mechanisms has to be expanded. This includes better characterisation and quantification of the generated ROS, as well as a feasible mechanism by which these ROS can induce cell death in the concentrations obtainable by SDT.

The goals of this part of the project were therefore to further characterise an in-house ultrasound exposure setup, in order to produce reliable sonication results for *in vitro* SDT experiments, as well as to use this setup to quantitatively characterise the ROS generation after the exposure of a widely-used PDT and SDT drug Rose Bengal to either light or ultrasound (Chapter 5). Next, the aim was to develop protocols for cell experiments in order to check the hypothesis that SDT-induced cell death is activated via a drug entering the sonoporated cells and exhibiting toxicity intracellularly, as opposed to the widely accepted but insufficiently tested assumption that SDT-induced ROS generation works analogously to PDT and sonoporation does not play a decisive role in the process (Chapter 6).

Chapter 2. Agent production and characterization

2.1 Introduction

As described in the previous chapter, a wide variety of agents has been used both in the areas of oxygen delivery and therapeutic ultrasound. This chapter will describe the main types of agents used in the present thesis, including the methods of their production, size characterization and determination of their oxygen-carrying properties.

2.1.1 Microbubbles

The principal agent used in both diagnostic and therapeutic ultrasound is microbubbles (MBs) filled with a heavy, low-diffusivity gas to enhance their stability[37]. The commonly used gases are sulfur hexafluoride (SF_6), perfluoropropane (PFP) and perfluorobutane (PFB); all three gases have been tested and compared for MB production in this study. The MB coating usually consists of a phospholipid component and an emulsifier; polymer and protein MBs are also used, although their response to ultrasound is expected to be weaker and less sustained due to a more rigid shell[114]. Lipid composition used in this work was 1,2-dibehenoyl-sn-glycero-3-phosphocholine (DBPC) with polyethylene glycol (40) stearate (PEG40S) in 9:1 molar ratio; lipid chain length of 22 carbons was chosen for optimal gas retention[115].

Various core and shell MB compositions have been optimised for different applications in laboratory use. A number of commercial MB agents are approved for diagnostic use, such as SonoVue (Bracco International B.V., The Netherlands), Definity (Lantheus Medical Imaging, USA) and Optison and Sonazoid (GE Healthcare, USA). Many of these agents have been in active clinical use for about two decades, and their safety profiles have been extensively reviewed[116–119].

Two main methods of MB production are sonication and shaking; both have their advantages and drawbacks. Other MB production methods have been explored as well, most notably the microfluidic method, which can produce agents with relatively narrow size distributions desirable in some applications, but is limited by scale-up difficulties[120]. For commercial applications, it is common to either provide pre-made dried bubbles to be suspended in the buffer right before usage, or even provide pre-made MB solutions, which is convenient for the end user but potentially problematic for agent stability; another option is providing lipid/surfactant solutions to be shaken and turned into MBs before usage. In this study, the sonication method was used.

A summary of commonly used commercial agents' compositions, compared to the MBs used in the current study, is presented in the Table 2.1.1.1.

Name	Core gas	Shell components	Preparation method
In-house MBs	SF_6/PFP/PFB	DBPC, PEG40S	Sonication
SonoVue	SF_6	DSPC, DPPG sodium, palmitic acid, Macrogol 4000	Resuspension of pre-made MBs
Definity	PFP	DPPA monosodium salt, DPPC, MPEG5000 DPPE	Shaking
Optison	PFP	Human albumin	Pre-made solution
Sonazoid	PFB	Hydrogenated egg phosphatidylserine sodium, sucrose	Resuspension of pre-made MBs

Table 2.1.1.1. Comparison of microbubbles produced for this study and commonly used clinically approved ultrasound contrast agents. All abbreviations are detailed in the List of Abbreviations.

2.1.2 Nanobubbles

Microbubbles are widely used and studied for both diagnostic and therapeutic ultrasound due to their strong ultrasound response and ability to induce bioeffects, as well as their good safety profile. However, they do have a number of limitations – most importantly their short circulation times and inability to extravasate because of their size, which for most agents is around 1 um. Other drawbacks include limited stability (due to the core gas dissolving out of the bubbles and their rupturing under pressures that are easily achievable by accident during handling) and limited modes of administration (by intravenous or intratumoral injections, while the oral route would be beneficial in some circumstances).

Consequently, some research efforts have been directed at developing sub-micrometre ultrasound-responsive particles, preferably with a better stability profile than that of MBs. Materials used for such nanobubbles include various lipids (including bio-derived lipid mixtures such as soybean lecithin), dextran and chitosan[50,121–125]. The lecithin-based nanobubbles used in this study were developed and manufactured in-house and were previously shown to alleviate tumour hypoxia and enhance sonodynamic therapy in a mouse model[53,126].

2.1.3 Nanodroplets

A different approach to reduce the agent size is to make use of phase change properties of perfluorocarbons. By choosing PFCs which have a gas-liquid transition temperature close to 37°C, it is possible to create agents that exist in superheated liquid form, stabilised by the coating, until they are activated by ultrasound and expand into the gas-filled microbubble form, thus combining the advantages of MBs with the smaller size of the droplet phase[69]. A number of techniques and materials have been proposed to produce such acoustically activated droplets[127]. The core and

shell materials are overall similar to those of MBs; in fact, one of the commonly used methods of producing NDs is condensation of pre-made or commercially acquired MBs. Other methods include shaking, sonication and microfluidics[69]. In this study, condensation of in-house produced microbubbles was used.

Similar to MBs, nanodroplets have been proposed for a wide range of therapeutic applications[128]. As in other areas of therapeutic ultrasound, safety monitoring is of utmost importance; a consideration specific to acoustically activated droplets is that the vaporisation threshold often differs significantly between *in vitro* and *in vivo*, depending on a number of parameters such as other components in solution and vessel diameter, and therefore droplets require a careful transition into *in vivo* experiments[69].

PFC-based nanodroplets, as described in the literature review, have also found broad applications as artificial blood substitutes. Naturally, in this case formulations that do not undergo a phase transition have to be used, in order to enhance their stability; consequently, these formulations are different from those used for ultrasound-responsive phase-change droplets, but many of their physical properties are nonetheless similar. Compositions for these agents were optimised from the point of view of optimal body retention times and other factors, most importantly biosafety for the typically large dosages used for blood replacement therapies. Some studies have looked into using stable, non-phase-change droplets in combination with ultrasound; in this case ultrasound is used in order to promote faster oxygen payload release and better extravasation, as opposed to a phase transition into a gas agent[73]. In this study, stable NDs were produced via the emulsification method, using materials commonly used for PFC-based blood substitutes.

A summary of two formulations of NDs (phase-change and non-phase-change), compared to some formulation examples from other studies and several PFC-based blood substitutes, is provided in Table 2.1.3.1.

Type	Name	Core material	Shell components	Preparation method
Phase-change NDs	In-house NDs	PFB	DBPC, PEG40S	Sonication and subsequent condensation
	Definity (condensed)	PFP	DPPA monosodium salt, DPPC, MPEG5000 DPPE	Shaking and subsequent condensation[129]
	Condensed MBs	PFP and PFB	DSPC, DSPE-PEG2000	Shaking and subsequent condensation[130]
Non-phase-change NDs	In-house non-phase-change NDs	PFOB	Soybean lecithin	Emulsification
	Oxygent	PFOB, PFDB	Egg yolk lecithin	Emulsification
	Fluosol-DA	PFD, PFTPA	Pluronic F-68, egg yolk lecithin	Emulsification
	Perftoran	PFD, PMCP	Proxanol 258	Emulsification
	"Shuttle" NDs for US-mediated O_2 delivery[73]	Perfluoro-15-crown-5-ether	HSA	US emulsification

Table 2.1.3.1. Comparison of nanodroplets produced for this study and examples of other commonly used formulations. Note that they are divided into phase-change agents, which undergo a phase transition under ultrasound stimulation, and stable non-phase-change agents, many of which are PFC-based blood substitutes. All abbreviations are detailed in the List of Abbreviations.

2.1.4 Other agents

The vast majority of ultrasound-responsive agents are either microbubbles, nanobubbles or nanodroplets, with the most common materials being PFC liquid or gas cores stabilised by lipids and surfactants. However, other materials or forms are also possible.

Some microbubbles are made with protein shells instead of lipid ones, which increases shell rigidity, resulting in better stability but also decreased echogenicity. Proteins or inorganic materials can also be used to construct a different kind of particle, which holds a gas bubble on its surface as opposed to having it fully surrounded by a stabilising shell. One example of such particle

is protein nanocups[131,132]. Nanocups have shown promise for various applications, including drug delivery to tumours and transdermal delivery[133]. Other examples include gas-stabilising gold nanocones[134] and mesoporous silica particles[135].

These agents may offer some advantages compared to the traditional ultrasound agents; however, as they are still an emerging area of research, more studies are needed to improve their safety and biocompatibility, as well as further clarify the mechanisms of gas entrapment[133]. They were therefore not investigated in this study.

2.1.5 Chapter overview and objectives

This chapter presents a description of the agents used throughout this thesis, detailing the protocols of their production and characterisation. For some agents, different compositions are compared, or the effect of some of the components on the final formulation is explored. Oxygen loading methods are described, and the agent stability before and after payload introduction is studied. Oxygen release in deoxygenated media or after ultrasound exposure is measured and compared to theoretical estimations.

2.1.6 Attribution of work

The MATLAB script used to perform optical particle sizing was previously developed in our group. The MATLAB script used to handle particle characterisation datasets from various devices was written by Dr Luca Bau. The non-phase-change droplet preparation was done by Dr Luca Bau.

The focused ultrasound oxygen release experiments (A 2.4.3) were performed in collaboration with Dr Catherine Paverd.

All other experimental and data processing work was performed by the author of this thesis.

2.2 Materials and methods

2.2.1 Materials

1,2-dibehenoyl-sn-glycero-3-phosphocholine (DBPC), polyethylene glycol (40) stearate (PEG40S), glycyrrhizic acid ammonium salt, glycerol (BioReagent, >= 99%), chloroform, citric acid (ACS reagent, >= 99.5%), sodium chloride, sodium phosphate monobasic, perfluorooctyl bromide (PFOB, 1-bromoheptadecafluorooctane) and Dulbecco's phosphate buffered saline (DPBS) were obtained from Sigma-Aldrich Company Ltd. (Gillingham, UK). Lecithin (90%, soybean) and di-sodium hydrogen orthophosphate dodecahydrate were purchased from Thermo Fisher Scientific (Waltham, USA). Sulfur hexafluoride (SF_6), O_2 and N_2 gases were obtained from The BOC Group (Guilford, UK). Perfluoropropane and perfluorobutane gas cylinders were ordered from FluoroMed (Round Rock, USA). SonoVue microbubbles were produced by Bracco (The Bracco Group, Italy).

2.2.2 Microbubble production

Microbubbles (MBs) were produced by sonicating the gas-liquid interface of the lipid/surfactant solution. Chloroform solutions of 1,2-dibehenoyl-sn-glycero-3-phosphocholine (DBPC) and polyethylene glycol (40) stearate (PEG40S) were mixed in a glass vial in 9:1 molar ratio and chloroform was evaporated using a rotor evaporator (10 min in alcohol regime, 20 min in aqueous regime, 45°C). When the lipids were fully dried, they were reconstituted in 5 mL of buffer (10% vol glycerol, 10% vol propylene glycol, 80% DPBS; or 100% DPBS) to final total concentration of 4 mg/mL and dissolved under constant stirring on a hot plate or a heating mixer set to 100°C until the solution became clear. Afterwards the solution was allowed to cool down to room temperature and sonicated at low intensity with an ultrasound probe at amplitude 20% (probe 20

kHz, 125 W, QSonica, NY, USA) until it became fully transparent. Then the sonicator probe tip was moved to the liquid-gas interface, the vial headspace was filled with the core gas (SF_6, PFP or PFB) and the probe was turned on at high intensity (30 seconds, amplitude 85%) under constant gas flow. After that the vials were capped with core gas headspace and put on ice for at least 10 minutes.

Before use, the MB solution was gently mixed and then allowed to separate until a clear border between the microbubble and the macroscopic foam was visible. The lower (microbubble) fraction was then separated into a clean vial and kept on ice for the duration of experiments. For longer experiments the MB solution was aliquoted into smaller vials with the headspace filled with the core gas for better stability.

2.2.3 Nanobubble production

To produce nanobubbles (NBs), 300 mg of lecithin, 500 mg of citric acid, 50 mg of glycyrrhizic acid and 1.25 mL of glycerol were added to a glass bottle. Then 100 mL of Milli-Q purified water or DPBS was added to the mixture, which was then stirred on a hot plate for 30-60 minutes until fully dissolved and afterwards allowed to cool down to room temperature. Before use NB mixture was shaken vigorously by hand for 1 minute.

2.2.4 Nanodroplet production

Phase-change nanodroplets were produced by condensing DBPC-PEG40S microbubbles filled with PFB and made in the high-viscosity buffer (10% vol glycerol, 10% propylene glycol, 80% PBS). To perform the condensation, 4 mL of MBs were loaded in a syringe via a 18G blunt needle, taking care to avoid introducing air or foam; the syringe was then capped and placed into a cold bath

filled with 40% ethylene glycol at -10°C for 4 min. After the incubation the syringe volume was adjusted to the new solution volume and then the formed droplets were transferred into Eppendorf tubes for washing by centrifugation (3 times 5 mins at 7000g, 4°C). Droplet solution was kept on ice at all stages.

To produce non-phase-change nanodroplets, a suspension of lecithin (108 mg) in MilliQ water (1 mL) was added to 1.8 g of perfluorooctyl bromide in an 8 mL glass vial. 0.3 mL of a solution of sodium chloride (3.6% w/v), sodium phosphate monobasic (0.69% w/v) and sodium phosphate dibasic (4.74% w/v) were added and the mixture was then diluted with MilliQ water (~0.9 mL) to a final volume of 3 mL. The mixture was pre-emulsified with an IKA turrax T10 basic homogenizer (IKA, Germany) at speed 5, 20000 rpm for 30 sec and immediately emulsified with an LV1 microfluidizer (Microfluidics, USA) primed with PBS (25000 psi, 3 passes). The resulting emulsion was filtered through a Millex 0.45 µm syringe filter (Merck Millipore, USA).

2.2.5 Agent characterization: size distributions and concentrations

MBs were characterized by diluting the MB solution 1:20 in PBS, placing a 10 uL sample on a hemacytometer and acquiring at least 15 images on an optical microscope (Bright-Line Hemacytometer Hausser Scientific, microscope Leica DM500, objective 40x, cameras Qimaging MicroPublisher 3.3 and Leica MC170 HD) and then processing the images with a custom MATLAB script. The sizing window was set to 0.5-10 um: particles smaller than 0.5 µm could not be reliably sized due to the resolution restrictions, and microbubbles larger than 10 µm represented foam contamination that was ideally isolated from the final sample.

Nanobubbles and nanodroplets were characterized by nanoparticle tracking analysis using a NanoSight NS300 particle sizer (Malvern Panalytical, UK). Samples were diluted in MilliQ water to

the concentration of approximately 10^8-10^9 particles/mL; acquisition and processing settings were adjusted to minimise background scattering noise.

Nanodroplets were additionally characterised with dynamic light scattering (DLS) (Zetasizer Nano ZS, Malvern Panalytical, UK).

2.2.6 Agent oxygenation and nitrogenation

For most experiments, loading agents (MBs, NBs or droplets) with oxygen or nitrogen was performed by aliquoting the agent solutions and saturating them with the payload gas. In the case of MBs and droplets, aliquots of approximately 500-700 uL were used and the headspace was filled with a gentle flow of the payload gas for 2 mins. Due to the better stability of NBs, they could be saturated in larger volumes of approximately 10 mL by actively sparging the gas through the solution for 3 mins. For sparging, a blunt needle was attached to the end of the gas line and the gas flow rate was regulated to promote solution agitation and mixing; the parts of the gas line that may come in contact with the solution were cleaned before and after with 70% ethanol.

For MBs, this method was compared with loading them with the payload gas or with a mixture of a low-diffusivity gas and a payload gas (O_2/N_2) directly during MB production. The gas flows were regulated by two Omega FL-1442-S gas rotameters (OMEGA engineering, Manchester, UK) with all gas pressures at the entrance to the rotameters kept at approximately 1 bar. For this method, the protocol was exactly the same as for the normal MB production, with the low-diffusivity gas replaced by its mixture with the payload.

2.2.7 Oxygen release characterisation

For microbubbles, O_2 release was measured after introducing MBs into degassed media and after sonication. For the degassed media measurement, 320 uL of MBs were added to 12.5 mL of non-degassed or degassed DPBS buffer (~35% airsat); then vials were closed and mixed and O_2 concentration was measured in the liquid phase. For ultrasound-mediated O_2 release, MB samples and lipid solution controls were added to non-degassed DPBS buffer and sonicated for 60 seconds in an ultrasound water bath (Eumax US cleaner UD150SH-6L, 150W, 40 kHz). O_2 concentration was measured with a non-invasive optical sensor (OXY MINI Minisensor Oxygen Meter (PreSens Precision Sensing GmbH, Germany) with SP-PSt3-NAU-D5 sensor dots); the sensor temperature probe was placed in room-temperature-equilibrated water.

For nanobubbles, the dynamics of oxygen release into deoxygenated (nitrogen-saturated) medium were measured. A sample was introduced into a vial with 100% N_2 headspace under constant mixing with a magnetic stirrer, and the released O_2 concentration in the vial was measured with an optical oxygen sensor (PreSens). The oxygen sensor temperature probe was placed into the solution for better measurement precision.

2.3 Characterization of agents

2.3.1 Microbubbles

It is known that the sonication protocol for microbubble preparation is dependent on the specifics such as the method of lipid solubilization, incubation times and speed of solution cooling after sonication[136,137], therefore care was taken to conduct MB production in a reproducible manner. The resulting size distribution was well-reproducible, with a peak below 1 μm (**Fig. 2.3.1.1**).

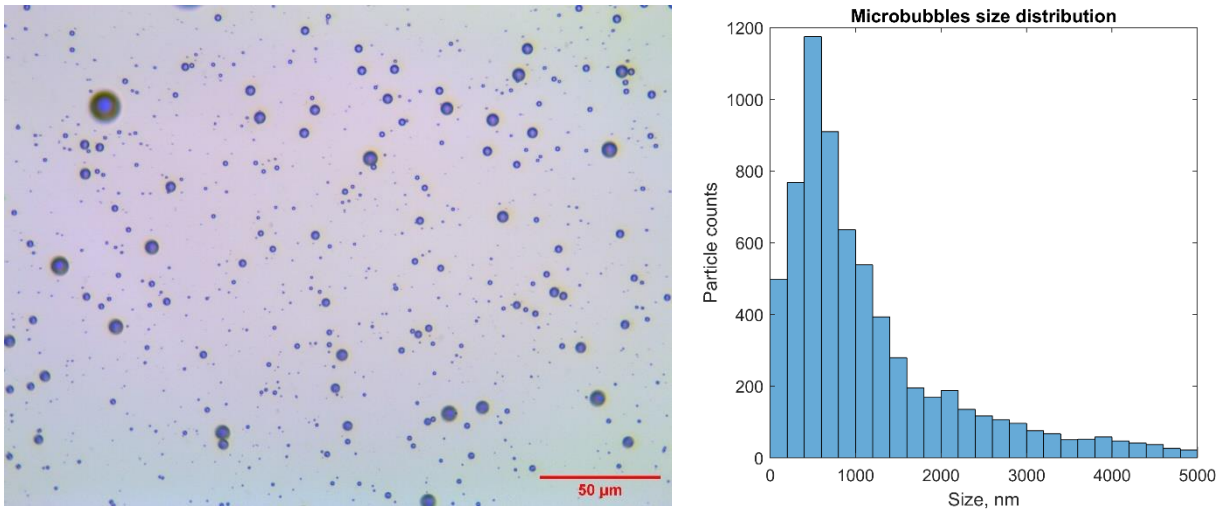

Fig. 2.3.1.1. Example of a microbubble micrograph and the corresponding size distribution.

As described in section **2.1.1**, the lipid composition of MBs in this study was fixed (DBPC-PEG40S), but three different low-diffusivity gases were compared for the core composition: SF_6, PFP and PFB. In agreement with other studies[138], PFC-based MBs showed larger concentrations at production and improved stability (**Figs. 2.3.1.2, 2.3.1.3**). For most of the following experiments, PFB-based MBs were used.

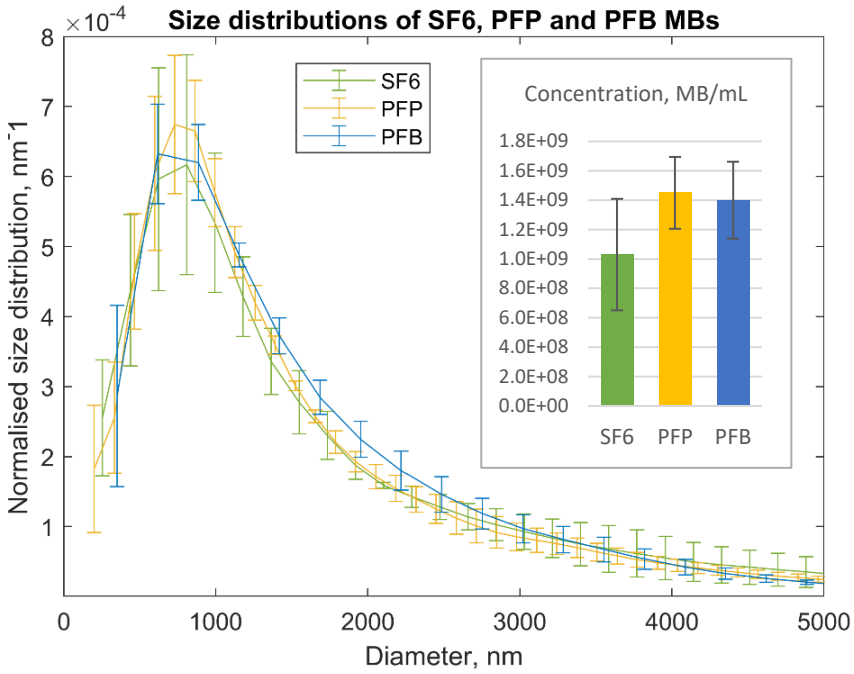

Fig. 2.3.1.2. Normalised size distributions and concentrations of DBPC-PEG40S microbubbles with different core gases (n = 5, error bars indicate standard deviations).

A. Sub-micrometre fraction

The optical sizing method that was used to characterise MBs has a resolution limit of several hundreds of nanometres, which is sufficient to measure the size fractions of the MB solution that contribute the most to the ultrasound response, i.e., the gas-filled particles of 1-2 micrometres in diameter. However, for the purposes of gas delivery applications it is also important to note that some lipid particles exist in the solution below the optical microscopy resolution limit. To check whether this fraction can have a meaningful contribution to the gas-loading capacity, the MB lipid solution (DBPC-PEG40S) before the sonication step and the smaller fraction of PFB-filled MBs after centrifugation (10 min, 500 g) were measured by NTA. It was found that for these samples particle concentrations in the hundreds of nanometres range were $1*10^{13}$/mL and $6*10^{12}$/mL correspondingly, meaning that the total volume of the sub-micrometre fraction is on the order of

magnitude of 1-10 uL/mL; this is comparable to the total gas volume of the larger fraction as measured by optical microscopy, which is around 5-15 uL/mL. Consequently, due to the large total volume and potentially better stability than MBs, the sub-micrometre fraction of the MB solution may play some role in the gas delivery; however, the gas-carrying capacity of this fraction depends on the nature of these small particles and therefore remains to be determined.

In addition, size distributions of the lipid solution and smaller MB fractions after centrifugation were measured by DLS (**Fig. 2.3.1.3**). They confirmed the presence of the sub-micrometre fraction, although, due to the nature of DLS, they could not confirm the concentrations. Interestingly, the subnatant samples exhibited a shift to larger sizes with time, possibly indicating the dynamic nature of these samples and resulting in the large error bars.

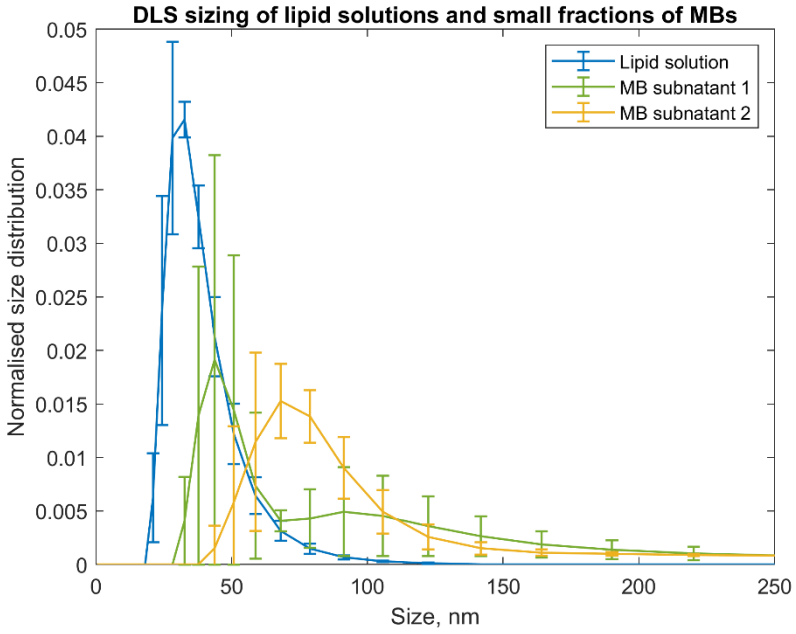

Fig. 2.3.1.3. DLS measurements of size distributions for DBPC-PEG40S lipid solution (n = 3), small fraction of PFB MBs after 15 min, 500 g centrigugation (subnatant 1, n = 2) and after subsequent 20 min, 500 g centrifugation (subnatant 2, n = 3) (error bars indicate standard deviations).

B. Stability

MB stability is well-researched, and it was confirmed in this study that the size distributions and concentrations did not undergo any major changes during 6-8 hours of storage of the stock solution on ice, signifying that the same stock could be used for a day of experiments. MB stability was also checked after dispersion in aqueous media at room temperature, which was also found to be sufficient for the purpose of these experiments (see below section **2.4.2**).

C. Commercial microbubbles (SonoVue)

In addition to in-house produced microbubbles, some experiments were performed with commercially available microbubbles (SonoVue, lipid shell with SF_6 gas core). SonoVue bubbles were characterised by optical microscopy, checking the stability during 3 hour storage at room temperature, which corresponds to storage during a typical experiment (**Fig. 2.3.1.4**). Three batches were also compared after dispersion, and size distributions and concentrations reproducibility was found to be comparable to that of in-house MBs (concentrations $2.11*10^8$/mL, $2.29*10^8$/mL and $2.49*10^8$/mL, with peaks around 1 um).

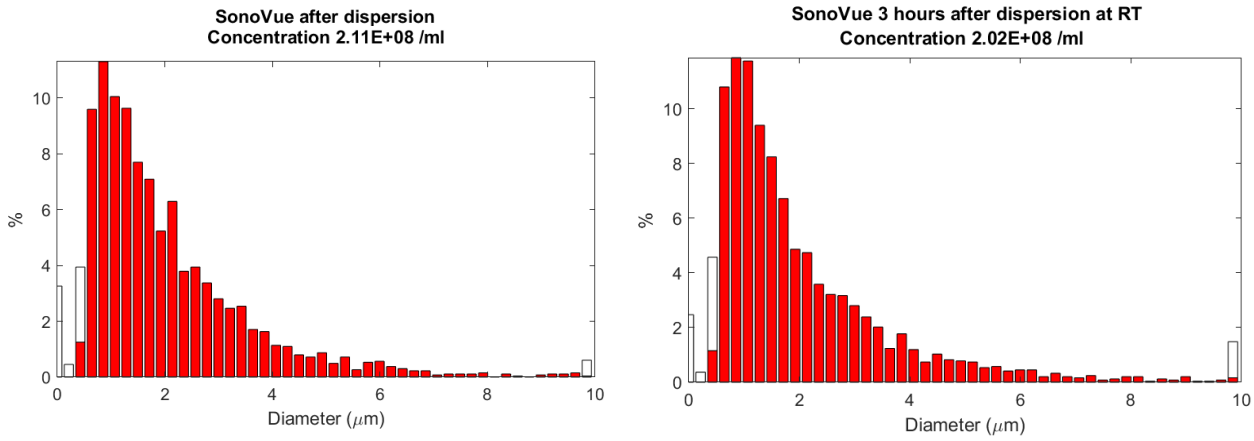

Fig. 2.3.1.4. SonoVue size distribution and concentration right after dispersion according to the manufacturer's protocol and after 3 hours of storage at room temperature.

2.3.2 Nanobubbles

Lecithin-based nanobubbles were produced via mixing the components (lecithin, citric acid, glycyrrhizin and glycerol) on a hot plate until the solution became homogenous, which resulted in the formation of nanoparticles (size distribution peak at approximately 100 nm and concentration on the order of magnitude of 10^{12}-10^{13} particles/mL as measured with nanoparticle tracking analysis (NTA)). NTA was used for all NB characterisation, as the NB samples were too polydisperse to produce a reliable result using DLS sizing.

Preliminary optimisation of nanobubble composition was performed prior to the current study and therefore is not shown here. As a part of the current project, some aspects of the NBs were studied, such as the importance of shaking and different components on the particle size distributions and stability at physiological temperatures.

The NB fabrication protocol involves shaking the solution by hand, and saturation with the payload gas involves solution agitation; therefore from the point of view of gas loading and delivery it is important to understand whether agitation influences the particle size distributions. Size distributions and concentrations were measured before and after the shaking step during production (Fig.2.3.2.1) and it was found that the shaking step has only a small effect on the increase of particle concentration and no significant effect on the size distribution, signifying that the agitation of solution during gas payload loading would not present an issue.

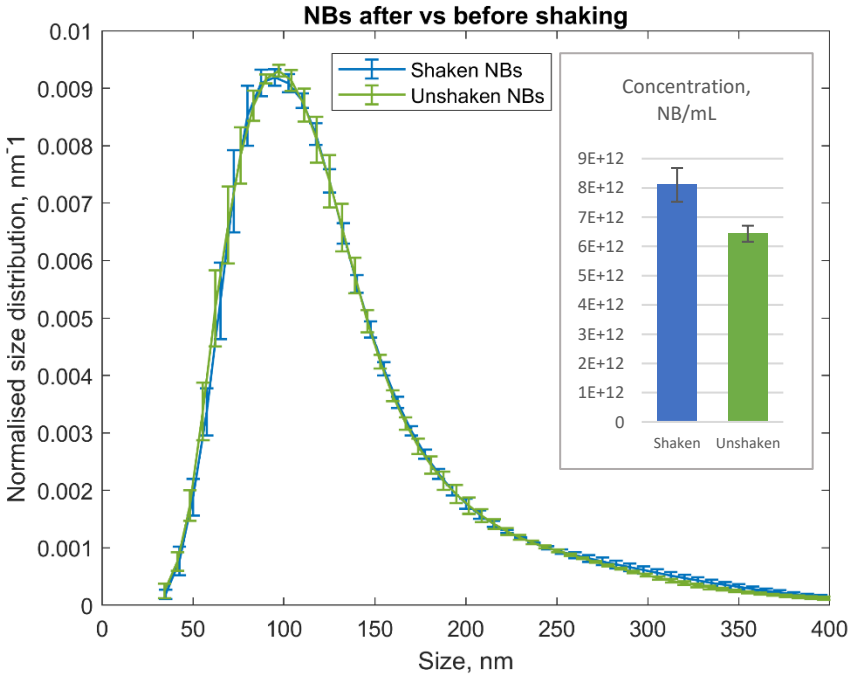

Fig. 2.3.2.1. Normalised size distributions and concentrations of nanobubble solutions before and after the shaking step of the production, measured with NTA (n = 3, error bars represent standard deviations).

The influence of different components on the process of particle formation was studied by excluding components from the formulation and comparing the resulting particles with the NB solution (Fig. 2.3.2.2). Lecithin is believed to be the main particle-forming agent, and therefore it is not surprising that it was found to be important for NB formation. Interestingly, citric acid was shown to be also important for particle formation, while other components had significant but small impacts on normalised size distributions.

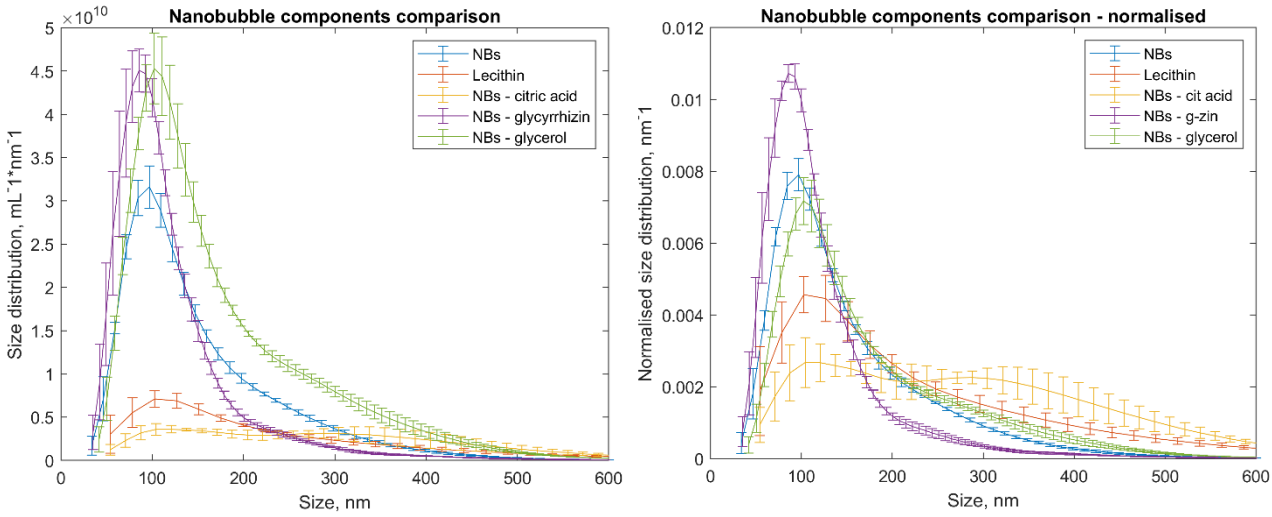

Fig. 2.3.2.2. Comparison of size distributions (raw and normalised) for nanobubbles (NBs), lecithin solution (at the same concentration as in NBs) and NB solutions without one of the components: citric acid, glycyrrhizin or glycerol, measured with NTA (n = 3, error bars represent standard deviations).

Citric acid is the component that makes the NB solution acidic (pH 2.0), therefore it was of interest to determine whether it influences the formation of particles via pH or directly, for example via incorporation of citric acid molecules into the particles. Size distributions were compared for neutral and acidic solutions of NBs and lecithin; pH adjustment was performed with HCl and NaOH. It was shown that adjusting the pH of NBs and lecithin produced only small changes in size distributions, while adding citric acid to lecithin resulted in a size distribution close to that of NBs; therefore the effect of citric acid on the formation of nanoparticles is more likely to be direct rather than pH-mediated, or else it is possible that pH is important during the formation of NBs and changing it afterwards has a smaller effect on the resulting formulation (**Fig. 2.3.2.3**).

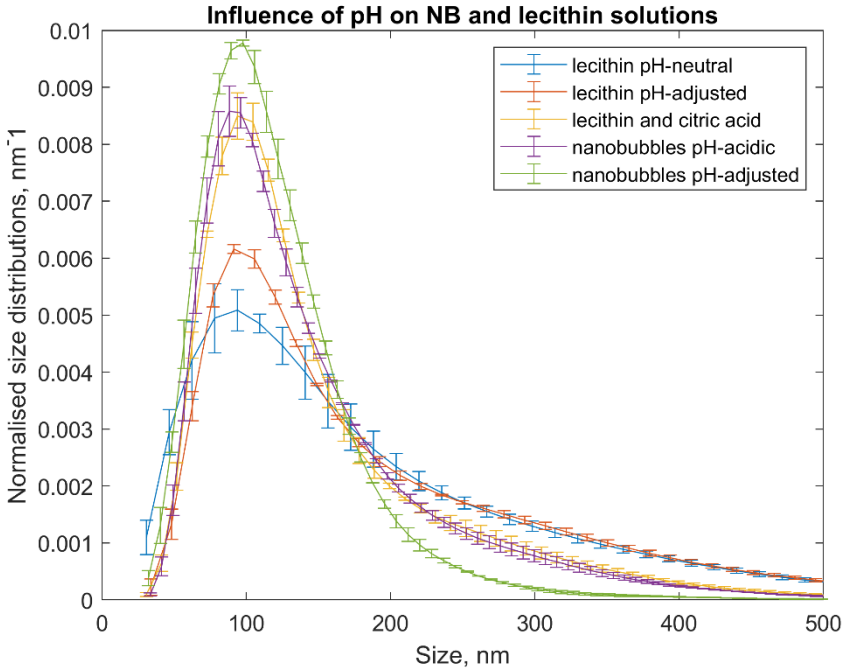

Fig. 2.3.2.3. Comparison of normalised size distributions of lecithin and NB solutions at different pH values: lecithin pH-neutral (pH = 6.7), lecithin pH-adjusted to acidic (pH = 2.0), NBs pH-acidic (pH = 2.0) and NBs pH-adjusted to neutral (pH = 7.5), measured with NTA (n = 3, error bars represent standard deviations).

While the stability and coalescence dynamics of lipid-shelled microbubbles are relatively well-understood, these phenomena are less studied for lecithin-based particles. For this reason, the stability of NB solution was studied when incubated at stock concentration in a 2 mL test tube submerged in a water bath heated to 35°C (**Fig. 2.3.2.4**). Measurements were conducted at timepoints t = 0 min, 5 min, 15 min, 30 min, 60 min and 120 min. Neither size distributions nor concentrations showed a significant change between the 0 min and 2 hours timepoints (with only the 60 mins measurement showing a size distribution change, which is small and does not agree with the 120 mins timepoint, meaning it is likely an experimental fluctuation). Therefore, NBs are stable within at least the 2-hour time window at physiological temperatures.

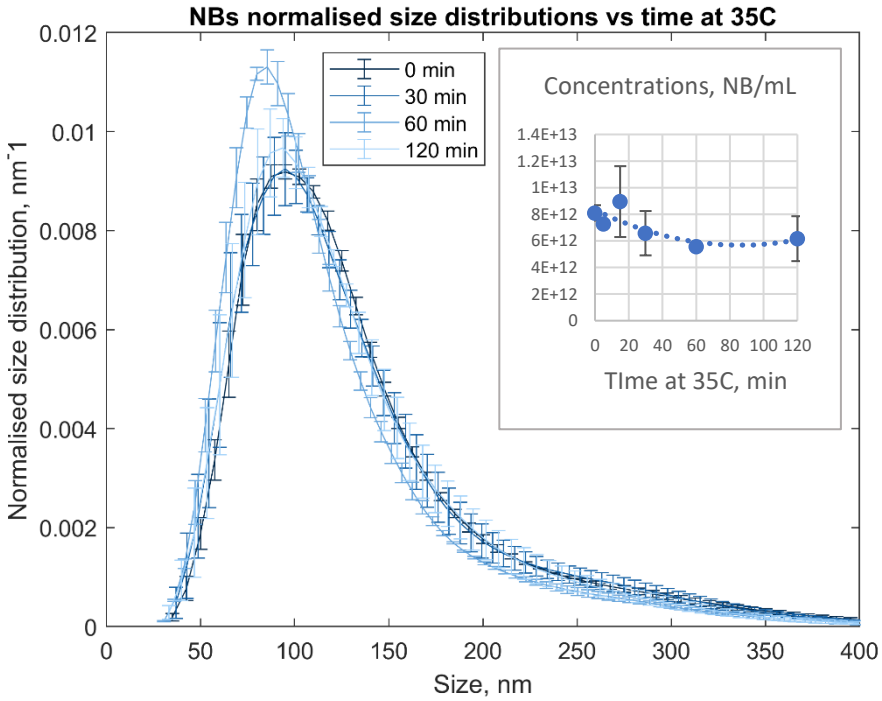

Fig. 2.3.2.4. Normalised size distributions and concentrations as a function of time at 35°C measured by NTA (n = 3, error bars represent standard deviations).

2.3.3 Nanodroplets

Firstly, phase-change droplets acquired by condensation of DBPC-PEG40S PFB MBs were fabricated and tested for their size distribution and stability. As expected, phase-change droplet stability was not optimal, with the drop in concentration by about one-third after 1 hour at room temperature in water, in 1:40 dilution from the stock solution (Fig. 2.3.3.1). Nonetheless, they were explored in some of the experiments under the restraints of running all sample and control measurements as quickly as possible to minimise the impact of droplet evaporation.

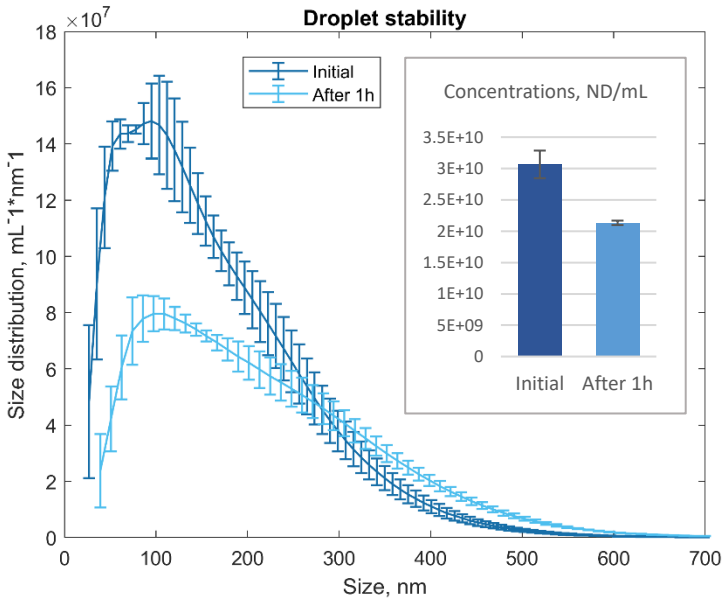

Fig. 2.3.3.1. Size-distributions and concentrations of DBPC-PEG40S PFB phase-change nanodroplets before and after 1 hour at room temperature in water, in 1:40 dilution from the stock solution, measured by NTA (concentrations adjusted to non-diluted samples, n = 3, error bars represent standard deviations).

In addition, a droplet sample was measured by the NTA in two different dilutions: 1:40 and 1:4000 from stock solution. The reason for this is that the optimal concentration range for the NTA is ~10^8/mL, and therefore the more concentrated dilution is optimal for measuring the droplets acquired from the MBs (the concentration of MBs is known to be ~2-4*10^9/mL, and the droplet concentration is therefore expected to be in the same range), while the more diluted sample allows to measure the more concentrated sub-micrometre fraction (**Fig. 2.3.3.2**). Interestingly, the more diluted sample did correspond in size distribution to the sub-micrometre fraction of microbubbles and the DBPC-PEG40S lipid solution discussed previously, and its concentration (~1.7*10^{11}/mL) was about 1-2 orders of magnitude lower than that of the small MB fraction or lipid solution (section **2.3.1**).

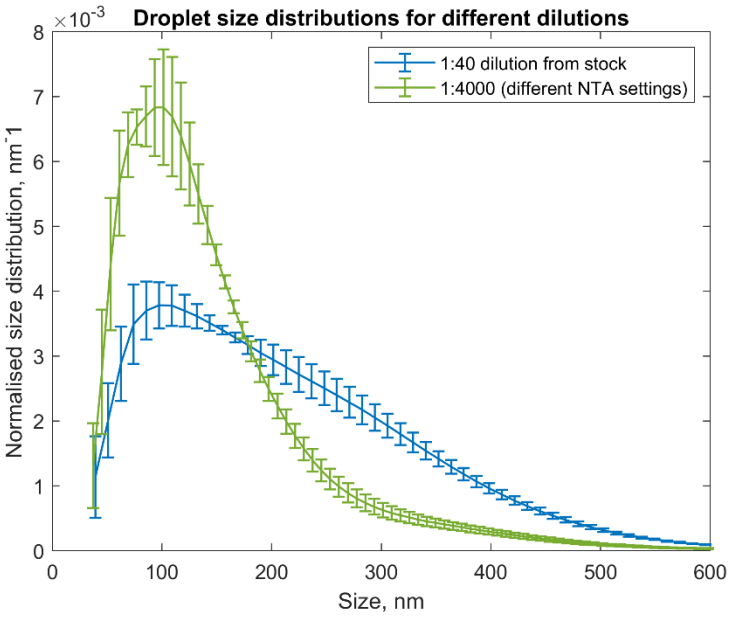

Fig. 2.3.3.2. Size distributions of DBPC-PEG40S PFB phase-change nanodroplets in two different dilutions, 1:40 from stock solution and 1:4000, measured with NTA with different settings for the two samples (n = 3, error bars represent standard deviations).

The non-phase-change ND formulation used in this study was based on perfluorooctyl bromide (PFOB, also known as perflubron) and lecithin – typical components of PFC-based blood substitutes. The size distributions acquired on DLS are shown in **Fig. 2.3.3.3**.

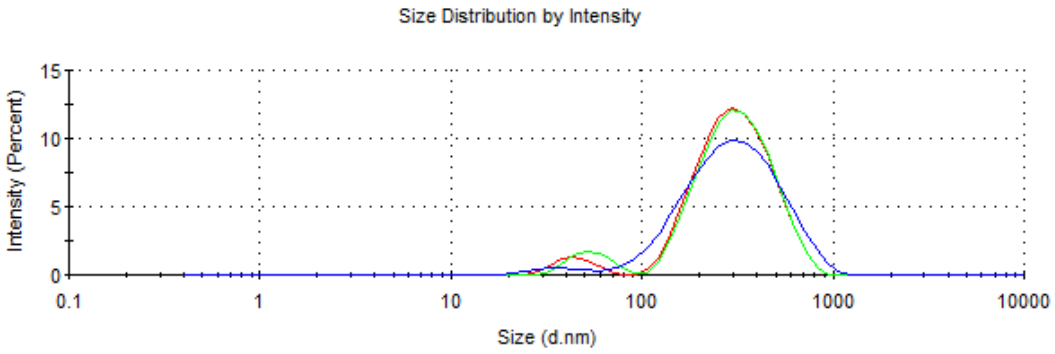

Fig. 2.3.3.3. Size distributions of lecithin PFOB non-phase-change droplets acquired by DLS (showing 3 repeats, distribution by intensity).

2.4 Agent saturation with payload gases

2.4.1 Methods of loading the gas into carriers

As discussed above (1.2.4.1 – 1.2.4.2), due to the high diffusivity of oxygen in physiological media, the loading of carrier agents with oxygen is transient and the excessive payload gas quickly dissolves out of the carriers after they start equilibrating with blood under the pO_2 below 20% of that of a full oxygen atmosphere. However, it is still of interest to investigate the loading of payload gases into carriers, for several considerations, such as checking their structural or chemical stability with various gas compositions, or practically investigating the gas volume held by these agents in order to support the theoretical estimations.

A number of methods are available to load an agent with a carrier gas. The ones most widely used in the literature are saturating the agent solution with the payload gas and allowing the loading to happen via concentration gradient-driven diffusion, or creating the agent in the atmosphere that is partially or fully saturated with the payload gas, in particular by mixing it with a low-diffusivity gas for a gas-based agent. Another option, especially convenient for commercial agents, is freeze-drying the agent and reconstituting it in the atmosphere of the payload gas.

The best method for each carrier depends on its properties and the practical considerations of its use. In particular, freeze-drying with reconstitution just before use has been widely implemented in commercial ultrasound agents due to its convenience for the end user and long-term storage possibility, and some studies chose this method for payload gas loading[64,65]. However, ensuring that the MBs remain stable during the freeze-drying process presents a substantial technical difficulty, and, since long-term storage was not a requirement for this study, the freeze-drying

method was not investigated in detail. Instead, saturation with a payload gas either during or after the carrier production was explored.

For the payload gas loading, it is important to consider the carrier stability, especially in the case of gas-based agents, and find an optimum between better stability and higher payload gas loading. Another important consideration is carrier storage after the payload is introduced: due to the high oxygen and nitrogen diffusion speed in aqueous solutions, the buffer in which the agents are stored has to be kept saturated with the payload gas to the desired concentration in the carrier until it is used in an experiment, in order to prevent the loss of the payload. These considerations are reflected in the gas loading protocols.

2.4.2 Size distributions before and after gas loading

Agent stability is an important consideration for gas loading, and therefore size distributions and concentrations were checked before and after gas loading.

A. Microbubbles

For microbubbles, which are less stable to gas phase change than nanobubbles or droplets, due to their gas cores, two different types of payload loading were considered: by payload saturation after production (designated below as PFB O_2), or by using a mixture of a payload gas and a low-diffusivity core gas during production. For the latter method, 50%, 80% and 95% O_2 by volume was used, as well as 100% O_2 at production with no PFB. These samples were compared to PFB MBs that did not undergo oxygenation.

First, size distributions and concentrations were compared after production or oxygenation (t = 0 for the stability study) (**Fig. 2.4.2.1**). As expected, all size distributions (except for 100% O_2 MBs)

were similar with a peak around 1 um, but the concentration decreased sharply with the increasing ratio of oxygen. Pure O_2 MBs yielded larger bubbles and low concentration and were quickly destroyed during storage.

The morphology of the produced MBs followed similar trends: while PFB, PFB O_2 and 50% O_2 MBs were round in shape in the optical microscopy images, some 80% O_2 MBs looked slightly misshapen, and most 95% O_2 and pure O_2 MBs were visibly misshapen, which agrees with lower yields, as rapid gas loss due to diffusion without a stabilising PFC core is expected to result in both irregular shapes and lower concentrations (Fig. 2.4.2.2).

Next, to explore MB stability, all samples were incubated for 3 hours in stock concentration on ice, mimicking MB storage during a typical experiment; for 4 hours in 1:20 dilution at room temperature; and for 3.5 hours in 1:20 dilution at 37°C; test tube headspaces were filled with corresponding core gases to decrease post-production payload gas loss (Fig. 2.4.2.3). Normalised size distributions and concentrations exhibited some changes, with the size distribution peaks shifting to larger values for some samples after storage at 37°C and concentrations dropping after storage at higher temperature, as expected. Particle morphology showed the same trends as seen at t = 0 , with 95% and 100% O_2 MBs becoming even more misshapen.

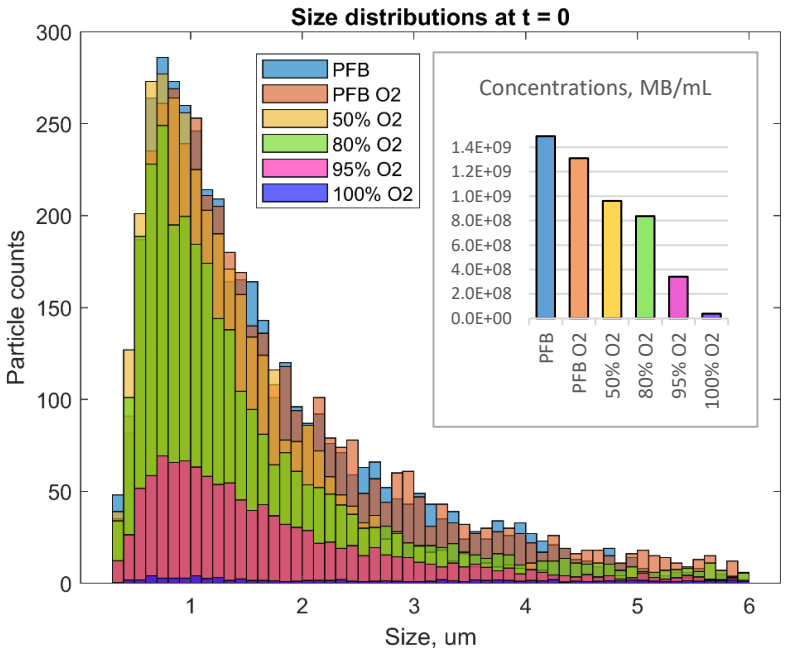

Fig. 2.4.2.1. Size distributions and concentrations of PFB non-oxygenated and oxygenated microbubbles measured by optical microscopy after production or oxygenation (t = 0). Samples are: PFB MBs; PFB MBs oxygenated by O_2 flow after production (PFB O_2); PFB:O_2 MBs produced with 50% / 80% / 95% vol O_2; MBs produced with 100% O_2 without PFB.

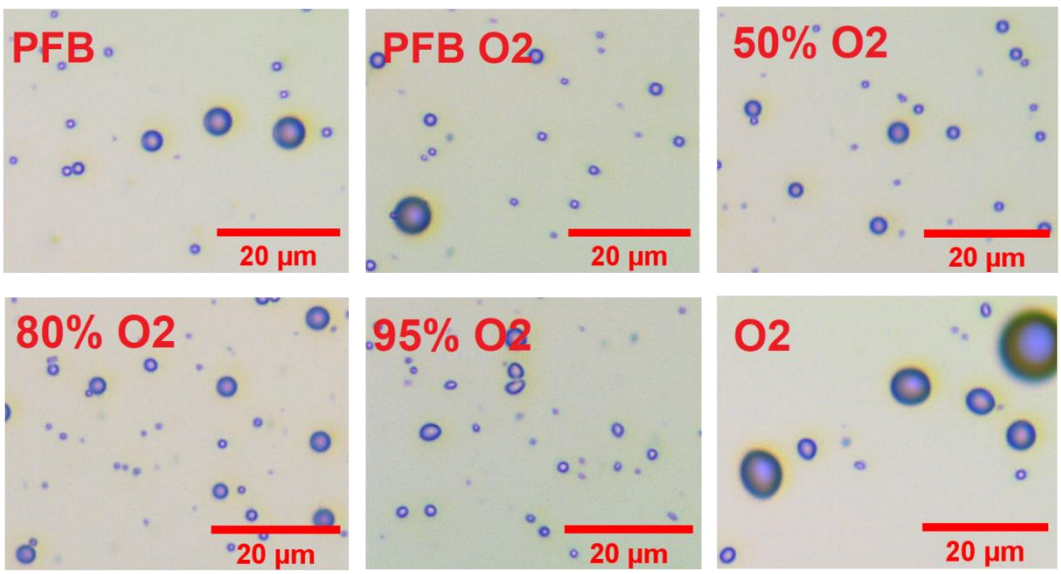

Fig. 2.4.2.2. Examples of bubble morphology from optical microscopy images for PFB non-oxygenated and oxygenated microbubbles measured by optical microscopy after production or oxygenation (t = 0). Note that these images do not represent MB concentrations, as each sample was diluted differently in order to have optimal concentrations for optical sizing.

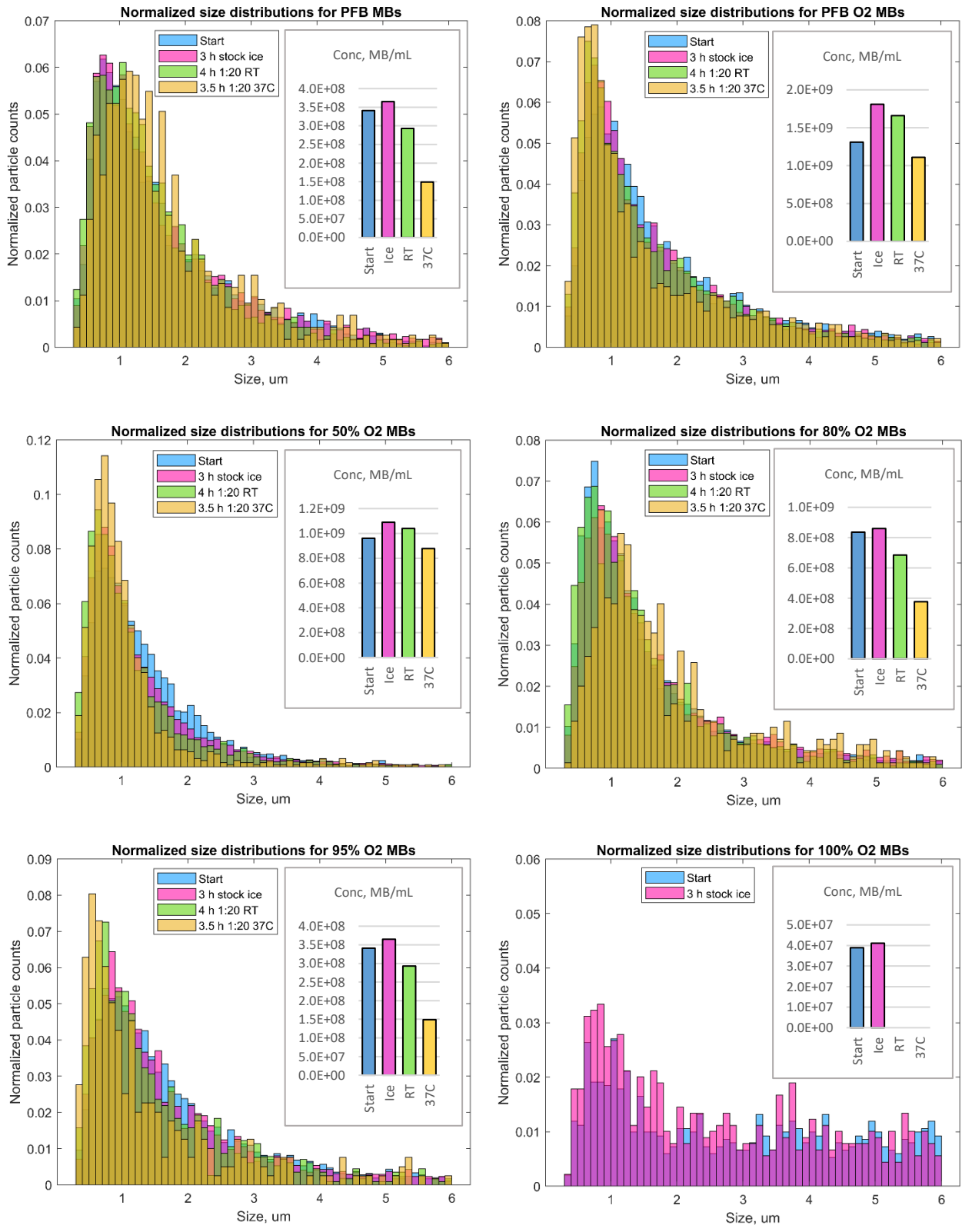

Fig. 2.4.2.3. Normalised size distributions and concentrations measured by optical microscopy at the start of the experiment (t = 0), after 3 hours in stock concentration on ice, after 4 hours in 1:20 dilution at room temperature and after 3.5 hours in 1:20 dilution at 37°C, shown separately for

each sample: PFB MBs; PFB MBs oxygenated by O_2 flow after production (PFB O_2); PFB:O_2 MBs produced with 50% / 80% / 95% vol O_2; MBs produced with 100% O_2 without PFB.

The results seen here agree with the literature. The lack of stability of pure oxygen microbubbles corresponds to the history of the development of ultrasound contrast agents, as the first lipid MBs were produced with air but were found insufficiently stable, which led to the use of high diffusivity gases such as SF_6 and PFCs in subsequent formulations; for this reason, all MBs in clinical use for ultrasound imaging today have low-diffusivity gas cores[37]. It has also been shown both theoretically and experimentally that, due to the fast oxygen diffusion, the addition of a low-diffusion gas is necessary to stabilise an ultrasound agent for the purpose of gas delivery and to achieve higher yields during production[44].

It is important to note that these experiments were conducted in air-saturated buffer solutions. Sometimes in the literature MB experiments are performed in a degassed buffer, for example to maximise the difference measured between oxygenated and non-oxygenated MBs, or to lower the background for reactive oxygen species measurements. However, it is known to have a detrimental effect on MB stability and reproducibility of experiments, especially for oxygen-loaded MBs[139]. For this reason, the size distributions of SF_6 MBs oxygenated by O_2 flow were checked after dilution in a normal buffer (100% air saturation (airsat) O_2 concentration) and a buffer degassed with a vaccum pump to approximately 60% or 40% airsat O_2 (as measured by a PreSens oxygen sensor). The MBs diluted in 60% and 40% airsat buffers lost concentration, as indicated by the opacity of the solution, quickly after dilution; size distributions, as measured within a few minutes after the dilution due to the speed limitations of optical sizing, show that most of MB concentration is lost within that time frame and remaining bubbles are big and visibly misshapen (**Fig. 2.4.2.4**). It was observed that non-oxygentaed SF_6 MBs also dissolve within a few minutes when diluted in 60% airsat buffer (visual observation, data not shown), which agrees with the

literature[139]. Consequently, all MB experiments in this project were carried out in non-degassed, 100% airsat O_2 buffers, except for the oxygen release experiments where the degassed buffer was used specifically to destroy the MBs and measure their payload.

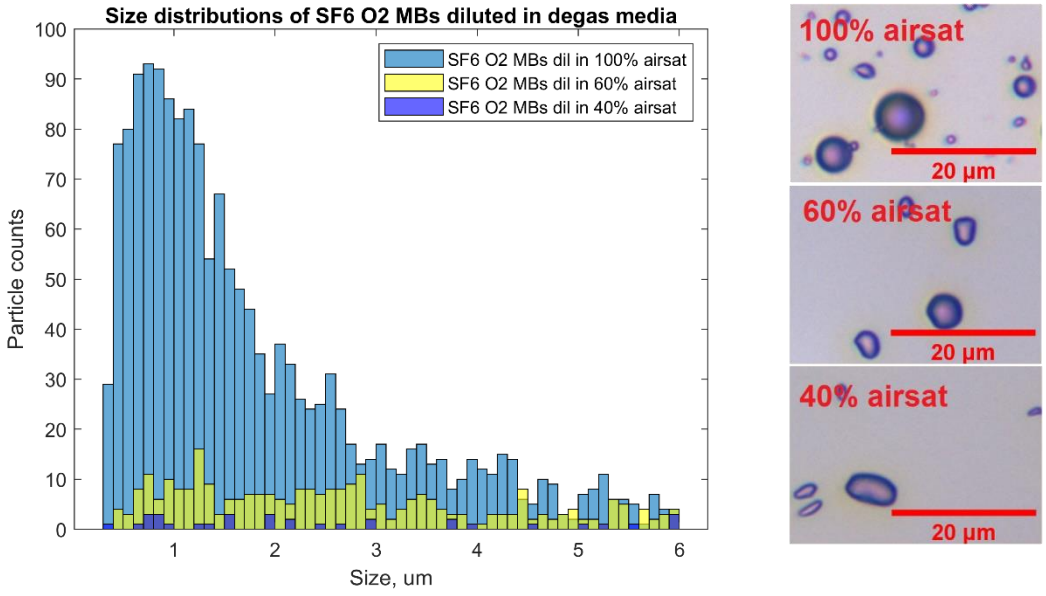

Fig. 2.4.2.4. Size distributions and bubble morphology examples captured by optical microscopy after oxygenated SF_6 MBs were diluted in a buffer at 100%, 60% and 40% air saturation O_2 concentration.

B. Nanobubbles

The nanobubble formulation used in this project did not utilise a low-diffusivity gas core; therefore, the method of oxygen loading during production was not tested and nanobubbles were loaded by payload gases by sparging after production. Normalised size distributions and concentrations of nanobubbles before loading with a payload gas (i.e., air-filled) and after loading with O_2 or N_2 are shown in **Fig. 2.4.2.5**. The differences in both size distributions and concentrations are small, signifying that NBs, as expected, remain stable during gas loading.

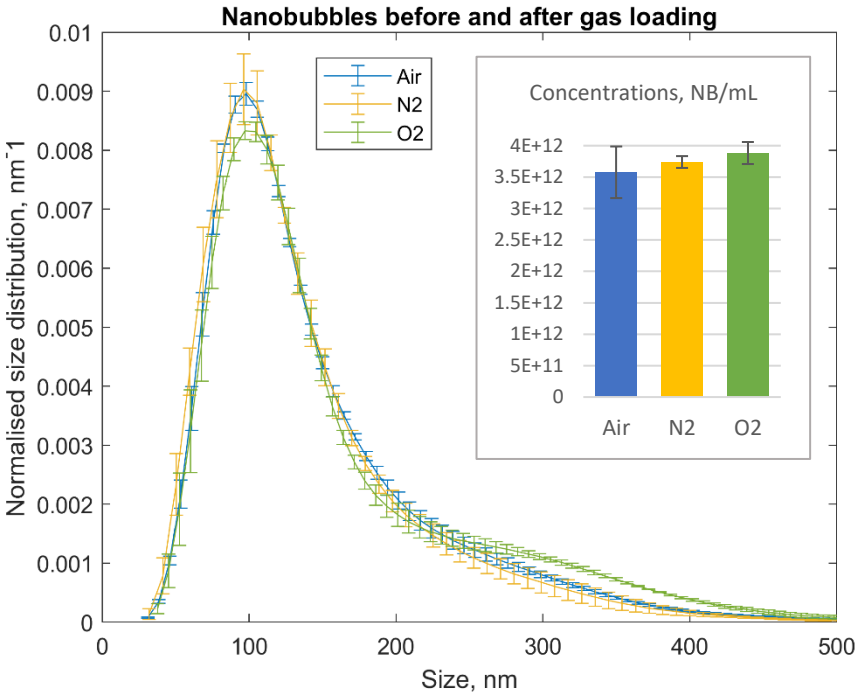

Fig. 2.4.2.5. Nanobubble normalised size distributions and concentrations before payload gas sparging (air) and after loading with O_2 or N_2, measured by NTA (n = 3, error bars represent standard deviations).

2.4.3 Measurements of oxygen release

To experimentally confirm the volume-based oxygen payload estimations detailed in the previous sections (**1.2.4.1 – 1.2.4.2**), measurements of oxygen payload release were performed after introducing the agents into deoxygenated medium or after sonication.

A. Microbubbles

O_2 release measurements were performed for PFP MBs and PFP MBs oxygenated by O_2 flow (concentration $1.9*10^9$/mL, total volume ~20 uL/mL). 320 uL of MBs were added to 12.5 mL of non-degassed or degassed DPBS buffer (~35% airsat); then vials were closed and mixed and O_2 concentration was measured in the liquid phase.

The results were compared to the values obtained by theoretical estimations. For the PFP MBs, it was assumed that the MBs and the buffer have equilibrated with air before this experiment. In these estimations, two values were calculated: the oxygen concentration increase from the microbubbles, calculated via the Henry's law (assuming that all MBs were destroyed during mixing and the payload is homogenously distributed in the solution; this is a reasonable assumption for the timeline of this experiment, which was checked during the stability studies of MBs in degassed buffers – see section **2.4.**2 and figure **2.4.2.4**) and the contribution of the MB buffer, calculated from the oxygen solubility values in aqueous solutions found in the literature; the buffer is also either air- or oxygen-saturated due to the process of oxygenation (**Fig. 2.4.3.1**).

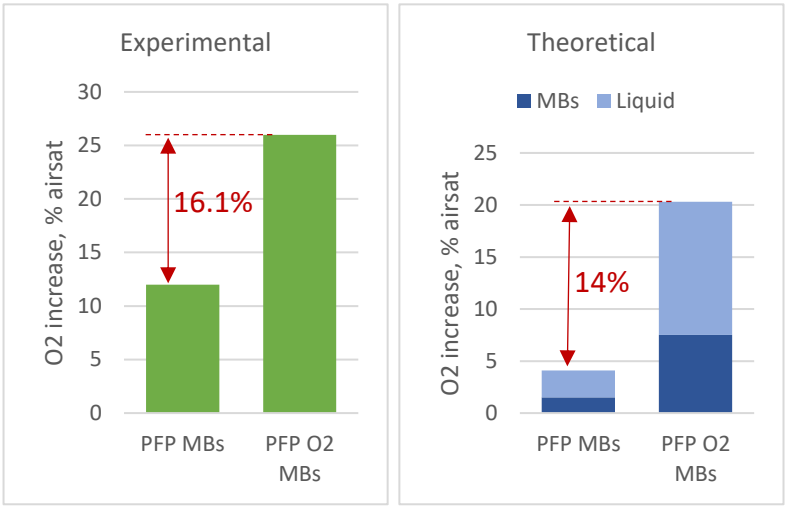

Fig. 2.4.3.1. Oxygen concentration in the liquid phase (expressed as % airsat) increase after the addition of PFP MBs and PFP O_2 MBs: comparison of the experimental result and theoretical estimations. For the theoretical estimations, the O_2 concentration rise from the MBs and the buffer is shown separately; PFP MBs and their buffer are assumed to be air-saturated at the start of the experiment.

The experimentally measured rise in O_2 concentration was larger than the theoretical estimation, due to the fact that the degassed solution mixed with the vial headspace during the experiment,

which increased the baseline O_2 concentration; however, this effect is much reduced if comparing the difference between the O_2 increase caused by PFP O_2 and PFP MBs. This difference agrees well between the experiment and the theoretical estimation (16.1% vs 14%, which is within the MB sizing error margins). This confirms the accuracy of theoretical estimations of O_2 dosages via the MB volumes, used throughout this thesis.

It is important to note that the contribution from the buffer was larger than that from the MBs (Fig. 2.4.3.1, right-hand side): although the oxygen solubility in aqueous media is smaller than in MBs, the small total volume of MBs compared to the buffer in which they are kept means that the buffer oxygen content is substantial. Consequently, care should be taken in using proper controls in oxygen release experiments, such as oxygenated buffer; and in interpreting the oxygen release results, since most of the released oxygen comes from the buffer.

For ultrasound-mediated O_2 release measurements, PFB MBs and PFB O_2 MBs, oxygenated by O_2 flow, were used. O_2 concentration was measured using an optical sensor (PreSens) in the sample vial. For this experiment, 570 uL of a sample were introduced into 12.5 mL of non-degassed DPBS and then sonicated (Fig. 2.4.3.2). In line with the considerations detailed above for the importance of accurate controls to determine the fraction of oxygen coming from the MBs and not the buffer, the controls in these experiment were DBPC-PEG40S lipid solutions in the same concentration as used for MB production, oxygenated or not oxygenated similarly to the MB samples; another control was ruptured MBs, which are similar to the lipid solution but may more accurately represent the MB solution lipid concentration due to the loss of lipid into foam during MB production. Sonication was performed in an ultrasound water bath (150 W, 40 kHz) for 60 sec.

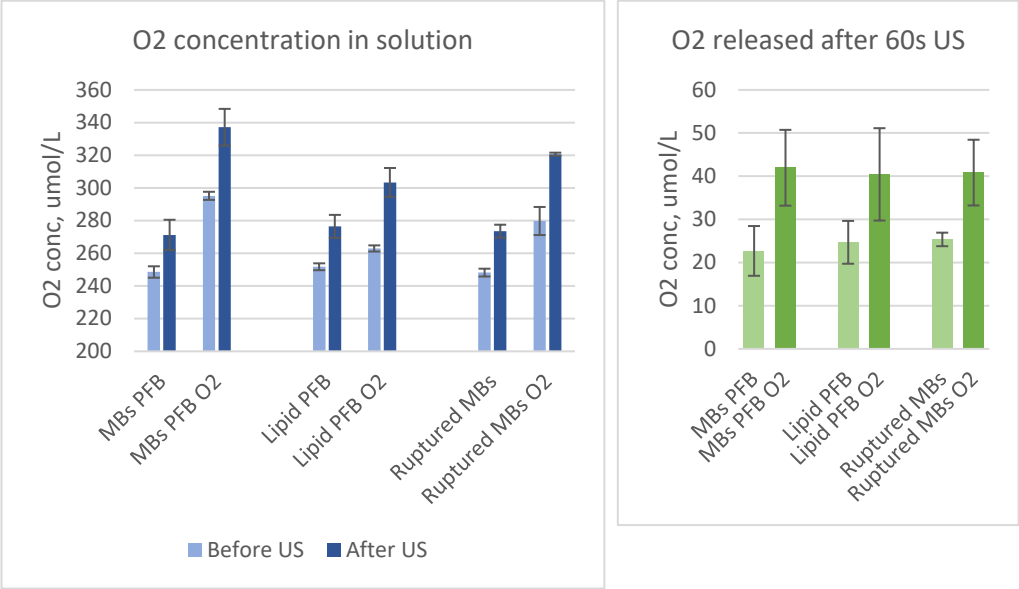

Fig. 2.4.3.2. O_2 concentrations before and after sonication and O_2 release for PFB MBs and PFB O_2 MBs with corresponding controls – DBPC-PEG40S lipid solutions in the same concentrations as used for MB production and ruptured MBs; controls were oxygenated by O_2 flow in the same way as MBs (n = 2, error bars represent standard deviations).

As expected, the O_2 concentration was elevated after ultrasound exposure, and more so for oxygenated samples than for non-oxygenated; however, this rise was, within the experimental error, similar for MBs and lipid controls. This demonstrates that, although O_2 MBs appeared to induce a rise in O_2 level after sonication, this result became experimentally insignificant after the comparison with buffer/lipid controls, which agrees with the considerations detailed above that MBs hold a small fraction of oxygen payload compared to the oxygenated buffer (**Fig. 2.4.3.1**).

Another important consideration is that, as shown by additional controls performed afterwards, at least some of the measured change in O_2 was due to sample heating and potentially other effects of ultrasound on the O_2 sensor, which provides even stronger motivation for appropriate controls in O_2 release experiments.

In order to attempt to construct a setup that would allow ultrasound-induced O_2 release monitoring in real time with reduced effects of heating or ultrasound interaction with the sensor,

a focused ultrasound setup was tested with an imbedded O_2 sensor that was located within the sample holder but away from the ultrasound focus. This experiment is described in the Appendix (A 2.4.3).

B. Nanobubbles

For the lecithin-based nanobubbles, the dynamics of O_2 release from the agent were measured after its introduction into a deoxygenated (nitrogen-saturated) buffer. A sample of O_2-sparged NBs or water was introduced into a vial with N_2-saturated buffer and 100% N_2 headspace under magnetic mixing, and the resulting O_2 concentration in the vial was measured with an optical sensor as a function of time (**Fig. 2.4.3.3**). NBs in this experiment do not show greater O_2 concentration at the initial peak than the control; however, they do demonstrate slightly longer O_2 retention than the water control. This underlines that, when characterising oxygen-carrying properties of an agent, it is important to take into account the dynamic properties as well as static or final equilibrium values.

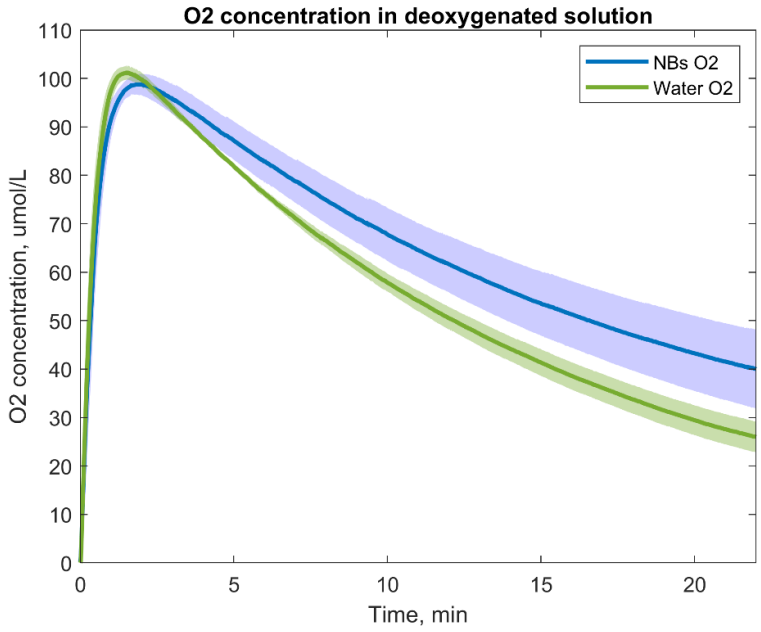

Fig. 2.4.3.3. O_2 release from oxygenated NBs and water after the sample is introduced into N_2-saturated solution under constant mixing (n = 3, shaded areas represent standard deviations).

Oxygen release was also checked for NBs and O_2 NBs after sonication, similarly to MBs (**Fig. 2.4.3.4**). Again, these experiments showed the importance of correct controls for O_2 release measurements, as DPBS controls showed an increase in O_2 levels after sonication, which could be explained by various effects such as heating or ultrasound interaction with the O_2 sensor. The difference between the O_2 levels of oxygen-saturated NBs and buffer before ultrasound could be explained by slightly different oxygen solubility in the NB solution – for example, it is known that oxygen solubility depends on solution salinity[140].

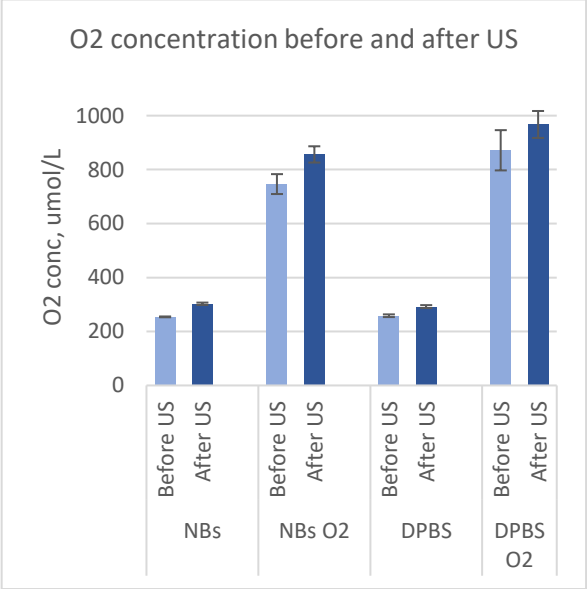

Fig. 2.4.3.4. O_2 concentrations before and after sonication in an ultrasound bath for NBs and O_2 NBs, oxygenated by sparging, in stock concentration compared to DPBS and O_2 DPBS, before and after 60 sec ultrasound (n = 2, error bars represent standard deviations).

2.5 Summary and conclusions

This chapter details the production and characterisation of various agents used throughout this project, most importantly PFC and SF_6 microbubbles, lecithin-based nanobubbles and two formulations of PFC droplets. Various questions relating to the production process and agent composition were checked and optimised. Stability of the agents was verified to be sufficient for the purposes of the experiments in this project. The oxygenation process was studied and agent stability was confirmed after oxygenation. Oxygen-loading capacity was checked experimentally and compared to theoretical estimations, confirming their accuracy. Oxygen release was measured in degassed or deoxygenated media or after ultrasound exposure, and it was found that most of the oxygen dose carried in the agent is stored in the buffer; however, the agent could slow down the payload release compared to the buffer controls.

The results shown in this chapter form the basis for the measurements described in later chapters and confirm the theoretical oxygen-loading capacity estimates based on agent volumes made in the literature review. Thus, they confirm the discrepancy between oxygen payloads in typical doses of oxygen-carrying agents and the *in vivo* effects of these carriers.

The following chapter returns to the discussion of possible solutions to this mismatch and focuses on the hypothesis of enhanced diffusion between red blood cells and tissue.

Chapter 3. Oxygen diffusion measurements

3.1 Introduction

3.1.1 The diffusion hypothesis

As discussed in the literature review (section 1.2.4), for several of the strategies proposed for mitigating tumour hypoxia, there exists a discrepancy between the small oxygen dose delivered by the agents and the *in vivo* effects reported in multiple studies. One promising hypothesis that could explain this mismatch has been proposed in the literature on PFC-based blood substitutes and will be referred to as the "diffusion hypothesis"[75,76,81]. It states that the total O_2 payload volume for a solubility-based agent is indeed too small to explain most *in vivo* effects by direct O_2 release or by the agents recirculating and transporting O_2 from the lungs into the tissue; instead, the particles decrease the average diffusion time of O_2 from red blood cells (RBCs) to the tissue, therefore increasing the efficiency of O_2 unloading from RBCs and, consequently, tissue oxygenation.

Indeed, oxygen diffusion speed in aqueous solutions is known as a speed-limiting factor in many processes. This is the reason why, for example, bacterial cultures in solutions require constant mixing to ensure sufficient oxygenation, or why some chemical reactions require optimal oxygenation designs for better outputs. Importantly, using particles with high oxygen solubility has been successfully explored to enhance oxygen delivery in these and many other oxygen-dependent processes[141–146]. More generally, enhancing mass transfer using a micro- or nanophase is a well-established approach[147].

In the case of enhanced oxygen delivery to tissues, although the diffusion hypothesis seems to be well-accepted for PFC-based carriers and can be theoretically applied to many other agents, direct

experimental evidence to support it has been limited to a small number of agents[79,80]. Establishing whether or not the diffusion enhancement mechanism plays a role in oxygen delivery by a wider range of agents, including ultrasound-responsive carriers, would be valuable, in particular for developing optimal carriers for enhancing oxygen-dependent therapies and establishing the role that initial gas loading of these agents plays in the process.

3.1.2 Other cases of enhanced oxygen diffusion

The diffusion hypothesis described above applies to a micro- or nanophase introduced into the solution that has enhanced oxygen solubility and in this way increases the speed of oxygen exchange. Interestingly, there are other agents that are claimed to enhance oxygen diffusion in solutions via a different mechanism.

An example of such a substance is trans-sodium crocetinate (TSC), which is believed to directly increase oxygen diffusion coefficients by rearranging water molecules via hydrophobic interactions[82,83].

Crocetin, which has the identical chemical structure to TSC, was also tested in the diffusion measurements in this chapter to provide comparison with an agent with a potentially different mechanism.

3.1.3 Chapter overview and objectives

The main goal of the work described in this chapter was to construct an experimental setup to test the diffusion hypothesis for a range of agents used for ultrasound-medicated oxygen delivery, such as microbubbles, nanobubbles and nanodroplets.

First, preliminary work was carried out by measuring oxygen diffusion coefficients in simple agent solutions without blood or flow; this allowed to develop experimental methods and compare measurement results with theoretical calculations that were carried out numerically in COMSOL. Following this, a capillary flow oxygen exchange setup was constructed, and calibrations and preliminary measurements were carried out in agent solutions without blood. Finally, the developed setup was used to compare blood oxygen exchange speed with or without the addition of oxygen-carrying agents.

3.1.4 Attribution of work

The OrganOx experiments were assisted by Tamsyn Clark and Daniel Voyce.

All other experimental and data processing work was performed by the author of this thesis.

3.2 Materials and methods

The materials and methods for the production of microbubbles, nanobubbles and nanodroplets used in this chapter are described in detail in Chapter 2.

3.2.1 Materials

Silicon tubing (HelixMark) was purchased from Avantor (PA, USA). O_2 and N_2 gases were obtained from The BOC Group (Guilford, Surrey, UK). EXPANCEL 551 DE 20 d60 microspheres were acquired from Nouryon (The Netherlands). Trans-Crocetin (70%) was obtained from Biosynth Carbosynth (Switzerland/UK).

Human blood was acquired from a volunteer with informed consent and its use was approved by the University of Oxford ethics committee. It was stored in BD Vacutainer K2E 10.8 mg vials with an anti-clotting agent (EDTA).

3.2.2 COMSOL simulations

To compare experimental results with theory, computer simulations of oxygen diffusion were performed with boundary conditions reproducing the experimental setup. Computer simulations were performed with the COMSOL Multiphysics 5.5 software in the Transport of Diluted Species (tds) regime.

The model used was a 1D simulation model of experiments described in section 3.3. Briefly, a sample layer was equilibrated with air, and then the headspace was replaced with oxygen at t = 0, and the oxygen concentration was measured at the bottom of the sample. In the simulations, the x axis was directed vertically down through the sample with x = 0 at the gas/sample border; x = 0

border had a fixed elevated oxygen concentration and the opposite border had a no-flux condition and an oxygen concentration probe (**Fig. 3.2.2.1**). The start conditions were for air-equilibrated solutions. The equation used for these calculations was the one-dimensional diffusion equation:

$$\frac{\partial c(x,t)}{\partial t} = D\frac{\partial^2 c(x,t)}{\partial x^2}$$

where $c(x,t)$ is the concentration of the diffusing agent at the position x and time t and D is the diffusion coefficient. The COMSOL numerical calculations were done on a physics-controlled extremely fine mesh.

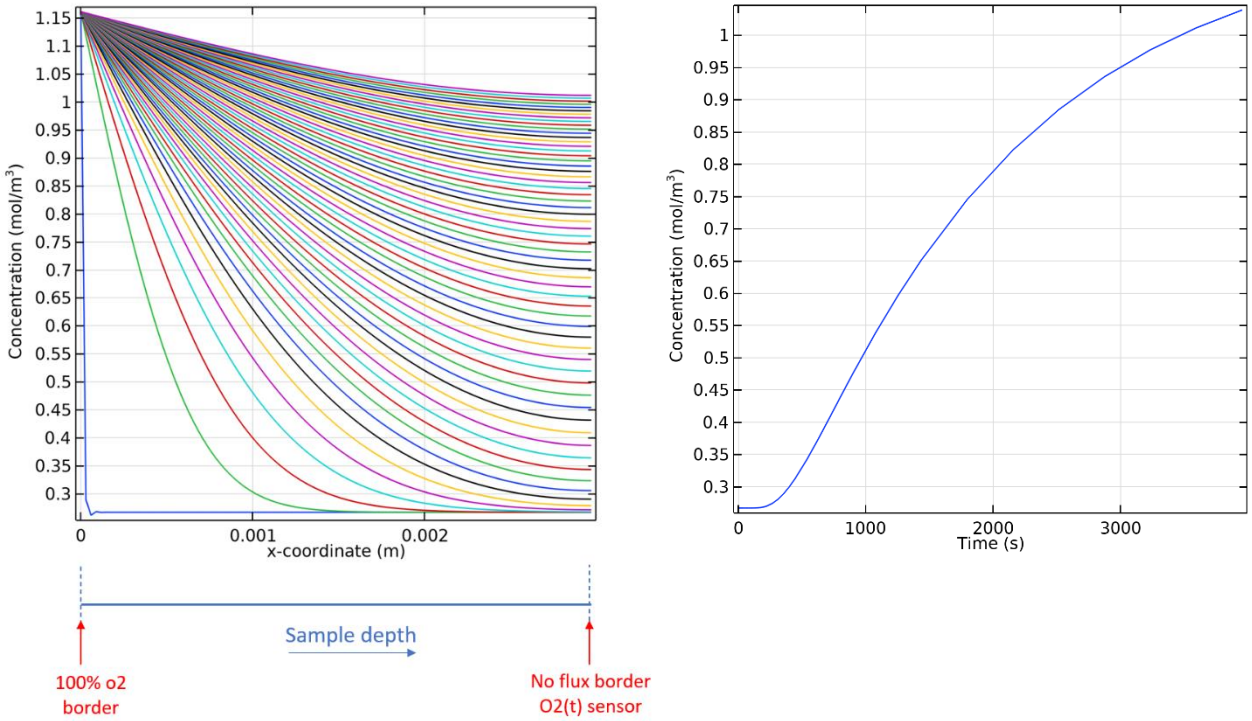

Fig. 3.2.2.1. Example of COMSOL simulation results with a geometry schematic. x-axis goes down through the sample with x = 0 at the sample/gas phase border (border with constant O_2 concentration condition), and the O_2 sensor is on the opposite border, which has a no-flux condition. The experiment starts at t = 0 when the gas phase is changed from air to oxygen and oxygen starts diffusing into the sample along the x axis. The series graph represents the simulated oxygen concentration as a function of x for 60 minutes of simulation with 1 min steps; the right-hand graph shows the oxygen concentration as a function of time on the no-flux border.

The values for the concentrations and the diffusion coefficient of oxygen in water and PBS were taken from the literature values for 20°C (Table 3.2.2.1). For the simulations modelling oxygen loss from the headspace, the O_2 concentration on the second end of the 1D model was changed from 100% (1 atm) oxygen to a slightly lower time-dependent value calculated as a 5^{th} degree polynomic approximation of the experimental measurement of $O_2(t)$ in an empty setup.

Parameter	Value
Water oxygen saturation in equilibrium with air	0.284 mol/m^3
Water oxygen saturation in equilibrium with 1 atm oxygen	1.352 mol/m^3
PBS oxygen saturation in equilibrium with air (calculated from the O_2 saturation of saline solutions and known PBS salinity)	0.267 mol/m^3
PBS oxygen saturation in equilibrium with 1 atm oxygen	1.271 mol/m^3
Diffusion coefficient of oxygen in water (estimated the same for PBS)	$2.0*10^{-5}$ cm^2/s

Table 3.2.2.1. Parameter values used in the COMSOL simulations.

3.2.3 Microbubble protocol adjustments

Some adjustments to the MB production protocol were made for the diffusion experiments. Firstly, lipid films were reconstituted in pure PBS to avoid the effect of MB buffer on viscosity. Secondly, MBs were put on ice for 10 mins following fabrication, but then kept at room temperature to prevent temperature-induced diffusion effects. And thirdly, MBs were allowed to float for approximately 1 hour (as opposed to several minutes) before separating the lower fraction, sizing it and sealing it with a headspace of PFB, which allowed better separation of the 1 µm MB fraction from larger bubbles and reduced flotation effects in the setup.

3.2.4 Oxygen diffusion experiments

The optical oxygen sensor used in all experiments was OXY MINI Minisensor Oxygen Meter with SP-PSt3-NAU-D5 sensor "dots" (PreSens Precision Sensing, Regensburg, Germany). The sensor dots were regularly replaced to avoid bleaching and each dot was calibrated relative to 100% air saturation of the corresponding buffer in the experiment (water or DPBS). In all experiments using % air saturation as a measure of oxygen concentration it is used relative to the corresponding buffer for each experiment. The oxygen sensor had a temperature probe for temperature corrections, which was placed directly into samples.

The gas rotameters used to regulate gas flow were Omega FL-1442-S gas rotameters (OMEGA engineering, Manchester, UK). Their maximum flow rate was checked manually and found to be approximately 200 mL/min.

For the artificial lung experiments (section **3.4**), we used an OrganOx perfusion system (OrganOx, Oxford, UK), a Terumo CDI Blood Parameter Monitoring System (Terumo, Tokyo, Japan) and LILLIPUT 2 ECMO artificial lungs (LivaNova, London, UK).

For the blood measurements (section **3.6**), we used a Thorlabs CCS175/M spectroscope (Thorlabs, NJ, USA), a SCHOTT KL 1500 compact broadband light source (SCHOTT, Mainz, Germany) and a syringe pump (NE 1000, World Precision Instruments, FL, USA). All spectra obtained with the Thorlabs spectroscope were processed in the Thorlabs software using the moving average smooth function (window width 11, number of passes 10) to reduce fluctuations.

Blood absorbance A was calculated as

$$A = -log_{10}\frac{I_{blood}}{I_{buffer}}$$

where I_{blood} and I_{buffer} are the spectroscope signal intensities for the blood samples and DPBS buffer controls respectively.

3.2.5 PDMS moulding

To produce microfluidic channel setups:

Positive models were produced in an in-house workshop. After they were cleaned with isopropanol and dried with nitrogen, they were filled with a 9:1 (by weight) mix of PDMS and a cross-linking agent, degassed for at least 40 minutes in a vacuum chamber and placed in an oven at 650°C overnight. Afterwards the negative moulds were placed in a plasma cleaner (Henniker Plasma Vacuum System HPT-200) (3 min, 80%) and treated with PVA (3 10-min cycles alternating with nitrogen drying and 15-min incubations on a hot plate at 150°C). Then these negative moulds were cleaned and filled with polymer and cross-linking agent mix (9:1), degassed for at least 40 minutes and incubated in an oven at 650°C overnight. After treatment in the plasma cleaner (settings same as above), sample holder parts were firmly pressed together. If hydrophilic coating of the inside of the sample holder was desired, it was again treated with PVA as described above.

To produce membranes:

A 9:1 (by weight) mix of PDMS and a cross-linking agent was degassed for at least 40 minutes in a vacuum chamber. Two glass slides were cleaned and a heat-resistant tape was placed on their edges. A small amount of PDMS solution was placed on one of the plates and the second slide was pressed to it, taking care to avoid creating air bubbles; the tape kept the slides apart at a fixed distance, resulting in reproducible membrane thickness. The slides were placed in an oven at 650°C overnight.

3.3 Measurement of oxygen diffusion speed in simple solutions with oxygen-carrying agents

3.3.1 Design of a liquid layer diffusion setup

Before attempting to account for various complicated phenomena such as the role of capillary size and the interaction of oxygen carriers with red blood cells, a setup was developed for measuring oxygen diffusion coefficients in solutions, in order to compare the diffusion coefficients of simple aqueous solutions of various agents in a simple geometry.

A literature analysis showed that one of the commonly used configurations for gas diffusion measurements is a layer of liquid sample separated by a gas-permeable membrane from a gas reservoir and an oxygen sensor at the opposite border; the gas in the reservoir is changed and the change in oxygen concentration is measured at the other end of the sample layer, with the resulting curve allowing to calculate diffusivity[148]. This project followed the same design concept. PDMS was chosen as the membrane material because of its good oxygen permeability, detailed studies present in the literature on its oxygen diffusion properties[149], as well as its ease of manufacturing and the possibility of precise thickness control.

A number of setups were designed and tested; this process is described in detail in the Appendix (A 3.3.1). Briefly, the most prominent issues underlined by this setup development process were the importance of avoiding temperature-induced convection and mechanical agitation, in order to characterise specifically diffusion and not other processes. In addition, the PDMS membrane decreased the measurement reliability, since, due to its flexibility, it decreased the precision of controlling the sample thickness. Consequently, the final setup was constructed without a membrane, with the sample layer being in direct contact with the gas phase, and precautions were

taken to decrease temperature changes and vibrations in the setup. This setup is shown in **Fig. 3.3.1.1**.

In a typical experiment, the setup and sample were allowed to equilibrate with air oxygen concentration and room temperature; afterwards, oxygen was introduced into the headspace with a syringe and the setup was sealed to perform the measurement of oxygen concentration at the bottom of the sample as a function of time with an optical oxygen sensor (PreSens). This setup was found to function with good reproducibility and agreement with theory, while having little oxygen loss during a 1-hour experiment; oxygen loss in an empty setup was measured regularly between experiments to ensure the setup sealing quality. COMSOL simulations confirmed that the small oxygen loss from the headspace during a 1-hour experiment had a negligible effect on the resulting measurement (**Fig. 3.3.1.1**).

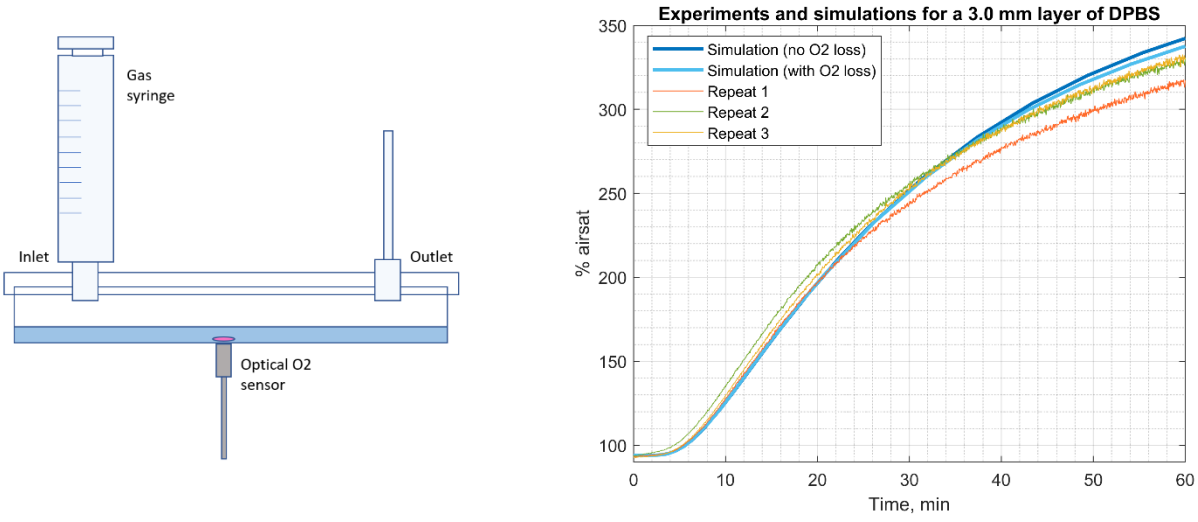

Fig. 3.3.1.1. Oxygen diffusion measurement setup for a sample layer without a PDMS membrane and DPBS controls. The diameter of the setup is approximately 8.5 cm and the typical sample layer thickness was 3 mm. The buffer controls were performed by equilibrating the DPBS layer with air and then introducing oxygen into the headspace at t = 0 and measuring the oxygen concentration

at the bottom of the sample; the three experimental runs are compared to COMSOL simulations with and without accounting for O_2 loss from the headspace during the experiment.

Oxygen diffusion measurements were conducted for DBPC-PEG40S PFB MBs and DBPC-PEG40S lipid solutions; MBs were pre-equilibrated with air to avoid oxygen scavenging, and MB concentration was similar to the concentration used in the reactive oxygen species experiments in this project and higher than typical *in vivo* values. Neither of these samples showed an increase in oxygen diffusivity (**Fig. 3.3.1.2**), which for MBs may be explained by MB flotation in the opposite direction from the sample, potentially nullifying the diffusion enhancement effect, and/or by insufficient concentration to produce a measurable effect in this setup.

Crocetin was used as a potential positive control for diffusion enhancement – it is chemically similar to trans-sodium crocetinate, which is claimed to produce a 30% increase in oxygen diffusion in water in a range of concentrations including the concentration used in this experiment[83] (**Fig. 3.3.1.2**). Interestingly, we did observe a significant increase in diffusivity, although only by approximately 10% (estimated by comparisons with COMSOL simulations of this experiment using different diffusion coefficients).

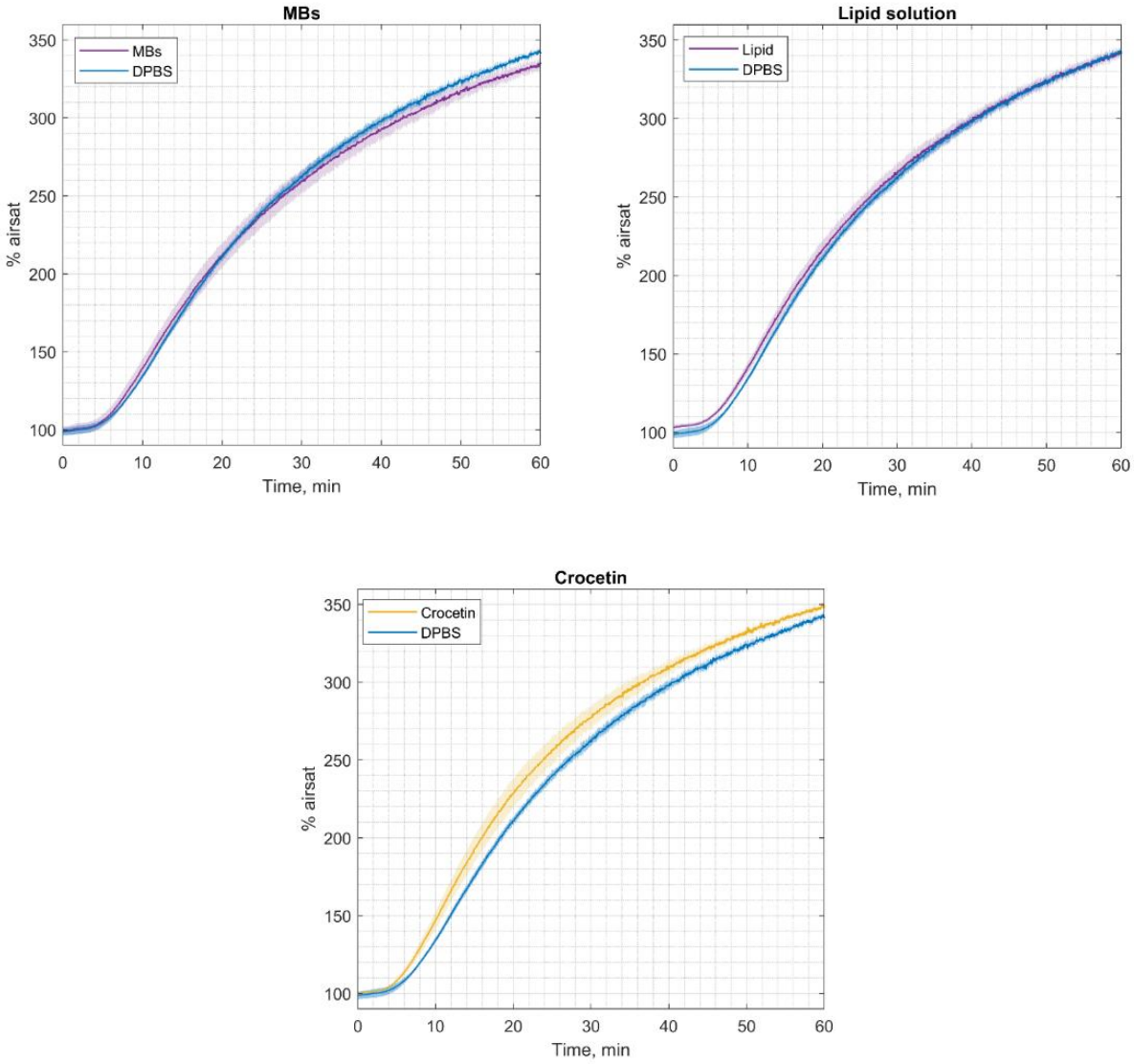

Fig. 3.3.1.2. Results for the diffusion measurements performed in the setup without a PDMS membrane: DBPC-PEG40S microbubbles in DPBS ($4*10^7$ particle/mL); DBPC-PEG40S lipid solution in DPBS (0.2 g/L) and crocetin (100 µM in DPBS, diluted 1:1000 from stock in DMSO). All samples are compared to corresponding buffer controls. (n = 3, shaded areas represent standard deviations)

Discussion

In order to explain the lack of measured oxygen diffusivity increase in the presence of microbubbles, some further COMSOL simulations were performed. Building a full theoretical model of oxygen diffusion in complex solutions lies beyond the scope of this project; instead, a

simplified model was built in order to have a rough theoretical estimate. It was based on the COMSOL model described in section 3.2.2 with an added gas layer in the middle of the liquid sample, which is a simplified representation of the gas phase introduced with the microbubbles (Fig. 3.3.1.3). These simulations confirm that the sensitivity of the setup is not enough to detect an oxygen diffusion difference with microbubbles, since their gas volume fraction is around 1% in stock solution and was around 0.01% in these experiments.

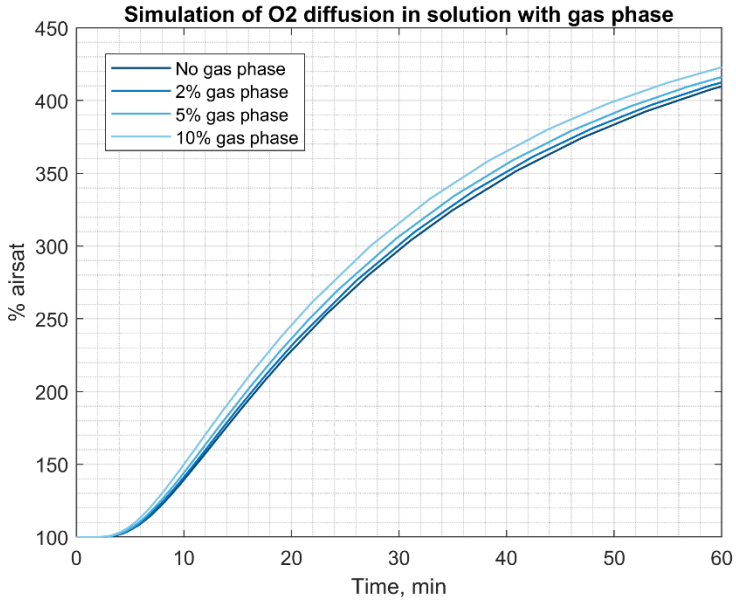

Fig. 3.3.1.3. Results for COMSOL simulations of oxygen diffusion experiments in a model with a single gas layer in the middle of the liquid sample. The presented results are for 3 mm total sample thickness with 60 um, 150 µm or 300 µm thick gas layer in the middle, corresponding to 2%, 5% or 10% gas phase by volume.

The lack of a positive result for microbubbles was therefore in agreement with theory, even without accounting for other factors such as flotation. Nonetheless, this does not disprove the diffusion theory, as the length scales in capillaries are on a different order of magnitude, and due to the near wall excess effect the agents can achieve a high volume fraction locally between RBCs and tissue.

In addition, an interesting result was seen for crocetin, confirming the literature claim that it can enhance the diffusion coefficient of oxygen in water. Consequently, crocetin was used as a positive control for diffusion enhancement in further experiments.

Furthermore, developing this setup provided a valuable step in the preparation of the capillary flow experiments described further, in particular underlining the importance of precise sample thickness and temperature control – these issues were considered during the design of flow setups.

3.4 Oxygen exchange setups with flow

In order to check the diffusion hypothesis *in vitro*, the characteristic that has to be measured is the RBC oxygenation or deoxygenation speed in flow in a gas-permeable capillary, in the presence or absence of various agents. The first attempts to do these measurements were performed using commercial extracorporeal oxygenation devices, or "artificial lungs".

3.4.1. Setup with commercial artificial lungs

The first attempts at oxygen exchange measurements in flow were performed using an organ perfusion setup. It was based on the OrganOx perfusion system[150] and comprised a flow loop with two artificial lungs (LILLIPUT 2 ECMO, paediatric hollow fiber oxygenator), one of which had either air or oxygen flowing through it and thus served as an oxygenator and the other was flowed with nitrogen to model hypoxic tissue. Oxygen partial pressure (pO_2) was measured after both lungs with clinical pO_2/pH sensors (Terumo) (**Fig. 3.4.1.1**). The flow loop could be heated to 37°C or left at room temperature, and liquid and gas flows could be regulated. The oxygen exchanged in the N_2 lung was measured in the outlet of the lung with a PreSens oxygen sensor in order to quantify the O_2 released in the lung.

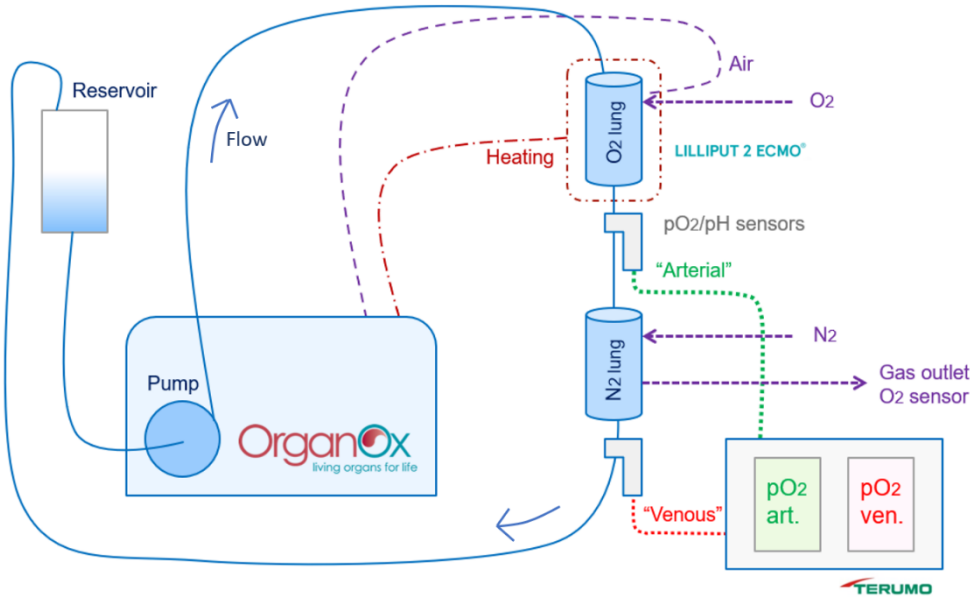

Fig. 3.4.1.1. Scheme of the OrganOx/Terumo setup. The solution passed through two artificial lungs in each cycle, with the first filled with either air or oxygen (O_2 lung) and the second with nitrogen (N_2 lung), presenting a simplified model of a blood flow cycle going through the lungs and then depositing the O_2 load in the hypoxic tumour tissue. Oxygen concentration was measured after both lungs by the clinical sensors; in addition, O_2 was measured in the N_2 lung outlet to quantify the O_2 exchanged in this lung.

A number of preliminary experiments were carried out in this setup with saline buffer controls, nanobubbles and microbubbles; however, it was found that the commercial artificial lungs and blood monitoring systems did not allow to perform the necessary measurements of oxygenation speed (data not shown). After the analysis of the results and setup parameters, it was concluded that the OrganOx/Terumo loop is not the optimal setup to observe the oxygenation speed effects for a number of reasons. Most importantly, the artificial lung used in this setup (LILLIPUT 2 ECMO) is a clinical device and provides efficient gas exchange, even for low gas flow rates; this makes observing gas exchange speed difficult, since the solution reached an equilibrium pO_2 level regardless of the possible oxygen diffusion speed changes. The artificial lung also had a fixed capillary diameter and material, which did not allow to check various capillary parameters closer

to the ones seen *in vivo* (e.g., smaller capillary diameter). Another issue is that the Terumo blood monitoring system is a clinical device and therefore does not provide raw data, which would have been important to correct for the solution composition (and other variables such as temperature) affecting the oxygen solubility. Moreover, due to the setup being clinical, the cost of a set of disposables for an experiment is high; an additional practical issue is the large loop volume (0.5 L) requiring a large volume of samples and blood.

3.4.2. Setup with simple artificial lung: preliminary experiments without blood

To address these limitations, alternative apparatus were designed that were less sophisticated, but allowed a much greater degree of control over the relevant parameters and enabled more direct measurements of oxygen diffusion speed.

The first version of the setup was constructed with a PDMS chip with a single channel, covered with a thin gas-permeable layer of PDMS, since the good oxygen permeability of PDMS is well-characterised and polymer moulding allows for creating channels with precise dimensions and geometry. However, the diffusion experiments described in the previous section (3.3) showed that the results are sensitive to liquid layer thickness, and PDMS membrane deformation introduces large variability.

For this reason the design was changed to a more robust version – a simple "artificial lung" consisting of a gas-permeable silicon tube in a bottle with controlled gas environment (Fig. 3.4.2.1), inspired by a design proposed by Hamilton et al[151]. The following paragraphs describe some of the most important design considerations.

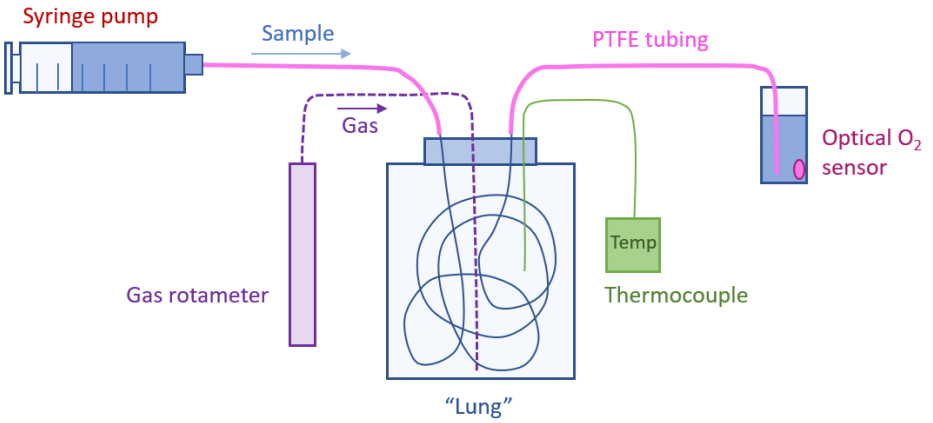

	"Small" tubing	"Big" tubing
ID	310 um	1.47 mm
OD	640 um	1.96 mm
Wall	165 um	245 um

Fig. 3.4.2.1. Schematic of the "simple artificial lung" setup for the buffer oxygen saturation experiments. It consists of a glass bottle, sealed except for a small outlet, and gas-permeable silicon tubing, connected outside the lung by gas-impermeable PTFE tubing. Gas flow is controlled by a rotameter and temperature is monitored with a thermocouple; O_2 concentration in output solution is measured with an optical O_2 sensor (PreSens). The table on the right shows the parameters of the two sizes of silicon tubing used inside of the lung: inner diameter (ID), outer diameter (OD) and wall thickness.

Firstly, an important parameter was the gas flow speed. A gas rotameter was used to control the gas flow into the system. The protocol for its use was optimised for stable O_2 levels inside of the lung, measured with an optical O_2 sensor, and stable temperature, measured with a thermocouple (data not shown); the resulting protocol required keeping the gas rotameter fully open (gas flow ~200 mL/min) for at least 5 min to fill the lung and then decreasing the flow to 50-100 mL/min for the duration of the experiments to ensue continuous oxygen delivery.

Next, temperature had proven to be an important parameter in previous diffusion experiments, and therefore it was carefully monitored. A thermocouple was inserted into the lung to monitor the lung temperature in the gas phase, and the output sample temperature was measured with a temperature probe that is part of the optical oxygen sensor setup. In order to avoid temperature gradients that could influence the oxygen exchange process in the sample, all samples and buffers

were allowed to fully equilibrate with the room temperature after production; purified water (MilliQ) was allowed to stand at room temperature at least overnight after filtration before the experiments.

Finally, it was important to consider the tubing. To prevent oxygen exchange outside of the lung, gas-impermeable PTFE tubing was used to connect the lung to the syringe pump and the output container with an oxygen sensor. Inside of the lung, gas-permeable silicon tubing of two sizes was used: smaller tubing with 0.31 mm inner diameter and 0.64 mm outer diameter and larger tubing with 1.47 mm inner and 1.96 mm outer diameter. The smaller tubing had the advantage of being closer to physiological capillary parameters, although still being larger than the smallest capillaries; but it presented more technical issues with elevated pressure in the sample. The bigger tubing was less representative of physiological conditions, but did not present pressure or agent stability challenges in the range of parameters used, and it was the same as the tubing used for an artificial lung in the literature[151]. Consequently, the smaller tubing was used for blood experiments, but first a number of calibrations and preliminary experiments was carried out in larger tubing in order to explore the setup's behaviour in a wider range of parameters.

A. Results with larger diameter silicon tubing (inner diameter 1.47 mm), lung with 1 atm O_2

First, the output O_2 measurements were performed with different tubing lengths and flow speeds using purified (MilliQ) water, with the lung filled with pure oxygen at 1 atm (**Fig. 3.4.2.2**). These measurements were found to be in good agreement with theory: output O_2 concentration in water increased with increasing tubing length (until it saturated at around 470% airsat, which corresponds to 1 atm of O_2) and decreased with increasing sample flow rate, experimentally confirming that O_2 content of the sample was closer to the O_2 levels in the lung with more time for O_2 exchange. The temperature levels were also monitored and found to be stable, mostly

fluctuating within a 0.4°C range both for the gas phase in the lung and the liquid phase in the sample (data not shown).

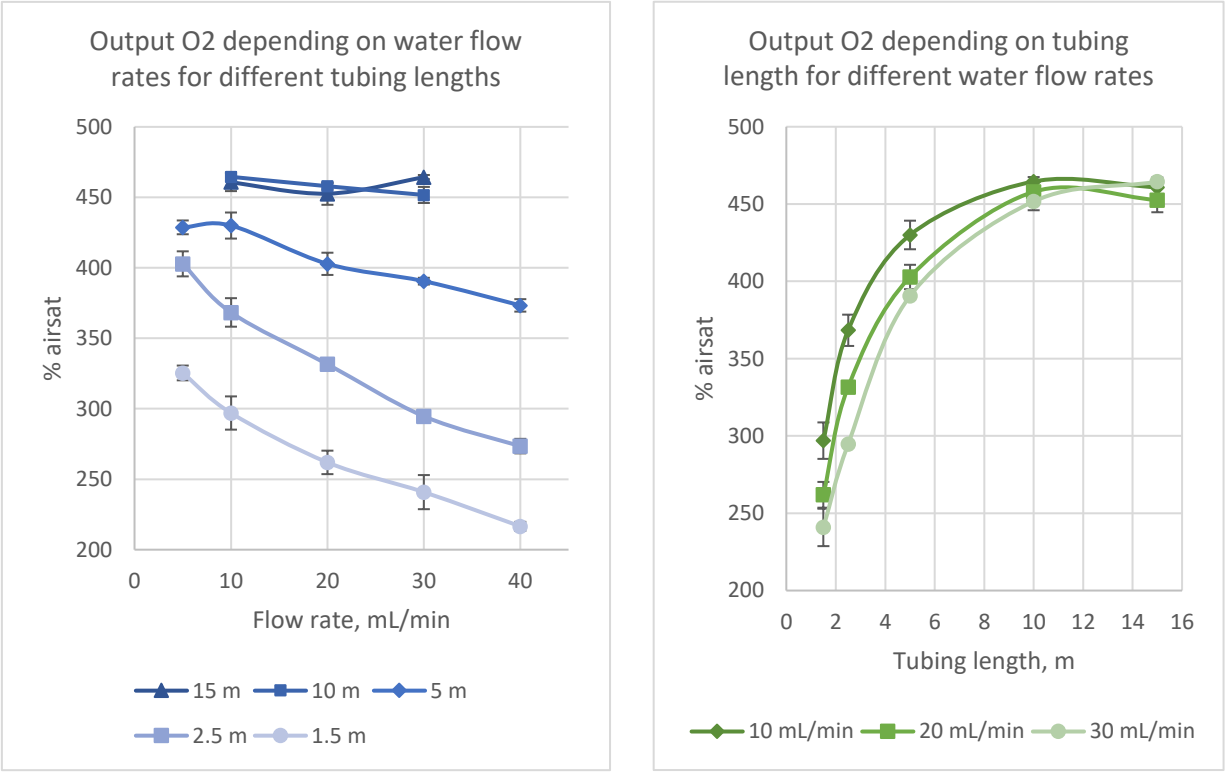

Fig. 3.4.2.2. Output oxygen concentration in water after passing through the artificial lung filled with 1 atm of oxygen depending on sample flow rates, measured with different lengths of silicon tubing inside of the lung; the graph on the right- hand side represents part of the dataset for the flow rates of 10, 20 and 30 mL/min represented as a dependence on tubing length (n = 3, error bars represent standard deviations).

For the experiments with oxygen-carrying agents, on order to see whether they have any impact on the O_2 output concentration, it was necessary for the output O_2 concentration of the setup to be well below saturation. In addition, a shorter length of tubing was preferable for better agent stability, and larger flow rates for faster equilibration of the output readings. Consequently, for the next set of experiments a tubing length of 1.5 m and flow rates of 10 and 20 mL/min were chosen.

Next, experiments with and without DBPC-PEG40S PFB microbubbles were performed. Importantly, since going through the setup can impair agent stability, MB size distributions and concentrations before and after going through the lung were compared, and it was confirmed that there was no concentration decrease or change in size distribution (**Fig. 3.4.2.3**). Then, oxygen concentration in the sample after going through the lung was compared between the MB solution and a water control (**Fig. 3.4.2.3** right-hand side). No significant increase in oxygen exchange was seen, which is likely due to the small gas phase percentage in the MB solution, similar to the diffusion layer experiments. Similar experiments with flow through the lung were performed for nanobubble and lecithin solutions, as well as crocetin and glycerol controls (**Appendix A 3.4.2**).

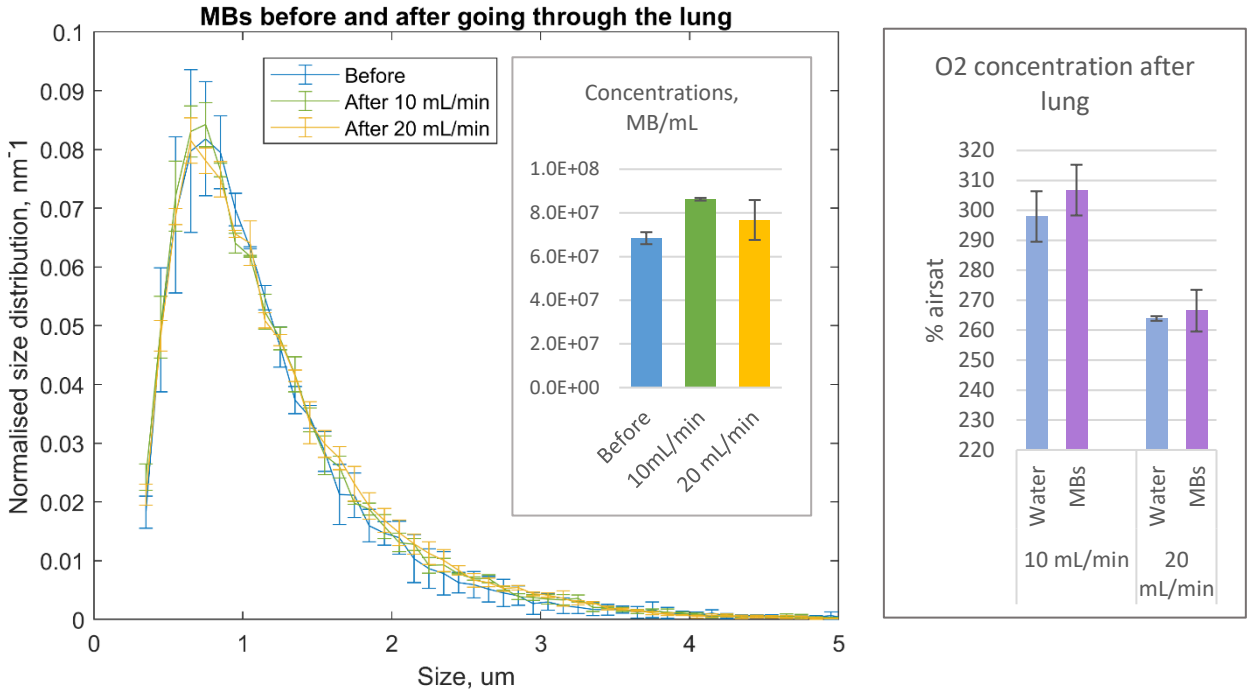

Fig. 3.4.2.3. DBPC-PEG40S PFB microbubbles size distributions and concentrations before going through the lung with 1.5 m tubing and after going through the lung at a flow rate of 10 mL/min or 20 mL/min (n = 3, error bars represent standard deviations). The graph on the right-hand side shows the output oxygen concentrations measured in this experiment.

B. Results with smaller diameter silicon tubing (inner diameter 310 um), lung with 1 atm O_2

After the preliminary experiments in the larger diameter silicone tubing, experiments were carried out in smaller (ID 310 um) silicone tubing. This tubing is closer to physiological blood capillary sizes and therefore was also used for the later blood experiments.

First, calibrations with water were performed for different sample flow rates and tubing lengths (Fig. 3.4.2.4). Since the smaller tubing presented more practical challenges in terms of the pressure required in the system, this calibration was done over a narrower range than that for the larger tubing; however, the trends that were seen in this calibration were similar and correspond to the theoretical understanding that increasing tubing length or decreasing flow speed leads to increased time for oxygen exchange, and therefore to higher output oxygen concentration.

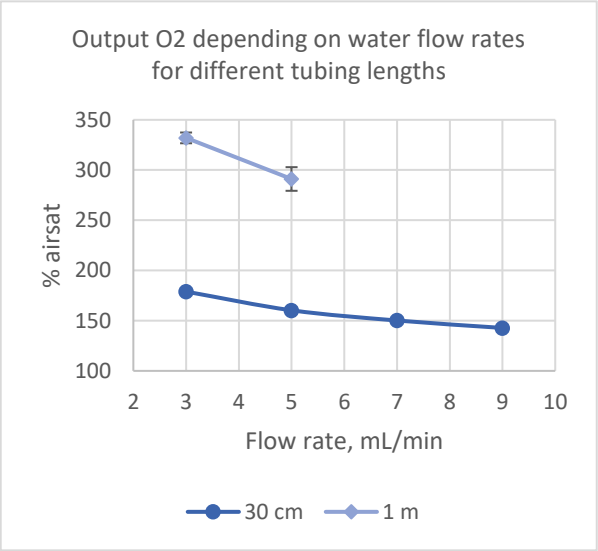

Fig. 3.4.2.4. Output oxygen concentration in water after passing through the artificial lung filled with 1 atm of oxygen depending on sample flow rates, measured with different lengths of silicon tubing inside of the lung (n = 3, error bars represent standard deviations).

Then, microbubble stability was checked after passing through 1 m of tubing in the lung (**Fig. 3.4.2.5**). MB stability was heavily impaired, with most MBs destroyed at the flow rate of 3 mL/min, and all of them destroyed at 5 mL/min. The size distributions and concentrations of output samples were measured with NTA in order to check whether any sub-micrometre agents remain; however, for both 3 mL/min and 5 mL/min flow rates, the output samples were similar to the sub-micrometre MB fractions and lipid solutions controls measured earlier, signifying agent destruction (**Fig. 3.4.2.6**).

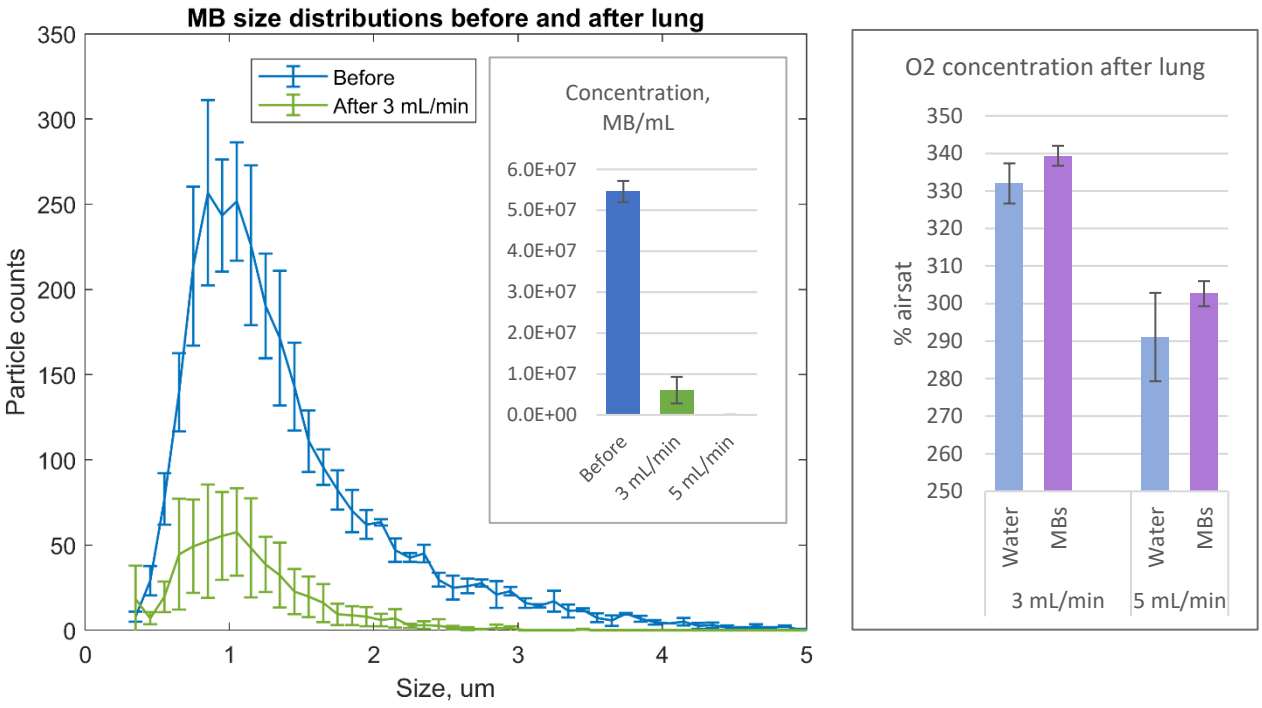

Fig. 3.4.2.5. DBPC-PEG40S PFB microbubbles size distributions and concentrations before passing through the lung with 1 m smaller diameter tubing and after going through the lung at a flow rate of 3 mL/min or 5 mL/min (n = 3, error bars represent standard deviations). The graph on the right-hand side shows the output oxygen concentrations measured in this experiment.

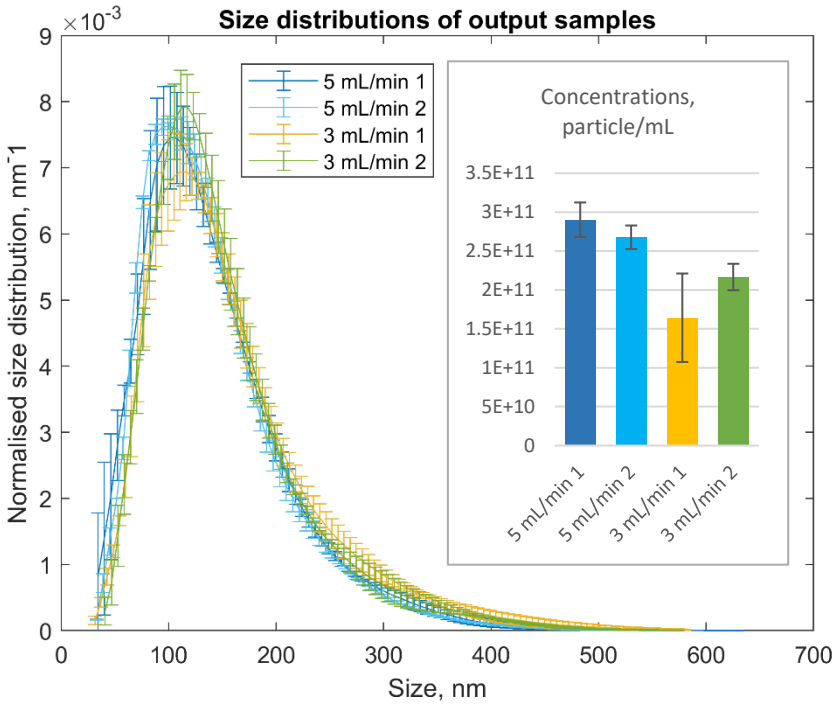

Fig. 3.4.2.6. Size distributions and concentrations of some of the MB samples after passing through the 1 m lung, measured by NTA (n = 3, error bars represent standard deviations).

An oxygen exchange experiment was attempted with a different type of microbubbles (EXPANCEL, copolymer shell (acrylonitrile and vinylidene chloride) microbubbles) with larger size and more rigid shells, in the hope that they would be more stable in this setup. Indeed, these bubbles were more stable than lipid-shelled MBs, and they produced a small but significant rise in output oxygen levels (Fig. 3.4.2.7); however, the large size led to impractically fast flotation times that prevented the use of these microbubbles in future experiments.

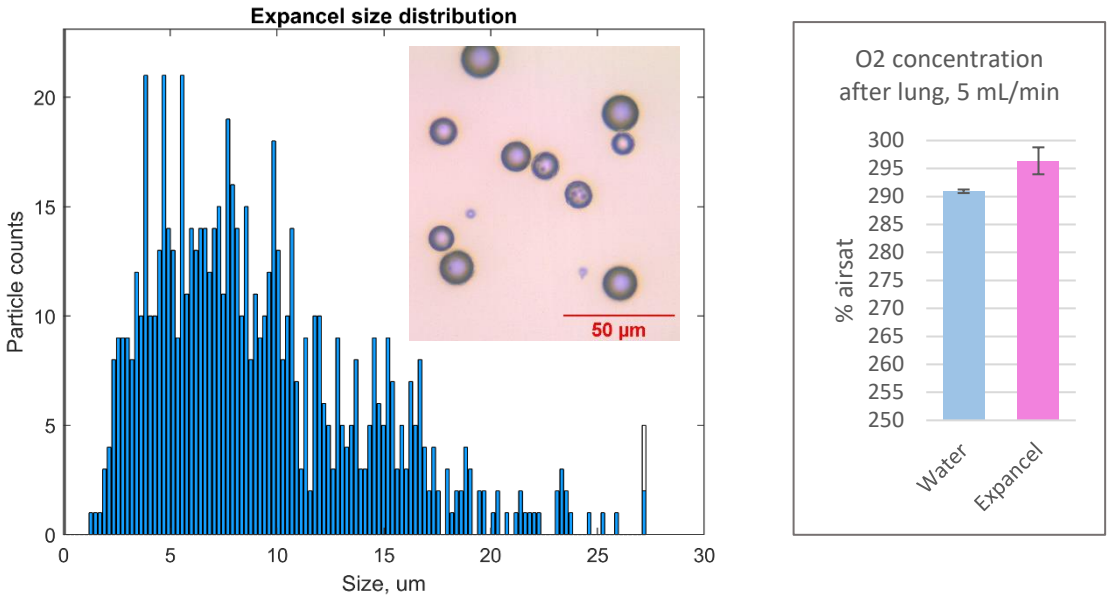

Fig. 3.4.2.7. The EXPANCEL microbubbles size distributions and morphology example (optical microscopy) and the output oxygen concentrations after the EXPANCEL solution (10^5/mL in water) and water control passing through the lung with 1 m smaller diameter tubing, filled with 1 atm O_2; sample flow speed 5 mL/min (n = 3, error bars represent standard deviations).

Lipid-based MBs were used in all subsequent experiments. Since they were not sufficiently stable under the experimental parameters described above, their stability was also checked in a lung with shorter (30 cm) tubing and at the lower flow rate of 3 mL/min (**Fig. 3.4.2.8**). MBs were characterised before loading into the system, as well as sampled after the syringe pump has been running for some time from the syringe (before going into the lung) and the output sample (after passing the lung), in order to check whether the pressure in the system is the main issue for the MB stability, or whether passing through the tubing impacts the stability further. In this experiment, MB stability was notably better than in the lung with 1 m tubing, although there was still considerable destruction; the syringe and output samples were not significantly different, signifying that the pressure is the main issue for MB stability and there is no additional destruction associated with passing through the lung.

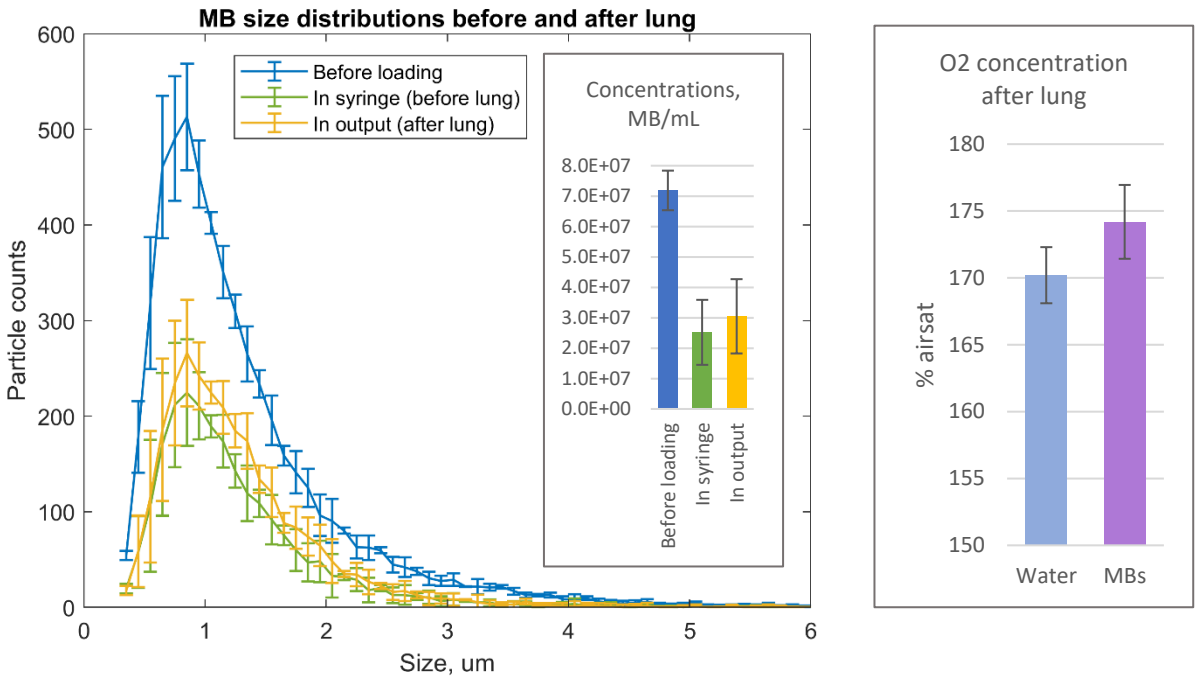

Fig. 3.4.2.8. DBPC-PEG40S PFB microbubbles size distributions and concentrations before being loaded into the setup; before going through the lung with 30 cm tubing (in syringe) and after passing through the lung (in output) at a flow rate of 3 mL/min (n = 3, error bars represent standard deviations). The graph on the right-hand side shows the output oxygen concentrations measured in this experiment.

Nanodroplet stability was also checked in this setup with the 1 m lung. For this experiment, phase-change NDs acquired from DBPC-PEG40S PFB MBs by condensation were used. Their storage stability was checked beforehand (**Fig. 2.3.3.1**) and it was shown that these droplets undergo notable changes after 1 hour at room temperature in 1:40 dilution. However, when the duration of the experiment was kept to the minimum to minimise the impact of storage stability, it was found that the droplet stability was not impaired by passing through the lung (**Fig. 3.4.2.9**). The fact that the lung stability of these droplets is much better than that of microbubbles from the same materials corresponds to the theoretical understanding of these agents, as droplets have liquid cores that are stable to positive pressure, unlike the gas cores of MBs.

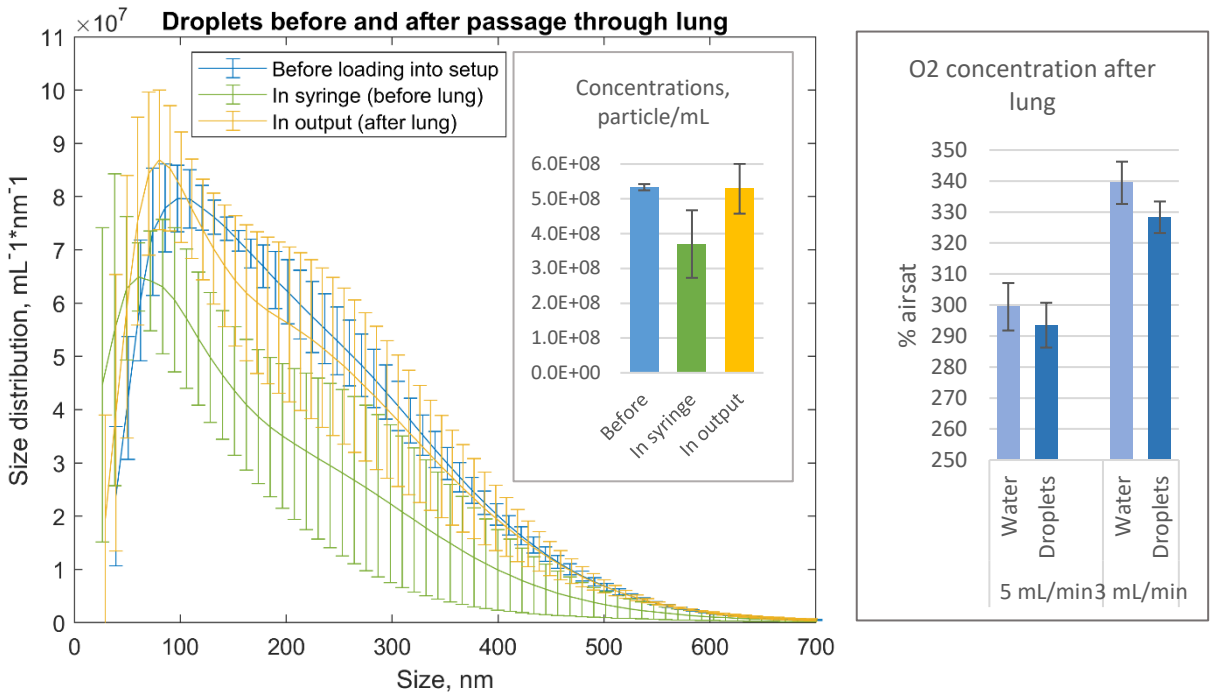

Fig. 3.4.2.9. DBPC-PEG40S PFB condensed droplet size distributions and concentrations before loading into the lung, sampled from the syringe before the lung and from the output sample after going through the lung, measured by NTA (n = 3, error bars represent standard deviations). The graph on the right-hand side shows the output oxygen concentrations measured in this experiment.

Output oxygen concentrations were measured for all the experiments with microbubbles and droplets described above, as well as some other samples such as nanobubbles and crocetin; these results are described in the **Appendix (A 3.4.2)**.

C. Results with smaller diameter silicon tubing, lung with 1 atm N_2

All the experiments above were performed with the lung filled with 1 atm of oxygen. This was done in order to perform the calibrations of O_2 concentrations in output samples and check agent stability, as well as try to measure whether there is any change in oxygen exchange speed in

samples vs controls without blood (results in **Appendix A 3.4.2**). The output sample O_2 levels were typically in the range of 200-300% airsat.

However, this is not the O_2 range needed for the experiments with blood. In order to see whether there is any change in RBC oxygenation, measurements have to be carried out in the O_2 concentration range in the buffer that corresponds to approximately 50% RBC oxygenation, which is around 20% airsat[152]. A lung loaded with oxygen cannot achieve sample airsat below 100%; consequently, for further experiments, including blood measurements, a lung filled with 1 atm of nitrogen was used.

Similar to the previous measurements in the O_2-filled lungs, calibrations with water for various tubing lengths and sample flow rates were performed (**Fig. 3.4.2.10**). For 30 cm tubing, the desirable output O2 of 20% airsat could not be achieved with flow rates reasonable for this setup, while for 1 m tubing the MB stability was insufficient. Therefore, as a compromise between O2 output, flow rates and MB stability, 60 cm tubing was used, in which 20% airsat in the output water sample corresponded to a sample flow rate of ~ 0.8 mL/min.

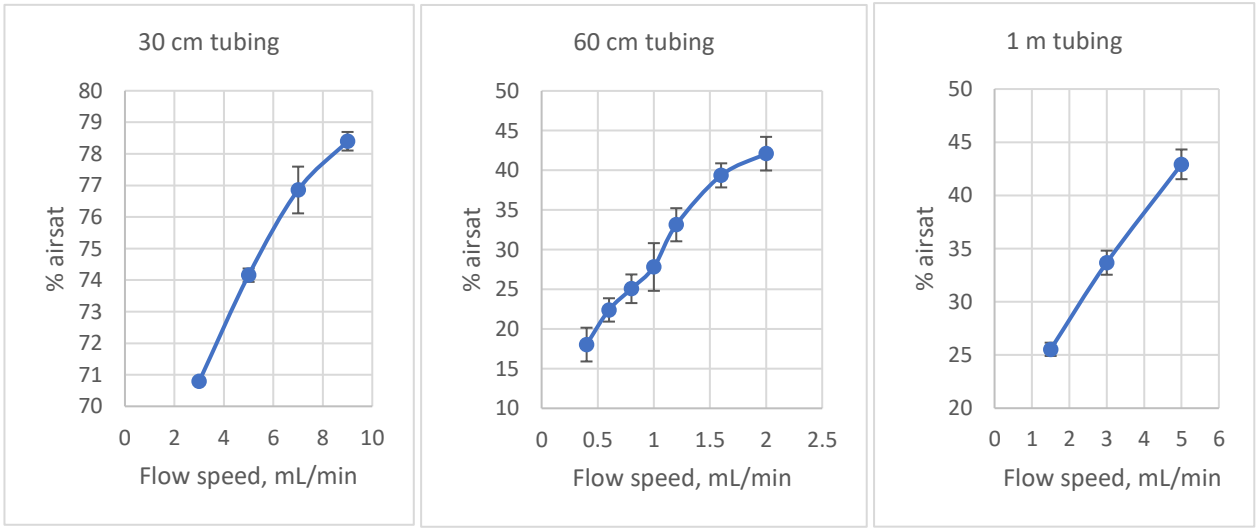

Fig. 3.4.2.10. Output oxygen concentration in water after passing through the artificial lung filled with 1 atm of nitrogen depending on sample flow rates, measured with different lengths of smaller diameter silicon tubing inside of the lung (n = 3, error bars represent standard deviations).

Microbubble stability was checked in the lung with 60 cm tubing at 0.8 and 2.0 mL/min and was markedly improved compared to the 1 m tubing; there was no significant change in size distribution or concentration of MBs after going through the lung (**Fig. 3.4.2.11**). MB stability under these conditions was therefore sufficient for subsequent blood experiments. Oxygen concentration in output was also measured; similar to previous experiments, it did not differ significantly between MBs and controls, however it did confirm the calibration reading for output O_2 concentrations (**Fig. 3.4.2.11** right-hand side).

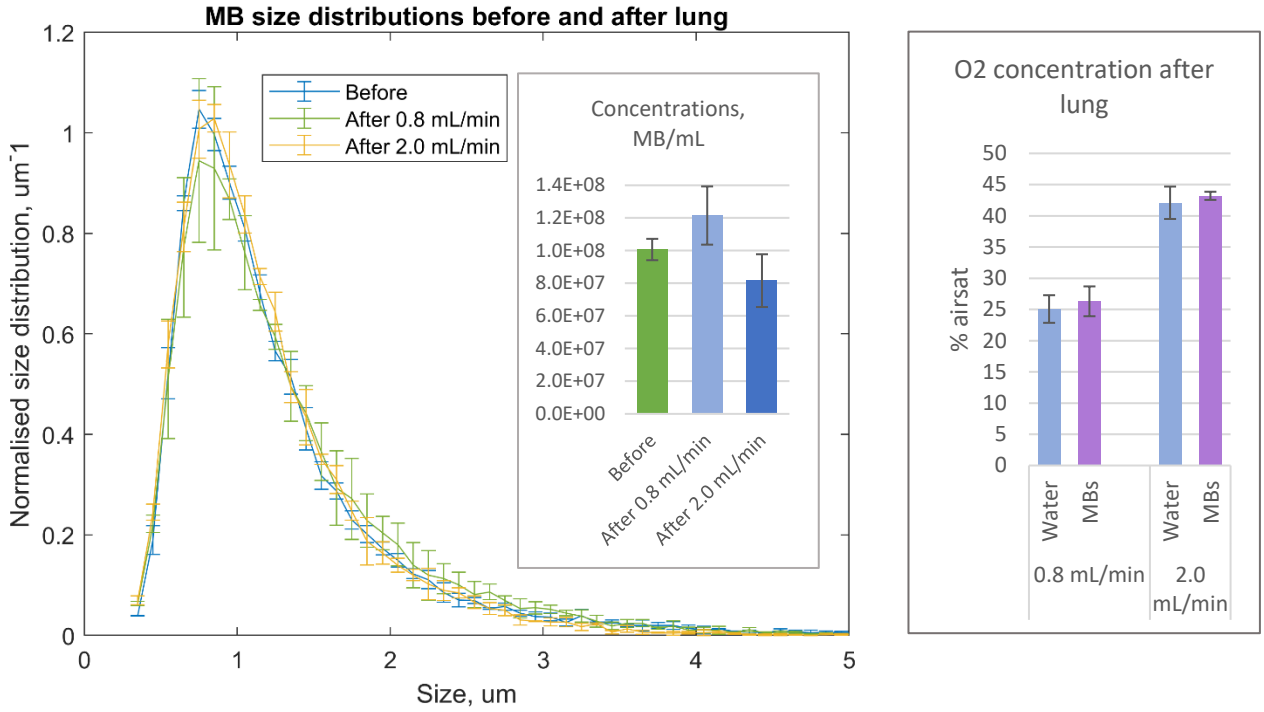

Fig. 3.4.2.11. DBPC-PEG40S PFB microbubbles size distributions and concentrations before and after going through the N_2 lung with 60 cm tubing at a flow rate of 0.8 or 2.0 mL/min (n = 3, error bars represent standard deviations). The graph on the right-hand side shows the output oxygen concentrations measured in this experiment.

3.4.3. Setup with simple artificial lung: experiments with blood

Based on the results of the preliminary experiments described in **3.4.2**, the parameters for the lung were chosen as follows: 60 cm small (ID 310 um) silicone tubing, lung filled with 1 atm N_2, flow speed of 0.8 mL/min corresponding to ~20% airsat in the output water control.

The setup was modified for blood oxygenation measurements. The output optical O_2 sensor was replaced by a lamp and an optical spectroscope, which allowed measurement of blood absorbance spectra and, consequently, oxygenation (**Fig. 3.4.3.1**).

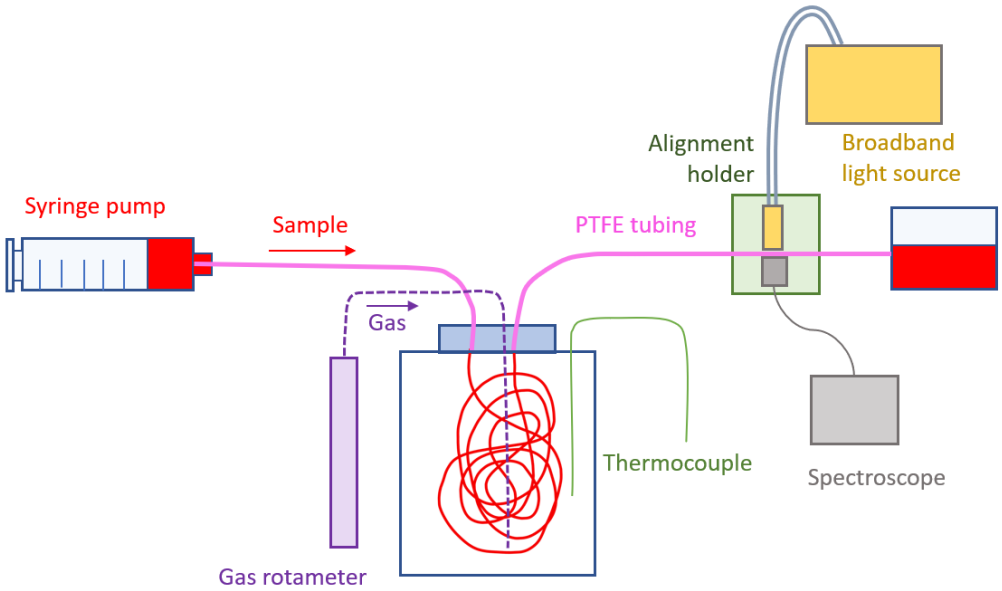

Fig. 3.4.3.1. The modification of the artificial lung setup for blood oxygenation measurements. To detect blood oxygenation via the absorbance spectra, a broadband light source was used to shine through the tubing with blood samples, and the light was detected on the other side of the sample by an optical spectroscope; the light source, spectroscope detector and outlet tubing were fixed in a custom-made holder in order to keep relative positions fixed during an experiment.

Preliminary experiments were carried out with porcine blood. The absorbance of undiluted blood was too high to detect the haemoglobin spectrum; different dilutions in DPBS were tested, and a

1:10 dilution was sufficiently transparent to reliably measure haemoglobin absorbance (**Fig. 3.4.3.2**). The blood in these experiments was equilibrated with air and therefore the absorbance spectrum shows the two characteristic peaks of oxygenated haemoglobin absorbance. Deoxygenated haemoglobin only has one peak in this part of the spectrum, which means that absorbance in the 520-590 nm range allows for quantification of RBC oxygen saturation.

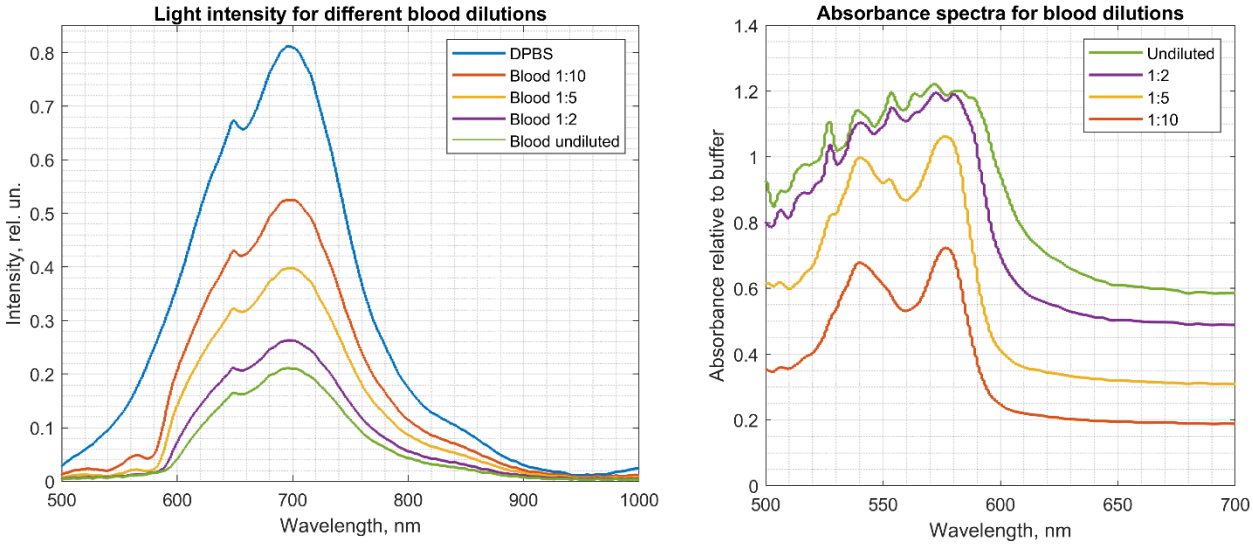

Fig. 3.4.3.2. Light intensity and absorbance relative to the DPBS buffer for different dilutions of air-equilibrated (fully oxygenated) porcine blood measured in the setup.

For further experiments, blood freshly collected from a human volunteer was used, instead of acquiring commercially available animal blood products. The reason for this is that blood is known to have reduced oxygen exchange properties after storage, due to the degradation of some oxygen release co-factors such as 2,3-DPG[153], and therefore in order to study oxygen exchange fresh blood was needed.

Spectra for air-equilibrated (fully oxygenated) and N_2-equilibrated (fully deoxygenated) human blood were measured with the lamp and spectroscope outside of the lung setup. It was found that

the measured spectra corresponded to the literature, with two peaks in the 500-600 nm range for oxygenated blood and one peak for deoxygenated blood[154] (**Fig. 3.4.3.3**).

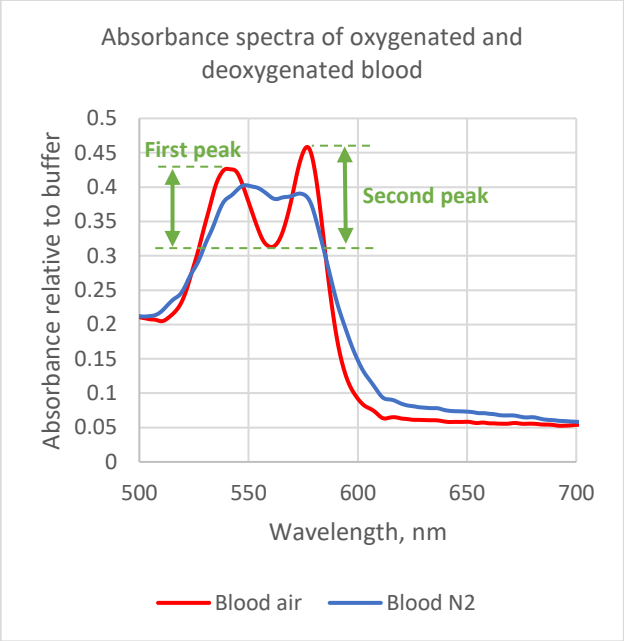

Fig. 3.4.3.3. Absorbance spectra relative to DPBS buffer for human blood, diluted 1:7 in DPBS, in a Luer µ-slide (0.2 mm height, glass bottom); blood was either air-equilibrated (oxygen-saturated) or subjected to a gentle flow of N_2 before loading into the sample holder (deoxygenated). The green arrows illustrate the blood oxygenation quantification, which was performed by subtracting the local minimum absorbance from the two local peak values.

The blood oxygenation quantification was performed by measuring the two local peaks seen in the oxygenated haemoglobin spectra (illustrated in **Fig. 3.4.3.3**). For each absorbance spectrum, the local maxima were found for the first peak (~542 nm) and second peak (~576 nm), and then the local minimum value (~560 nm) was subtracted from these numbers, resulting in the two peak heights:

$$H_{peak} = -log_{10}\frac{I_{blood}\,(peak)}{I_{buffer}\,(peak)} - \left(-log_{10}\frac{I_{blood}\,(min)}{I_{buffer}\,(min)}\right) = \; log_{10}\frac{I_{blood}\,(min)\,/\,I_{buffer}\,(min)}{I_{blood}\,(peak)\,/\,I_{buffer}\,(peak)}$$

It was observed that the obtained spectra had small variations between repeats, most likely due to slight light output variations from the source or shifts in alignment, which could be almost fully corrected by shifting the spectra by a small constant value, i.e., multiplying the intensity by a constant factor close to 1 (checked on a buffer controls dataset, data not shown). Quantifying the blood oxygenation levels by calculating the peak heights as shown above allowed for these small shifts to be corrected, since the correction factor for intensities would be reduced in the fraction on the right-hand side, providing a metric that allows for meaningful comparison between experiment runs.

After these preliminary experiments, blood oxygenation measurements were performed in the lung filled with N_2 at 1 atm. The first set of lung parameters was chosen from the buffer calibrations (**Fig. 3.4.2.9**) in order to achieve output buffer O_2 concentration corresponding to ~50% haemoglobin oxygen saturation: 60 cm of smaller diameter tubing, 0.8 mL/min sample flow speed. The air-saturated blood sample (diluted 1:10 in saline buffer) was therefore expected to go from 100% to around 50% Hb O_2 saturation after going through the lung under these conditions. No haemolysis was detected in the blood samples after going through the lung (data not shown); however, it was observed that the output blood samples in these experiments were still almost fully oxygenated. This was likely caused by the blood dilution, since it is known that dilution can affect the RBC oxygen dissociation curve, shifting it towards higher affinity to oxygen[155].

In order to experimentally determine better flow conditions for this blood dilution, measurements were performed with various sample flow speeds – 0.1, 0.4 and 0.8 mL/min (**Fig. 3.4.3.4**). It was seen that lowering the sample flow speed improved gas exchange, with blood becoming less oxygenated after going through the lung at slower speeds.

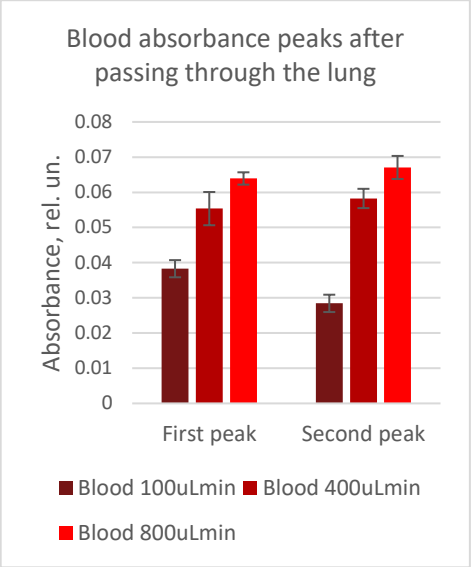

Fig. 3.4.3.4. First and second peak in blood absorbance spectra (human blood in 1:10 dilution in saline buffer, air-equilibrated before the experiment) after going through the lung filled with 1 atm N_2 (60 cm smaller diameter silicon tubing) at the flow speeds of 0.1, 0.4 or 0.8 mL/min; as explained above, higher peaks indicate more oxygenated blood, and lower peaks in this experiment therefore signify more gas exchange with the lung (n = 3, error bars represent standard deviations).

Next, experiments were performed in the same setup (60 cm smaller diameter tubing, lung filled with N2 at 1 atm) with blood samples with or without added oxygen-carrying agents. The runs were performed at three flow speeds as above, with the expectation that at the lower flow rate (0.1 mL/min) the potential effect from the added agents would be more pronounced due to the increased gas exchange time. In all cases the blood and agent solutions were equilibrated with air oxygen concentration and room temperature before the experiments, and temperature stability was monitored in the gas phase of the lung throughout the runs. The agents used were DBPC-PEG40S PFB microbubbles, lecithin PFOB non-phase-change droplets and lecithin-based nanobubbles (detailed characterisations are provided in **Chapter 2**), as well as crocetin (**Figs. 3.4.2.5 – 3.4.2.8**).

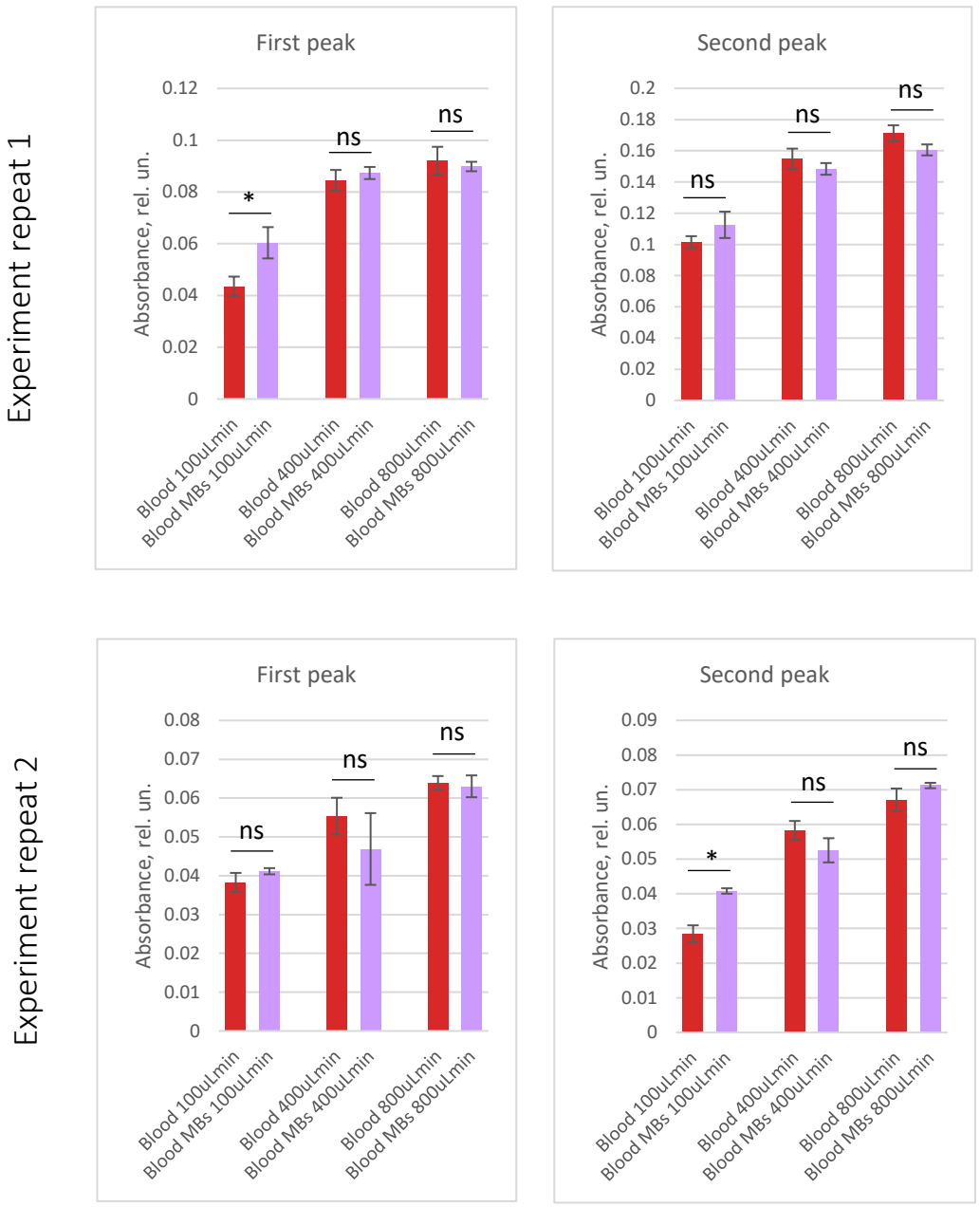

Fig. 3.4.3.5. First and second peaks of the absorbance spectra of blood (diluted 1:10 in DPBS buffer) with or without DBPC-PEG40S PFB MBs (dilution 1:10 from stock, concentration in final solution ~$1*10^8$/mL) after passing through the lung (60 cm smaller tubing, 1 atm N_2) at the flow rates of 0.1, 0.4 or 0.8 mL/min; results are shown for two independent experiments carried out with different samples on different days (n = 3, error bars represent standard deviations). * indicates significant difference ($p < 0.05$ as calculated with a two-tailed t-test), ns – not significant ($p >= 0.05$).

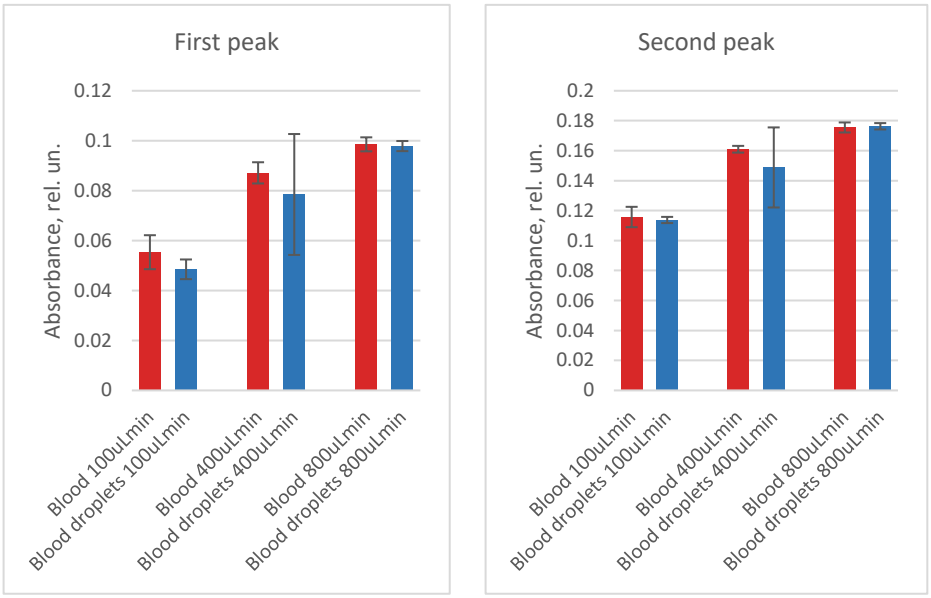

Fig. 3.4.3.6. First and second peaks of the absorbance spectra of blood (diluted 1:10 in DPBS buffer) with or without lecithin PFOB droplets (approximately 0.06 g/mL PFOB in final solution) after passing through the lung (60 cm smaller tubing, 1 atm N_2) at the flow rates of 0.1, 0.4 or 0.8 mL/min (n = 3, error bars represent standard deviations).

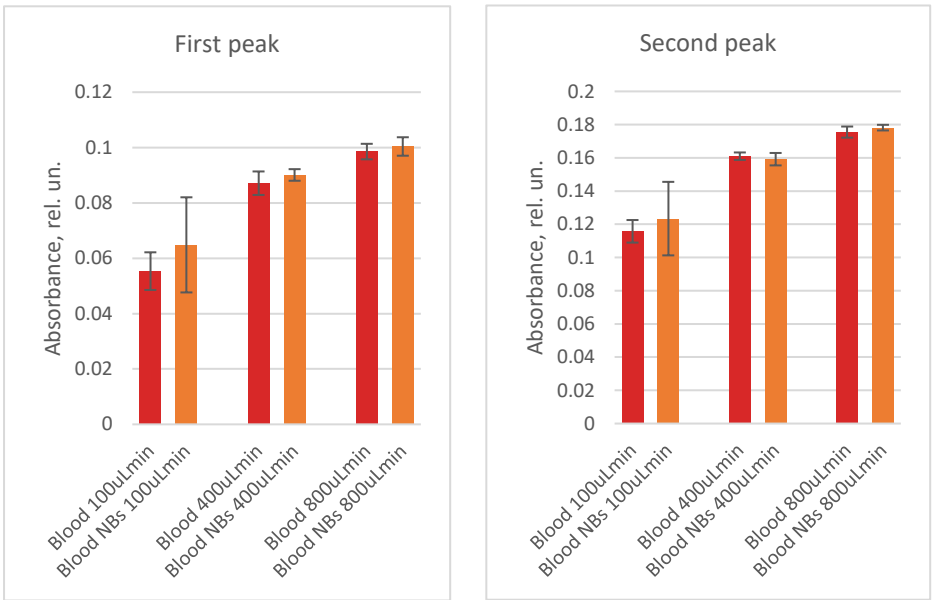

Fig. 3.4.3.7. First and second peaks of the absorbance spectra of blood (diluted 1:10 in DPBS buffer) with or without lecithin-based nanobubbles (dilution 1:10 from stock, concentration in final solution ~$5*10^{11}$/mL, pH of stock adjusted to neutral) after passing through the lung (60 cm smaller tubing, 1 atm N_2) at the flow rates of 0.1, 0.4 or 0.8 mL/min (n = 3, error bars represent standard deviations).

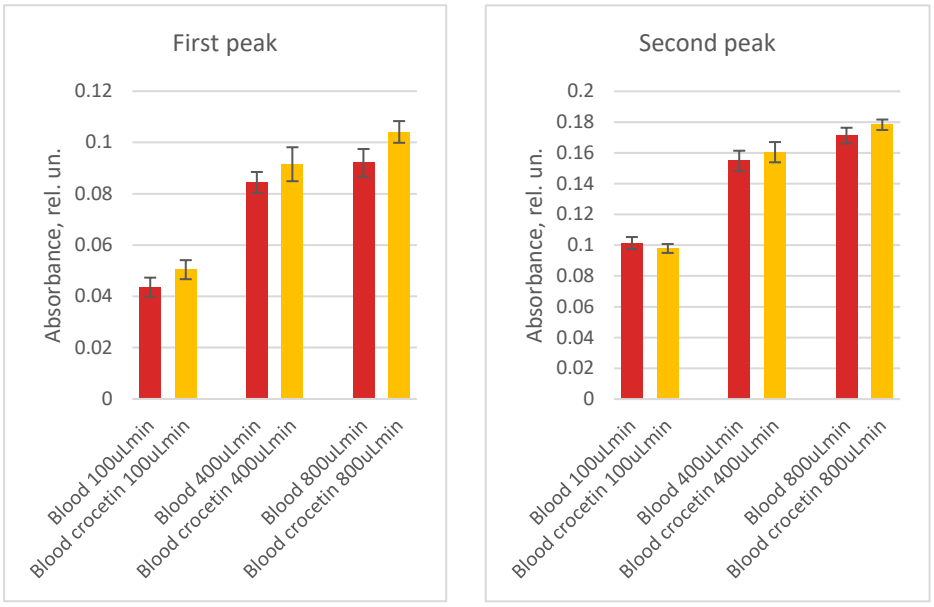

Fig. 3.4.3.8. First and second peaks of the absorbance spectra of blood (diluted 1:10 in DPBS buffer) with or without crocetin (concentration 100 µM in final solution) after passing through the lung (60 cm smaller tubing, 1 atm N_2) at the flow rates of 0.1, 0.4 or 0.8 mL/min (n = 3, error bars represent standard deviations).

For the droplet, nanobubble and crocetin samples, the difference between the blood samples with and without the agent was insignificant ($p >= 0.05$ as calculated with a two-tailed t-test) (**Figs. 3.4.3.6 – 3.4.3.8**). A large and significant change in peak heights was observed in some cases for microbubbles added to the blood samples for the lower flow rate of 0.1 mL/min (**Fig. 3.4.3.5**); interestingly, however, the absorbance peaks increased with added MBs, signifying more oxygenated blood and, consequently, less – not more – gas exchange with the lung; a similar result was observed in the same experiment repeated independently on a different day.

This effect could be explained by comparing two characteristics of the MB solutions: diffusion speed and solubility. The diffusion speed through the MB solution is increased compared to the buffer, as the gas phase provides faster oxygen and nitrogen diffusion; the payload gas passing through the lipid layer, although potentially slowing the diffusion down, does not nullify this speed increase[156]. However, oxygen and nitrogen solubility in MB solutions is also increased due to the

presence of the gas phase. This does not impact the gas diffusion speed in the dynamic equilibrium, but solubility becomes important when MBs are introduced into a medium with a different gas content, as for example in the lung experiments. In this case, when oxygen and nitrogen gases start exchanging when the sample begins passing through the setup, there are two competing processes: the diffusion speed increasing due to the presence of MBs, but also the MBs taking up the gases, which would lead to slower gas exchange. The diffusion theory relies on the first process being dominant; however, the second process may also be substantial depending on the parameters of the system.

3.5 Summary and conclusions

Based on the discrepancy between the small total volume in one dose of PFC-based oxygen carriers and the oxygenation effects that they have been shown to produce *in vivo*, a hypothesis has been proposed that these agents act by shortening the speed-limiting diffusion path of oxygen through plasma and thus enhancing oxygen diffusion between red blood cells and tissue. The experimental support for this hypothesis is limited to only a few agents, and therefore the aim of this chapter was to develop a setup to test the diffusion hypothesis for a wider variety of oxygen carriers, including ultrasound-responsive agents.

Preliminary work was carried out by developing a setup for measuring oxygen diffusion speed in a sample layer without blood or flow, which allowed to determine important setup design considerations for future work. Then, preliminary tests with flow were carried out in a clinical organ perfusion setup with artificial lungs, but it was found that this setup does not provide enough control over the parameters of the experiment to efficiently measure the speed of oxygen exchange.

Consequently, a simple artificial lung setup was constructed to measure oxygen saturation of RBCs in a flow setting after they undergo gas exchange in a controlled gas environment. A number of experiments were undertaken in order to perform calibrations and optimise the setup parameters for optimal agent stability and output oxygen levels. Final experiments undertaken with this optimised setup showed no significant oxygenation changes for blood samples with PFOB droplets, lecithin nanobubbles and crocetin compared to blood controls; however, a change was detected for blood samples with DBPC-PEG40S microbubbles at lower flow speeds, signifying that the microbubbles slowed down the gas exchange process, as opposed to speeding it up. This was explained by the increased gas solubility in the microbubbles, which taken together with the

diffusion processes can, under certain experiment parameters, lead to overall decreased gas exchange speed in non-equilibrium situations.

Although this observation does not disprove the diffusion hypothesis, it leads to the conclusion that more detailed calculations are needed to understand the space- and timescales of the competing processes of the gas exchange processes being sped up by enhanced diffusion and slowed down by enhanced solubility.

Future work

The experiments described in this chapter do not conclusively support or contradict the diffusion hypothesis for the tested agents. In order to test this hypothesis further, different experimental parameters are needed.

Most importantly, the smallest silicon tubing inner diameter used in this study was 310 um, as smaller gas-permeable tubing could not be obtained, and there are practical challenges in producing smaller channels in other suitable materials such as PDMS; in addition, the setup would have to be carefully designed in order to avoid pressure increases that would damage the agent or RBC stability, and suitable adjustments would have to be made to the absorbance spectra detecting part of the setup. If these challenges could be solved, smaller tubing or channels would provide a better model for the capillaries that conduct most of the gas exchange in the body, therefore making this a more reliable model of *in vivo* conditions, as the size is important not only for the timescales of all the processes, but also to better model the radial agent distribution in the vessel and the wall excess phenomenon.

Another aspect that was not explored in this project in sufficient detail is the potential interaction between the RBCs and oxygen-carrying agents: in addition to the diffusion enhancement through

the plasma, the carriers may be able to fuse with the RBC membranes. It is known that at least some of the agents used in this project can transfer material into the cell membranes during ultrasound exposure; therefore it would be of interest to check whether this applies to RBCs in suspension as well, and to test whether any of the agents can go into the RBC membranes after incubation without ultrasound. Preliminary experiments were carried out to this end, but agent labelling requires further optimisation.

Finally, more detailed theoretical simulations or calculations of the dynamics of oxygen diffusion in a mixture of RBCs and agent flowing in a vessel, for example using the microphase framework[147], would also be of interest. This would allow to better understand this system and make informed predictions of the experimental parameters that would be needed to reproduce the possible diffusion effects *in vitro*.

Chapter 4. Characterisation of the ultrasound exposure setups

4.1 Introduction

The previous chapter describes the investigation of the mechanisms of oxygen delivery by various carrying agents, which is an important aspect for oxygen-dependent therapies such as sonodynamic therapy (SDT). This chapter addresses a different aspect of SDT, namely reactive oxygen species (ROS) generation and mechanisms of cell killing.

As described in the literature review (section 1.3), there are some discrepancies in the types of ROS reported in the literature for SDT with various drugs under various exposure conditions, and there is a mismatch between the quantities of ROS produced by drugs that exhibit both photo- and sonosensitivity when exposed to either light or sound. The following part of this project explored this issue, studying ROS production during SDT and testing a cell kill mechanism hypothesis.

An important preparatory step for sonication experiments, in order for the results to be reliable and appropriately reported, is the design and characterisation of the ultrasound exposure setup. This chapter details the ultrasound setups used in this project, describing the motivation behind their design, as well as various characterisation experiments.

4.1.1 Importance of the characterisation and monitoring of therapeutic ultrasound experiments

One of the reasons for the discrepancies in the reported characterisation of ROS produced with ultrasound is the ongoing lack of standards for the characterisation, monitoring and subsequent reporting of therapeutic ultrasound exposures. While some studies utilise carefully designed and calibrated setups, many others use commercially available ultrasound sources and common

sample holders such as 96-well plates without proper ultrasound output monitoring, which makes comparing the results across different studies difficult or even impossible. There has been an active push across the therapeutic ultrasound field to implement better experimental practices and literature reporting standards[157]; however, this issue is still ongoing.

For this reason, particular attention in this project was devoted to good experimental practice with regard to the ultrasound setup usage. It included publication work carried out in collaboration with Dr Michael Gray, Veerle Brans and Prof Eleanor Stride, which provided experimental protocol guidelines and representative measurements with the ultrasound setup used in the current project[103].

4.1.2 Chapter overview and objectives

This chapter aims to summarise the characterisation of ultrasound setups used in this project and, importantly, discuss some of the good practice experimental guidelines that were followed.

4.1.3 Attribution of work

The system for acoustic transfection (SAT) 2 setup described in this chapter was designed and built in-house, as reported in the paper by Carugo et al[158]. SAT2 setup schematic image (**Fig. 4.3.1.1**) was provided by Dr Michael Gray. Transducer calibration in **Fig. 4.3.1.2** was performed by the project author with the help of Dr Michael Gray.

SAT2E setup was designed and characterised by Dr Michael Gray (**Figs. 4.4.1.1 – 4.4.1.2**).

The PCD processing MATLAB script was written by Dr Michael Gray and adjusted by the thesis author.

All other experimental and data processing work was performed by the author of this thesis.

4.2 Materials and methods

The materials and methods for microbubbles and other agent production and characterisation are described in detail in Chapter 2.

4.2.1 List of equipment

The SAT2 and SAT2E setups used a 1 MHz transducer (Imasonic 8233 A101, Imasonic SAS, France). The transducer was driven by an amplified signal from a waveform generator (generator Agilent 33250A, Agilent Technologies, USA; amplifier ENI A300, Electronic Navigation Industries, USA, or 1140LA, Electronics & Innovation, Ltd., USA). The amplifier output was monitored with an oscilloscope (Teledyne LeCroy, USA) via a high voltage probe.

The passive cavitation detection was performed with a PCD probe (7.5 MHz centre frequency, either focused in the centre of the sample dish or unfocused depending on experiment, Olympus V320, Olympus, UK). Drive frequency was removed from the signal with a high-pass filter (2 MHz, Allen Avionics, Inc., USA, or 1.8 MHz, ThorLabs, USA). Afterwards the signal was preamplified 5x (SR445A, SRS, Sunnyvale, USA) and recorded using a digital oscilloscope (TiePie HS3 or HS5 depending on experiment, TiePie engineering, The Netherlands).

4.2.2 PCD processing

The PCD signals, after passing through a 2 MHz high-pass filter and a pre-amplifier, were recorded with a digital oscilloscope (TiePie) at a sampling frequency of 25 MHz (100 000 samples per record). The recorded traces were fitted with a Tukey window and analysed using a Fast Fourier Transform

in MATLAB (data was processed with Welch's method for power spectral density). Harmonic and ultraharmonic intensities were estimated from the signal at harmonic and ultraharmonic frequencies within a frequency bin window (5 kHz).

4.2.3 PDMS moulding

The sample holder is a PDMS lid designed to fit a 35 mm cell culture dish[158] (μ-Dish, Thistle Scientific, UK).

To produce sample holder lids, an in-house manufactured mould form was cleaned with 70% ethanol, filled with a 9:1 (by weight) mix of PDMS and a cross-linking agent and was degassed for at least 40 minutes in a vacuum chamber; the level of PDMS was controlled so that the surface of the sample holder is as thin as possible (~1 mm). Then it was placed in an oven at 650°C overnight.

4.3 SAT2 setup

4.3.1 Description of the setup

The SAT2 ultrasound exposure setup was designed and built in-house[158] (Fig. 4.3.1.1). The main rationale behind its design was to provide a blueprint for constructing a ultrasound setup that can provide a reproducible ultrasound field and the possibility of PCD monitoring, but at the same time is easy to assemble and use.

The setup consists of a small water tank (volume ~1L, filled with filtered MilliQ water after degassing for at least 1 h down to approximately 50% air saturation with a vacuum pump), which contains the transducer (1 MHz) and the sample holder. The sample holder is a PDMS lid designed to fit a 35 mm cell culture dish (Ibidi µ-Dish); during the experiments the sample is sealed and the cell dish is inverted, in order to ensure good microbubble contact with cells via flotation, as well as to avoid having the plastic of the cell culture dish in the ultrasound path between the transducer and the sample.

The chamber lid contains an ultrasound absorber and a slot for a passive cavitation detector (PCD, 7.5 MHz centre frequency, either focused in the centre of the sample dish or unfocused depending on experiment).

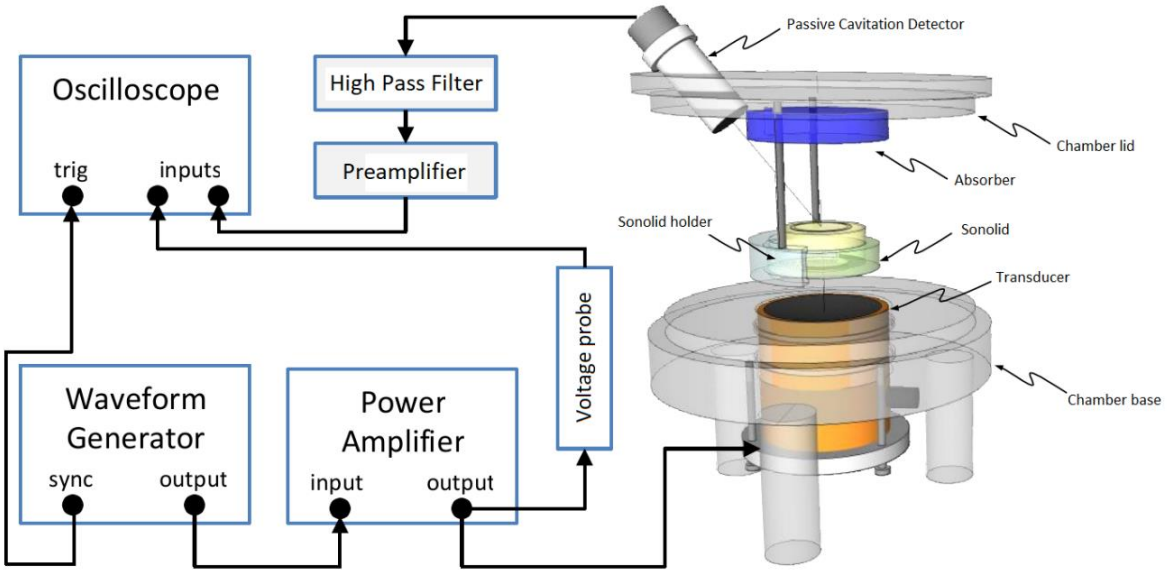

Fig. 4.3.1.1. Schematic of the SAT2 setup (design and image courtesy of Dr Michael Gray).

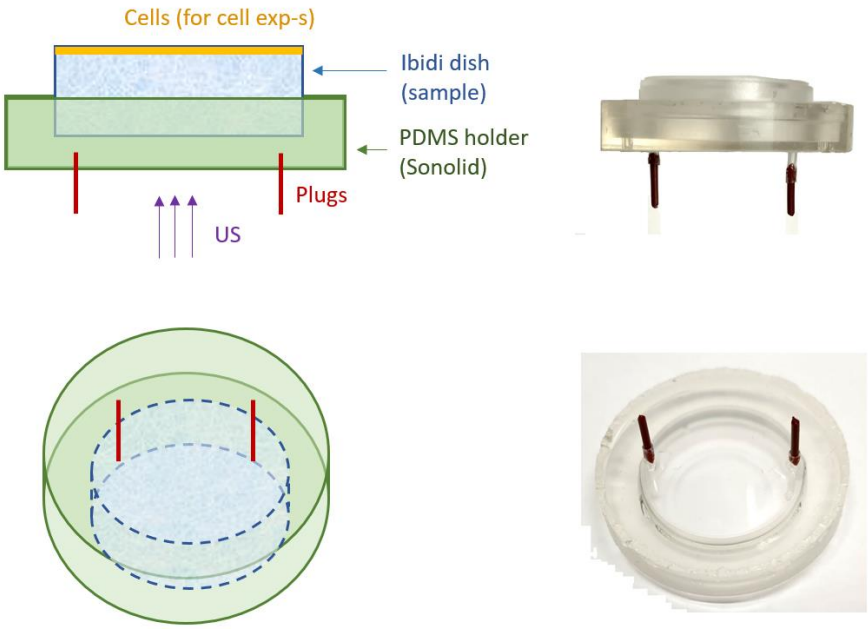

Fig. 4.3.1.2. Schematic and photographs (side view and top view) of the sample holder: PDMS lid (SonoLid) with an inserted cell culture dish (35 mm Ibidi dish); the PDMS lid has holes for sample filling that are plugged for ultrasound exposures. In the setup the sample holder is positioned with the cell-adherent surface facing up (in order to assist cell-MB interactions through MB flotation)

and the ultrasound transducer is positioned below the sample (as PDMS is more transparent to ultrasound than the cell dish plastic).

The pressure calibration of the transducer across the sample plane is shown in **Fig. 4.3.1.3**. As the field was not homogenous, it was averaged over the sample surface area for the pressures indicated in suspension experiments; a modification of this setup (SAT2E, see section **4.4**) was constructed in order to achieve a bigger area of homogenous pressure for dish-adherent cell experiments.

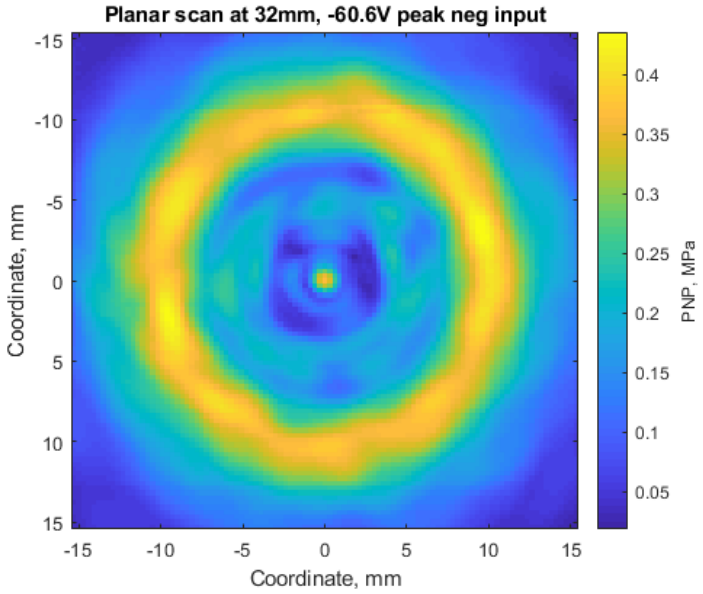

Fig. 4.3.1.3. Peak negative pressure field of the SAT2 transducer in the plane corresponding to the sample plane (32 mm away from the transducer surface) at the input peak negative voltage of 60.6 V. For suspension experiments, the centre of the sample was approximately aligned to this plane, while for cell experiments, the top of the sample (i.e., the cell dish surface) was put into this position (the sample height on the sample holder is adjustable).

4.3.2 Experiments with SAT2

To obtain robust and well-reproducible ultrasound exposure data, it is important to keep in mind several technical issues regarding the experiments and ultrasound agent sample preparation.

A. Buffer oxygenation

One of the principal issues is the gas content of the sample buffer. For some *in vitro* experiments, especially for ROS measurements or experiments with oxygen-containing samples, buffers are degassed to reduce the background; however, this can negatively impact the stability of the microbubbles; in addition, buffer air content has to be controlled for the whole duration of the experiment to ensure reproducibility[139]. Moreover, degassed buffers cannot be used for cell work experiments. Consequently, the optimal buffer gas content depends on the type of the experiment conducted and the microbubbles/other ultrasound-responsive agents used.

From the point of view of microbubble stability, this issue has been discussed above, and it was shown that MB stability is severely impaired in degassed media (**Fig. 2.4.2.4**). Here, this issue was also investigated from the point of view of PCD emissions. **Fig. 4.3.2.1** shows an example of PCD detection for a sample of commercially available SonoVue microbubbles diluted in DPBS at 100% and ~50% air saturation, with the degassed buffer sample showing lower broadband intensity and larger variability in harmonic and ultraharmonic peak heights. This confirms that measurements in degassed media are not well-suited for microbubble experiments; all further experiments were carried out in air-equilibrated buffers.

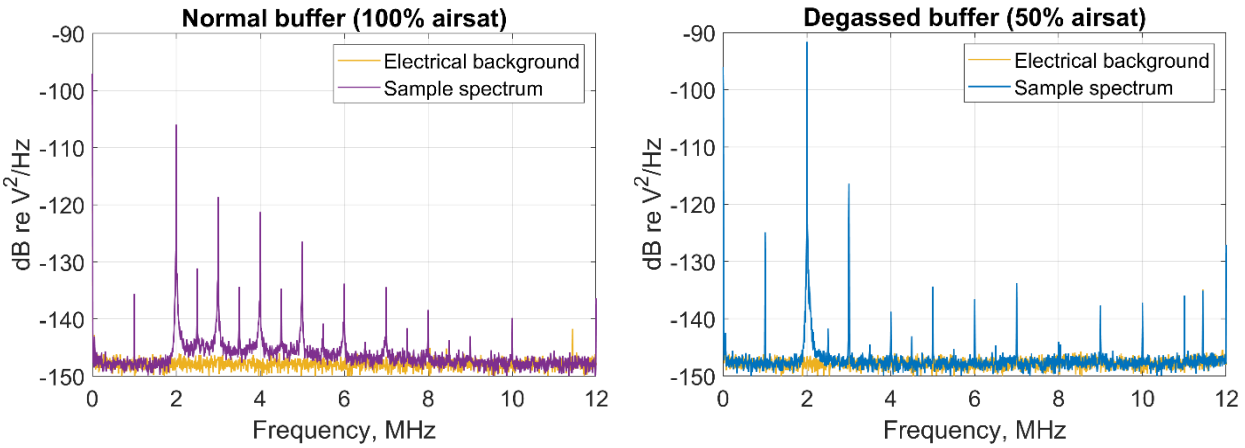

Fig. 4.3.2.1. Sample power spectra for a microbubble sample (SonoVue, 10^7 MB/mL) measured in DPBS at 100% air saturation and ~50% air saturation. Signals detected with a focused PCD with a 7.5MHz center frequency. Ultrasound parameters: 1 MHz, 1.06 MPa peak to peak, 30% duty cycle, 100 Hz pulse repetition frequency.

B. Focused and unfocused passive cavitation detectors

Another important issue for ultrasound experiments is signal monitoring. In particular, the choice of PCD center frequency and focal parameters may impact the interpretation of the detected signal. For these studies, a PCD with the center frequency of 7.5 MHz was used, and focused and unfocused PCD detectors were compared for a microbubble sample (**Fig. 4.3.2.2**). Due to the small focal area of the focused PCD, it was expected that the signal would be lower and variability over time higher than for unfocused PCD due to microbubbles (or macroscopic bubbles/foam formed during the sonication) floating in and out of the focal region; indeed, this was what was observed experimentally. Due to these results, most of the experiments reported in **Chapter 6** used an unfocused PCD.

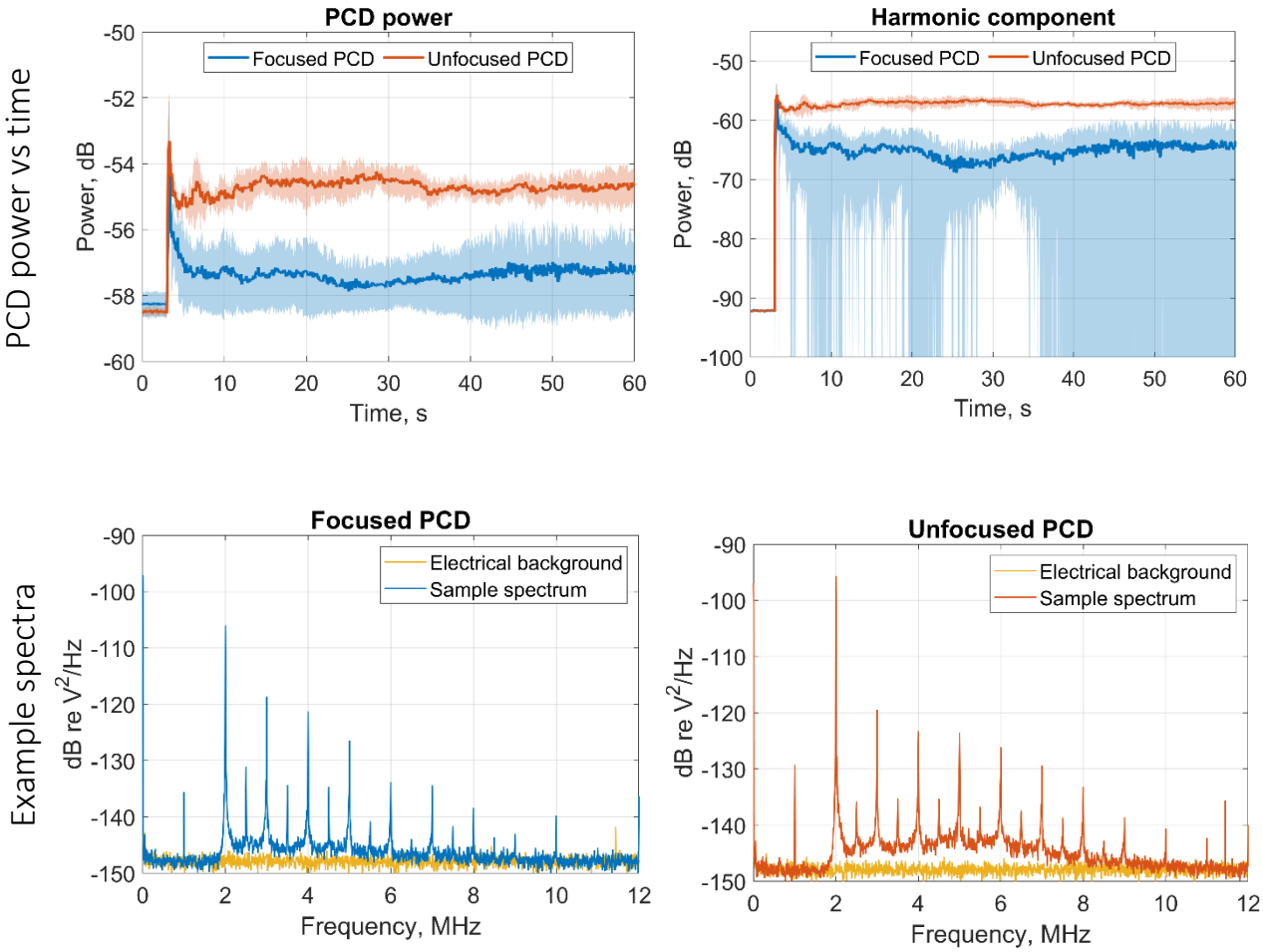

Fig. 4.3.2.2. PCD signal vs time (full power and its harmonic component) for a microbubble sample (SonoVue, 10^7 MB/mL in 100% airsat DPBS) measured with a focused and unfocused PCD. Both PCDs had a center frequency of 7.5 MHz; for the focused PCD the focus was in the middle of the sample holder. Filled areas represent standard deviations for n = 3 repeats (cut off at -100dB for the harmonic component due to large variability). Ultrasound parameters: 1 MHz, 1.06 MPa peak to peak, 30% DC, 100 Hz PRF. Ultrasound was switched on at t = 3 sec.

C. Macroscopic air bubbles in the setup

In order to obtain reliable data, one more technical issue is avoiding cavitation and scattering outside of the sample. For this reason, water is purified and degassed to ~50% airsat prior to loading into the setup, and visible bubbles are removed from the water tank before and between experiments. Care should also be taken when loading sample solutions into the sample holder. **Fig.**

4.3.2.3 illustrates the importance of this in an example of PCD data obtained with a macroscopic air bubble deliberately introduced into the sample holder, with the air bubble signal being much more noisy.

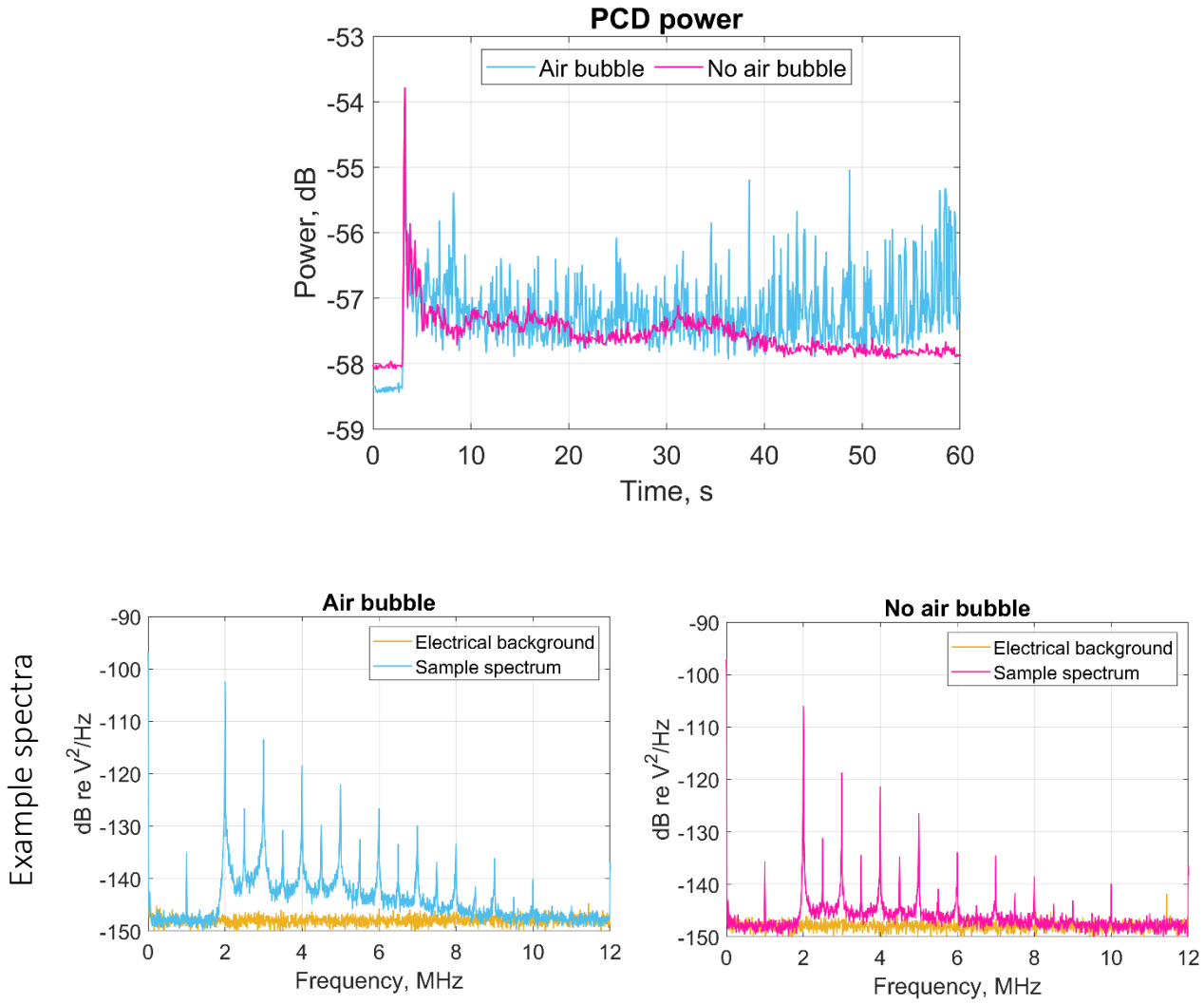

Fig. 4.3.2.3. PCD power vs time and example power spectra for a sample holder with a large air bubble compared to a fully filled sample holder. SonoVue concentration 10^7 MB/mL, sample volume 10mL in DPBS (100% airsat). Signals detected with a focused PCD with a 7.5MHz center frequency. Ultrasound parameters: 1 MHz, 1.06 MPa peak to peak, 30% DC, 100 Hz PRF. Ultrasound was switched on at t = 3 sec.

The issues above illustrate only some of the considerations that should go into designing ultrasound exposure experiments, and they were taken into consideration for the experiments described in Chapters 5 and 6.

4.4 SAT2E setup

4.4.1 Description of the setup

The SAT2 setup was used for a number of experiments in which the sample (microbubbles with or without various sonosensitisers and/or ROS sensors) was in suspension inside of the sample holder; for the purpose of these experiments, the ultrasound pressure was spatially averaged across the sample area under the assumption that the mixing within the sample during the experiment is sufficient. However, such an assumption is not applicable for experiments with cells that are adherent to the sample holder dish; in this case, a sufficiently large area of homogenous pressure is needed in order to characterise the pressure field that the observed cells were subjected to. The inhomogeneity of the pressure fields in the SAT2 setup was too large for this goal (Fig. 4.3.1.2), and therefore the setup was re-designed with a larger tank that would allow to place samples further from the transducer and therefore obtain a more homogenous pressure field.

This setup was named SAT2E (Fig. 4.4.1.1). The electrical components of this setup, including the transducer and the PCD circuit, were identical to the SAT2, as was the sample holder polymer dish; the tank configuration was the only change. This resulted in a more homogenous field across the sample plane (Fig. 4.4.1.2); the central area of approximately 5 mm diameter, which is a feasible size scale for microscopy imaging, had less than 10% pressure field standard deviation.

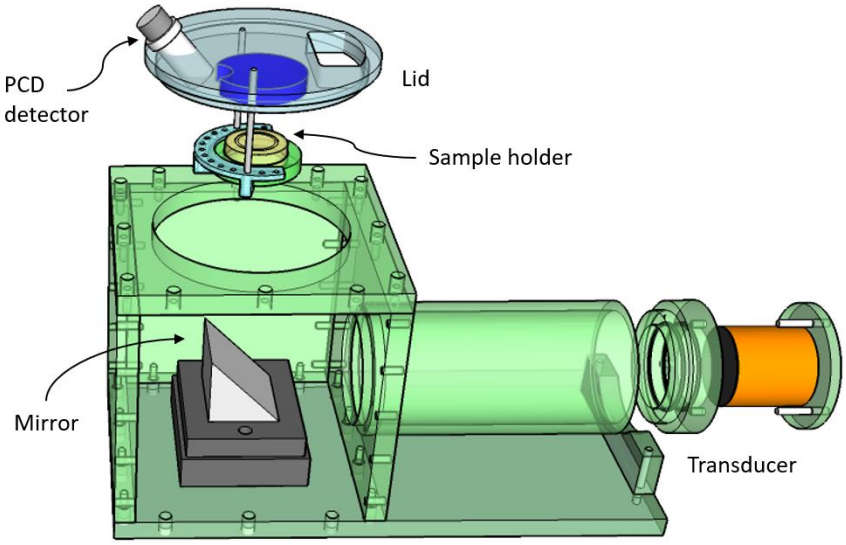

Fig. 4.4.1.1. SAT2E tank schematic (design and image courtesy of Dr Michael Gray).

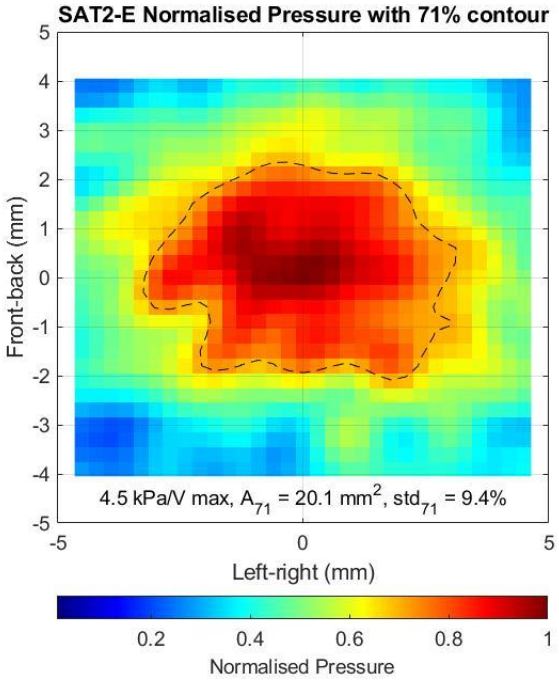

Fig. 4.4.1.2. Transducer normalised pressure field across the sample plane; the dashed line indicates the 20 mm^2 central region with the pressure >= 71% of the maximum value (i.e., less than 10% pressure standard deviation across the region) (data and image courtesy of Dr Michael Gray).

4.5 Summary and conclusions

This chapter described the main ultrasound setups used for the current project (named SAT2 and SAT2E), which were designed and assembled in-house. Good experimental practice for the field of therapeutic ultrasound was discussed. Experimental data illustrating some of these issues (sample buffer gas content, focused vs unfocused PCD and macroscopic air bubbles in sample) was given using the SAT2 setup and commercially available SonoVue microbubbles. The guidelines described here for reliable ultrasound exposure experiments were followed throughout this project.

Chapter 5. Reactive oxygen species generation and measurement

5.1 Introduction

In order to aid in the transition of SDT into clinical use, better understanding of its mechanisms has to be developed (see section 1.3 of the literature review). In particular, this entails further characterisation of reactive oxygen species (ROS) that are produced during sonication.

Chapter 4 discusses the technical side of the sonication experiments, in particular the ultrasound setup characterisation and important consideration for the reliability of experiments. The current chapter moves on to the issue of ROS detection and quantification during ultrasound exposures of sonosensitive drugs.

5.1.1 Sonodynamic therapy drugs

Sonodynamic therapy employs a wide array of active compounds (usually referred to as sonosensitizers). As SDT initially emerged from PDT, it is not surprising that many SDT drugs were initially developed for PDT and exhibit light, as well as ultrasound, responsiveness.

Small-molecule SDT drugs can be roughly divided into several types[159]:

- Porphyrin-based: these drugs include photosensitizers such as porphyrin and photofrin, as well as their derivatives such as protoporphyrin and chlorin e6; this is the oldest class of SDT drugs, as first publications on SDT used hematoporphyrin[88,89].

- Xanthene-based: xanthene dyes such as erythrosine B and rose bengal (RB).

- Non-steroidal anti-inflammatory-based, including fluoroquinolone antibiotics, ciprofloxacin, gatifloxacin, lomefloxacin, sparfloxacin, tenoxicam and piroxicam.

- **Other sonosensitizers:** a wide variety of molecules[159], including curcumin, indocyanine green, acridine orange, hypocrellin B, 5-ALA and IR780.

A number of nanoparticle-based agents have also been developed, such as titanium dioxide particles and even black phosphorus semiconductor nanosheets hybridised with gold particles, as well as a wide array of agents for combining SDT with imaging, or chemo- or immunotherapy[94]. Similar to many areas of nanobiotechnology, these particles offer a number of advantages, but still require a long development process before they may be tested clinically. Small molecule drugs, despite their much more limited function versatility, are better-studied, especially in the case of many SDT drugs, which have been repurposed from other applications for which their safety profiles and pharmacokinetic properties are already known.

The SDT drug used in this project is Rose Bengal (4,5,6,7-tetrachloro-2',4',5',7'-tetraiodofluorescein, or RB; structure is shown in **Fig. 5.1.1.1**). Like many other drugs, RB was initially used as a textile dye; now RB sodium salt is a commonly used dye used in eye drops in order to identify damaged cells, and it is used in some other applications where staining of dead cells is needed. (Note that in the literature RB sodium salt is also often referred to as simply Rose Bengal; in this thesis, the distinction is also not generally drawn unless it is important to the discussion.)

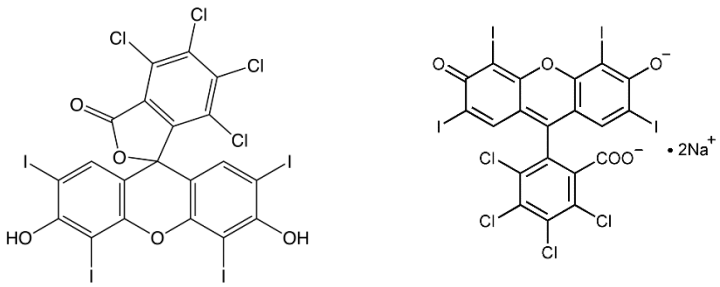

Fig. 5.1.1.1. Rose Bengal and Rose Bengal disodium salt structure (image source: Wikipedia.org).

RB was discovered to have photo- and sonosensitive properties, which has led to its application in therapy. A number of studies showed that RB enhanced ultrasound-induced cell killing in cell experiments and (when delivered in suitable form or carrier vehicles) slowed down tumour growth in animal models[160].

(An important note on the cell studies is that they characterised the effect of RB or its derivatives on cells in different ways, some of which could be reliable live/dead cell markers, while others may not be able to distinguish between reversibly and irreversibly sonoporated cells, depending on the exact protocol and the timelines of the experiment; care should therefore be taken when interpreting some of the results. This is a notable issue in the field of sonoporation studies and will be covered in more detail in Chapter 6.)

One of the barriers to using Rose Bengal in cancer therapy is its fast clearance from the body that does not allow for therapeutically relevant concentrations to be generated in a tumour. One of the ways to overcome this issue is chemical modification, in particular to make the molecule more amphiphilic, and indeed it has been attempted[161,162]. Another strategy is loading or attaching Rose Bengal to delivery vehicles, such as microbubbles that have additional functionality for SDT as cavitation nuclei[41,42].

Some attention has been directed at elucidating the RB-induced cell killing mechanisms. Its light-activation mechanism is well-studied: in PDT terminology, it is a type II sensitizer, meaning that its activation by green light (532 nm) leads to the generation of singlet oxygen. The understanding of the ultrasound-induced action of RB is less well-developed. One study showed that RB-induced cell effects were suppressed by the addition of histidine, which is known to scavenge singlet oxygen and possibly hydroxyl radicals[97]. Another study argued that singlet oxygen, or indeed any other sensitizer-derived free radicals, do not play a role in RB-induced cell killing, and the effects

are mainly mechanical[163]. Yet another paper concluded that singlet oxygen is not the principal mechanism of ultrasound-induced RB toxicity and instead suggests peroxyl and alkoxyl radicals[98].

This is illustrative of an issue common to many SDT drugs, which is that the mechanisms of activation and/or action are not yet fully understood[93]. One of the aims of the presented thesis was therefore to contribute to better understanding of SDT, with the current chapter discussing *in vitro* ROS measurements with Rose Bengal, and the following chapter presenting cell experiments and discussing a sonoporation mechanism hypothesis.

5.1.2 Reactive oxygen species measurements

There are various methods of ROS detection; one of the most popular is using fluorescent chemicals as markers for one or several ROS species, but other methods such as sensor quantification by HPLC or other methods of optical detection (e.g., by specific infrared emissions for singlet oxygen) are also used. A number of literature reviews have summarised these methods in great detail[164,165]; in this introduction, only the sensors used in the current study are discussed.

A. Singlet Oxygen Sensor Green (SOSG)

SOSG is an optical sensor that exhibits fluorescence when exposed to singlet oxygen. As it is a commercial agent, its structure was not disclosed, but a feasible structure has been suggested in the literature based on fluorescein and anthracene[166].

It has become popular for singlet oxygen detection due to its alleged specificity to this ROS species; a number of studies showed its use for *in vitro* and *in vivo* ROS measurements[167,168]. However, due to its widespread use, SOSG has also been widely studied to understand its mechanisms and limitations, and a number of problems have been reported, such as photodecomposition, singlet

oxygen generation (i.e., self-activation)[169], efficient binding to proteins that can impede its use in cells and, *in vivo*[166], unwanted activation in the presence of ionizing radiation[100], in alkaline pH or in the presence of certain solvents, as well as other off-target interactions.

Interestingly, a study that was published after the experiments presented in this chapter were carried out also stated that SOSG is activated by ultrasound in aqueous solutions and that hydroxyl radicals may be involved in this process[101].

Taken together, this body of work signifies that care should be taken when using SOSG and designing appropriate controls.

B. 9,10-anthracenediyl-bis(methylene)dimalonic acid (ABDA)

While the SOSG results emphasize the need for great care when using this sensor, one of the SOSG photochemistry studies also noted that problems like photodegradation and self-activation are common for fluorescein-based sensors[169]. In addition, fluorescence measurements in general, despite their marked advantages, also bring a number of technical issues, especially in complex solutions. Consequently, a chemically different sensor was explored with the goal of detecting singlet oxygen via the change in absorbance spectra, as opposed to fluorescence.

ABDA is a water-soluble derivative of anthracene (Fig. 5.1.2.1) that can be photobleached by singlet oxygen to the corresponding endoperoxide. It has a characteristic absorbance spectrum with four peaks in the 340 – 420 nm range that can be used to monitor changes in singlet oxygen concentration[170].

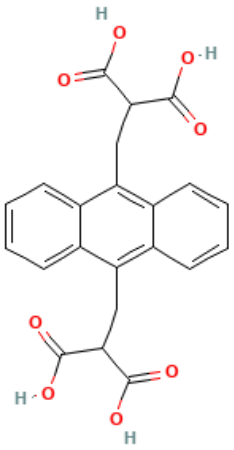

Fig. 5.1.2.1. Structure of ABDA (image source: PubChem; PubChem Identifier: 3458978; URL: https://pubchem.ncbi.nlm.nih.gov/compound/9_10-Anthracenediyl-bis_methylene_dimalonic-acid#section=2D-Structure).

C. 1,3-diphenylisobenzofuran (DPBF)

Another sensor that was tested due to its widespread use in singlet oxygen detection, including ultrasound-induced ROS studies, was DPBF. It is a diene (**Fig. 5.1.2.2**) that interacts with singlet oxygen, resulting in its transformation into a colourless substance 1,2-dibenzoylbenzene, which allows to optically quantify the presence of singlet oxygen. The fact that DPBF interacts with singlet oxygen was noticed around half a century ago[171], and it has been widely used as a singlet oxygen sensor since, making it well-established in the field.

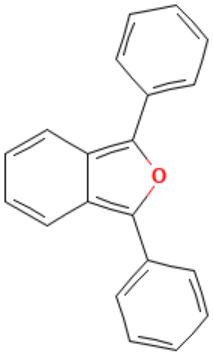

Fig. 5.1.2.2. Structure of DPBF (image source: PubChem; PubChem Identifier: 21649; URL: https://pubchem.ncbi.nlm.nih.gov/compound/1_3-Diphenylisobenzofuran#section=2D-Structure).

A notable shortcoming of DPBF is its poor water solubility, which makes it unsuitable for most biological applications. Attempts have been made to develop water-soluble derivatives of DPBF[172,173], but these do not seem to have been translated into widespread use.

D. Furfuryl alcohol (FFA)

Finally, ROS measurements were attempted in a non-optical way, in order to provide a different detection mechanism that is free of challenges associated with fluorescent sensors, via HPLC detection of FFA (**Fig. 5.1.2.3**). It is known that FFA reacts with singlet oxygen[174], and an HPLC protocol for its detection was developed for this project.

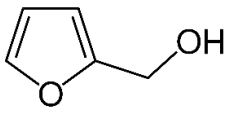

Fig. 5.1.2.3. Furfuryl alcohol structure (image source: Wikipedia.org).

5.1.3 Chapter overview and objectives

The goal of the present chapter was to perform ROS measurements after activating Rose Bengal and in particular to compare the ROS output between the light and ultrasound stimulation of the drug. Emphasis was placed on developing suitable and reliable protocols, and limitations of the current methods were discussed.

5.1.4 Attribution of work

The HPLC FFA protocol was developed by Dr Luca Bau and Dr Richard Browning, and HPLC measurements for the current project were performed by Dr Bau.

The green LED setup characterisation was performed by Victor Choi.

Preliminary work on the infrared detector setup was done in collaboration with Dr Shamit Shrivastava.

All other experimental and data processing work was performed by the author of this thesis.

5.2 Materials and methods

The materials and methods for microbubbles and other agent production and characterisation are described in detail in Chapter 2. The ultrasound setups description and characterisation is provided in Chapter 4.

5.2.1 Materials

Singlet Oxygen Sensor Green (special packaging) was purchased from Thermo Fisher Scientific (USA). Rose Bengal (95%) was purchased from Sigma-Aldrich (USA).

9,10-anthracenediyl-bis(methylene)dimalonic acid (ABDA) (90%) and 1,3-diphenylisobenzofuran (DPBF) (97%) and furfuryl alcohol (FFA) were purchased from Sigma-Aldrich (USA)

5.2.2 Ultrasound exposure setups

US exposures were performed in the SAT2 setup, which is described and characterised in Chapter 4. The experimental protocol was as follows:

Stock solutions of reagents were prepared in purified MilliQ water (Rose Bengal) and methanol (SOSG). RB stock was stored in the fridge between experiments; new SOSG stock was prepared for each day. DBPC-PEG40S PFB MBs were prepared on the day of experiments.

Experiments were performed in the dark. The sample solution (consisting of Rose Bengal, SOSG or other sensor and microbubbles in the DPBS buffer) was prepared in a vial, loaded into a syringe and introduced into the SonoLid sample holder (sample volume ~10mL). Then the sample holder was inserted into the SAT2 ultrasound setup, macroscopic air bubbles were removed from the sample holder and the PCD, and the sample was sonicated. A control was obtained by preparing

and loading the solution into a syringe and then applying manual pressure to burst microbubbles in the sample.

The sample (after sonication) or control solutions were then put into a black-walled 96-well plate with flat transparent bottoms, covered to avoid light exposure and measured by a FLUOstar plate reader (section 5.2.4).

If oxygenated MBs were used, they were oxygenated immediately prior to the experiment, and care was taken to conduct the measurements quickly and in a reproducible timeline.

For some experiments, an ultrasound water bath was used (Eumax US cleaner UD150SH-6L (150W, 40kHz)). For these experiments, samples were exposed in 2 mL plastic vials (Eppendorf Ltd, UK).

Another setup used for ultrasound experiments was a Sonidel SP100 transducer (1 MHz, 100 Hz PRF, with regulated duty cycle and power; SONIDEL limited, Ireland). For these experiments, a 96-well plate with black walls and a thin flat transparent bottom was used (Greiner Bio One Ltd, UK) and ultrasound gel (Anagel) was applied to connect the bottom of the plate and the ultrasound transducer.

All experiments were performed in the dark to avoid false positive Rose Bengal activation, and care was taken to avoid light exposure when transferring the samples from the setup to the plate reader or HPLC.

5.2.3 Light exposure setup

To perform light exposures, the following setup was used: a green LED (M565L3 – 565 nm, bandwidth 104 nm, 880 mW (Min), ThorLabs, USA), with the light passing through an excitation filter (MF559-34, TXRED, 559 nm, bandwidth 34 nm, ThorLabs, USA) and reflected from a dichroic mirror (MD588, CY3.5/TXRED, reflection band 533 – 580 nm, ThorLabs, USA).

As the light passed through a filter and a dichroic mirror (due to the geometry of the setup), the light intensity in the sample was lower than the output intensity of the LED. Light intensity was checked with a USB power meter (PM16-121, 400 – 1100 nm, 500 mW max, ThorLabs, USA).

5.2.4 Optical measurements

The fluorescence and absorbance spectra detection was performed with the FLUOstar OMEGA plate reader (BMG LABTECH, UK) in black-walled 96-well plates with flat transparent bottoms.

For SOSG (excitation peak 504 nm / emission peak 525 nm), the fluorescence filters used were 490 nm / 520 nm. The gain was adjusted so that the biggest value in the experiment was ~90% of the device maximum, and the gain was preferably left unchanged for a set of experiments; if the gain did have to be adjusted, the results were either all recalculated to the same gain or only compared as relative to the corresponding control.

For DPBF (excitation peak 410 nm / emission peak 455 nm), the fluorescence filters used were 410 nm / 455 nm.

For ABDA, absorbance spectra were measured. Fluorescence could also be measured (excitation peak 380 nm / emission peak 407 nm; fluorescence filters 340 nm / 410 nm).

5.2.5 HPLC measurements

For HPLC measurements, furfuryl alcohol (FFA) was used, in concentration 2.5 mM in final sample.

HPLC analyses were performed on an Agilent 1260 Infinity II (Agilent, USA) with spectrophotometric detection at 230 nm. An Atlantis T3 column (3 mm, 2.1 mm × 50 mm; Waters, USA) was used for chromatographic separation. The samples were eluted isocratically with a

mobile phase consisting of water and acetonitrile (98:2) with 0.1% formic acid at a flow rate of 0.5 mL/min and a temperature of 32°C over 3 minutes. The injection volume was 4 µL.

The measured signal was the area under the HPLC curve peak corresponding to the product of the reaction of FFA with singlet oxygen.

5.3 Measurement of Rose Bengal ROS production with optical sensors

5.3.1 Singlet Oxygen Sensor Green

The first measurements of Rose Bengal ROS production were performed with Singlet Oxygen Sensor Green (SOSG); this choice was dictated by its widespread use for singlet oxygen measurements in biological systems, as well as its previous use in our laboratory. Preliminary ultrasound parameters and reagent concentrations were also taken from previous optimisations of the RB/SOSG system[175].

The initial experiments were aimed at quantifying the ROS production with RB and oxygenated or non-oxygenated microbubbles, with the goal of assessing the MB-mediated oxygen delivery and its impact on the ROS production in this system, and in this way complementing the oxygen delivery mechanism studies described in Chapter 3. However, what was found was that MB oxygenation did not lead to the expected increase in ROS generation (Fig. 5.3.1.1 shows a representative experiment out of a number of runs that gave similar results). This prompted more detailed investigations into the components of this experiment.

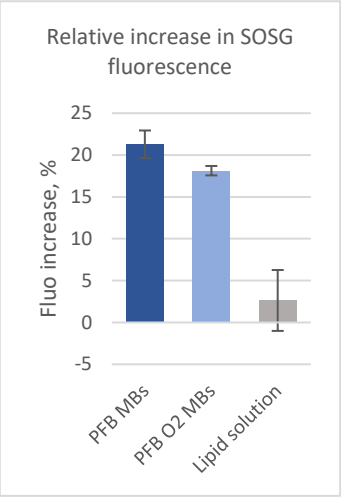

Fig. 5.3.1.1. Relative increase in SOSG fluorescence intensity for sonicated samples vs non-sonicated controls for samples of Rose Bengal and SOSG with: DBPC-PEG40S PFB MBs; oxygenated MBs (PFB O_2 MBs) and a lipid solution of DBPC and PEG40S in similar concentrations as used for producing MBs. Samples were diluted in DPBS (3 µM RB, 1.5 µM SOSG, $5*10^7$ MBs/mL or corresponding lipid concentration). Ultrasound exposure was performed in SAT2 (US parameters: 1 MHz, 0.7 MPa pk-pk spatial average, 30% duty cycle, 100 Hz pulse repetition frequency, time 30 sec). (n = 2, error bars represent standard deviations)

A number of troubleshooting investigations were carried out, optimising and revising various technical aspects of the experiment; none of them however answered the question of why additional doses of oxygen did not have a positive impact on SOSG fluorescence.

One of the issues explored was RB purity. Measurements were made comparing 90% purity Rose Bengal (which was used for the experiments in **5.3.1.1**) and 95% RB, in order to check whether the results were caused by insufficient drug purity. 90% and 95% RB were compared with HPLC, which did not show any notable differences (data not shown), as well as in several SOSG ultrasound exposure experiments (**Fig. 5.3.1.2**). Interestingly, these and some other experiments showed that Rose Bengal decreased SOSG fluorescence compared to SOSG alone, while it was expected to do the opposite. (There was no difference seen between 90% and 95% RB in this effect, and most further experiments used 95% RB.)

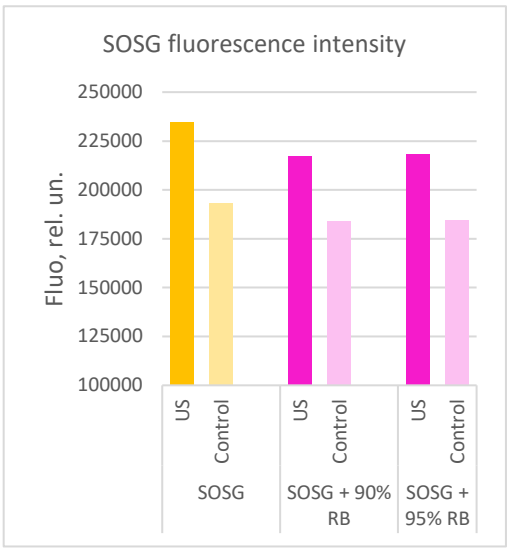

Fig. 5.3.1.2. Influence of Rose Bengal purity on SOSG ultrasound experiments: SOSG fluorescence for sonicated samples vs non-sonicated controls for SOSG without RB; SOSG + 90% RB and SOSG + 95% RB. All samples were diluted in DPBS and contained DBPC-PEG40S PFB MBs (~$5*10^7$ MBs/mL); reagent concentrations were 3 µM RB, 1.5 µM SOSG. Ultrasound exposure was performed in SAT2 (US parameters: 1 MHz, 1.4 MPa pk-pk, 30% duty cycle, 100 Hz pulse repetition frequency, time 30 sec).

The influence of the Rose Bengal concentration on the results was further explored, and it was confirmed that increasing RB concentration decreased both baseline SOSG concentration and its increase after sonication in a wide range of RB concentrations (representative experiment is shown on Fig. 5.3.1.3).

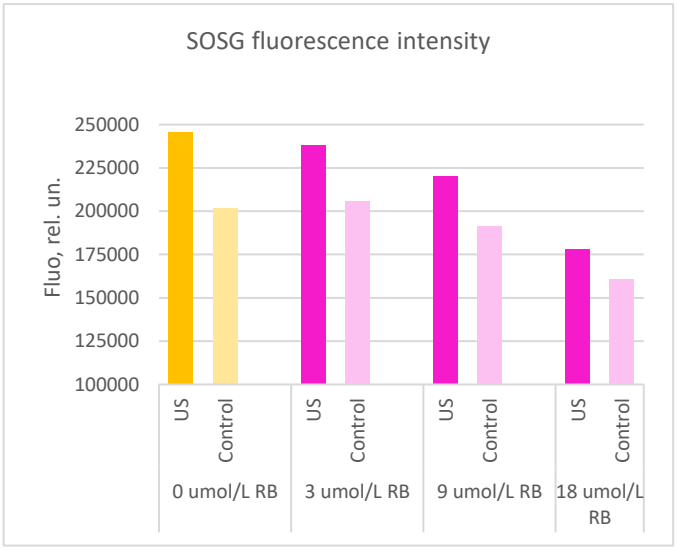

Fig. 5.3.1.3. SOSG fluorescence intensity for sonicated samples and non-sonicated controls with varying RB concentration: no RB, 3 uM, 9 µM and 18 µM. All samples were diluted in DPBS and had 1.5 µM SOSG and DBPC-PEG40S PFB MBs (~$5*10^7$ MBs/mL). Ultrasound exposure was performed in SAT2 (US parameters: 1 MHz, 1.4 MPa pk-pk, 30% duty cycle, 100 Hz pulse repetition frequency, time 60 sec).

The possible reasons for this were explored. One hypothesis was that the substantial overlap between the SOSG emission and RB absorbance spectra could lead to increasing RB concentration absorbing the SOSG emissions faster than the corresponding rise in ROS generation (SOSG emission peak 525 nm, RB absorbance peak 548 nm).

Some insight into this issue could be gained by comparing the ultrasound exposure results for RB with light exposure (**Fig. 5.3.1.4**). For this set of experiments, an ultrasound bath was used (40 kHz) in order to check whether a different ultrasound frequency would change the result; the time-dependence of signals was as expected, with SOSG fluorescence growing with ultrasound time, but the dependence on RB concentration was again not in agreement with theory. For the light experiments, on the other hand, both the dependence on light exposure duration and on RB concentration were positive as expected.

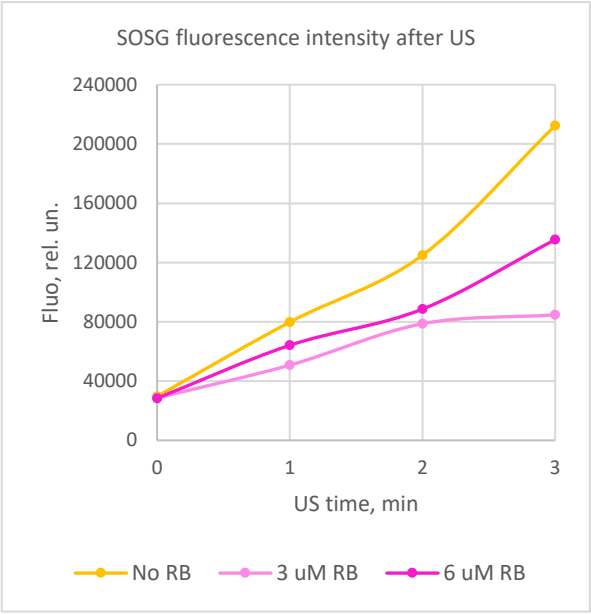

Fig. 5.3.1.4. SOSG fluorescence after a sample with RB was either sonicated or exposed to green light. Samples had 1.5 µM SOSG and varying concentrations of RB; sonicated samples had DBPC-PEG40S MBs (~$5*10^7$ MBs/mL), and for ultrasound t = 0 were ruptured manually in a syringe. In this experiment, sonication was performed in an ultrasound bath (150W, 40kHz) in 2 mL plastic tubes, and exposure to light was carried out as described in the Methods section. For the laser measurements, fluorescence gain setting was 1800, and for the sonicated samples it was 1450.

A similar result was obtained in a different ultrasound setup (Sonidel transducer with a 96-well plate) for the same samples (ultrasound parameters were 1 MHz, 50% duty cycle, 100 Hz PRF, 3.5 W/cm^2). This setup was less well-characterised than the SAT2 setup and had no PCD monitoring; therefore, similar to the ultrasound bath setup, it did not meet the good ultrasound experiment guidelines discussed in **Chapter 4**. Nonetheless, these experiments were carried out, in order to check whether the setup can explain the results seen with SOSG and RB, and to provide some comparison to the literature using ultrasound baths or 96-well-plate ultrasound setups for ROS experiments. However, similar results were seen in this setup, with added RB increasing SOSG fluorescence after exposure to light but not ultrasound (**Fig. 5.3.1.5**). Therefore, neither the specific ultrasound setup nor exposure parameters could have been responsible for this effect.

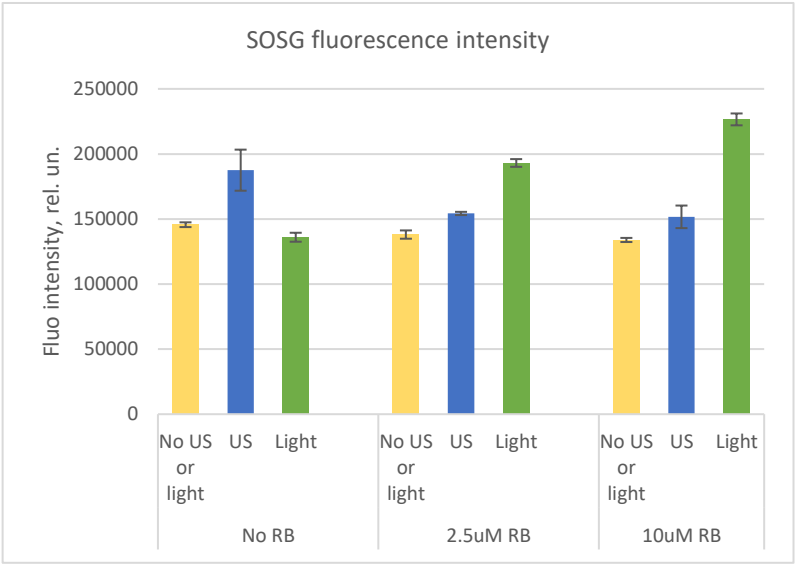

Fig. 5.3.1.5. SOSG fluorescence after exposure to ultrasound in a 96-well plate in Sonidel (1 MHz, 50% duty cycle, 100 Hz PRF, 3.5 W/cm^2, 2 min) or to light (2 min). All samples had 6 µM SOSG, DBPC-PEG40S PFB MBs (3*10^6/mL) and varying concentration of RB (no RB, 2.5 µM or 10 µM); for non-sonicated samples MBs were ruptured by applying manual pressure before the measurement. (n = 3, error bars represent standard deviations)

The spectral overlap also does not seem to explain the unexpected dependence of SOSG signal on RB concentration, since it would similarly affect the laser-exposure experiments. It should be noted that RB has a slightly shifted spectra in the presence of lipids or microbubbles[176]; however, it does not appear to be sufficient to explain why the light and ultrasound exposure results behave so differently.

5.3.2 Optical measurements of ROS with ABDA and DPBF

In order to attempt to explain the decreasing SOSG fluorescence with increasing RB concentration, other ROS sensors were tested.

One of them was 9,10-anthracenediyl-bis(methylene)dimalonic acid (ABDA). It is a water-soluble sensor that allows to detect singlet oxygen by measuring its absorbance spectrum, which bypasses

some problems associated with fluorescence, and has no spectral overlap with Rose Bengal (see Fig. 5.3.2.1). However, absorbance detection is often less sensitive than fluorescence methods, and in the case of ABDA preliminary experiments showed that its sensitivity was insufficient for the amounts of ROS produced in typical ultrasound experiments (Fig. 5.3.2.1 shows a representative experiment, where no difference was seen in ABDA spectra between sonicated and non-sonicated samples within the limits of experimental error).

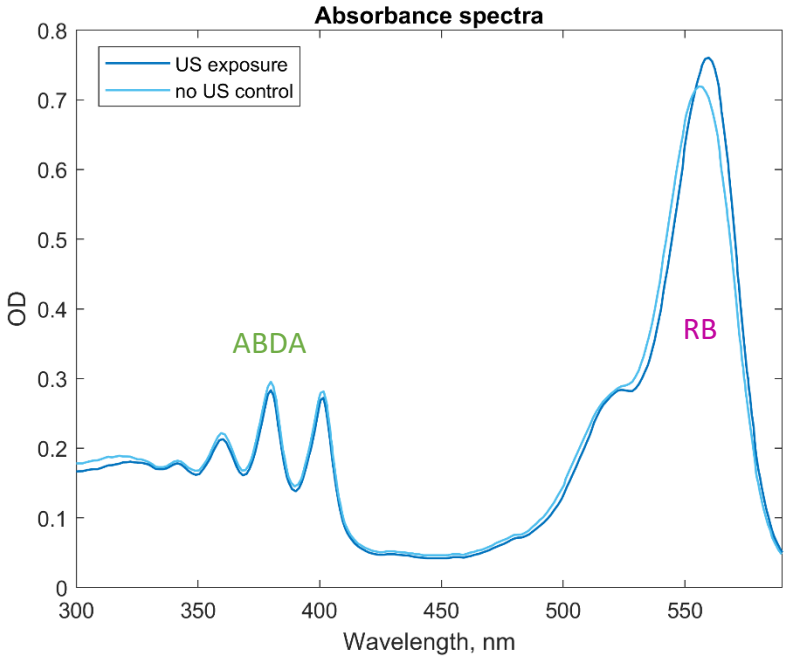

Fig. 5.3.2.1. Representative experiment of absorbance spectra of a solution of 10 µM RB, 30 µM ABDA and DBPC-PEG40S MBs after ultrasound (3 min in SAT2, 1 MHz, 1.4 MPa pk-pk, 30 % duty cycle, 100 Hz pulse repetition frequency) compared to a non-sonicated control (MBs ruptured by hand).

Another sensor that was tested was 1,3-diphenylisobenzofuran (DPBF). It is a popular and well-studies singlet oxygen sensor, but it has a major limitation of poor water solubility. Initial experiments were carried out in the hope that a suitable buffer could be found for both DPBF and

lipid microbubbles; however, it was found that DPBF is soluble in 100% and 50% ethanol, but not 30% ethanol, making a biologically-compatible buffer not feasible. Attempts to use DPBF in aqueous buffers did not lead to any meaningful results.

5.3.3 HPLC measurements of ROS with FFA

As optical measurements of ROS proved to have some technical challenges, an alternative protocol was developed by members of the group using furfuryl alcohol (FFA) as an HPLC singlet oxygen sensor.

Measurements of Rose Bengal ROS production were performed after exposing the sample to ultrasound in the SAT2 setup (1 MHz) (**Fig. 5.3.3.1**) or the ultrasound water bath (40 kHz) (**Fig. 5.3.3.2**) and compared to the same samples activated optically by a green LED.

Interestingly, the results seen with RB and SOSG (with increasing RB concentration leading to the decreased sensor signal) were not seen in these experiments: increasing RB concentration led to a small but significant increase in the FFA signal (see **Fig. 5.3.3.2**), which is encouraging from the point of view of the reliability of FFA as a Rose Bengal-compatible ROS sensor.

However, it was also seen consistently across several experiments and ultrasound setups that the amounts of ROS generated with ultrasound were small compared to the same time of exposure to light. In the SAT experiments, a small rise in FFA signal was seen with increasing ultrasound time (although it was still smaller than the light control) (**Fig. 5.3.3.1**); for the ultrasound bath experiments, no significant rise in FFA signal was seen with increasing ultrasound time, while the signal rose in a linear manner with increasing time of light exposure (**Fig. 5.3.3.2**).

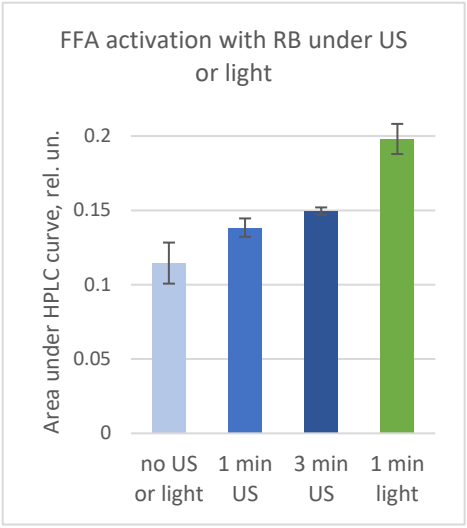

Fig. 5.3.3.1. Detection of the product of reaction of FFA with singlet oxygen using HPLC. The samples (prepared in DPBS) contained 2.5 mM FFA and 2.5 µM RB; ultrasound samples contained DBPC-PEG40S PFB MBs (~$2*10^7$/mL), and MBs in non-sonicated controls were ruptured by applying manual pressure; sonication was performed in SAT2 (1 MHs, 1 MPa pk-pk, 30% duty cycle, 100 Hz PRF), and light exposure was done with a green LED (see Methods) (n = 3, error bars represent standard deviations).

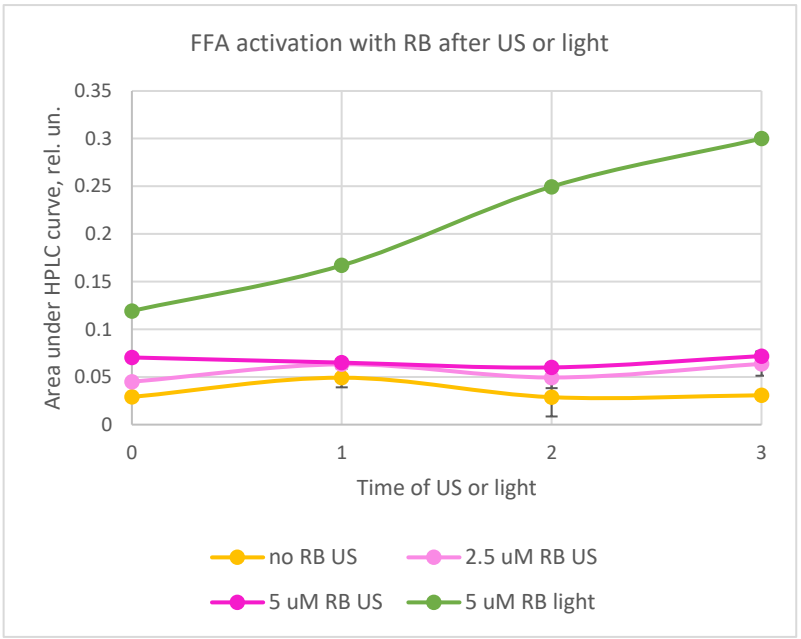

Fig. 5.3.3.2. Detection of the product of reaction of FFA with singlet oxygen using HPLC. The samples (prepared in DPBS) contained 2.5 mM FFA, varying concentration of RB (no RB, 2.5 µM or 5 µM); ultrasound samples contained DBPC-PEG40S PFB MBs (~$2*10^7$/mL), and MBs in non-sonicated controls were ruptured by applying manual pressure; sonication was performed in an ultrasound bath (40 kHz) in 2 mL vials, and light exposure was done with a green LED (see Methods) (n = 3 for ultrasound samples and n = 1 for light; each sample was measured at 4 timepoints by taking 50 uL for HPLC measurement and continuing light or ultrasound exposure, error bars represent standard deviations).

5.4 Summary and conclusions

Measurements of reactive oxygen species produced with Rose Bengal were obtained after exposure to ultrasound and light. Several ROS sensors were tested for this purpose (SOSG, ABDA and DPBF), but all presented challenges that made reliable measurements impossible. The most notable of these was SOSG, as it was used for ROS measurements of light-activated RB both in the literature and in the presented project, but did not function as expected for ultrasound-activated RB.

A different sensor (FFA) that did not require the use of direct optical measurements was then used for RB ROS detection. The results obtained with FFA corresponded to theoretical expectations in terms of the increase of produced ROS with increasing RB concentration; however, the amount of ROS produced by both 1 MHz and 40 kHz ultrasound was much smaller than for the same samples after exposure to green light, which is especially important as the green light intensity was much lower than typical therapeutic values.

The experiments presented in this chapter underline, firstly, the technical difficulties associated with ultrasound-induced reactive oxygen species and the need for careful design of control experiments; and, secondly, the difference between the quantities of ROS generated by ultrasound and light activation, as measured with FFA for several ultrasound setups and sets of ultrasound parameters.

Future work

The Rose Bengal studies presented in this project mostly focused on singlet oxygen quantification, as this is the ROS associated with photoactivation of RB. However, some studies suggested that

other ROS may be involved in ultrasound-induced activation of RB. It is clear that a more detailed investigation of this issue is needed.

In particular, it would be of interest to conduct a thorough investigation of ROS production by ultrasound and light for a number of drugs with ROS sensors that detect different ROS classes and comparing whether the ROS profiles are similar for photo- and ultrasound-induced activation. A number of papers in the literature have attempted investigations into ROS classes produced by some drugs; however, these studies are difficult to compare directly due to the fact that they use different drugs and ultrasound parameters and setups. In the discussions in these studies, when comparisons to other SDT studies are drawn, there tends to be an implied suggestion that ROS mechanisms are the same across all of the SDT field regardless of specific parameters. This suggestion, however, requires validation and having a comprehensive dataset comparing ROS production under the same conditions would be of great value when attempting to draw conclusions on drug activation/action and whether there is indeed one overarching mechanism.

Regardless of the findings from such an experiment, there remain further questions. If the ROS classes are found to be different for photo- and sonoactivation of the same drug, a molecular-level mechanism explanation will be required. If the ROS classes are the same, an explanation would be needed as to how the relatively small amounts of ROS seen in several studies correspond to the comparable cell death seen with the same drugs in PDT and SDT; the latter question is the subject of Chapter 6.

Another issue underlined in this chapter is the difficulties associated with optical ROS sensors, especially in complex solutions. One way to overcome this problem is detecting ROS directly by their optical emissions; for example, this is possible for singlet oxygen in the infrared range. Such setups were reported in the literature, including for the purposes of quantifying PDT ROS generation[177]. In the current project, an attempt was made to construct such a setup using an

infrared detector module (C12483-250, ThorLabs, USA); however, preliminary experiments found that the setup sensitivity required significant optimisation in order to be useful for ultrasound experiments. As it was found in FFA studies that the ROS levels generated by typical ultrasound parameters were much lower than those seen in light exposures, the IR setup optimisation was decided to be a complex task that is outside of the scope of the current project, and it would be an interesting direction for future work, as measurements seen in the literature for IR singlet oxygen detection are usually done for light and not ultrasound-mediated excitation of drugs.

Chapter 6. Sonoporation hypothesis of sonodynamic therapy mechanism

6.1 Introduction

6.1.1 Issue of SDT mechanism

As discussed in the Chapter 5, there is still no consensus on the ROS types produced by sonosensitive drugs during sonodynamic therapy (SDT), which is caused by various factors, including the technical difficulties of ROS sensing and the broad range of ultrasound parameters used in therapeutic ultrasound studies.

Aside from the question of ROS types, another issue is their quantity. As seen above in the experiments with FFA, as well as in other recent observations (personal communication Victor Choi), the amounts of ROS produced by drugs activated with ultrasound compared to light is low when the ultrasound and light parameters are comparable to those used in therapeutic ultrasound and PDT respectively. However, there is ample evidence that a combination of certain drugs and ultrasound can kill cells *in vitro* and slow down tumour growth *in vivo*[93]. A question that stems from these observations leads back to the discussion of the mechanisms of SDT: if the amounts of ROS produced appear to be much lower than for PDT, then the cell kill mechanisms of SDT must somehow differ from PDT to explain the comparable cell kill rates[90].

Some solutions have been proposed in the literature. One proposal is that the ultrasound effect is mediated via immune system modulation. However, while ultrasound has indeed been explored for the purposes of immunotherapy[178] and has some potential in this area, in order to explain the *in vivo* results better understanding of the interaction of SDT drugs with these processes is needed. Moreover, immunomodulation is not a viable explanation for the reported in vitro results.

It is important to highlight that there are a number of effects associated with ultrasound that are not usually discussed in the context of SDT. These include enhanced drug extravasation and sonoporation, which can be reversible (with possible intracellular delivery of the drug) and irreversible, resulting in cell death. In the SDT literature, enhanced extravasation is sometimes mentioned as a factor that (independently from the main mechanism) improves the SDT-induced effects, and ultrasound-induced cell killing is also discussed as a separate enhancing factor. These effects are, however, not seen as essential for SDT success. Here it is proposed that this separation should be questioned, as it is difficult experimentally to separate the ultrasound-induced activation of the drug from other ultrasound-induced processes, such as sonoporation.

6.1.2 Sonoporation hypothesis of SDT mechanism

It is hypothesised that sonoporation plays a key part in SDT by enabling the drugs to enter the cells so that they may produce toxic effects at concentrations that extracellularly would be harmless. Cell death may be due to ROS production, or through other mechanisms that are independent of ultrasound-mediated activation.

Controlling for the role of sonoporation during SDT experiments is challenging and requires careful experiment design. In most published studies of SDT, the selected experimental groups do not allow for the contribution of sonoporation to be assessed. Interestingly, this means that the hypothesis above (referred to hereafter as the sonoporation hypothesis) does not contradict the existing literature, rather it provides a possible explanation for the discrepancy in ROS generation between SDT and PDT.

In order to test this hypothesis, experiments were designed in order to attempt to pry apart sonoporation-induced drug internalisation by cells and ultrasound-induced drug activation. This was done by introducing the drug either during ultrasound exposure or at various timepoints

afterwards. Microscopy was performed to directly observe drug uptake by cells and to assess the number of cells dying as the result of treatment.

The same drug that was used in Chapter 5 – Rose Bengal – was used in the studies described in this chapter. Several different cell lines were tested, as cell lines may have substantially different survival rates and sonoporation window lengths when exposed to ultrasound.

6.1.3 Chapter overview and objectives

The aims of this chapter were:

- to develop protocols for cell work, including ultrasound exposures, identification of live/dead and sonoporated cells and microscopy;
- to verify the reliability of these protocols, in particular the accurate assessment of live, dead and sonoporated cells;
- to assess sonoporation efficiency and time windows for several cell lines;
- to determine whether Rose Bengal enters the cells if introduced after the ultrasound exposure and compare the cell death rates for RB added at different time points of the experiment;
- to use the data to test the sonoporation hypothesis.

6.1.4 Attribution of work

In the preliminary experiments, the cell culture and microscopy was performed by Veerle Brans, and MB preparation and ultrasound exposures were done by the thesis author.

In the subsequent experiments, the cell culture (for HeLa and A549 cells) and microscopy was performed by Kritika Singh, and MB preparation and ultrasound exposures were done by the thesis author. Cell culture for GFP VE cells was done by Olive Jung.

All other experimental and data processing work was performed by the author of this thesis.

6.2 Materials and methods

The materials and methods for microbubble and other agent production and characterisation are described in detail in Chapter 2. The description of the ultrasound setups and characterisation is provided in Chapter 4.

6.2.1 Materials

Cell-compatible dishes for ultrasound experiments (μ-dish, 35 mm, high) were obtained from Thistle Scientific (UK).

Calcein AM, Cell Mask Deep Red and DMEM media were purchased from Thermo Fisher Scientific (USA).

6.2.2 Cell culture

HeLa (cervical cancer cells) and A549 (adenocarcinomic human alveolar basal epithelial cells) cell lines were routinely cultured in DMEM supplemented with 10% FBS. HeLa and A549 cell lines were obtained through collaborations and originally were purchased from ATCC. All cell lines were used within 15 passages of their initial freeze down.

GFP-tagged VE (vascular endothelial) Cadherin brain microvascular endothelial cells were thawed and plated directly onto either T-75 or coverslips that have been pre-treated with the QuickCoating solution. The media was usually changed every other day, and the components in the basal media were 5 ng/ml rhFGF, 50 ug/ml ascorbic acid, 1 ug/ml hydrocortisone, 10 mM L-glutamine, 15 ng/ml rh IGF-1, 5 ng/ml rhVEGF, 0.75 U/ml heparin sulphate and 2% FBS.

6.2.3 Ultrasound exposures

Preliminary experiments were performed on the SAT2 setup, but the setup used for the majority of ultrasound exposures in this chapter was SAT2E (see Chapter 4). Briefly, it is a modified version of the SAT2 setup that has sufficient homogeneity of the pressure field in the sample plane (the central area with a diameter of 5 mm has a standard deviation in the peak negative pressure of less than 10%). All pressures shown in this chapter were calculated as spatial averages for this central area, and cell imaging was only performed within this region.

For both set ups, the sample was prepared and loaded with a syringe into the sample holder comprising the cell dish with a PDMS lid (SonoLid) and sealed. The sample holder was oriented with the cell dish facing upwards and inserted into the ultrasound setup; importantly, there was a pause of 1 min between inserting the sample and performing the sonication, in order to allow for microbubbles to float and come into contact with the cell layer.

6.2.4 Microscopy

Preliminary experiments were carried out in the SAT2 and imaging performed using either a confocal microscope (Zeiss LSM 780, ZEISS, Germany) or Nikon microscope (Nikon ECLIPSE Ti, Nikon Instruments Inc., USA). The imaging region was not confined to the central area in this case.

For the other experiments shown here, only the Nikon microscope was used. The images were taken in the central 5 mm diameter area.

6.2.5 Imaging cell death and sonoporation

For the purposes of these experiments, it was important to distinguish between cell death and reversible sonoporation. For most other applications, the lack of integrity of the cellular membrane indicates cell death, and therefore some of the most popular cell death markers, such as propidium iodide (PI), mark the cells which they are able to enter. This is notably different however for the field of ultrasound: PI can only be used as a marker of sonoporated cells (reversibly or otherwise), and an additional marker is needed to distinguish between cells that are dead and those that are alive. In this study, we used Calcein AM (CAM) in combination with PI, where CAM marked metabolically active (and therefore alive) cells, and PI marked sonoporated cells (dead or alive), using as a basis a protocol developed previously in our group and then correcting it for more appropriate reagent usage.

6.2.5.1 Preliminary experiments (SAT2)

The steps of the preliminary experiments shown in this chapter were as follows:

- Cell staining with Cell Mask Green; wash cells with buffer (2 times)
- Cell dish was closed with PDMS lid (SonoLid) and sample was loaded into it (RB and MBs for no ultrasound and RB before ultrasound samples, only MBs for RB after ultrasound samples)
- Sample holder inserted into SAT2 setup, cell dish facing up, and MBs were allowed to rise for at least 30 seconds
- US sonication (30 sec)
- Wash cells with buffer (2 times)
- For RB after ultrasound sample, 1 min of incubation with RB, followed by wash (2 times)
- Incubation to allow for reversible sonoporation to close (10-30 mins in DPBS)
- Incubation with PI, followed by washing and microscopy (CAM imaging was not done for these experiments)

6.2.5.2 Final experiments (with calcein AM, SAT2E)

The timeline for the final experiments was as follows:

- Cells incubated 5 min with Cell Mask Deep Red (CMDR)
- Wash with buffer (2 times)
- Cell dish put into the SonoLid
- Pre-made sample solution in DPBS is filled into the sample holder
    - For the sample with RB added before ultrasound: DBPC-PEG40S MBs (~$8*10^6$/mL and RB (5 uM)
    - For the sample with RB added after ultrasound: DBPC-PEG40S MBs (~$8*10^6$/mL)
    - For PI ultrasound controls: DBPC-PEG40S MBs (~$8*10^6$/mL) and PI (4 ug/mL)
- SonoLid with the sample (cell side up) inserted into the SAT2E, major bubbles are removed
- 1 min pause to allow for MB flotation
- US exposure
- Cell dish is taken out
- Wash with buffer (2 times)
    - For the sample with RB added right after ultrasound, a RB solution is added to the sample (5 µM in DPBS) for 1 min and the sample is washed 2 more times
    - For the sample with RB added 20 min after ultrasound, cells are incubated in cell media for 20 mins, then a RB solution is added to the sample (5 µM in DPBS) for 1 min and the sample is washed 2 more times
- 10 minutes incubation with CAM (5 µM in DPBS)
- Wash with buffer (2 times)
- 10 minutes incubation in cell media
- Wash with buffer (2 times)
- Microscopy (in DPBS)

Note that this is the protocol for the final set of experiments, and the details of the protocols of some of the presented experiments differed in some details (if there were differences to this protocol, they are pointed out in the relevant results).

Care was taken to do the washing step gently in order to avoid cell damage or detachment. For the A549 cells, the cell layer was always kept in the buffer or media, and its contact with air was minimised. For incubations longer than 5 mins the cell dishes were kept in a cell incubator at 37°C.

An overview of experimentally relevant details for the chemicals and agents used is presented in Table 6.2.5.2.1.

	Stock	Dilution in sample	Nikon channel	Notes
Calcein AM (CAM)	1 mg/mL (approx. 1 mM) In DMSO	5 uL / 1 mL (to 5 uM)	FITC	- To be used in buffer or serum-free medium - Incubation in cell medium required after CAM to avoid false positives
Propidium Iodide (PI)	1 mg/mL in mQ	4 uL / 1 mL	TRITC (RB overlap)	- Potentially toxic intracellularly (see Results)
Cell Mask Deep Red (CMDR)	In DMSO	1 uL / 1 mL	Cy5	- Cell Mask Blue was attempted, but did not function as expected
Rose Bengal (RB)	1 mM in mQ	5 uL / 1 mL (currently)	TRITC (PI overlap)	- Rapid bleaching and potential activation under microscope light, which has to be accounted for in experiment design
Microbubbles (MBs)	DBPC-PEG40S PFB in DPBS, around 1.4*10^9/mL	35 uL / 10 mL for ~8*10^6/mL		- Concentration adjusted for each batch - MB fraction transferred into a clean vial before experiments (to remove macroscopic foam)

Table 6.2.5.2.1. Experimental protocol details for the used chemicals and agents: concentrations and buffers in stock and in sample, Nikon microscope imaging channel and notes on usage.

6.2.5.3 Cell image processing

The image processing shown in this chapter was performed with Fiji[179], which is an open source image processing package based on ImageJ. Image contrast was automatically adjusted for cell

counting (as the fluorophore intensity was not quantified, the contrast enhancement was also not quantified and was only used for the purposes of cell counting). As some of the cell lines did not grow in a strictly monolayer fashion, they presented a challenge for automated cell counting, and therefore for the purpose of this thesis cell counting was performed manually.

For the cell counting processing, the counts for CAM-positive, PI-positive or total cells were summed for all microscopy fields of view (FOVs) for each sample.

For A549 and GFP-VE cells, % of alive cells was calculated as % of CAM-positive cells relative to total cells for each sample, and the % of dead cells was calculated as % of CAM-negative cells. HeLa cells detach easily after death, and therefore it was impossible to use the same field of view to calculate total cells; for this reason, total cells count was calculated as average for n = 3 non-sonicated controls, and % of alive cells was calculated as % of CAM-positive cells for each sample relative to this average total cell number in non-sonicated control, all normalised by the number of microscopy FOVs; % of dead cells was estimated as the % of alive cells calculated in this manner subtracted from 100%.

6.3 Preliminary experiments

6.3.1 Experiments and results

In order to test the sonoporation hypothesis, some preliminary experiments were carried out using the SAT2 and A549 cells, with Rose Bengal (RB) added before, immediately after or at different time points after ultrasound exposure to determine the effect on cell internalisation. Propidium iodide (PI) was added 10-30 mins after the ultrasound exposure, on the assumption that this time would be sufficient for resealing of the cell membrane and that PI would therefore serve as a cell death marker.

The results of this experiment are presented in Figs. 6.3.1.1-3. A sample with added RB but no ultrasound exposure showed little cell death, as marked by PI, and no RB internalisation by cells. Samples with RB added before or immediately after the sonication, interestingly, showed qualitatively similar rates of RB internalisation. Quantitative cell counting was not performed for these experiments, since the highly non-homogenous ultrasound field in SAT2 means that cells in different images were subjected to different pressures and should not be compared; this issue was solved in the final experiments.

Almost all cells with internalised RB were also positive for PI. This suggests that, if PI is a reliable cell death marker, then the cell kill rate for intracellular RB was almost 100%. The question remains as to whether RB caused cell death, or only entered irreversibly sonoporated cells and this was studied in further experiments.

One practical issue for imaging RB and PI is their spectral overlap. On the confocal microscope used in these experiments, RB and PI could be separated into two optical channels, but still showed substantial cross-talk. They could, however, be easily distinguished by their localisation in the cell in addition to the optical channel, as RB was seen in the cytoplasm and PI was bound in the nucleus.

Fig. 6.3.1.2 shows an example picture of cells with RB but no PI present; Fig. 6.3.1.3 represents the different optical channels for a sample of cells with both RB and PI present.

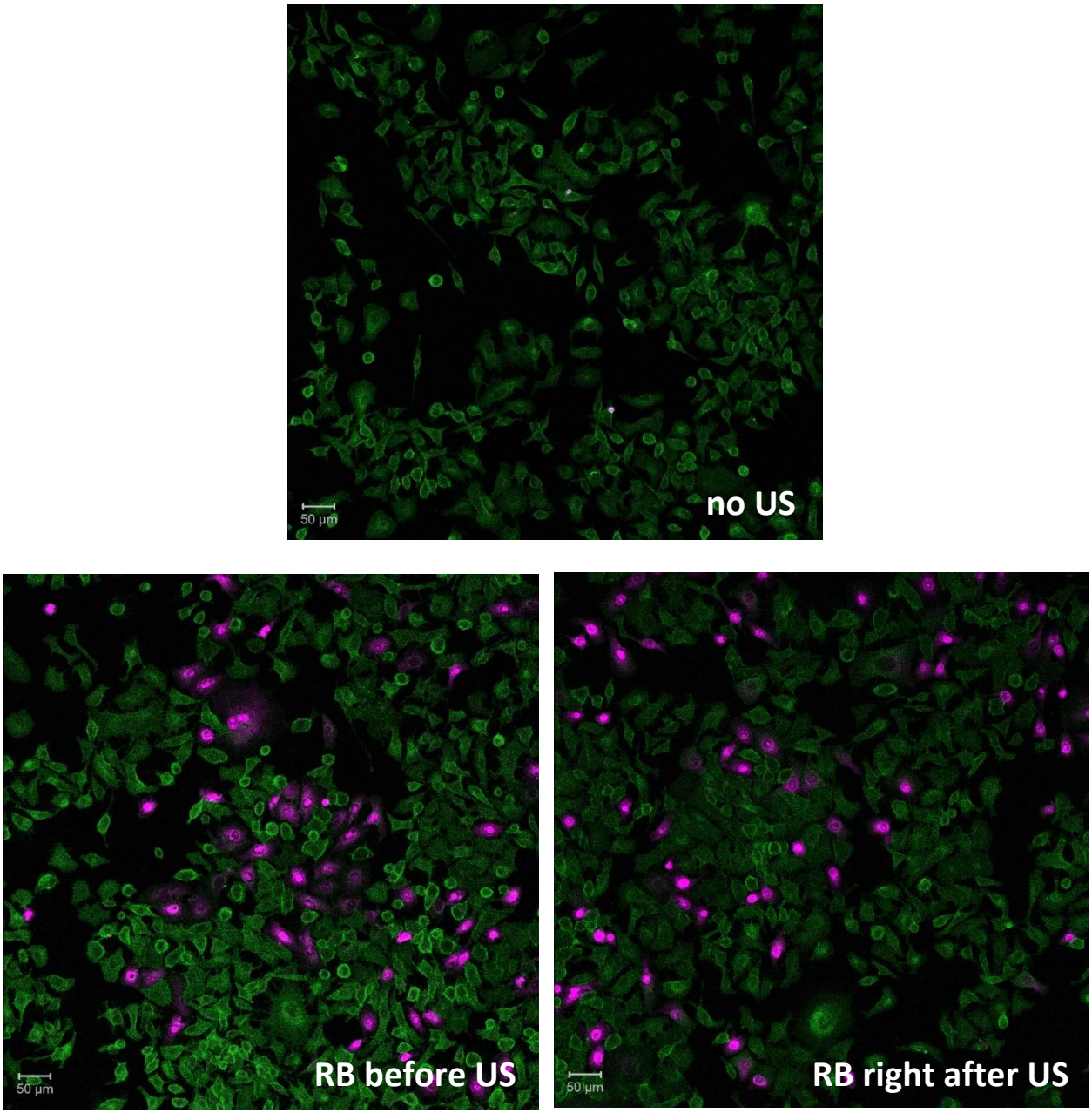

Fig. 6.3.1.1. Results of an experiment with Rose Bengal (RB) added either before or immediately after ultrasound, with a no ultrasound control. Sonication was performed in SAT2 (250 kPa pk-pk spatial average over the cell dish surface, 30% duty cycle, 10 Hz PRF, 30 sec). Reagent concentrations were 5 µM RB and $7*10^6$ MBs/mL (DBPC-PEG40S PFB MBs); no ultrasound controls were handled in the same way as sonicated samples, with adding RB and MBs, but without ultrasound exposure. No CAM imaging was done in these experiments; PI was added 10 to 30 minutes after ultrasound. Colours indicate: green – cell stain (Cell Mask Green), purple – Rose

Bengal (and PI due to spectral overlap). n = 2 independent repeats for each sample (no ultrasound, RB before ultrasound, RB after ultrasound), images show representative microscopy results. Images courtesy of Veerle Brans.

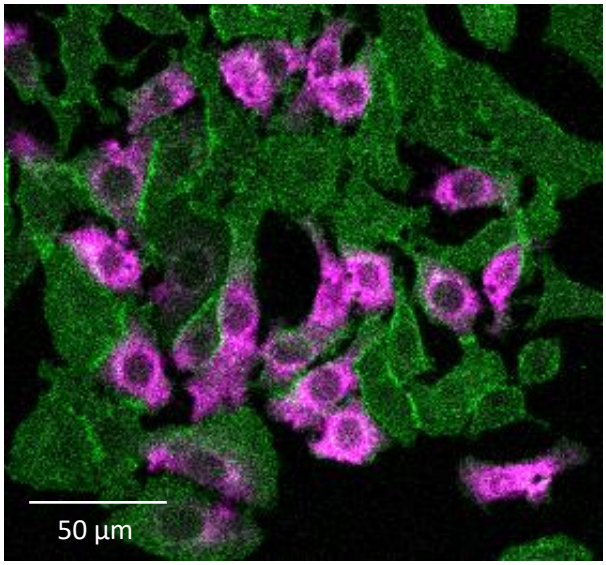

Fig. 6.3.1.2. Representative image of Rose Bengal distribution in A549 cells after the cells were exposed to ultrasound in the presence of RB (no PI present in this sample; green colour represents Cell Mask Green, purple - RB). Images courtesy of Veerle Brans.

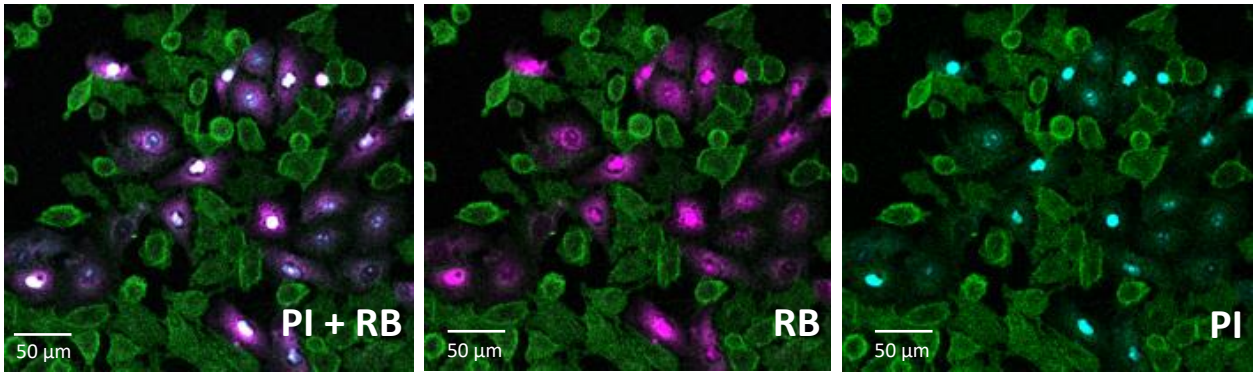

Fig. 6.3.1.3. Representative image of Rose Bengal and PI distribution in A549 cells after the cells were exposed to ultrasound in the presence of RB, with PI added 30 mins after ultrasound exposure (green colour represents Cell Mask Green, purple – Rose Bengal, cyan – PI). Images show optical channels for RB and PI merged, as well as separately RB and PI channels. Images courtesy of Veerle Brans.

6.4 Final experiments (with CAM in SAT2E)

6.4.1 Rationale and design considerations

The preliminary experiments described in section 6.3 brought promising results, showing that RB is efficiently internalised by cells with comparable efficiency if introduced during or right after sonication, and almost all of the RB-containing cells also internalise PI that was introduced 10 to 30 minutes after the sonication, which was hypothesized to be outside of the cell sonoporation window.

While this shows that drug uptake after sonication is still efficient and seems to correlate to cell death, there were still a number of questions remaining. Firstly, the cause and effect issue: did Rose Bengal cause cell death, or did it enter irreversibly sonoporated cells killed by ultrasound exposure? Secondly, can the PI-marked cells be reliably considered dead, or should another marker be introduced to verify cell viability? And finally, what is the time window of reversible sonoporation resealing and the fraction of reversible vs irreversible sonoporation?

To address these issues and to perform quantitative measurements, a new set of experiments in an improved ultrasound setup was conducted.

The setup used for current experiments was SAT2E (see Chapter 4), which is similar to SAT2 but provides a sufficiently large region of homogenous pressure field in the sample plane (standard deviation < 10%); this region was used to calculate the spatial-average pressures in the experiments and to acquire the microscopy images.

Adjustments were also made to the protocol. As opposed to using PI as a cell death marker after the reversible sonoporation window is expected to close, PI was used as a sonoporation marker and added to some of the samples during ultrasound exposure. To distinguish between reversible

and irreversible sonoporation, calcein AM (CAM) was introduced, which exhibits fluorescence in metabolically active cells; presence of CAM was therefore interpreted as a live cell, and its absence in a cell marked by Cell Mask was interpreted as a dead cell. The initial hypothesis was that, for samples with PI added during ultrasound and CAM added right after, cells that contain CAM but not PI were not sonoporated; cells that contain CAM and PI are reversibly sonoporated; and cells that contain PI but not CAM are irreversibly sonoporated.

The results of the initial experiments showed, however, that PI itself may be toxic when it enters the cell, therefore making it unsuitable for the marking of reversibly sonoporated cells. In all the experiments reported in this chapter, only a vanishingly small number of cells exhibited both PI and CAM fluorescence, with almost 100% of cells being either PI-positive or CAM-positive only. This was surprising, since PI is widely used in sonoporation studies as a marker of permeabilization. Further experiments are ongoing to confirm the intracellular PI toxicity; but for the purposes of the results shown in this chapter, PI-positive cells were interpreted as sonoporated, without making the distinction of whether they were reversibly or irreversibly sonoporated, as this conclusion does not depend on PI toxicity.

6.4.2 Note on the use of CAM

Initial experiments were carried out with the CAM imaging performed after a 5 minute incubation of cells with CAM in DPBS, in accordance with previously published protocols. However, it was found that most of the PI-positive cells exhibited positive but weak CAM fluorescence (see for example cells marked with yellow dashed rectangle in Fig. 6.4.2.1). This raised the question as to whether these cells were alive but metabolically less active due to the sonoporation, or dead but exhibiting some residual signal.

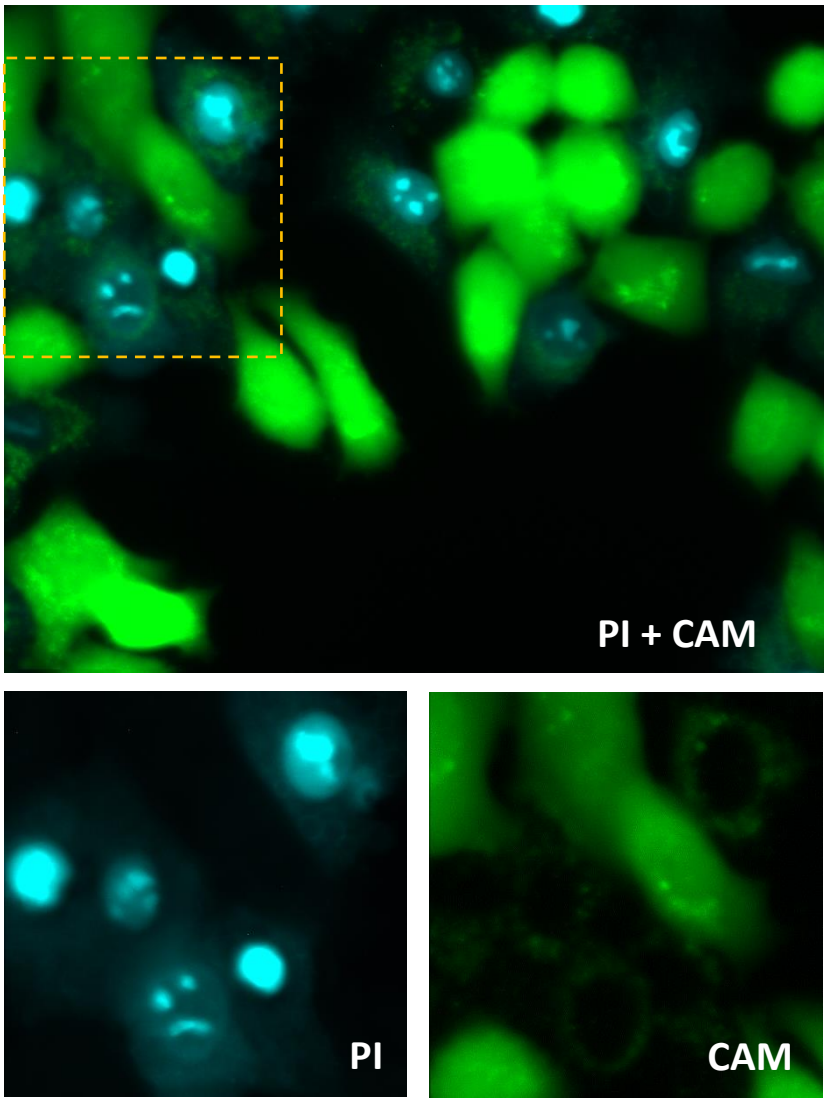

Fig. 6.4.2.1. Example of CAM and PI experiment **without** media incubation after CAM: A549 cells sonicated with PI and MBs (~5*10^6/mL MBs, ultrasound parameters: 250 kPa pk-pk, 30% duty cycle, 100 Hz PRF, 30 sec), washed and incubated for 5 mins in DPBS with CAM, with no subsequent media incubation. Green indicates CAM, cyan – PI, no cell mask shown; close-ups of the sector indicated with yellow dashed lines (approximately 70x70 µm) show PI and CAM channels separately. Images courtesy of Kritika Singh, processed by the thesis author.

The CAM imaging protocol was therefore adjusted to include 10 minutes of cells incubation with CAM in DPBS, followed by subsequent washing and a further 10 minutes of incubation without CAM in cell media, in order for the cells to either recover, or loose the residual CAM fluorescence if they were dead. The results showed that this new protocol vastly reduced or removed fully the

weak CAM fluorescence seen around many PI-positive cells, leading to the conclusion that residual CAM fluorescence should not be counted as a marker of alive cells in this experiment, and that post-CAM incubation is needed for cleaner CAM results, which was corrected correspondingly in the final protocol. Some cells still exhibited weak fluorescence in the CAM channel, which is possibly due to cell autofluorescence[180].

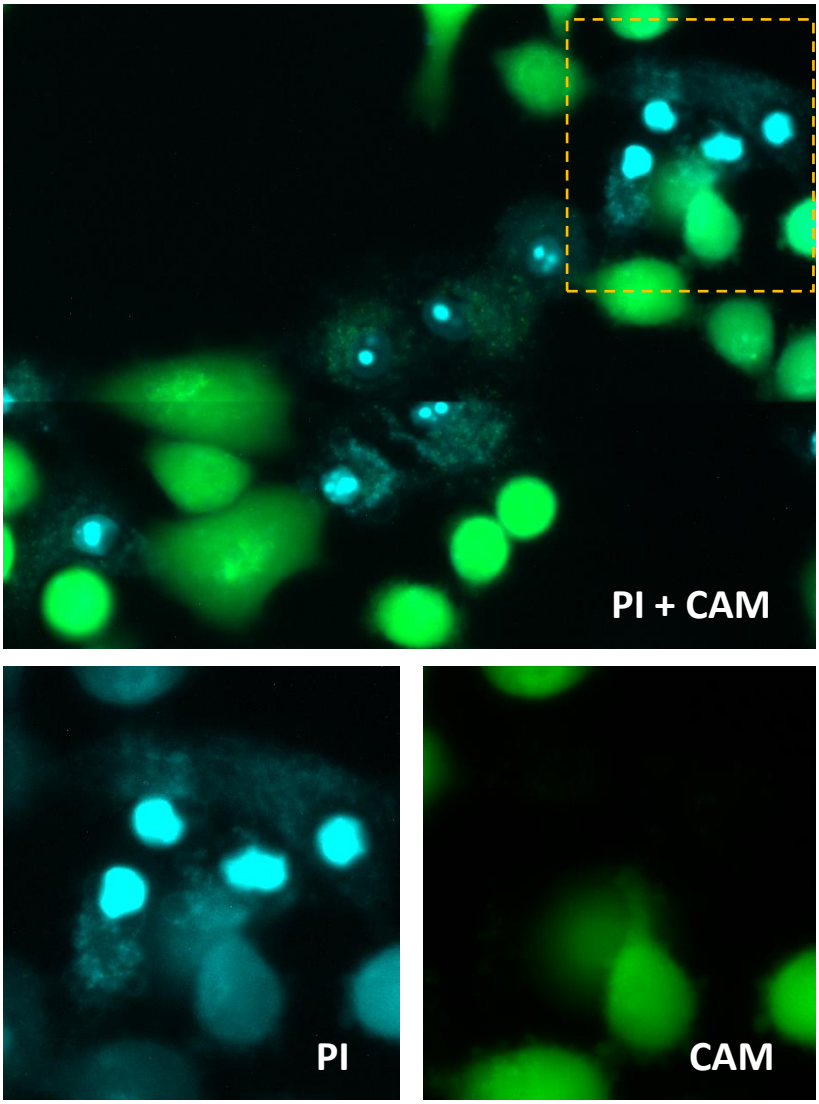

Fig. 6.4.2.2. Example of CAM and PI experiment with media incubation after CAM: A549 cells sonicated with PI and MBs ($8*10^6$/mL MBs, ultrasound parameters: 250 kPa pk-pk, 30% duty cycle, 100 Hz PRF, 30 sec), washed and incubated for 10 mins in DPBS with CAM, washed and incubated for 10 mins in cell media (see Methods). Green indicates CAM, cyan – PI, no cell mask shown;

close-ups of the sector indicated with yellow dashed lines (approximately 62 x 67 µm) show PI and CAM channels separately. Images courtesy of Kritika Singh, processed by the thesis author.

6.4.3 Role of ultrasound parameters

A number of ultrasound parameters was tested in the setup in order to check its performance and to determine the parameters allowing for substantial sonoporation fractions; for this, A549 cells were sonicated in the presence of MBs and PI. It was seen that, as expected, the PI-positive cells fraction grew with increasing duty cycle (Table 6.4.3.1, Fig. 6.4.3.1). Interestingly, in the experiment performed at 0.5% duty cycle increasing the pressure from 250 kPa pk-pk to 500 kPa pk-pk had only a small effect on the sonoporation efficiency.

For most of the subsequent experiments, the parameters of 250 kPa pk-pk, 100 Hz PRF, 30% duty cycle were used.

Pressure (pk-pk)	PRF	N cycles	Duty cycle	Total cells	Sonoporation (cells w PI) %
No US				925	0%
250 kPa	1 Hz	10	0.001%	1514	0.30%
250 kPa	100 Hz	50	0.5%	1942	5.40%
500 kPa	100 Hz	50	0.5%	2691	6.30%
250 kPa	100 Hz	3000	30%	1197	24.70%

Table 6.4.3.1. Sonoporation efficiency (calculated as % of PI-positive cells to total cells counted for each sample) for a range of ultrasound parameters (all sonications 30 seconds) and a no ultrasound control. Experiments performed with A549 cells in SAT2E with $5*10^6$/mL DBPC-PEG40S PFB MBs and PI added during the sonication, and CAM and cell media incubations performed after the ultrasound (see Methods).

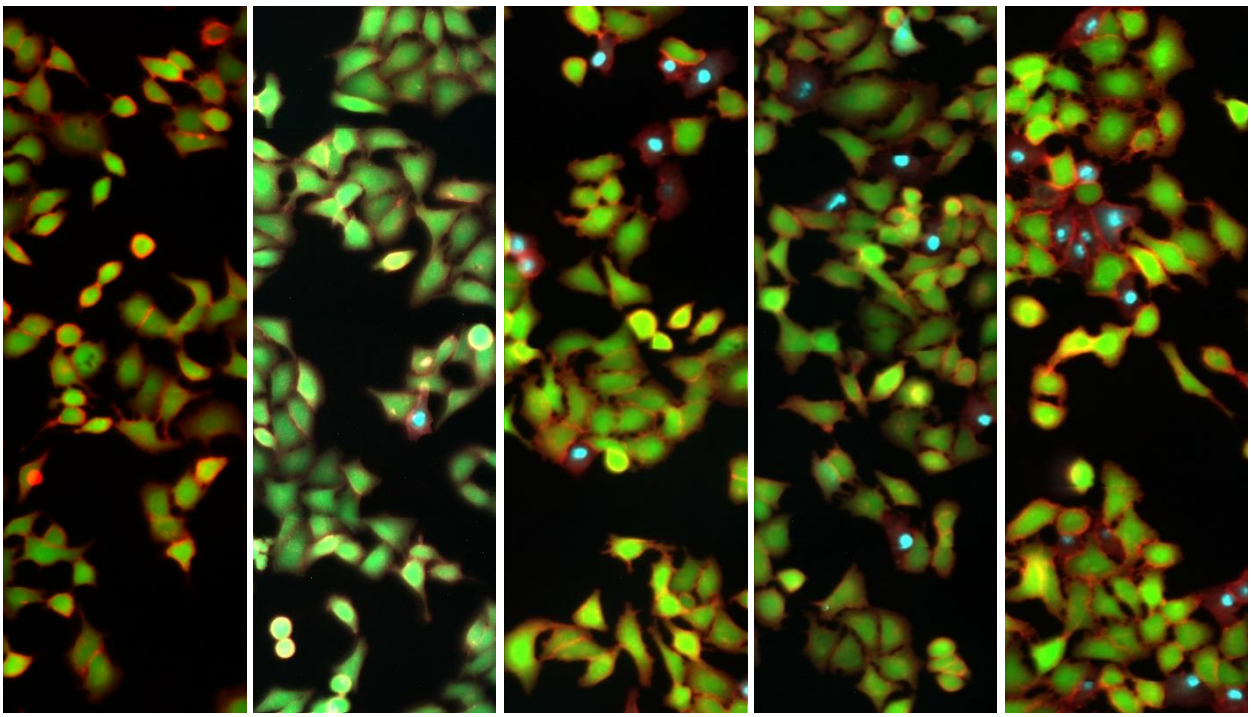

0% PI cells	0.3% PI cells	5.4% PI cells	6.3% PI cells	24.7% PI cells
No US	250 kPa pkpk	250 kPa pkpk	500 kPa pkpk	250 kPa pkpk
	1 Hz PRF	100 Hz PRF	100 Hz PRF	100 Hz PRF
	10 cycles	50 cycles	50 cycles	3000 cycles

Fig. 6.4.3.1. Example microscopy images of A549 cells from the experiment described in **Table 6.4.3.1**. Red indicates the cell mask staining the plasma membrane, green indicates CAM as a marker for live cells, cyan indicates PI as a marker of cell permeabilization; each image width approximately 205 µm. Images courtesy of Kritika Singh, processed by the thesis author.

6.4.4 Role of microbubbles

A separate experiment was carried out in order to assess the role of microbubbles in the ultrasound-mediated cell sonoporation and killing. A549 cells were sonicated with PI with or without microbubbles at the ultrasound parameters chosen in section **6.4.3**. This resulted in **24.2%** of PI-positive cells (1637 cells counted), showing good agreement with the previous result, vs no PI-positive cells, i.e., **0%** sonoporation, for the sample without MBs (1459 cells counted) (example microscopy images in **Fig. 6.4.4.1**).

This confirmed that MBs are needed to achieve substantial cell sonoporation at the ultrasound parameters used in this project, and therefore they were used in subsequent sonications.

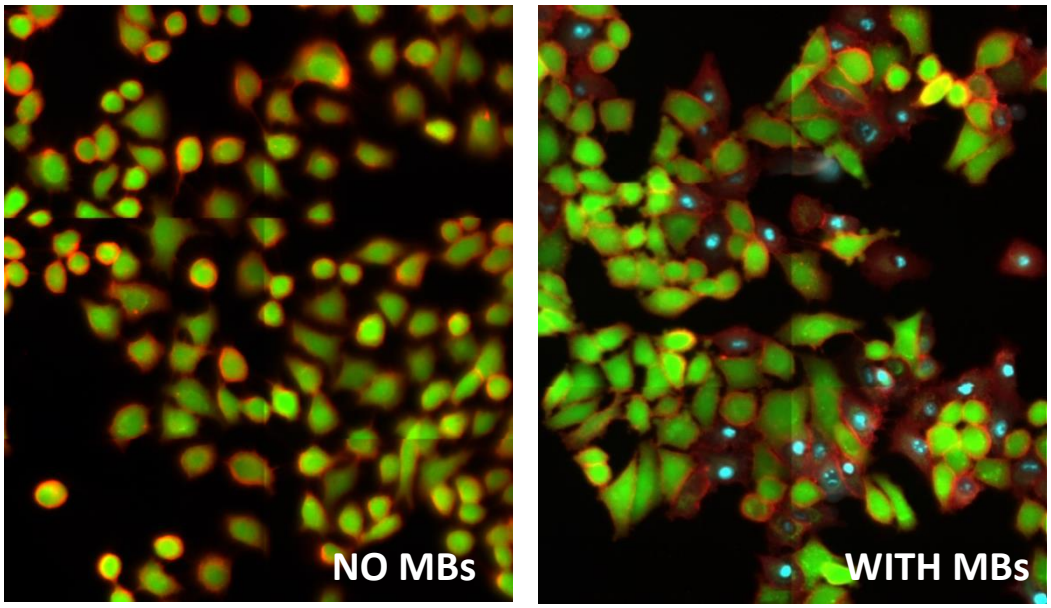

Fig. 6.4.4.1. Representative images for A549 cells after the sonication in SAT2E (US parameters: 250 kPa pk-pk, 30% duty cycle, 100 Hz PRF, 30 sec) with PI, with or without MBs (DBPC-PEG40S PFB MBs, $5*10^6$/mL). In this experiment the incubation with CAM was 5 minutes long with no post-incubation in cell media; each image width approximately 410 µm. Images courtesy of Kritika Singh, processed by the thesis author.

6.4.5 Rose Bengal added at different time points for three cell lines

Finally, in order to investigate the sonoporation hypothesis, measurements were performed with RB added at different time points of the experiment: before ultrasound, immediately after ultrasound (within approximately 10-15 seconds) or 20 mins after ultrasound. PI was not added to these samples in order to avoid optical overlap with RB, but separate experiments were performed with cells that were sonicated with PI but without RB, and PI was also added to no ultrasound controls. As cell type is known to be important in sonoporation, three different cell lines were tested in this experiment. The results are shown in Fig. 6.4.5.1, and Fig. 6.4.5.2 presents example microscopy images.

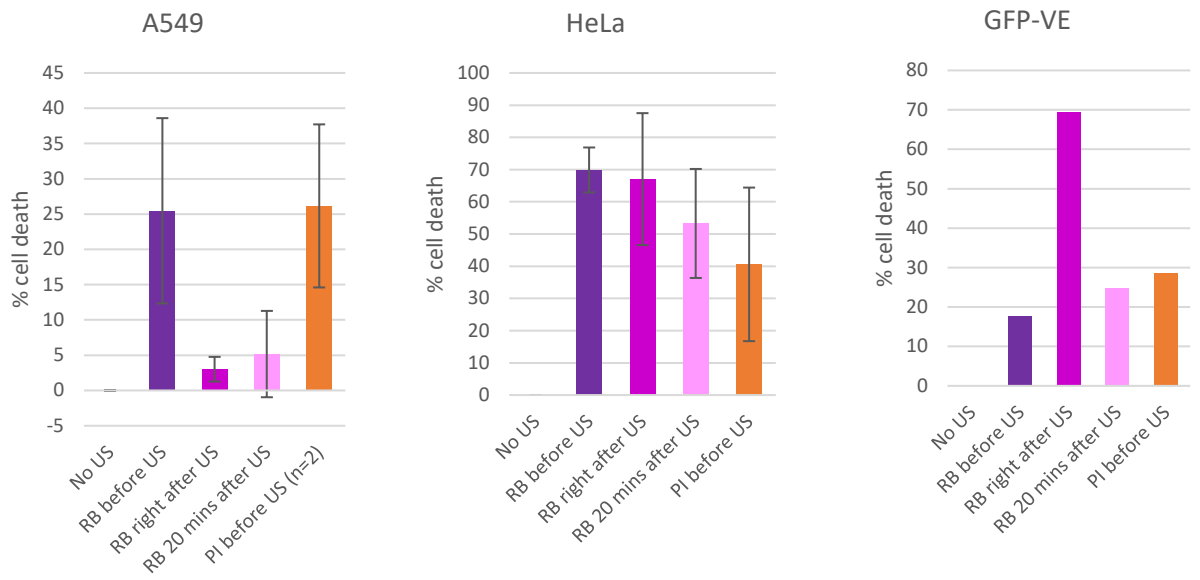

Fig. 6.4.5.1. Cell death results in sonication experiments for A549, HeLa and GFP-VE cells (see section **6.2.5.3** for the protocol of quantifying cell death from the microscopy images). Samples were: no ultrasound control (with incubations with PI and CAM, but without ultrasound); RB added before ultrasound; RB added right after ultrasound; RB added 20 mins after ultrasound; and PI added before ultrasound (no RB). All ultrasound samples had DBPC-PEG40S PFB MBs ($8*10^6$/mL); ultrasound parameters 250 kPa pk-pk, 100 Hz PRF, 30% DC, 30 sec. n = 3 repeats for HeLa and A549 cells (except for PI control for A549) and n = 1 repeat for GFP-VE cells; error bars indicate standard deviations.

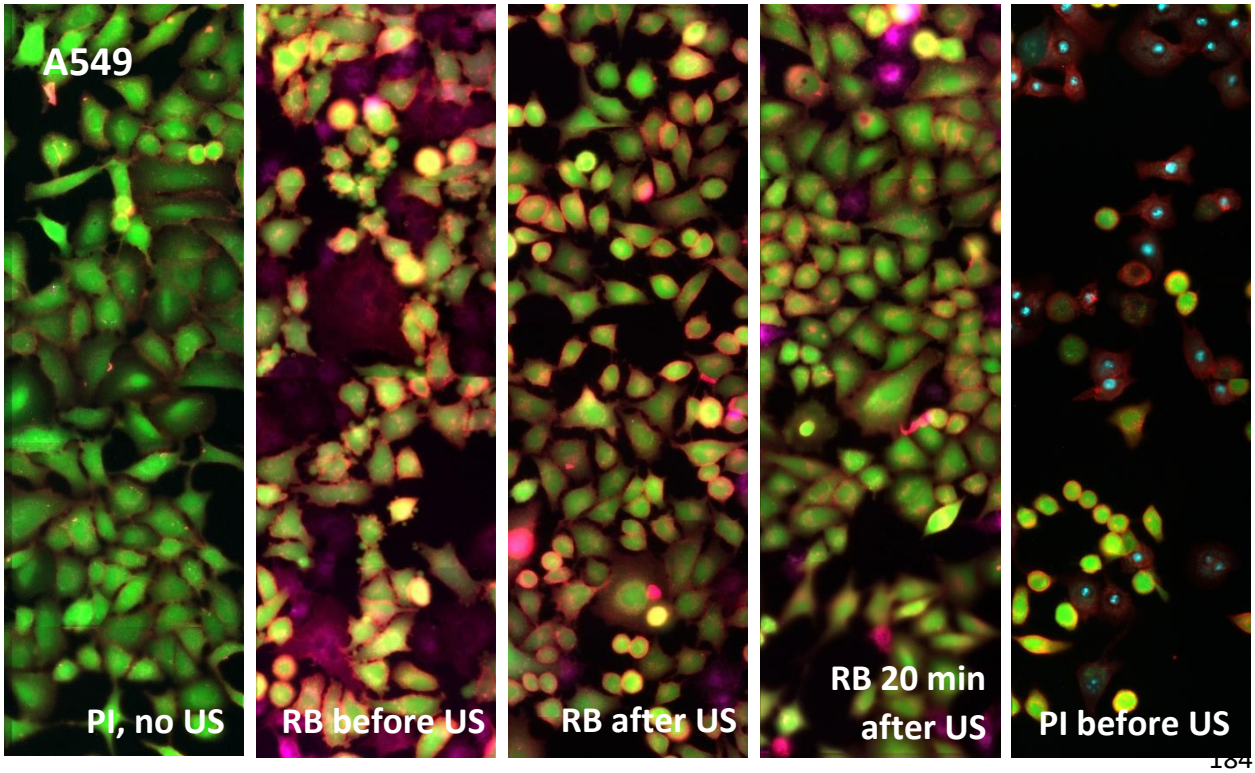

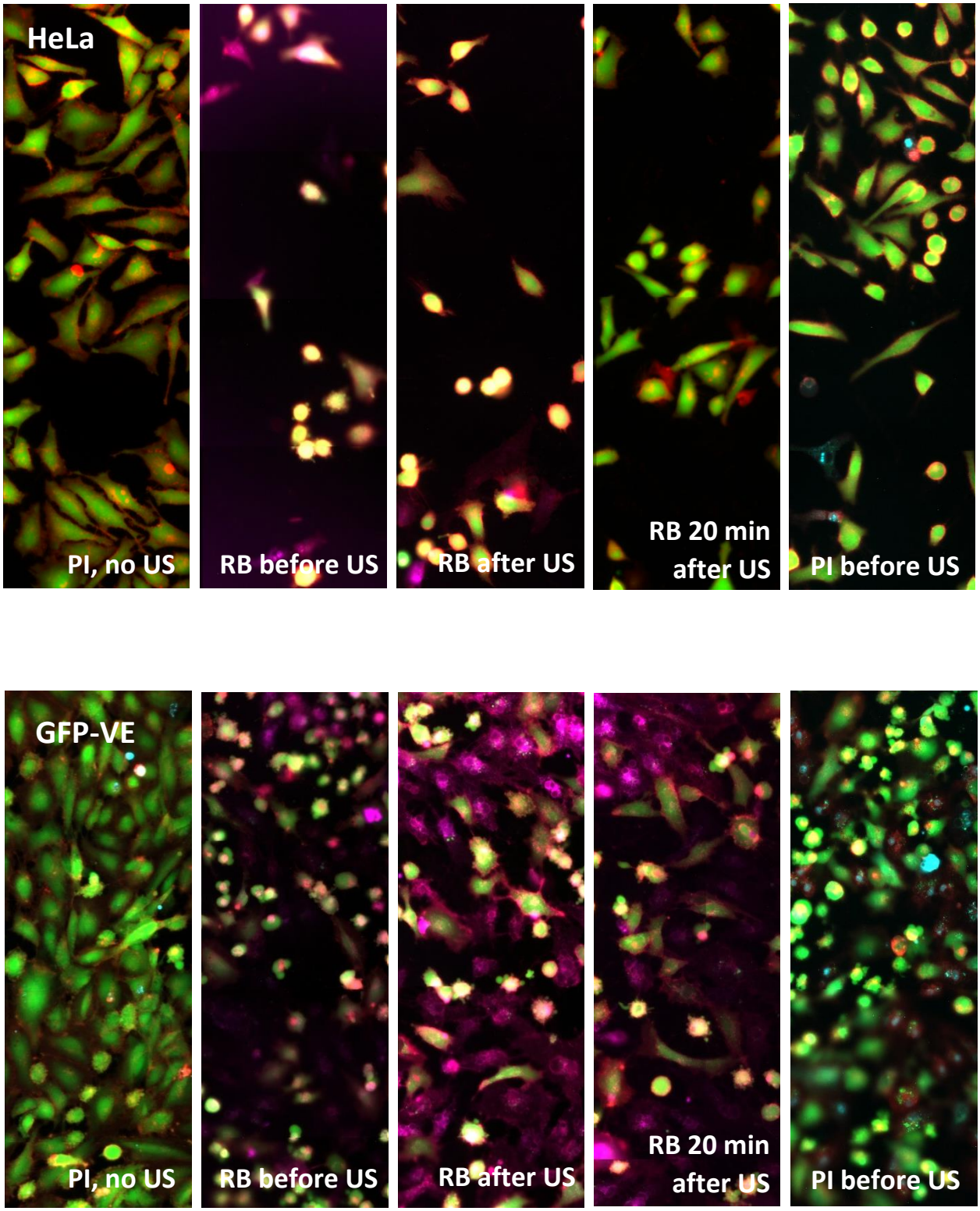

Fig. 6.4.5.2. Example microscopy images for experiments in Fig. 6.4.5.1. Red colour indicates cell mask, green – CAM, cyan – PI, magenta – RB; each image width approximately 205 µm. Images courtesy of Kritika Singh, processed by the thesis author.

The cell death results differed considerably between cell lines. A549 cells when sonicated with PI exhibited similar levels of sonoporation as seen in several experiments before (~25%), which is encouraging for the reproducibility of these experiments and the reliability of the setup. RB showed higher toxicity when added before ultrasound, compared to right after or 20 mins after, although some toxicity was still seen for the latter samples. In addition, the cell death levels seen after ultrasound exposure with RB and PI were similar (within the experimental uncertainty), which again points to the possibility of intracellular PI toxicity, which will be discussed later.

HeLa cells exhibited high levels of cell death, on comparable levels between all ultrasound controls with RB or PI. However, the technical difficulty of HeLa cell death quantification is that these cells detach easily upon death, and therefore further analysis of detached cells would be needed to corroborate these results.

GFP-VE cells showed higher cell death levels for RB added right after ultrasound compared to before ultrasound; however, as these experiments were done in only one repeat, no conclusions should be drawn from this before more repeats are performed, and the experiment shown here for this cell line should be treated as a preliminary result.

6.5 Conclusions

An experimental protocol was developed for cell sonication experiments and viability quantifications. A number of controls were performed, showing good reproducibility of cell sonoporation ratios between different runs of the same experiment, the necessity of the presence of MBs to achieve sonoporation at the ultrasound parameters used here, as well as the necessity of the correct use and interpretation of cell markers such as CAM and PI. Contrary to some previous literature reports, uptake of Rose Bengal was clearly observed following ultrasound exposure, indicating that sonoporation does occur under conditions relevant to SDT.

Further experiments were performed to compare the toxicity of RB when added before, right after or 20 mins after ultrasound, in order to assess its effect when it's present during the sonication, compared to added after the sonication within the sonoporation window, or after most of the cells have resealed. The results indicated that cell death was highest for RB added before sonication, but some cell death was still observed with RB added after the sonication, to a different degree in the cell lines that were used in this experiment.

From the point of view of the sonoporation SDT hypothesis, this may indicate that sonoporation and other ultrasound-induced effects do play some role in the SDT-induced cell death, to a different extent depending on the cell line; the sonoporation hypothesis is not able to fully explain the results seen in the A549 cells, but it may still contribute to some of the cell death, as seen in the results with RB added post-ultrasound. It is also possible that, in order to achieve the highest cell death rate, both sonoporation and ultrasound-induced drug activation are needed: as RB can achieve high intracellular concentrations in the sonoporated cells, it may lead to the levels of ROS generated by its ultrasound activation to be sufficient to induce cell death; however, checking this experimentally would present a considerable challenge.

Interestingly, PI was found to produce high levels of cell death, indicating that it should be used with caution as a marker of cell permeabilization.

Future work

These experiments show encouraging results for the reproducibility of the protocols developed here and the reliability of the setup. The results demonstrate that sonoporation does occur under ultrasound exposure conditions used in SDT and that internalisation of a sensitiser, Rose Bengal, does take place. A number of further questions still have to be answered, however, to test the sonoporation hypothesis.

Firstly, it would be of interest to perform these experiments with other cell lines and drugs, as sonoporation dynamics and general behaviour are different for different cell lines, and different types of drugs may vary in their mechanisms of action. Most of the experiments in this Chapter were performed on A549 cells, with some preliminary experiments with HeLa and GFP-VE cells; further experiments should be performed in these and other cell lines in order to more fully assess the potential of the sonoporation hypothesis. A number of measurements that were not carried out in this project, such as assessing the intracellular ROS production, may also be of interest.

Another important factor is the sonoporation window length. 20 minutes were assumed to be enough for most of the sonoporated cells to either close or to die, but literature reports vastly different lengths of sonication windows for different cell lines and ultrasound parameters, and therefore this should be verified. Preliminary checks carried out in this study did not produce conclusive results.

Further studies are also needed to assess the intracellular toxicity of PI: although the results here indirectly point towards it, this requires more experiments. If confirmed, this would be an

important note for sonoporation experiments, as PI is a popular marker of either cell death or sonoporation, and if it is indeed toxic intracellularly, it would artificially decrease the rates of reversible compared to irreversible sonoporation.

Chapter 7. Conclusions

One of the barriers faced by sonodynamic therapy on the way to clinical use is better understanding of its mechanisms. The overall goal of this thesis was to contribute to this understanding by developing robust protocols and experiments and testing hypotheses that could explain some of the effects observed *in vivo*.

The first part of the thesis addressed the discrepancy between the small delivered oxygen doses and substantial *in vivo* results in ultrasound-mediated oxygen-enhanced sonodynamic therapy and in ultrasound-mediated targeted oxygen delivery more generally. A hypothesis proposed in the blood substitute literature, which states that artificial agents may be able to speed up the oxygen exchange between red blood cells and tissue, was tested in application to other agents, in particular those used for ultrasound-mediated delivery, and an experimental setup was developed to this end. Although the experimental sensitivity was not sufficient to detect changes in oxygenation speed for the parameters tested here, it is still possible that this setup could be used to study blood oxygenation under a wider range of parameters – in particular, smaller channel size would be of interest.

The second part focused on reactive oxygen species generation. It was observed that a widely used optical probe Singlet Oxygen Sensor Green did not produce theoretically predictable results when sonicated in the presence of sonosensitive drug Rose Bengal. An HPLC protocol was developed to detect singlet oxygen, which showed that the amount of reactive oxygen species produced by the combination of Rose Bengal and ultrasound was much lower than that for the light activation of this drug, even for light intensities that are much lower than those used for therapeutic applications. In order to explain the discrepancy between the low amounts of reactive oxygen species and the observed *in vivo* effects, in particular when comparing sonodynamic and

photodynamic therapy, it was proposed that ultrasound-induced permeabilization of cell membranes plays an important role by substantially increasing intracellular concentrations of drugs and therefore potentially making them toxic at concentrations that are non-toxic extracellularly. A number of experiments were carried out in several cell lines, and it was observed that there is indeed marked uptake of a drug by cells, even if the drug is introduced right after the sonication and not before. Cell death results were different for different cell lines; for the cell line most studied in this project (A549) it was seen that Rose Bengal toxicity is highest if the drug is added before ultrasound, but there is still some toxicity if a drug is added after the sonication, showing that sonoporation may indeed play some part in overall toxicity of sonodynamic therapy. Further investigations are ongoing with a broader range of cell lines and drugs.

Separate chapters were dedicated to agent and ultrasound setup characterisation, and substantial attention was paid to good experimental practice, reproducibility issues and reliability of protocols used in this study.

It is the hope of this author that the protocols, setups and results presented here will help in further elucidating the mechanisms of sonodynamic therapy and ultrasound-mediated oxygen delivery.

APPENDIX

A 2.4.3 Oxygen release measurements with focused ultrasound

Introduction

As explained in section 2.4.3, ultrasound-mediated O_2 release measurements suffer from a number of technical difficulties, one of which is the sample heating (and potentially the effect of ultrasound on the O_2 sensor) that lead to artificially elevated results of O_2 release. This may be mitigated with proper controls; however, it would also be of interest to develop a setup for real-time ultrasound-mediated O_2 release measurement that did not have these issues.

To this end, a setup was proposed using a focused ultrasound transducer. The sample holder was designed so that the focus of the transducer would be located in the centre of the sample, and the O_2 sensor is placed on the periphery of the sample, this way hopefully avoiding the direct interaction between the ultrasound and the sensor. This setup was tested in a proof-of-concept experiment, which is described here.

This experiment was performed in collaboration with Dr Catherine Paverd.

Materials and methods

Materials and protocols for MB production are described in Chapter 2. In this experiment, DBPC-PEG40S MBs with PFP cores were used.

Focused Ultrasound (FUS) experiments were performed using a 0.5 MHz focused single element transducer made by Sonic Concepts (H107 series). Signals were recorded using a Verasonics Vantage 256 channel array (128 channels used in this experiment). Sample holder made of ultrasound-transparent materials was modified to accommodate a PreSens oxygen sensor (PreSens, Germany); a waterproof channel was attached to the sample holder to accommodate the oxygen sensor cable (Fig. A 2.4.3.1 a). The sample holder, transducer and array were put in a water tank (water degassed to ~30% airsat), with the Verasonics probe positioned horizontally in

order to avoid the influence of the coalescent bubble foam that can accumulate on the top of the sample after sonication, and a custom B-Mode and Passive Acoustic Mapping (PAM) acquisition script was used to position the holder and then to acquire the raw signal traces. These traces were then beamformed using an RCB (Robust Capon Beamformer) PAM algorithm to form a cavitation energy map on a 12x12 spatial grid (Fig. A 2.4.3.1 b). Total cavitation energy was calculated as sum of energies over the detection grid.

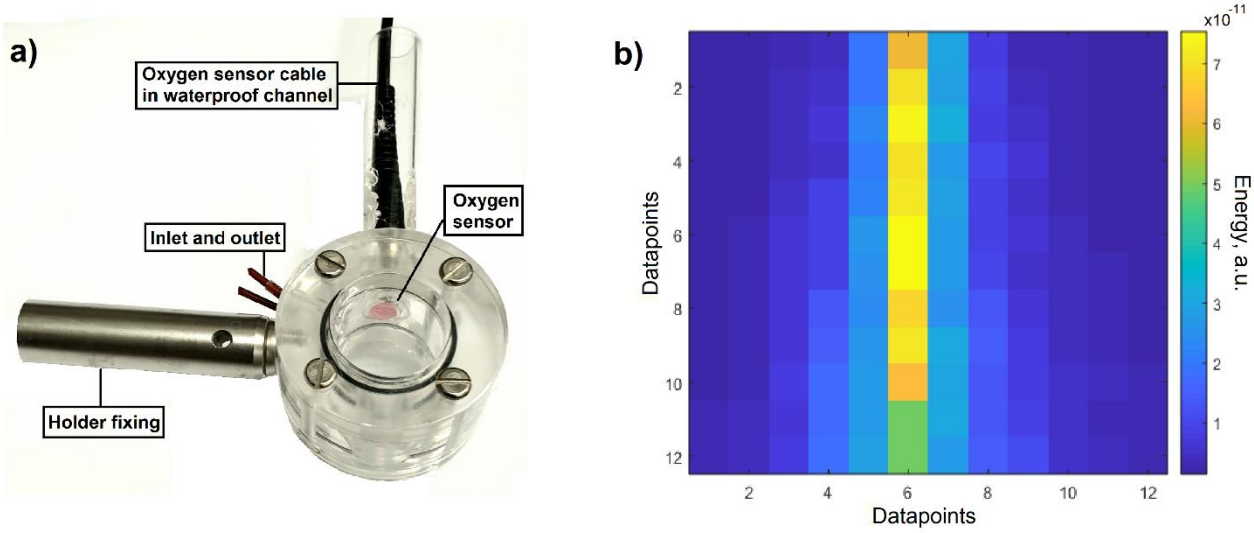

Fig. A 2.4.3.1. a) Sample holder with an optical oxygen sensor for the focused ultrasound setup; b) example of cavitation energy map processed for a 12x12 spatial grid.

Samples of DBPC-PEG40S PFP microbubbles diluted to the concentration of $5*10^7$ MB/mL were prepared in DPBS with 3 µM Rose Bengal and 1.5 µM Singlet Oxygen Sensor Green to quantify ROS production. Sample solution was injected into the holder, sealed and subjected to ultrasound (0.5 MHz, 1.6 MPa peak negative pressure, 1 Hz pulse repetition frequency, 10% duty cycle, 10 min sonication time).

Results and discussion

O_2 release measurements were performed for oxygenated and non-oxygenated PFP microbubbles (**Fig. A 2.4.3.2**). A general trend for O_2 concentration, observed for all MB samples, was oxygen decrease before the ultrasound, then increase with a sharp peak, followed by a decrease until the end of the sonication period, after which O_2 levels remained stable for the time of observation (at least 1 minute).

Initial oxygen increase was slightly larger for oxygenated bubbles than for non-oxygenated samples (**Fig. A 2.4.3.3**). However, this is overshadowed by the large decrease in O_2 concentration seen during the ultrasound time, which has to be increased. Additional experiments showed that part of this effect could be caused by oxygen leaking from the sample holder into the degassed water tank, but that it could only account for about 20% of the O_2 decrease seen in the experiments.

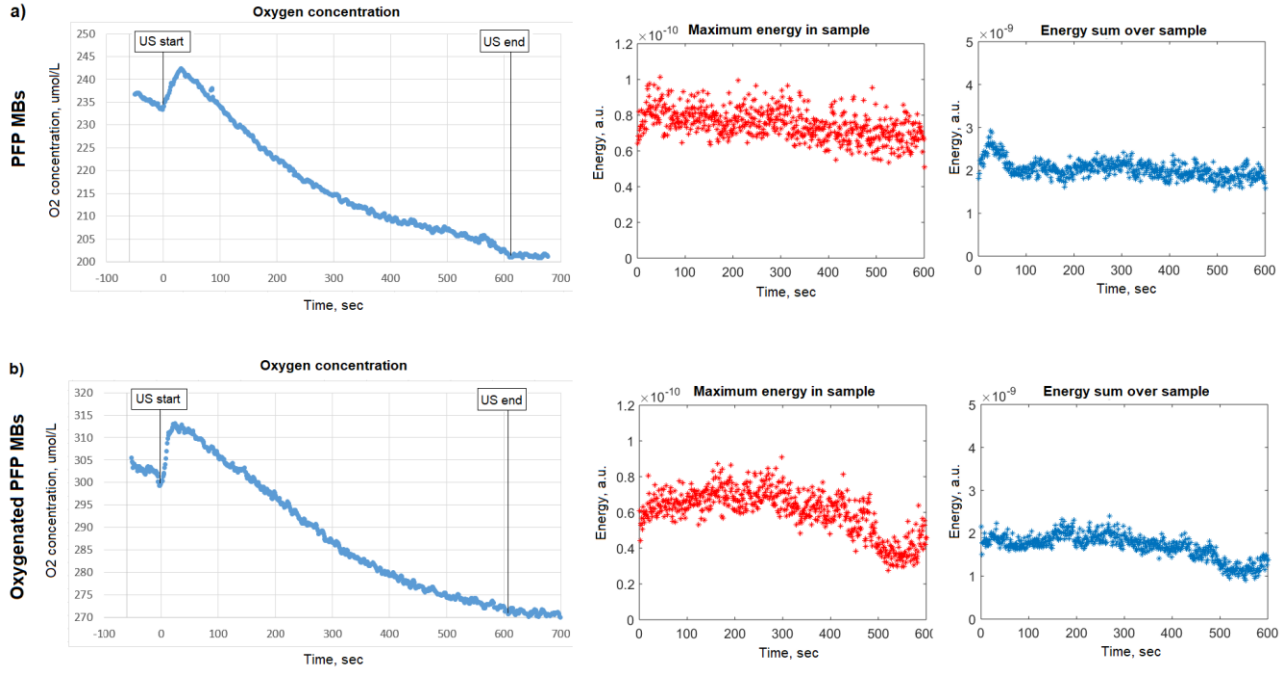

Fig. A 2.4.3.2. Oxygen concentration vs time, maximum cavitation energy vs time and total cavitation energy vs time in the sample for a) non-oxygenated and b) oxygenated PFP MBs.

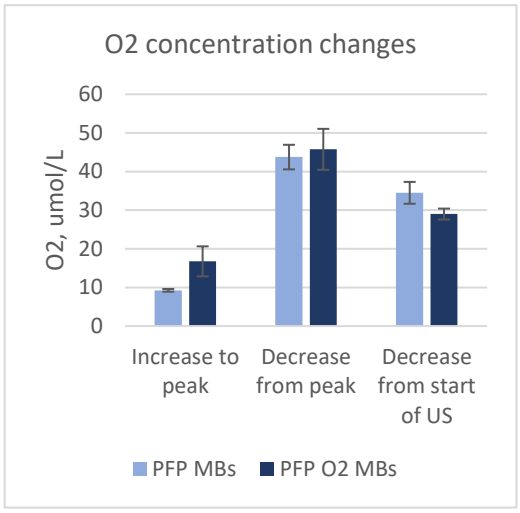

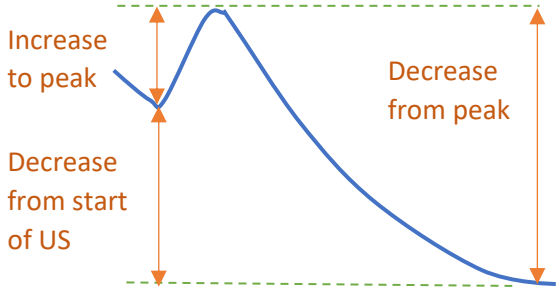

Fig. A 2.4.3.3. Oxygen concentration parameters (increase from start of ultrasound to peak: decrease from peak to end of ultrasound; decrease from start to end of ultrasound) for non-oxygenated and oxygenated PFP MBs; the schematic on the right-hand side explains the definitions of these parameters) (n = 3, error bars represent standard deviations).

In conclusion, this experiment showed the technical feasibility of using focused ultrasound to monitor real-time O_2 release; however, troubleshooting is needed for the setup to be used reliably. The large O_2 concentration drop seen during the experiments could not be readily explained; in addition, some further artefacts were seen with O_2 concentration oscillations for some of the lipid control samples (data not shown).

Although this setup could be developed further to study the time-dependence of oxygen release from O_2-carrying agents, this goal was not within the principal aims of this thesis, and for this reason this setup was not developed further.

A 3.3.1 Development of the oxygen diffusion measurement setup for simple agent solutions without blood or flow

This section details the development of the setup for measuring oxygen diffusion in simple solutions without blood or flow. This development process allowed to establish the experimental principles for further diffusion setups, such as the utmost importance of avoiding temperature-induced convection or mechanical agitation, which agree with what is underlined in the experimental literature on oxygen diffusion measurements[181].

Liquid layer diffusion setup – version 1

The first rudimentary version of the setup is shown in **Fig. A 3.3.1.1**. However it was quickly established that the size of such a setup was too large and the layer thickness needed for a 1-hour experiment was below approx. 3 mm (**Fig. A 3.3.1.1 b**).

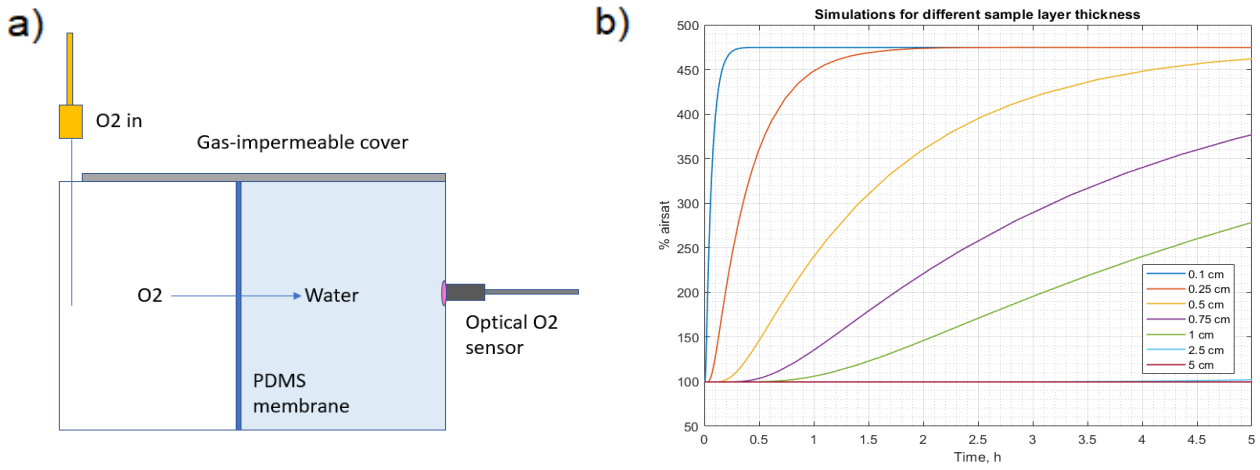

Fig. A 3.3.1.1. a) Oxygen diffusion setup for a sample layer, version 1; b) COMSOL simulations for a 5-hour experiment with water layers of various thickness.

Liquid layer diffusion setup – version 2

An updated version of the setup was made using a polymer sample holder (SonoLid[158]) with an inlet and outlet for gas flow (regulated via a gas rotameter); the membrane was removed from this setup to avoid membrane deformation and oxygen delay issues (Fig. A 3.3.1.2 a). The function of slow but continuous gas flow was to 1) counterbalance any oxygen leaks from the system and 2) to avoid mechanical agitation of the system that could be caused by plugging an outlet. The flow rate of approximately 250mL/min was shown to fill the setup quickly and to maintain the oxygen levels inside it (Fig. A 3.3.1.2 b).

Several iterations of adjustments were made to the sample holder supporting the setup to avoid mechanical agitation during sample handling, after which the experimental repeats showed an acceptable degree of reproducibility (Fig. A 3.3.1.2 c). However comparison with a theoretical estimation (calculated with COMSOL software) showed that the oxygen levels were rising much faster than they should due to diffusion alone, and this large discrepancy could not be explained by experimental imprecisions such as an error in measuring the liquid layer thickness. Due to the good reproducibility of results, it was still possible but not likely that this was caused by accidental mechanical agitation. Temperature changes in the sample due to the gas flow were determined as a likely cause for the results, since even a small temperature gradient could induce convection in the sample, with the top colder layers going down and therefore significantly accelerating oxygen exchange, and reproducible temperature curve could also account for the good reproducibility of the incorrect diffusion measurements (Fig. A 3.3.1.2 d).

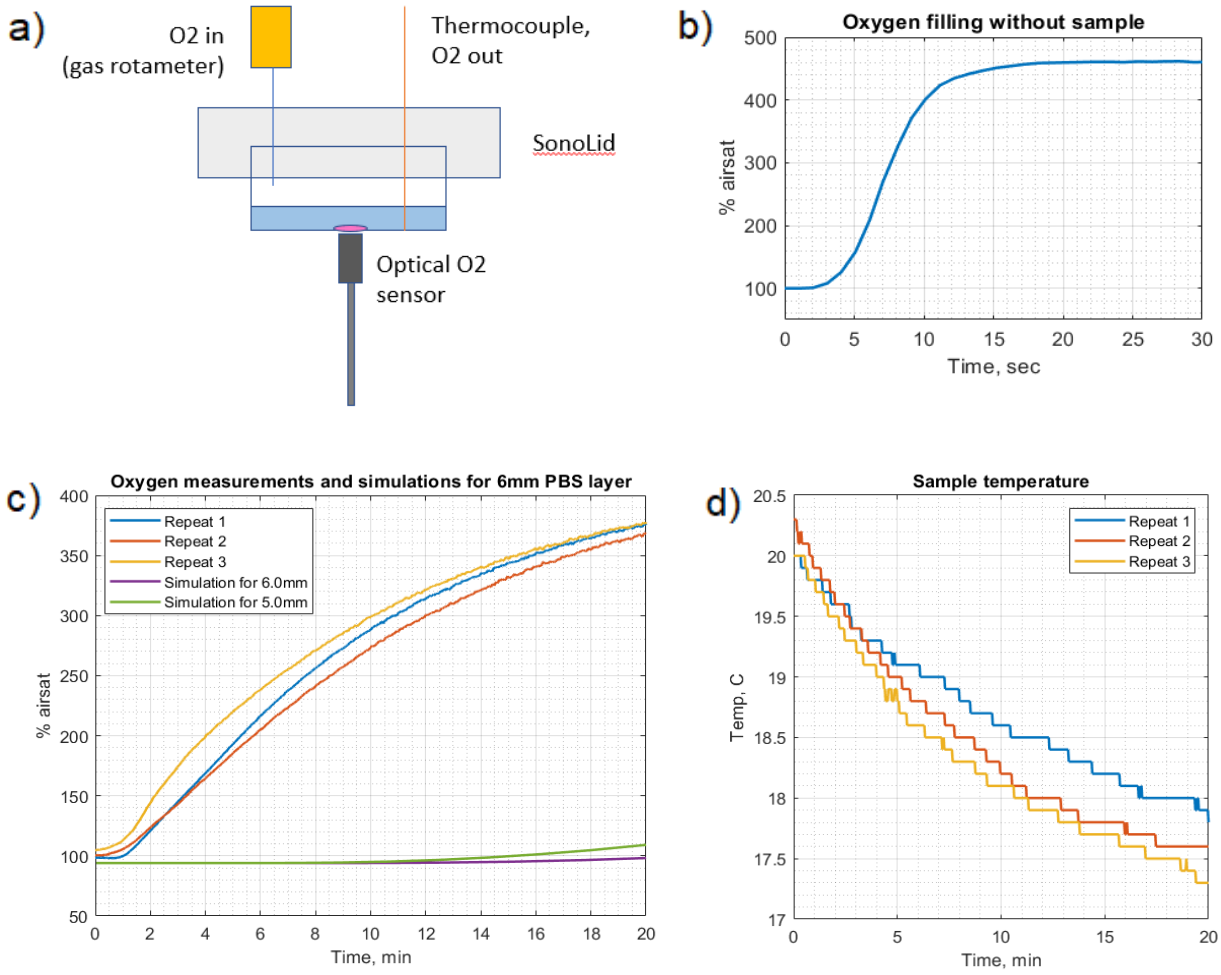

Fig. A 3.3.1.2. Oxygen diffusion setup for a sample layer, version 2: a) schematic of the setup; b) oxygen filling speed check without a sample present (oxygen flow at approximately 250mL/min); c) oxygen concentration measurements and COMSOL simulation results for a 6 mm layer of PBS (simulation results for 5.0 mm are also included to demonstrate that the discrepancy was not caused by imprecise measurement of the layer thickness); d) sample temperature changes during the PBS experiments shown in c).

Liquid layer diffusion setup – version 3

The next version of the setup was designed taking these shortcomings into account (Fig. A 3.3.1.3). The sample was separated by a PDMS membrane to minimize mechanical disturbance and avoid the surface curving due to the surface tension in the sample. The sample area diameter was small

(1 cm) in order to decrease the potential membrane deformation magnitude. The gas compartment above it could be filled with a syringe with oxygen equilibrated to the room temperature and then sealed off. The setup was fixed with a clamp on an optical tabletop plate to further decrease the mechanical disturbance. Parts of the setup were pressed together with O-rings and all connections were covered with sealant to prevent oxygen or sample loss.

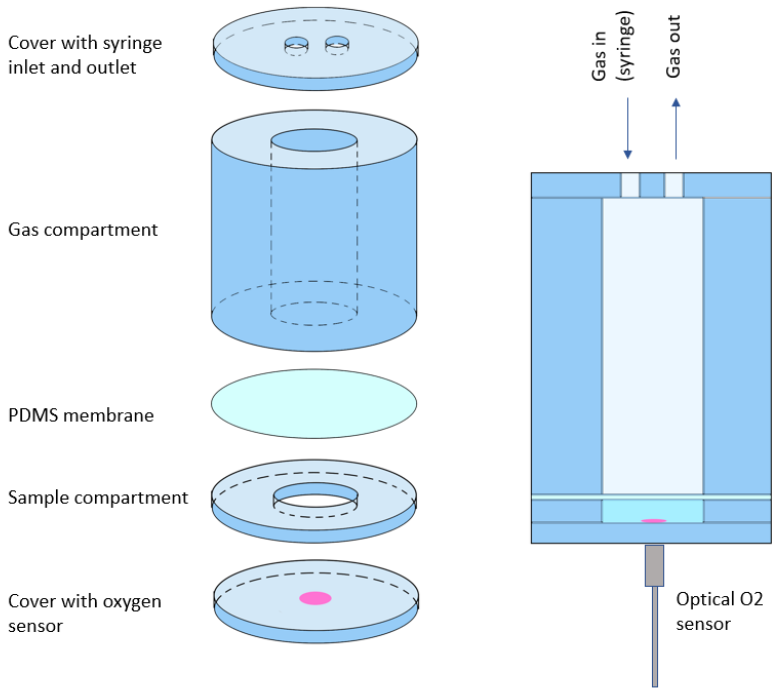

Fig. A 3.3.1.3. Oxygen diffusion setup for a sample layer, version 3. The covers were attached to the gas compartment with 4 screws (omitted in the schematic for clarity). The diameter of the sample compartment was 1 cm and its height was 3 mm.

To check the achievable oxygen concentrations and losses, the empty setup was filled with oxygen, sealed and monitored for the duration of a typical experiment. This was repeated periodically to monitor the sensor calibration and setup insulation state; a representative example is shown in **Fig. A 3.3.1.4 a**. It was found that the setup has some degree of oxygen loss, but this could be mitigated by incorporating the measured loss into the theoretical COMSOL model that was used to determine the diffusion coefficient (**Fig. A 3.3.1.4 b** presents COMSOL simulations for oxygen diffusion in a 3.0 mm PBS layer with a 200 µm PDMS membrane implementing 4 different experimental runs for oxygen levels in the setup, showing that, while oxygen loss could not be fully

eliminated in this setup, it could be included into the theoretical model with a good degree of reproducibility).

The results obtained with this setup agreed with the theoretical predictions much better, indicating that the problems of thermally induced convection or mechanical agitation have been eliminated or at least mitigated (Fig. A 3.3.1.4 c). The remaining issue in this setup was the PDMS membrane deformation, since even a small layer deformation induced a significant relative increase in the oxygen path length (a deformation on the order of magnitude of the PDMS layer thickness would constitute a 10% change, which corresponds to the remaining variability of results – shown in Fig. A 3.3.1.4 c with a comparison to a COMSOL simulation for a 10% change in sample thickness). Introducing a thicker and hopefully more rigid PDMS layer and making small constructive changes to the setup did not resolve this issue, leading to persisting result variability (Fig. A 3.3.1.4 d).

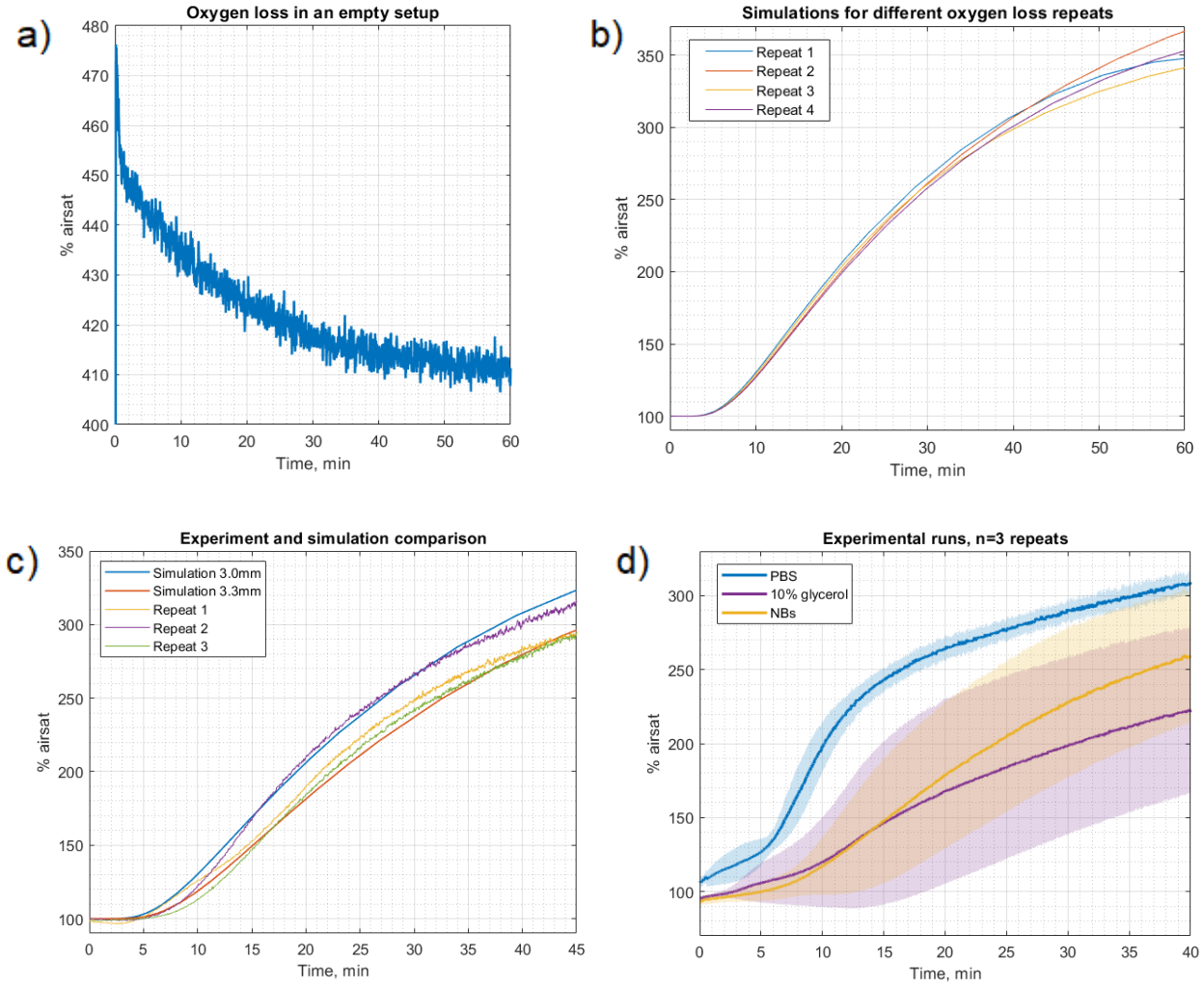

Fig. A 3.3.1.4. Results for the diffusion setup, version 3: a) oxygen concentration in an empty setup after it was filled with oxygen and sealed; b) COMSOL simulations for a 3.0 mm PBS layer with a 200 µm PDMS membrane using 4 experimental repeats of oxygen loss measured in an empty setup; c) a comparison of 3 experimental repeats with PBS samples to COMSOL simulations for different sample layer thickness; d) experimental runs with a 670 µM PDMS membrane for PBS, 10% glycerol in PBS and nanobubble samples; shaded area indicates standard deviation for n = 3 repeats.

A 3.4.2 Oxygenation speed experiments for agent solutions in flow without blood

This section of the Appendix describes the results of the experiments described in section 3.4.2 for various types of agents. Briefly, air-equilibrated oxygen-carrying agent solutions were put through a section of gas-permeable silicon tubing that was immersed in 1 atm oxygen or nitrogen at the parameters corresponding to non-complete oxygen exchange, and the output oxygen concentrations were measured for agent solution samples compared to buffer control. A difference in output oxygen concentration in this experiment would signify a different oxygen exchange speed, or different oxygen solubility.

Results with 1.5 m larger diameter silicon tubing, 1 atm O_2 lung

The experiments in this section were performed with the artificial lung setup with 1.5 m of big (1.47 mm ID) silicon tubing, described in section 3.4.2.

In addition to microbubble experiments described in section 3.4.2, a number of measurements were carried out with other samples (lecithin, nanobubbles, crocetin and glycerol) comparing oxygen content before and after going through the lung (Figs. A 3.4.2.1 - A 3.4.2.3). Due to nanobubbles being much more stable than microbubbles, and other samples having no stability concerns under the experimental conditions, no stability checks were performed for these samples.

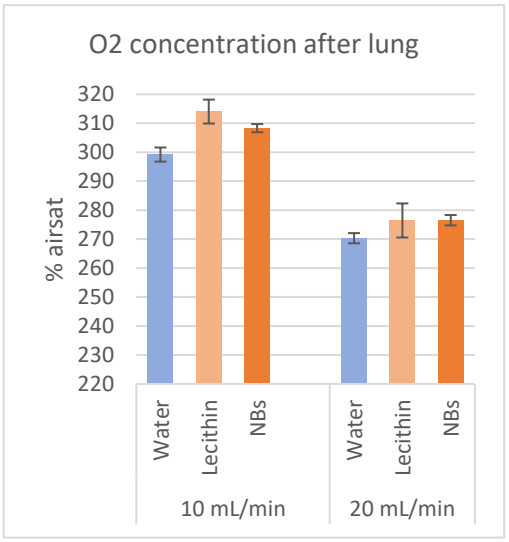

Fig. A 3.4.2.1. Oxygen concentration in lecithin solutions in water (3 g/L) and lecithin-based nanobubbles (prepared in water) compared to water controls after passing through the lung with 1.5 m tubing filled with 1 atm O_2 at flow rates of 10 or 20 mL/min (n = 2 for NBs in flow experiments, n = 3 for all other measurements, error bars represent standard deviations).

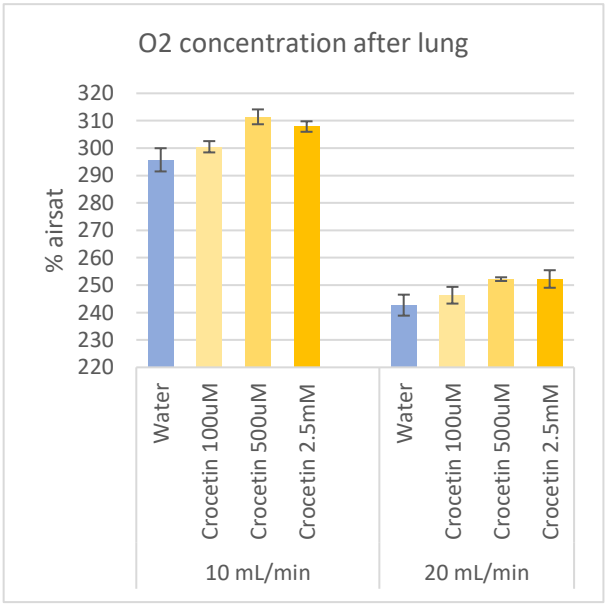

Fig. A 3.4.2.2. Oxygen concentration in crocetin solutions in water (100 µM, 500 µM or 2.5 mM) compared to water controls after passing through the lung with 1.5 m tubing filled with 1 atm O_2 at flow rates of 10 or 20 mL/min (n = 2 for water control in flow experiments, n = 3 for all other measurements, error bars represent standard deviations).

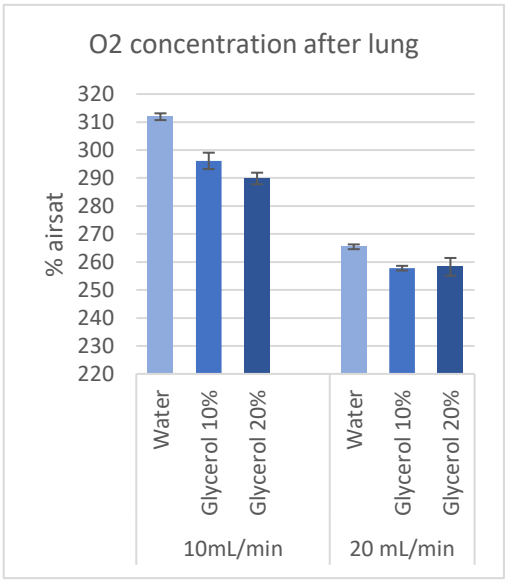

Fig. A 3.4.2.3. Oxygen concentration in glycerol solutions in water (10% or 20% vol) compared to water controls after passing through the lung with 1.5 m tubing filled with 1 atm O_2 at flow rates of 10 or 20 mL/min (n = 3, error bars represent standard deviations).

Discussion

The samples with lecithin, NBs and crocetin showed a significant increase in output oxygen concentration relative to water controls, and glycerol samples demonstrated a marked decrease. However, care should be taken when interpreting whether these changes were seen due to oxygen diffusivity differences; in particular, two factors that should be taken into account are oxygen solubility in the samples, and the temperature of the samples in the experiment.

Oxygen solubility can be measured as oxygen content in air-saturated samples (**Fig. A 3.4.2.4**), and for some of the samples literature data exist for comparison. Interestingly, the measurements showed oxygen concentrations above 100% (relative to water). For nanobubbles, literature comparison for oxygen solubility is not available, however there is data separately on citric acid (which is one of the NB components in concentration of 3 g/L) showing that it decreases the oxygen solubility of water slightly (to ~99.5% airsat at 3 g/L) due to the salting-out effect[182]. Literature comparison for crocetin was not found. However, the solubility of oxygen in glycerol solutions was showed by several studies to be low; data from at least two papers allows to estimate oxygen solubility in 10% vol glycerol at ~87% airsat, and in 20% vol glycerol at ~72% airsat (at 20°C)[182,183]. The air-saturated samples measurements for glycerol do not therefore correspond

to the literature. One possible explanation for this could be oxygen sensor errors – some time after the sensor calibration the water oxygen saturation was shown to be around 102% instead of 100% (**Fig. A 3.4.2.4**), indicating that a small signal drift upwards is possible; it is however insufficient to explain the big difference with the literature for glycerol. It is possible that glycerol affects the performance of the oxygen sensor; for this reason, glycerol controls that were measured for some of the experiments were excluded from the final data sets until this issue can be understood better.

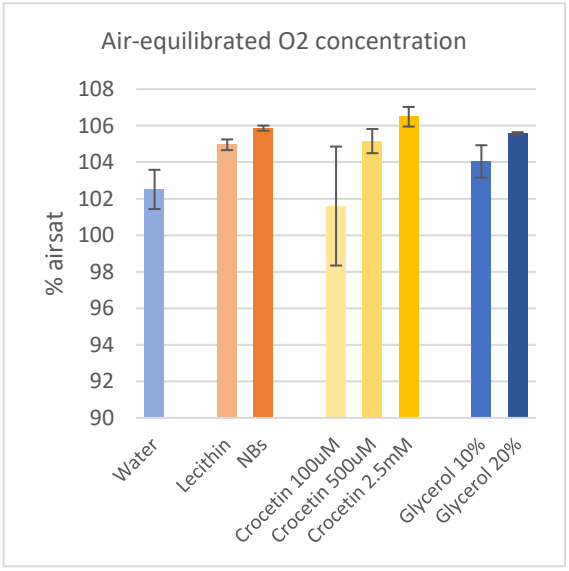

Fig. A 3.4.2.4. Oxygen concentration in air-equilibrated samples used in experiments above (% air saturation expressed relative to water): lecithin (3 g/L in water); lecithin-based nanobubbles; crocetin in different concentrations in water; 10% and 20% vol glycerol in water (n = 3, error bars represent standard deviations).

The second important consideration is the sample temperature. Despite the efforts to keep the temperature constant throughout the experiments, some changes in temperature were still seen in samples after going through the lung (**Fig. A 3.4.2.5**). The biggest increases were seen for crocetin and glycerol. For crocetin, notable heating was observed during solution preparation, and it is possible that additional mixing during the lung experiment could prompt further solubilisation of crocetin if it had not been full at the start of the experiment, therefore explaining the heating; for glycerol, it is possible that the heating is connected to the relatively high viscosity. Increased temperature is known to decrease oxygen solubility in aqueous solutions by about 1.5% airsat per 1°C around room temperature[184].

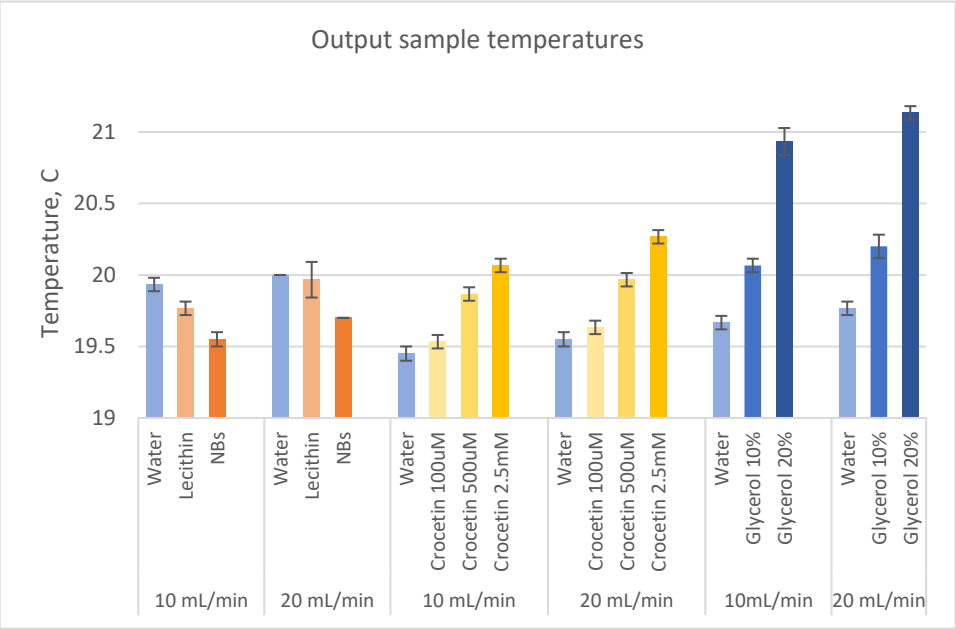

Fig. A 3.4.2.5. Temperatures in the samples after going through the lung, measured during the experiments described above (**Figs. A 3.4.2.1 – A 3.4.2.3**): lecithin (3 g/L in water); lecithin-based nanobubbles; crocetin in different concentrations in water; 10% and 20% vol glycerol in water (n = 2 for NBs and water controls in crocetin experiments, n = 3 for all other measurements, error bars represent standard deviations).

When all of these considerations are taken together, it becomes clear that the results seen in **Figs. A 3.4.2.1 – A 3.4.2.3** may be caused by various factors; oxygen diffusion speed can still play some role, but its contribution is unclear.

Results with 1.0 m smaller diameter silicon tubing, 1 atm O_2 lung

Similar to the experiments described above, output O_2 concentrations were measured in the same setup with 1 m smaller diameter silicon tubing (ID 310 um) for nanobubble and lecithin solution samples (**Fig. A 3.4.2.6**). Oxygen concentration was also measured in air-equilibrated samples (**Fig. A 3.4.2.7**).

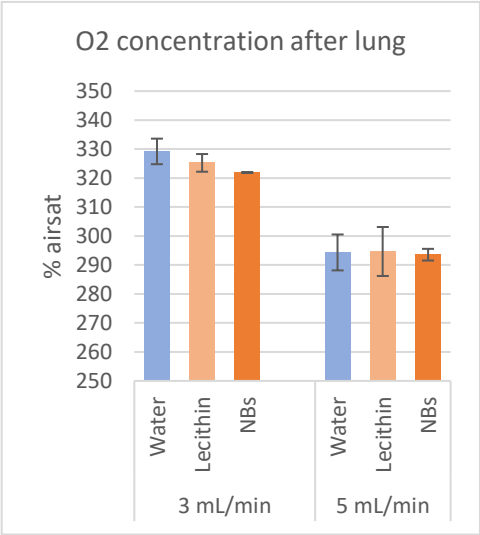

Fig. A 3.4.2.6. Oxygen concentration in lecithin solutions in water (3 g/L) and lecithin-based nanobubbles (prepared in water) compared to water controls after passing through the lung with 1.0 m tubing filled with 1 atm O_2 at flow rates of 10 or 20 mL/min (n = 3, error bars represent standard deviations).

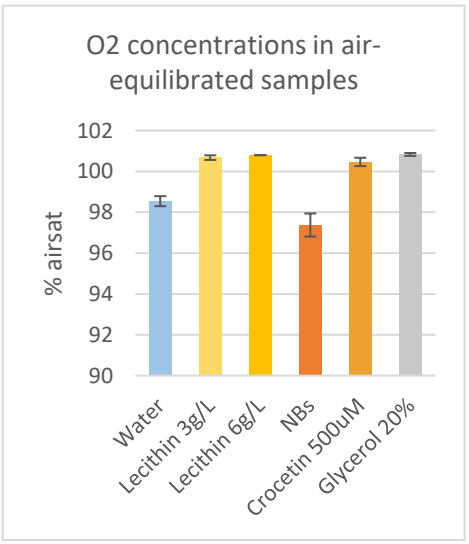

Fig. A 3.4.2.7. Oxygen concentration in air-equilibrated samples used in experiments above (% air saturation expressed relative to water): lecithin (3 g/L and 6 g/L in water); lecithin-based nanobubbles; crocetin (500 µM in water); 10% and 20% vol glycerol in water (n = 3, error bars represent standard deviations).

References

1. Siemann, D. W. The unique characteristics of tumor vasculature and preclinical evidence for its selective disruption by Tumor-Vascular Disrupting Agents. *Cancer Treat. Rev.* **37,** 63–74 (2011).

2. Vaupel, P. & Harrison, L. Tumor Hypoxia: Causative Factors, Compensatory Mechanisms, and Cellular Response. *Oncologist* **9,** 4–9 (2004).

3. Vaupel, P. & Mayer, A. Hypoxia in cancer: Significance and impact on clinical outcome. *Cancer Metastasis Rev.* **26,** 225–239 (2007).

4. Harrison, L. B., Chadha, M., Hill, R. J., Hu, K. & Shasha, D. Impact of Tumor Hypoxia and Anemia on Radiation Therapy Outcomes. *Oncologist* **7,** 492–508 (2002).

5. Rebucci, M. & Michiels, C. Molecular aspects of cancer cell resistance to chemotherapy. *Biochem. Pharmacol.* **85,** 1219–1226 (2013).

6. Vaupel, P. Hypoxia and Aggressive Tumor Phenotype: Implications for Therapy and Prognosis. *Oncologist* **13,** 21–26 (2008).

7. Narang, A. S. & Varia, S. Role of tumor vascular architecture in drug delivery. *Adv. Drug Deliv. Rev.* **63,** 640–658 (2011).

8. Al-Waili, N. S., Butler, G. J., Beale, J., Hamilton, R. W., Lee, B. Y. & Lucas, P. Hyperbaric oxygen and malignancies: A potential role in radiotherapy, chemotherapy, tumor surgery and phototherapy. *Med. Sci. Monit.* **11,** 279–289 (2005).

9. Overgaard, J. & Horsman, M. R. Modification of hypoxia-induced radioresistance in tumors by the use of oxygen and sensitizers. *Semin. Radiat. Oncol.* **6,** 10–21 (1996).

10. Martin, L., Lartigau, E., Weeger, P., Lambin, P., Le Ridant, A. M., Lusinchi, A., Wibault, P., Eschwege, F., Luboinski, B. & Guichard, M. Changes in the oxygenation of head and neck tumors during carbogen breathing. *Radiother. Oncol.* **27,** 123–130 (1993).

11. Stüben, G., Pöttgen, C., Knühmann, K., Schmidt, K., Stuschke, M., Thews, O. & Vaupel, P. Erythropoietin restores the anemia-induced reduction in radiosensitivity of experimental human tumors in nude mice. *Int. J. Radiat. Oncol. Biol. Phys.* **55,** 1358–1362 (2003).

12. Shannon, A. M., Bouchier-Hayes, D. J., Condron, C. M. & Toomey, D. Tumour hypoxia, chemotherapeutic resistance and hypoxia-related therapies. *Cancer Treat. Rev.* **29,** 297–307 (2003).

13. Crokart, N., Jordan, B. F., Baudelet, C., Cron, G. O., Hotton, J., Radermacher, K., Grégoire, V., Beghein, N., Martinive, P., Bouzin, C., Feron, O. & Gallez, B. Glucocorticoids modulate tumor radiation response through a decrease in tumor oxygen consumption. *Clin. Cancer Res.* **13,** 630–635 (2007).

14. Snyder, S. A., Lanzen, J. L., Braun, R. D., Rosner, G., Secomb, T. W., Biaglow, J., Brizel, D. M. & Dewhirst, M. W. Simultaneous administration of glucose and hyperoxic gas achieves greater improvement in tumor oxygenation than hyperoxic gas alone. *Int. J. Radiat. Oncol. Biol. Phys.* **51,** 494–506 (2001).

15. Song, C. W., Park, H. J., Lee, C. K. & Griffin, R. Implications of increased tumor blood flow and oxygenation caused by mild temperature hyperthermia in tumor treatment. *Int. J. Hyperth.* **21,** 761–767 (2005).

16. Kim, J., Cho, H. R., Jeon, H., Kim, D., Song, C., Lee, N., Choi, S. H. & Hyeon, T. Continuous O2-Evolving MnFe2O4 Nanoparticle-Anchored Mesoporous Silica Nanoparticles for Efficient Photodynamic Therapy in Hypoxic Cancer. *J. Am. Chem. Soc.* **139,** 10992–10995 (2017).

17. Zhu, W., Dong, Z., Fu, T., Liu, J., Chen, Q., Li, Y., Zhu, R., Xu, L. & Liu, Z. Modulation of Hypoxia in Solid Tumor Microenvironment with MnO2 Nanoparticles to Enhance Photodynamic Therapy. *Adv. Funct. Mater.* **26,** 5490–5498 (2016).

18. Huang, C. C., Chia, W. T., Chung, M. F., Lin, K. J., Hsiao, C. W., Jin, C., Lim, W. H., Chen, C. C. & Sung, H. W. An Implantable Depot That Can Generate Oxygen in Situ for Overcoming Hypoxia-Induced Resistance to Anticancer Drugs in Chemotherapy. *J. Am. Chem. Soc.* **138,** 5222–5225 (2016).

19. Varlotto, J. & Stevenson, M. A. Anemia, tumor hypoxemia, and the cancer patient. *Int. J. Radiat. Oncol. Biol. Phys.* **63,** 25–36 (2005).

20. Jahr, J. S., Nesargi, S. B., Lewis, K. & Johnson, C. Blood substitutes and oxygen therapeutics: an overview and current status. *Am. J. Ther.* **9,** 437–443 (2002).

21. Alayash, A. I. Hemoglobin-based blood substitutes: Oxygen carriers, pressor agents, or oxidants? *Nat. Biotechnol.* **17,** 545–549 (1999).

22. Haruki, R., Kimura, T., Iwasaki, H., Yamada, K., Kamiyama, I., Kohno, M., Taguchi, K., Nagao, S., Maruyama, T., Otagiri, M. & Komatsu, T. Safety Evaluation of Hemoglobin-Albumin Cluster 'HemoAct' as a Red Blood Cell Substitute. *Sci. Rep.* **5,** 1–9 (2015).

23. Alayash, A. I. Blood substitutes: Why haven't we been more successful? *Trends Biotechnol.* **32,** 177–185 (2014).

24. Jahr, J. S., Guinn, N. R., Lowery, D. R., Shore-Lesserson, L. & Shander, A. Blood Substitutes and Oxygen Therapeutics. *Anesth. Analg.* **132,** 119–129 (2021).

25. Chen, J. Y., Scerbo, M. & Kramer, G. A review of blood substitutes: Examining the history, clinical trial results, and ethics of hemoglobin-based oxygen carriers. *Clinics* **64,** 803–813 (2009).

26. Riess, J. G. Understanding the fundamentals of perfluorocarbons and perfluorocarbon emulsions relevant to in vivo oxygen delivery. *Artif. Cells. Blood Substit. Immobil. Biotechnol.* **33,** 47–63 (2005).

27. Lowe, K. C. *Fluosol®. The first commercial injectable perfluorocarbon oxygen carrier*. *Blood Substitutes* (Woodhead Publishing Limited, 2006).

28. Latson, G. W. Perftoran (Vidaphor)-Introduction to Western medicine. *Shock* **52,** 65–69 (2019).

29. Krafft, M. P. & Riess, J. G. Therapeutic oxygen delivery by perfluorocarbon-based colloids Marie. *Adv. Colloid Interface Sci.* **294,** 102407 (2021).

30. Castro, C. I. & Briceno, J. C. Perfluorocarbon-based oxygen carriers: Review of products and trials. *Artif. Organs* **34,** 622–634 (2010).

31. Nozue, M., Lee, I., Manning, J. M., Manning, L. R. & Jain, R. K. Oxygenation in tumors by modified hemoglobins. *J. Surg. Oncol.* **62,** 109–114 (1996).

32. Horinouchi, H., Yamamoto, H., Komatsu, T., Huang, Y., Tsuchida, E. & Kobayashi, K. Enhanced radiation response of a solid tumor with the artificial oxygen carrier 'albumin-heme'. *Cancer Sci.* **99,** 1274–1278 (2008).

33. Yu, M., Dai, M., Liu, Q. & Xiu, R. Oxygen carriers and cancer chemo- and radiotherapy sensitization: Bench to bedside and back. *Cancer Treat. Rev.* **33,** 757–761 (2007).

34. Zhao, H., Li, L., Zheng, C., Hao, Y., Niu, M., Hu, Y., Chang, J., Zhang, Z. & Wang, L. An intelligent dual stimuli-responsive photosensitizer delivery system with O2-supplying for efficient photodynamic therapy. *Colloids Surfaces B Biointerfaces* **167,** 299–309 (2018).

35. Song, R., Peng, S., Lin, Q., Luo, M., Chung, H. Y., Zhang, Y. & Yao, S. PH-Responsive Oxygen Nanobubbles for Spontaneous Oxygen Delivery in Hypoxic Tumors. *Langmuir* **35,** 10166–10172 (2019).

36. Song, G., Liang, C., Yi, X., Zhao, Q., Cheng, L., Yang, K. & Liu, Z. Perfluorocarbon-Loaded Hollow Bi2Se3 Nanoparticles for Timely Supply of Oxygen under Near-Infrared Light to Enhance the Radiotherapy of Cancer. *Adv. Mater.* **28,** 2716–2723 (2016).

37. Ferrara, K., Pollard, R. & Borden, M. Ultrasound Microbubble Contrast Agents: Fundamentals and Application to Gene and Drug Delivery. *Annu. Rev. Biomed. Eng.* **9,** 415–447 (2007).

38. Sirsi, S. R. & Borden, M. A. State-of-the-art materials for ultrasound-triggered drug delivery. *Adv. Drug Deliv. Rev.* **72,** 3–14 (2014).

39. Liu, L., Chang, S., Sun, J., Zhu, S., Yin, M., Zhu, Y., Wang, Z. & Xu, R. X. Ultrasound-mediated destruction of paclitaxel and oxygen loaded lipid microbubbles for combination therapy in ovarian cancer xenografts. *Cancer Lett.* **361,** 147–154 (2015).

40. Yang, C., Xiao, H., Sun, Y., Zhu, L., Gao, Y., Kwok, S., Wang, Z. & Tang, Y. Lipid Microbubbles as Ultrasound-Stimulated Oxygen Carriers for Controllable Oxygen Release for Tumor Reoxygenation. *Ultrasound Med. Biol.* **44,** 416–425 (2018).

41. McEwan, C., Kamila, S., Owen, J., Nesbitt, H., Callan, B., Borden, M., Nomikou, N., Hamoudi, R. A., Taylor, M. A., Stride, E., McHale, A. P. & Callan, J. F. Combined sonodynamic and antimetabolite therapy for the improved treatment of pancreatic cancer using oxygen loaded microbubbles as a delivery vehicle. *Biomaterials* **80,** 20–32 (2016).

42. McEwan, C., Owen, J., Stride, E., Fowley, C., Nesbitt, H., Cochrane, D., Coussios, C. C., Borden, M., Nomikou, N., McHale, A. P. & Callan, J. F. Oxygen carrying microbubbles for

enhanced sonodynamic therapy of hypoxic tumours. *J. Control. Release* **203,** 51–56 (2015).

43. Chang, S., Si, T., Zhang, S., Merrick, M. A., Cohn, D. E. & Xu, R. X. Ultrasound mediated destruction of multifunctional microbubbles for image guided delivery of oxygen and drugs. *Ultrason. Sonochem.* **28,** 31–38 (2016).

44. Kwan, J. J., Kaya, M., Borden, M. A. & Dayton, P. A. Theranostic oxygen delivery using ultrasound and microbubbles. *Theranostics* **2,** 1174–1184 (2012).

45. Fix, S. M., Borden, M. A. & Dayton, P. A. Therapeutic gas delivery via microbubbles and liposomes. *J. Control. Release* **209,** 139–149 (2015).

46. Eisenbrey, J. R., Albala, L., Kramer, M. R., Daroshefski, N., Brown, D., Liu, J. Bin, Stanczak, M., O'Kane, P., Forsberg, F. & Wheatley, M. A. Development of an ultrasound sensitive oxygen carrier for oxygen delivery to hypoxic tissue. *Int. J. Pharm.* **478,** 361–367 (2015).

47. Schad, K. C. & Hynynen, K. In vitro characterization of perfluorocarbon droplets for focused ultrasound therapy. *Phys. Med. Biol.* **55,** 4933–4947 (2010).

48. Krupka, T. M., Solorio, L., Wilson, R. E., Wu, H., Azar, N. & Exner, A. A. Formulation and characterization of echogenic lipid-pluronic nanobubbles. *Mol. Pharm.* **7,** 49–59 (2010).

49. Abdalkader, R., Kawakami, S., Unga, J., Higuchi, Y., Suzuki, R., Maruyama, K., Yamashita, F. & Hashida, M. The development of mechanically formed stable nanobubbles intended for sonoporation-mediated gene transfection. *Drug Deliv.* **24,** 320–327 (2017).

50. Cavalli, R., Bisazza, A., Rolfo, A., Balbis, S., Madonnaripa, D., Caniggia, I. & Guiot, C. Ultrasound-mediated oxygen delivery from chitosan nanobubbles. *Int. J. Pharm.* **378,** 215–217 (2009).

51. Bhandari, P. N., Cui, Y., Elzey, B. D., Goergen, C. J., Long, C. M. & Irudayaraj, J. Oxygen nanobubbles revert hypoxia by methylation programming. *Sci. Rep.* **7,** 1–14 (2017).

52. Khan, M. S., Hwang, J., Seo, Y., Shin, K., Lee, K., Park, C., Choi, Y., Hong, J. W. & Choi, J. Engineering oxygen nanobubbles for the effective reversal of hypoxia. *Artif. Cells, Nanomedicine Biotechnol.* **46,** S318–S327 (2018).

53. Owen, J., Logan, K., Nesbitt, H., Able, S., Vasilyeva, A., Bluemke, E., Kersemans, V., Smart, S., Vallis, K. A., McHale, A. P., Callan, J. F. & Stride, E. Orally administered oxygen

nanobubbles enhance tumor response to sonodynamic therapy. *Nano Sel.* **3,** 394–401 (2022).

54. Dijkhuizen, P., Buursma, A., Fongers, T. M. E., Gerding, A. M., Oeseburg, B. & Zijlstra, W. G. The oxygen binding capacity of human haemoglobin - Hüfner's factor redetermined. *Pflügers Arch. Eur. J. Physiol.* **369,** 223–231 (1977).

55. Winslow, R. M. Blood substitutes. *Curr. Opin. Hematol.* **9,** 146–151 (2002).

56. Sander, R. Compilation of Henry's law constants (version 4.0) for water as solvent. *Atmos. Chem. Phys.* **15,** 4399–4981 (2015).

57. Dias, A. M. A., Freire, M., Coutinho, J. A. P. & Marrucho, I. M. Solubility of oxygen in liquid perfluorocarbons. *Fluid Phase Equilib.* **222–223,** 325–330 (2004).

58. Millard, R. W. Oxygen solubility, rheology and hemodynamics of perfluorocarbon emulsion blood substitutes. *Artif. Cells, Blood Substitutes, Biotechnol.* **22,** 235–244 (1994).

59. Hsia, C. C. W. Respiratory Function of Hemoglobin. *N. Engl. J. Med.* **338,** 239–247 (1998).

60. Dunn, J. O. C., Mythen, M. G. & Grocott, M. P. Physiology of oxygen transport. *BJA Educ.* **16,** 341–348 (2016).

61. Hall, C., Lueshen, E., Mošat', A. & Linninger, A. A. Interspecies scaling in pharmacokinetics: A novel whole-body physiologically based modeling framework to discover drug biodistribution mechanisms in vivo. *J. Pharm. Sci.* **101,** 1221–1241 (2012).

62. Dohm, M. R., Hayes, J. P. & Garland, T. The quantitative genetics of maximal and basal rates of oxygen consumption in mice. *Genetics* **159,** 267–277 (2001).

63. Zeng, Q., Qiao, L., Cheng, L., Li, C., Cao, Z., Chen, Z., Wang, Y. & Liu, J. Perfluorohexane-Loaded Polymeric Nanovesicles with Oxygen Supply for Enhanced Sonodynamic Therapy. *ACS Biomater. Sci. Eng.* **6,** 2956–2969 (2020).

64. Eisenbrey, J. R., Shraim, R., Liu, J. Bin, Li, J., Stanczak, M., Oeffinger, B., Leeper, D. B., Keith, S. W., Jablonowski, L. J., Forsberg, F., O'Kane, P. & Wheatley, M. A. Sensitization of Hypoxic Tumors to Radiation Therapy Using Ultrasound-Sensitive Oxygen Microbubbles. *Int. J. Radiat. Oncol. Biol. Phys.* **101,** 88–96 (2018).

65. Delaney, L. J., Ciraku, L., Oeffinger, B. E., Wessner, C. E., Liu, J. Bin, Li, J., Nam, K., Forsberg,

F., Leeper, D. B., O'Kane, P., Wheatley, M. A., Reginato, M. J. & Eisenbrey, J. R. Breast Cancer Brain Metastasis Response to Radiation After Microbubble Oxygen Delivery in a Murine Model. *J. Ultrasound Med.* **38,** 3221–3228 (2019).

66. Pu, C., Chang, S., Sun, J., Zhu, S., Liu, H., Zhu, Y., Wang, Z. & Xu, R. Ultrasound-Mediated Destruction of LHRHa-Targeted and Paclitaxel- Loaded Lipid Microbubbles for the Treatment of Intraperitoneal Ovarian Cancer Xenografts. *Mol. Pharm.* **11,** 49–58 (2014).

67. Sun, J., Yin, M., Zhu, S., Liu, L., Zhu, Y., Wang, Z., Xu, R. X. & Chang, S. Ultrasound-mediated destruction of oxygen and paclitaxel loaded lipid microbubbles for combination therapy in hypoxic ovarian cancer cells. *Ultrason. Sonochem.* **28,** 319–326 (2016).

68. Ho, Y. J., Chu, S. W., Liao, E. C., Fan, C. H., Chan, H. L., Wei, K. C. & Yeh, C. K. Normalization of tumor vasculature by oxygen microbubbles with ultrasound. *Theranostics* **9,** 7370–7383 (2019).

69. Lea-Banks, H., O'Reilly, M. A. & Hynynen, K. Ultrasound-responsive droplets for therapy: A review. *J. Control. Release* **293,** 144–154 (2019).

70. Haworth, K. J., Arunkumar, P., Goldstein, B. H., Su, H., Mercado-Shekhar, K. P., Privitera, E. M., Srivastava, R., Holland, C. K. & Redington, A. N. Dissolved oxygen scavenging by acoustic droplet vaporization using intravascular ultrasound. *IEEE Int. Ultrason. Symp. IUS* 0–3 (2017).

71. Radhakrishnan, K., Holland, C. K. & Haworth, K. J. Scavenging dissolved oxygen via acoustic droplet vaporization. *Ultrason. Sonochem.* **31,** 394–403 (2016).

72. Mercado-Shekhar, K. P., Su, H., Kalaikadal, D. S., Lorenz, J. N., Manglik, R. M., Holland, C. K., Redington, A. N. & Haworth, K. J. Acoustic droplet vaporization-mediated dissolved oxygen scavenging in blood-mimicking fluids, plasma, and blood. *Ultrason. Sonochem.* **56,** 114–124 (2019).

73. Song, X., Feng, L., Liang, C., Yang, K. & Liu, Z. Ultrasound Triggered Tumor Oxygenation with Oxygen-Shuttle Nanoperfluorocarbon to Overcome Hypoxia-Associated Resistance in Cancer Therapies. *Nano Lett.* **16,** 6145–6153 (2016).

74. Huang, B., Chen, S., Pei, W., Xu, Y., Jiang, Z., Niu, C. & Wang, L. Oxygen-Sufficient Nanoplatform for Chemo-Sonodynamic Therapy of Hypoxic Tumors. *Front. Chem.* **8,** 1–13

(2020).

75. Padnick, L. B., Linsenmeier, R. A. & Goldstick, T. K. Perfluorocarbon emulsion improves oxygenation of the cat primary visual cortex. *J. Appl. Physiol.* **86,** 1497–1504 (1999).

76. Spiess, B. D. Basic mechanisms of gas transport and past research using perfluorocarbons. *Diving Hyperb. Med.* **40,** 23–28 (2010).

77. Bush, A. J. A Theoretical Investigation of Oxygen Carriers to Relieve Tissue Hypoxia in Cancer Therapy. *MSc Thesis* (2021).

78. Mannaris, C., Bau, L., Grundy, M., Gray, M., Lea-Banks, H., Seth, A., Teo, B., Carlisle, R., Stride, E. & Coussios, C. C. Microbubbles, Nanodroplets and Gas-Stabilizing Solid Particles for Ultrasound-Mediated Extravasation of Unencapsulated Drugs: An Exposure Parameter Optimization Study. *Ultrasound Med. Biol.* **45,** 954–967 (2019).

79. Perevedentseva, E. V., Zaritskiy, A. R., Fok, M. V. & Kuznetsova, I. N. Perfluorocarbon emulsions increase transfer of oxygen in plasma from erythrocyte to tissues. *Artif. Cells. Blood Substit. Immobil. Biotechnol.* **26,** 223–229 (1998).

80. Vaslef, S. N. & Goldstick, T. K. Enhanced Oxygen Delivery Induced by Perfluorocarbon Emulsions in Capillary Tube Oxygenators. *ASAIO J.* **40,** M643-648 (1994).

81. Simon Faithfull, N. & Cain, S. M. Critical levels of O2 extraction following hemodilution with dextran or fluosol-DA. *J. Crit. Care* **3,** 14–18 (1988).

82. Laidig, K. E., Gainer, J. L. & Daggett, V. Altering diffusivity in biological solutions through modification of solution structure and dynamics. *J. Am. Chem. Soc.* **120,** 9394–9395 (1998).

83. Stennett, A. K., Dempsey, G. L. & Gainer, J. L. trans-Sodium crocetinate and diffusion enhancement. *J. Phys. Chem. B* **110,** 18078–18080 (2006).

84. Sheehan, J., Ionescu, A., Pouratian, N., Hamilton, D. K., Schlesinger, D., Oskouian, R. J. & Sansur, C. Use of trans sodium crocetinate for sensitizing glioblastoma multiforme to radiation: Laboratory investigation. *J. Neurosurg.* **108,** 972–978 (2008).

85. Lafond, M., Yoshizawa, S. & Umemura, S. ichiro. Sonodynamic Therapy: Advances and Challenges in Clinical Translation. *J. Ultrasound Med.* **38,** 567–580 (2019).

86. D'ammando, A., Raspagliesi, L., Gionso, M., Franzini, A., Porto, E., Meco, F. Di, Durando, G., Pellegatta, S. & Prada, F. Sonodynamic therapy for the treatment of intracranial gliomas. *J. Clin. Med.* **10,** 1–16 (2021).

87. Dos Santos, A. F., De Almeida, D. R. Q., Terra, L. F., Baptista, M. S. & Labriola, L. Photodynamic therapy in cancer treatment - an update review. *J. Cancer Metastasis Treat.* **2019,** (2019).

88. Yumita, N., Nishigaki, R., Umemura, K. & Umemura, S. Hematoporphyrin as a Sensitizer of Cell-damaging Effect of Ultrasound. *Japanese J. Cancer Res.* **80,** 219–222 (1989).

89. Umemura, S. I., Yumita, N., Nishigaki, R. & Umemura, K. Sonochemical activation of hematoporphyrin: A potential modality for cancer treatment. *Ultrason. Symp. Proc.* **2,** 955–960 (1989).

90. McEwan, C., Nesbitt, H., Nicholas, D., Kavanagh, O. N., McKenna, K., Loan, P., Jack, I. G., McHale, A. P. & Callan, J. F. Comparing the efficacy of photodynamic and sonodynamic therapy in non-melanoma and melanoma skin cancer. *Bioorganic Med. Chem.* **24,** 3023–3028 (2016).

91. Nonaka, M., Yamamoto, M., Yoshino, S., Umemura, S. I., Sasaki, K. & Fukushima, T. Sonodynamic therapy consisting of focused ultrasound and a photosensitizer causes a selective antitumor effect in a rat intracranial glioma model. *Anticancer Res.* **29,** 943–950 (2009).

92. Wang, H., Wang, P., Li, L., Zhang, K., Wang, X. & Liu, Q. Microbubbles enhance the antitumor effects of sinoporphyrin sodium mediated sonodynamic therapy both in vitro and in vivo. *Int. J. Biol. Sci.* **11,** 1401–1409 (2015).

93. Choi, V., Rajora, M. A. & Zheng, G. Activating Drugs with Sound: Mechanisms behind Sonodynamic Therapy and the Role of Nanomedicine. *Bioconjug. Chem.* **31,** 967–989 (2020).

94. Zhang, Y., Zhang, X., Yang, H., Yu, L., Xu, Y., Sharma, A., Yin, P., Li, X., Kim, J. S. & Sun, Y. Advanced biotechnology-assisted precise sonodynamic therapy. *Chem. Soc. Rev.* **50,** 11227–11248 (2021).

95. Beguin, E., Shrivastava, S., Dezhkunov, N. V., Mchale, A. P., Callan, J. F. & Stride, E. Direct

Evidence of Multibubble Sonoluminescence Using Therapeutic Ultrasound and Microbubbles. *ACS Appl. Mater. Interfaces* **11,** 19913–19919 (2019).

96. Garcia-Diaz, M., Huang, Y. Y. & Hamblin, M. R. Use of fluorescent probes for ROS to tease apart Type I and Type II photochemical pathways in photodynamic therapy. *Methods* **109,** 158–166 (2016).

97. Umemura, S. ichiro, Yumita, N., Umemura, K. & Nishigaki, R. Sonodynamically induced effect of rose bengal on isolated sarcoma 180 cells. *Cancer Chemother. Pharmacol.* **43,** 389–393 (1999).

98. Miyoshi, N., Igarashi, T. & Riesz, P. Evidence against singlet oxygen formation by sonolysis of aqueous oxygen-saturated solutions of Hematoporphyrin and Rose Bengal. The mechanism of sonodynamic therapy. *Ultrason. Sonochem.* **7,** 121–124 (2000).

99. Koh, E. & Fluhr, R. Singlet oxygen detection in biological systems: Uses and limitations. *Plant Signal. Behav.* **11,** 1–5 (2016).

100. Liu, H., Carter, P. J. H., Laan, A. C., Eelkema, R. & Denkova, A. G. Singlet Oxygen Sensor Green is not a Suitable Probe for 1O2 in the Presence of Ionizing Radiation. *Sci. Rep.* **9,** 1–8 (2019).

101. Li, E., Sun, Y., Lv, G., Qin, F., Zhang, X., Zhang, Z., Zhang, R., Hu, Z. & Cao, W. The Abnormal Physicochemical Phenomena of Singlet Oxygen Sensor Green in Water in the Presence of Ultrasound. *ChemistrySelect* **6,** 6631–6635 (2021).

102. Barati, A. H., Mokhtari-Dizaji, M., Mozdarani, H., Bathaie, Z. & Hassan, Z. M. Effect of exposure parameters on cavitation induced by low-level dual-frequency ultrasound. *Ultrason. Sonochem.* **14,** 783–789 (2007).

103. Gray, M., Vasilyeva, A. V., Brans, V. & Stride, E. Studying cavitation enhanced therapy. *J. Vis. Exp.* **2021,** 1–25 (2021).

104. Arvanitis, C. D., Bazan-Peregrino, M., Rifai, B., Seymour, L. W. & Coussios, C. C. Cavitation-Enhanced Extravasation for Drug Delivery. *Ultrasound Med. Biol.* **37,** 1838–1852 (2011).

105. Hu, Y., Wan, J. M. F. & Yu, A. C. H. Membrane Perforation and Recovery Dynamics in Microbubble-Mediated Sonoporation. *Ultrasound Med. Biol.* **39,** 2393–2405 (2013).

106. Pepe, J., Rincón, M. & Wu, J. Experimental comparison of sonoporation and

electroporation in cell transfection applications. *Acoust. Res. Lett. Online* **5,** 62–67 (2004).

107. Helfield, B., Chen, X., Watkins, S. C. & Villanueva, F. S. Biophysical insight into mechanisms of sonoporation. *Proc. Natl. Acad. Sci. U. S. A.* **113,** 9983–9988 (2016).

108. van Wamel, A., Kooiman, K., Harteveld, M., Emmer, M., ten Cate, F. J., Versluis, M. & de Jong, N. Vibrating microbubbles poking individual cells: Drug transfer into cells via sonoporation. *J. Control. Release* **112,** 149–155 (2006).

109. Zeghimi, A., Escoffre, J. M. & Bouakaz, A. Role of endocytosis in sonoporation-mediated membrane permeabilization and uptake of small molecules: A electron microscopy study. *Phys. Biol.* **12,** (2015).

110. Delalande, A., Leduc, C., Midoux, P., Postema, M. & Pichon, C. Efficient gene delivery by sonoporation is associated with microbubble entry into cells and the clathrin-dependent endocytosis pathway. *Ultrasound Med. Biol.* **41,** 1913–1926 (2015).

111. Lentacker, I., De Cock, I., Deckers, R., De Smedt, S. C. & Moonen, C. T. W. Understanding ultrasound induced sonoporation: Definitions and underlying mechanisms. *Adv. Drug Deliv. Rev.* **72,** 49–64 (2014).

112. Shi, D., Guo, L., Duan, S., Shang, M., Meng, D., Cheng, L. & Li, J. Influence of tumor cell lines derived from different tissue on sonoporation efficiency under ultrasound microbubble treatment. *Ultrason. Sonochem.* **38,** 598–603 (2017).

113. Riccardi, C. & Nicoletti, I. Analysis of apoptosis by propidium iodide staining and flow cytometry. *Nat. Protoc.* **1,** 1458–1461 (2006).

114. Bloch, S. H., Wan, M., Dayton, P. A. & Ferrara, K. W. Optical observation of lipid- and polymer-shelled ultrasound microbubble contrast agents. *Appl. Phys. Lett.* **84,** 631–633 (2004).

115. Borden, M. A. & Longo, M. L. Oxygen permeability of fully condensed lipid monolayers. *J. Phys. Chem. B* **108,** 6009–6016 (2004).

116. Wei, K., Mulvagh, S. L., Carson, L., Davidoff, R., Gabriel, R., Grimm, R. A., Wilson, S., Fane, L., Herzog, C. A., Zoghbi, W. A., Taylor, R., Farrar, M., Chaudhry, F. A., Porter, T. R., Irani, W. & Lang, R. M. The Safety of Definity and Optison for Ultrasound Image Enhancement: A Retrospective Analysis of 78,383 Administered Contrast Doses. *J. Am. Soc. Echocardiogr.*

21, 1202–1206 (2008).

117. Jokela, M., Virtanen, M., David Batty, G. & Kivimaki, M. Research letter. *JAMA Psychiatry* **73,** 87–88 (2016).

118. Dolan, M. S., Gala, S. S., Dodla, S., Abdelmoneim, S. S., Xie, F., Cloutier, D., Bierig, M., Mulvagh, S. L., Porter, T. R. & Labovitz, A. J. Safety and Efficacy of Commercially Available Ultrasound Contrast Agents for Rest and Stress Echocardiography. A Multicenter Experience. *J. Am. Coll. Cardiol.* **53,** 32–38 (2009).

119. Main, M. L. Ultrasound Contrast Agent Safety. From Anecdote to Evidence. *JACC Cardiovasc. Imaging* **2,** 1057–1059 (2009).

120. Pulsipher, K. W., Hammer, D. A., Lee, D. & Sehgal, C. M. Engineering Theranostic Microbubbles Using Microfluidics for Ultrasound Imaging and Therapy: A Review. *Ultrasound Med. Biol.* **44,** 2441–2460 (2018).

121. De Leon, A., Perera, R., Hernandez, C., Cooley, M., Jung, O., Jeganathan, S., Abenojar, E., Fishbein, G., Sojahrood, A. J., Emerson, C. C., Stewart, P. L., Kolios, M. C. & Exner, A. A. Contrast enhanced ultrasound imaging by nature-inspired ultrastable echogenic nanobubbles. *Nanoscale* **11,** 15647–15658 (2019).

122. Cavalli, R., Bisazza, A., Giustetto, P., Civra, A., Lembo, D., Trotta, G., Guiot, C. & Trotta, M. Preparation and characterization of dextran nanobubbles for oxygen delivery. *Int. J. Pharm.* **381,** 160–165 (2009).

123. Khan, M. S., Hwang, J., Lee, K., Choi, Y., Jang, J., Kwon, Y., Hong, J. W. & Choi, J. Surface composition and preparation method for oxygen nanobubbles for drug delivery and ultrasound imaging applications. *Nanomaterials* **9,** 4–9 (2019).

124. Cai, W. Bin, Yang, H. L., Zhang, J., Yin, J. K., Yang, Y. L., Yuan, L. J., Zhang, L. & Duan, Y. Y. The Optimized Fabrication of Nanobubbles as Ultrasound Contrast Agents for Tumor Imaging. *Sci. Rep.* **5,** 1–11 (2015).

125. Wang, Y., Li, X., Zhou, Y., Huang, P. & Xu, Y. Preparation of nanobubbles for ultrasound imaging and intracelluar drug delivery. *Int. J. Pharm.* **384,** 148–153 (2010).

126. Owen, J., McEwan, C., Nesbitt, H., Bovornchutichai, P., Averre, R., Borden, M., McHale, A. P., Callan, J. F. & Stride, E. Reducing tumour hypoxia via oral administration of oxygen

nanobubbles. *PLoS One* (2016).

127. Sheeran, P. S., Matsuura, N., Borden, M. A., Williams, R., Matsunaga, T. O., Burns, P. N. & Dayton, P. A. Methods of generating submicrometer phase-shift perfluorocarbon droplets for applications in medical ultrasonography. *IEEE Trans. Ultrason. Ferroelectr. Freq. Control* **64,** 252–263 (2017).

128. Zhou, Y. Application of acoustic droplet vaporization in ultrasound therapy. *J. Ther. Ultrasound* **3,** 1–18 (2015).

129. Sheeran, P. S., Yoo, K., Williams, R., Yin, M., Foster, F. S. & Burns, P. N. More Than Bubbles: Creating Phase-Shift Droplets from Commercially Available Ultrasound Contrast Agents. *Ultrasound Med. Biol.* **43,** 531–540 (2017).

130. Sheeran, P. S., Luois, S., Mullin, L., Matsunaga, T. O. & Dayton, P. A. Fluorocarbons. *Biomaterials* **33,** 3262–3269 (2012).

131. Kwan, J. J., Myers, R., Coviello, C. M., Graham, S. M., Shah, A. R., Stride, E., Carlisle, R. C. & Coussios, C. C. Ultrasound-Propelled Nanocups for Drug Delivery. *Small* **11,** 5305–5314 (2015).

132. Kwan, J. J., Graham, S., Myers, R., Carlisle, R., Stride, E. & Coussios, C. C. Ultrasound-induced inertial cavitation from gas-stabilizing nanoparticles. *Phys. Rev. E - Stat. Nonlinear, Soft Matter Phys.* **92,** 1–5 (2015).

133. Thomas, R. G., Jonnalagadda, U. S. & Kwan, J. J. Biomedical Applications for Gas-Stabilizing Solid Cavitation Agents. *Langmuir* **35,** 10106–10115 (2019).

134. Mannaris, C., Teo, B. M., Seth, A., Bau, L., Coussios, C. & Stride, E. Gas-Stabilizing Gold Nanocones for Acoustically Mediated Drug Delivery. *Adv. Healthc. Mater.* **7,** 1–8 (2018).

135. Zhao, Y., Zhu, Y., Fu, J. & Wang, L. Effective cancer cell killing by hydrophobic nanovoid-enhanced cavitation under safe low-energy ultrasound. *Chem. - An Asian J.* **9,** 790–796 (2014).

136. Langeveld, S. A. G., Beekers, I., Collado-Lara, G., van der Steen, A. F. W., de Jong, N. & Kooiman, K. The impact of lipid handling and phase distribution on the acoustic behavior of microbubbles. *Pharmaceutics* **13,** 1–21 (2021).

137. Borden, M. A., Pu, G., Runner, G. J. & Longo, M. L. Surface phase behavior and

microstructure of lipid/PEG-emulsifier monolayer-coated microbubbles. *Colloids Surfaces B Biointerfaces* **35,** 209–223 (2004).

138. Omata, D., Maruyama, T., Unga, J., Hagiwara, F., Munakata, L., Kageyama, S., Shima, T., Suzuki, Y., Maruyama, K. & Suzuki, R. Effects of encapsulated gas on stability of lipid-based microbubbles and ultrasound-triggered drug delivery. *J. Control. Release* **311–312,** 65–73 (2019).

139. Mulvana, H., Stride, E., Tang, M. X., Hajnal, J. V. & Eckersley, R. J. The Influence of Gas Saturation on Microbubble Stability. *Ultrasound Med. Biol.* **38,** 1097–1100 (2012).

140. Truesdale, B. G. A., Downing, A. L. & Lowden, G. F. The solubility of oxygen in pure water and sea-water. *J. Appl. Chem.* **5,** 53–62 (1955).

141. Lowe, K. C., Davey, M. R. & Power, J. B. Perfluorochemicals: Their applications and benefits to cell culture. *Trends Biotechnol.* **16,** 272–277 (1998).

142. Sklodowska, K. & Jakiela, S. Enhancement of bacterial growth with the help of immiscible oxygenated oils. *RSC Adv.* **7,** 40990–40995 (2017).

143. Moolman, F. S., Rolfes, H., Merwe, S. W. Van Der & Focke, W. W. Optimization of perfluorocarbon emulsion properties for enhancing oxygen mass transfer in a bio-artificial liver support system. *Biochem. Eng. J.* **19,** 237–250 (2004).

144. White, J. C., Godsey, M. E. & Bhatia, S. R. Perfluorocarbons enhance oxygen transport in alginate-based hydrogels. *Polym. Adv. Technol.* **25,** 1242–1246 (2014).

145. Lee, Y. H. & Yeh, Y. L. Reduction of oxygen inhibition effect for microalgal growth using fluoroalkylated methoxy polyethylene glycol-stabilized perfluorocarbon nano-oxygen carriers. *Process Biochem.* **50,** 1119–1127 (2015).

146. Junker, B. H., Hatton, T. A. & Wang, D. I. C. Oxygen transfer enhancement in aqueous/perfluorocarbon fermentation systems: I. experimental observations. *Biotechnol. Bioeng.* **35,** 578–585 (1990).

147. Mehra, A. Intensification of multiphase reactions through the use of a microphase-I. theoretical. *Chem. Eng. Sci.* **43,** 899–912 (1988).

148. Ferrell, R. T. & Himmelblau, D. M. Diffusion Coefficients of Nitrogen and Oxygen in Water. *J. Chem. Eng. Data* **12,** 111–115 (1967).

149. Markov, D. A., Lillie, E. M., Garbett, S. P. & McCawley, L. J. Variation in diffusion of gases through PDMS due to plasma surface treatment and storage conditions. *Biomed. Microdevices* **16,** 91–96 (2014).

150. Nasralla, D., Coussios, C. C., Mergental, H., Akhtar, M. Z., Butler, A. J., Ceresa, C. D. L., Chiocchia, V., Dutton, S. J., García-Valdecasas, J. C., Heaton, N., Imber, C., Jassem, W., Jochmans, I., Karani, J., Knight, S. R., Kocabayoglu, P., Malagò, M., Mirza, D., Morris, P. J., Pallan, A., Paul, A., Pavel, M., Perera, M. T. P. R., Pirenne, J., Ravikumar, R., Russell, L., Upponi, S., Watson, C. J. E., Weissenbacher, A., Ploeg, R. J. & Friend, P. J. A randomized trial of normothermic preservation in liver transplantation. *Nature* **557,** 50–56 (2018).

151. Hamilton, R. L., Berry, M. N., Williams, M. C. & Severinghaus, E. M. A simple and inexpensive membrane 'lung' for small organ perfusion. *J. Lipid Res.* **15,** 182–186 (1974).

152. Thomas, H. M., Lefrak, S. S., Irwin, R. S., Fritts, H. W. & Caldwell, P. R. B. The oxyhemoglobin dissociation curve in health and disease. Role of 2,3-diphosphoglycerate. *Am. J. Med.* **57,** 331–348 (1974).

153. Zubair, A. C. Clinical impact of blood storage lesions. *Am. J. Hematol.* **85,** 117–122 (2010).

154. Nitzan, M., Nitzan, I. & Arieli, Y. The various oximetric techniques used for the evaluation of blood oxygenation. *Sensors (Switzerland)* **20,** 1–28 (2020).

155. Hill, R. & Wolvekamp, H. P. The oxygen dissociation curve of haemoglobin in dilute solution. *Proc. R. Soc. London. Ser. B - Biol. Sci.* **120,** 484–495 (1936).

156. Ju, L. -K, Lee, J. F. & Armiger, W. B. Effect of the interfacial surfactant layer on oxygen transfer through the oil/water phase boundary in perfluorocarbon emulsions. *Biotechnol. Bioeng.* **37,** 505–511 (1991).

157. Padilla, F. & ter Haar, G. Recommendations for Reporting Therapeutic Ultrasound Treatment Parameters. *Ultrasound Med. Biol.* **00,** 1–10 (2022).

158. Carugo, D., Owen, J., Crake, C., Lee, J. Y. & Stride, E. Biologically and acoustically compatible chamber for studying ultrasound-mediated delivery of therapeutic compounds. *Ultrasound Med. Biol.* **41,** 1927–1937 (2015).

159. Wan, G. Y., Liu, Y., Chen, B. W., Liu, Y. Y., Wang, Y. S. & Zhang, N. Recent advances of sonodynamic therapy in cancer treatment. *Cancer Biol. Med.* **13,** 325–338 (2016).

160. Vanerio, N., Stijnen, M., De Mol, B. A. J. M. & Kock, L. M. Biomedical Applications of Photo- and Sono-Activated Rose Bengal: A Review. *Photobiomodulation, Photomedicine, Laser Surg.* **37,** 383–394 (2019).

161. Sugita, N., Iwase, Y., Yumita, N., Ikeda, T. & Umemura, S. I. Sonodynamically induced cell damage using rose bengal derivative. *Anticancer Res.* **30,** 3361–3366 (2010).

162. Sugita, N., Kawabata, K. I., Sasaki, K., Sakata, I. & Umemura, S. I. Synthesis of amphiphilic derivatives of rose bengal and their tumor accumulation. *Bioconjug. Chem.* **18,** 866–873 (2007).

163. Hiraoka, W., Honda, H., Feril, L. B., Kudo, N. & Kondo, T. Comparison between sonodynamic effect and photodynamic effect with photosensitizers on free radical formation and cell killing. *Ultrason. Sonochem.* **13,** 535–542 (2006).

164. Freinbichler, W., Colivicchi, M. A., Stefanini, C., Bianchi, L., Ballini, C., Misini, B., Weinberger, P., Linert, W., Varešlija, D., Tipton, K. F. & Della Corte, L. Highly reactive oxygen species: Detection, formation, and possible functions. *Cell. Mol. Life Sci.* **68,** 2067–2079 (2011).

165. Gomes, A., Fernandes, E. & Lima, J. L. F. C. Fluorescence probes used for detection of reactive oxygen species. *J. Biochem. Biophys. Methods* **65,** 45–80 (2005).

166. Gollmer, A., Arnbjerg, J., Blaikie, F. H., Pedersen, B. W., Breitenbach, T., Daasbjerg, K., Glasius, M. & Ogilby, P. R. Singlet oxygen sensor green®: Photochemical behavior in solution and in a mammalian cell. *Photochem. Photobiol.* **87,** 671–679 (2011).

167. Lin, H., Shen, Y., Chen, D., Lin, L., Wilson, B. C., Li, B. & Xie, S. Feasibility Study on quantitative measurements of singlet oxygen generation using singlet oxygen sensor green. *J. Fluoresc.* **23,** 41–47 (2013).

168. Shen, Y., Lin, H., Huang, Z., Xiao, L., Chen, D., Li, B. & Xie, S. Kinetic analysis of singlet oxygen generation in a living cell using Singlet Oxygen Sensor Green. *Opt. Heal. Care Biomed. Opt. IV* **7845,** 78451F (2010).

169. Kim, S., Fujitsuka, M. & Majima, T. Photochemistry of singlet oxygen sensor green. *J. Phys. Chem. B* **117,** 13985–13992 (2013).

170. Yuan, Y., Zhang, C. J., Xu, S. & Liu, B. A self-reporting AIE probe with a built-in singlet

oxygen sensor for targeted photodynamic ablation of cancer cells. *Chem. Sci.* **7,** 1862–1866 (2016).

171. Merkel, P. B. & Kearns, D. R. Comment Regarding the Rate Constant for the Reaction between 1.3-Diphenylisobenzofuran and Singlet Oxygen. *J. Am. Chem. Soc.* **49,** 462–463 (1975).

172. Schmitz, C., Aubry, J. M. & Rigaudy, J. A new access to the anthracene core. Synthesis of two water soluble singlet oxygen traps derived from 1,3-diphenylisobenzofuran and 9,10-diphenylanthracene. *Tetrahedron* **38,** 1425–1430 (1982).

173. Amat-Guerri, F., Lempe, E., Lissi, E. A., Rodriguez, F. J. & Trull, F. R. Water-soluble 1,3-diphenylisobenzofuran derivatives. Synthesis and evaluation as singlet molecular oxygen acceptors for biological systems. *J. Photochem. Photobiol. A Chem.* **93,** 49–56 (1996).

174. Appiani, E., Ossola, R., Latch, D. E., Erickson, P. R. & McNeill, K. Aqueous singlet oxygen reaction kinetics of furfuryl alcohol: Effect of temperature, pH, and salt content. *Environ. Sci. Process. Impacts* **19,** 507–516 (2017).

175. Béguin, E. Sonodynamic Therapy of Hypoxic Tumours. *DPhil Thesis* (2018).

176. Chang, C. C., Yang, Y. T., Yang, J. C., Wu, H. Da & Tsai, T. Absorption and emission spectral shifts of rose bengal associated with DMPC liposomes. *Dye. Pigment.* **79,** 170–175 (2008).

177. Orsi, D., Vaccari, M., Baraldi, A. & Cristofolini, L. A portable NIR fluorimeter directly quantifies singlet oxygen generated by nanostructures for Photodynamic Therapy. *Spectrochim. Acta - Part A Mol. Biomol. Spectrosc.* **265,** 120357 (2022).

178. Ho, Y. J., Li, J. P., Fan, C. H., Liu, H. L. & Yeh, C. K. Ultrasound in tumor immunotherapy: Current status and future developments. *J. Control. Release* **323,** 12–23 (2020).

179. Schindelin, J., Arganda-Carreras, I., Frise, E., Kaynig, V., Longair, M., Pietzsch, T., Preibisch, S., Rueden, C., Saalfeld, S., Schmid, B., Tinevez, J. Y., White, D. J., Hartenstein, V., Eliceiri, K., Tomancak, P. & Cardona, A. Fiji: An open-source platform for biological-image analysis. *Nat. Methods* **9,** 676–682 (2012).

180. Aubin, J. E. Autofluorescence of Viable Cultured Mammalian Cells. *J. Histochem. Cytochem.* **27,** 36–43 (1979).

181. Goldstick, T. K., Ciuryla, V. T. & Zuckerman, L. in *Oxyg. Transp. to Tissue - II* (eds. Grote, J.,

Reneau, D. & Thews, G.) 183–190 (Plenum Press, 1976).

182. Lawrence Clever, H., Battino, R., Miyamoto, H., Yampolski, Y. & Young, C. L. IUPAC-NIST Solubility Data Series. 103. Oxygen and Ozone in Water, Aqueous Solutions, and Organic Liquids (Supplement to Solubility Data Series Volume 7). *J. Phys. Chem. Ref. Data* **43,** (2014).

183. Kutsche, I., Gildehaus, G., Schuller, D. & Schumpe, A. Oxygen Solubilities in Aqueous Alcohol Solutions. *J. Chem. Eng. Data* **29,** 286–287 (1984).

184. Battino, R. *Solubiliy Data Series*. *Oxyg. Ozone* **7,** (1981).